

# **Stony Brook University**



OFFICIAL COPY

**The official electronic file of this thesis or dissertation is maintained by the University Libraries on behalf of The Graduate School at Stony Brook University.**

**© All Rights Reserved by Author.**

# Search for jet interactions with quark-gluon plasma

A Dissertation Presented

by

**Chin-Hao Chen**

to

The Graduate School

in Partial Fulfillment of the

Requirements

for the Degree of

**Doctor of Philosophy**

in

**Physics**

**Stony Brook University**

**August 2011**

Copyright by  
**Chin-Hao Chen**  
2011

**Stony Brook University**

The Graduate School

**Chin-Hao Chen**

We, the dissertation committee for the above candidate for the **Doctor of Philosophy** degree, hereby recommend acceptance of this dissertation.

Professor Barbara V. Jacak , Thesis Advisor  
Department of Physics and Astronomy

Professor Edward Shuryak, Chairman of the defense committee  
Department of Physics

Professor Robert L. McCarthy  
Department of Physics and Astronomy

Dr. David Morrison, Outside member  
Department of Physics, Brookhaven National Laboratory

This dissertation is accepted by the Graduate School.

Lawrence Martin  
Dean of the Graduate School

**Abstract of the Dissertation**  
**Search for jet interactions with quark-gluon  
plasma**

by

**Chin-Hao Chen**

**Doctor of Philosophy**

in

**Physics**

**Stony Brook University**

**2011**

A hot, dense QCD medium is created in heavy ion collisions at the Relativistic Heavy Ion Collider at Brookhaven National Laboratory. This new type of matter is opaque to energetic partons, which suffer a strong energy loss in the medium. Two particle correlations are a powerful tool to study the jet properties in the medium and provide information about the energy loss mechanism and jet-medium interactions. When triggering on high  $p_T$  particles, the away-side shape depends strongly on the  $p_T$  of the associated particles.

In this analysis, we present the inclusive photon-hadron two particle azimuthal correlations measured in Au+Au collisions at  $\sqrt{s_{NN}} = 200$  GeV by PHENIX experiment. In order to study jet-medium interactions, we focus on intermediate  $p_T$ , and subtract particle pairs from the underlying event. Jet-like correlations appear modified in central Au+Au compared to p+p, in both the trigger and opposing jet. The trigger jet is elongated in pseudorapidity (the “ridge”), while the opposing jet shows a double peak

structure (“head” and “shoulder”). We decompose the structures in  $\Delta\eta$  and  $\Delta\phi$  to disentangle contributions from the medium and the punch-through and trigger jets. Upon correcting the underlying event for elliptic flow, the ridge is observed for associated particle  $p_T$  below 3 GeV/c; it is broad in rapidity and narrow in  $\Delta\phi$ . The away side correlated particle yield is enhanced in central collisions. The yield of particles in the shoulder grows with centrality while the away side punch-through jet is suppressed. Remarkably, the ridge closely resembles the shoulder in the centrality dependence of particle yield and spectra.

There has been great debate about the origin of the ridge and shoulder. A favored explanation is that the structure is due to features of the collective flow of particles in the underlying event, particularly the fluctuation-driven triangular flow, quantified by the third Fourier component,  $v_3$ . We measure higher order Fourier harmonics in two ways, and use the results to give the shape of particle correlations in the underlying event. We decompose the power spectrum for the medium and for jets measured in p+p collisions.

When including the higher harmonics of the collective flow ( $v_3$ ,  $v_4$ ) in the shape of the underlying events in two particle correlations, the ridge and shoulder no longer exist after subtraction. The jet function in Au+Au looks like p+p in which the away side jet is suppressed and broadened. There is also a pedestal-like structure in the jet function. Since the higher harmonics only change the shape of the underlying background, the pedestal is simply the redistribution of the ridge and shoulder particle yields.

In conclusion, when jets pass through the medium, the away side jet is suppressed and the shape is broadened. This also brings out extra particles with spectra slightly harder than the medium, but softer than jet fragments. These are probably from the jet-medium interaction.

To my parents.

# Contents

List of Figures	ix
List of Tables	xviii
Acknowledgements	xx
<b>I Introduction</b>	<b>1</b>
<b>1 Physics Introduction and Motivation</b>	<b>2</b>
1.1 Quantum Chromodynamics . . . . .	2
1.2 The Quark Gluon Plasma . . . . .	4
1.3 Different Stages of Heavy Ion Collisions . . . . .	5
1.3.1 $0 < \tau < \tau_0$ , Pre-equilibrium and Thermalization . . . . .	6
1.3.2 $\tau_0 < \tau < \tau_f$ , Hydrodynamical Evolution and Freeze-out . . . . .	6
1.3.3 $\tau_f < \tau$ , Freeze-out and Post-equilibrium . . . . .	7
1.4 Definition of terms . . . . .	7
1.5 General Properties of QGP . . . . .	8
1.5.1 Temperature of QGP . . . . .	8
1.5.2 Elliptic Flow . . . . .	9
1.5.3 Jet Quenching . . . . .	11
1.6 Two Particle Correlations . . . . .	14
1.6.1 The Definition of Two Particle Correlations . . . . .	14
1.6.2 High $p_T$ Correlations . . . . .	16
1.6.3 Intermediate $p_T$ correlations . . . . .	17
1.6.4 $\Delta\eta$ - $\Delta\phi$ Correlations . . . . .	19
1.7 Motivation for this Dissertation Work . . . . .	21
<b>2 Experiment</b>	<b>23</b>
2.1 RHIC . . . . .	23
2.2 PHENIX . . . . .	24



2.2.1	Beam Beam Counter and Zero Degree Calorimeter . . .	24
2.2.2	Central Arm . . . . .	26
<b>II Analysis: correlation function</b>		<b>33</b>
<b>3</b>	<b>Correlation Function</b>	<b>34</b>
3.1	Introduction . . . . .	34
3.2	Definition of Correlation Function . . . . .	35
3.3	Data Selection . . . . .	38
3.3.1	Data and Selection . . . . .	38
3.3.2	Analysis Scheme . . . . .	38
3.4	Background Subtraction . . . . .	39
3.5	Measurement of $v_2$ . . . . .	40
3.5.1	Reaction plane resolution, $\Delta$ . . . . .	41
3.5.2	$v_2$ of Inclusive Photons . . . . .	41
3.5.3	$v_2$ of inclusive charged hadron . . . . .	43
3.6	Photon Distribution . . . . .	46
3.7	Normalization . . . . .	48
3.8	Efficiency Correction . . . . .	49
3.9	Multiplicity Cross Check . . . . .	50
3.10	Systematic Error . . . . .	51
<b>4</b>	<b>Decomposing the Correlation Functions</b>	<b>56</b>
4.1	Introduction . . . . .	56
4.2	$\Delta\eta$ - $\Delta\phi$ Correlation Functions . . . . .	56
4.2.1	$\Delta\phi$ Correlation Functions in Different $\Delta\eta$ Region . . .	59
4.3	Near Side Projection along $\Delta\eta$ Direction . . . . .	60
4.4	Extracting the Near Side Yield . . . . .	62
4.5	Ridge Extraction . . . . .	62
4.5.1	Definition of Ridge in PHENIX . . . . .	62
4.5.2	Results . . . . .	67
4.6	Extracting the Away Side Yields . . . . .	69
4.6.1	Decomposing Different Components . . . . .	69
4.6.2	Results . . . . .	72
4.7	Punch Through $I_{AA}$ . . . . .	73
4.8	Comparison of the Ridge, the Shoulder and the Underlying Event Background . . . . .	75
4.8.1	Medium Modification and Comparison of Near-side and Away-side . . . . .	80

4.8.2	Transverse Momentum in Near and Away side . . . . .	85
4.9	Spectra and Truncated Mean $p_T$ . . . . .	88
4.10	Summary . . . . .	89
<b>III Analysis: <math>v_n</math></b>		<b>92</b>
<b>5</b>	<b>Measurement of Effects on Higher Harmonics of the Collective Flow Correlations</b>	<b>93</b>
5.1	Introduction . . . . .	93
5.2	$v_n$ in Event Plane Method . . . . .	94
5.3	Analysis . . . . .	96
5.4	$v_n$ from Correlation Function Method . . . . .	96
5.4.1	Fourier Expansion . . . . .	96
5.4.2	Correlation Functions . . . . .	98
5.4.3	Extracting $c_n$ . . . . .	100
5.4.4	Extracting $v_n$ . . . . .	100
5.5	Factorization of $v_n$ . . . . .	105
5.6	$\Delta\eta$ dependence . . . . .	106
5.7	Comparison with $v_2$ measurements from PHENIX . . . . .	106
5.7.1	$p_T$ vs $N_{part}$ . . . . .	106
5.7.2	$v_2$ vs $p_T$ . . . . .	112
5.7.3	Systematic Uncertainties of $v_n$ . . . . .	114
5.7.4	$v_n\{2P\}$ vs $v_n\{\psi_n\}$ . . . . .	114
5.8	Glauber Monte Carlo Simulation . . . . .	119
5.8.1	Eccentricity and Triangularity . . . . .	121
5.8.2	Glauber Monte Carlo Simulation . . . . .	123
5.8.3	Calculating Eccentricity from Glauber Simulation . . . . .	124
5.8.4	Systematic Error of $\varepsilon_n$ . . . . .	126
5.9	Scaling . . . . .	127
5.9.1	Scaling with $p_T$ Integrated $v_n$ . . . . .	130
5.9.2	Scaling with Glauber $\varepsilon_2$ and $\varepsilon_3$ . . . . .	134
<b>6</b>	<b>Fourier Spectra and Jet Quenching</b>	<b>139</b>
6.1	Introduction . . . . .	139
6.2	Measuring the Fourier Coefficients of the Correlation Function	140
6.2.1	Fourier Coefficients and Correlation Function . . . . .	140
6.2.2	Fourier Spectra of the Jet Function . . . . .	142
6.3	Background Subtraction with Modulations from Higher Harmonics . . . . .	145

6.4	Motivation and Verification of the p+p reference . . . . .	148
6.5	Au+Au Compared with p+p . . . . .	150
<b>IV</b>	<b>Discussion</b>	<b>156</b>
<b>7</b>	<b>Discussion</b>	<b>157</b>
7.1	QGP: the Most Perfect Fluid . . . . .	157
7.1.1	$v_2$ and Geometry . . . . .	158
7.1.2	$v_2$ and Quark Number Scaling . . . . .	158
7.1.3	How Perfect is QGP? Extracting $\eta/s$ . . . . .	160
7.1.4	Further Constraints on $\eta/s$ : $v_n$ . . . . .	164
7.2	$v_n$ in Two Particle Correlation: the Ridge and Shoulder . . . . .	165
7.2.1	The Ridge and Shoulder with $v_2$ -modulated Background Subtraction . . . . .	165
7.2.2	The Ridge, Shoulder and Higher Order $v_n$ Background Modulation . . . . .	166
7.2.3	Ridge, Shoulder and the Energy Loss . . . . .	167
<b>V</b>	<b>Conclusion</b>	<b>169</b>
<b>8</b>	<b>Conclusion</b>	<b>170</b>
	<b>Bibliography</b>	<b>172</b>
<b>A</b>	<b>Flow background shape</b>	<b>178</b>
A.1	Introduction . . . . .	178
A.2	Derivation . . . . .	179

## List of Figures

1.1	The QCD coupling constant, $\alpha_s$ , as a function of the momentum exchange, $Q$ . [1, 2]. . . . .	3
1.2	Energy density, $\varepsilon$ , as a function of temperature from Lattice QCD calculations [5]. $\varepsilon_{SB}/T^4$ represent the Stefan–Boltzmann limit of non–interacting gluon gas. . . . .	5
1.3	Invariant cross section (p+p) and invariant yield (Au+Au) of direct photons as a function of $p_T$ . The black dashed curves are modified power law fit to the p+p data, scaled by the number of binary collisions. Low mass di–electrons excess in Au+Au shows the thermal radiation of QGP [14]. . . . .	10
1.4	When two nuclei collide, the colliding area has an almond–like shape. . . . .	11
1.5	$v_2$ and $v_4$ of inclusive charged hadrons vs $p_T$ of several centralities [19]. . . . .	12
1.6	Hard scattering in a proton-proton collision. The blue arrows are the direction of the protons, the red arrows are the outgoing partons. The upper out going parton fragment into a jet. . . .	13
1.7	$R_{AA}$ of $\pi^0$ vs $p_T$ in various centralities [20]. Error bars are statistical and $p_T$ –uncorrelated errors, boxes around the points indicate $p_T$ –correlated errors. Single box around $R_{AA} = 1$ on the left is the error due to $N_{coll}$ , whereas the single box on the right is the overall normalization error of the p+p reference spectrum. . . . .	15
1.8	Integrated $R_{AA}$ of $\pi^0$ vs $N_{part}$ [20]. The error bars/bands are the same as in Fig. 1.7. The two lines at unity show the errors on $N_{coll}$ . The last two points correspond to partially overlapping centrality bins. . . . .	16
1.9	A typical correlation function. On the top are the jet pairs. On the bottom are uncorrelated underlying backgrounds . . . . .	17
1.10	High $p_T$ $\pi^0$ –h jet correlations in central Au+Au (0–20%) in solid circles and p+p collisions in empty circles [24]. . . . .	18

1.11	Shape of jet functions in Au+Au/Cu+Cu at $\sqrt{S_{NN}} = 200/62.4$ GeV/c at intermediate $p_T$ [22]. . . . .	19
1.12	Shape parameters of jet functions in various colliding systems and energies [22]. RMS(kurtosis) in top panel describes the shape of the away side jet function. D in the bottom panel is used to describe the peak position of the double peak structure.	20
1.13	$\Delta\eta$ - $\Delta\phi$ jet function in central Au+Au (a) and in d+Au (b) [25].	22
2.1	Detector configuration of PHENIX during the 2004 run. Top panel: Beam view; bottom panel: side view. . . . .	25
2.2	The correlations between the charge sum in BBC and the energy in ZDC. The line contains the centrality interval of 5%. The far right region corresponds to centrality 0-5%. . . . .	26
2.3	Shape of the frame of the drift chamber [33]. . . . .	27
2.4	Left: Wire position of a sector of drift chamber. Also a map of the anode plane. Right: Top view of the wire orientation in a sector [33]. . . . .	28
2.5	Illustration of the Hough transform parameters for drift chamber track reconstruction. The outline shows the drift chamber active volume. The circles represent drift chamber hits along the particle trajectory. [35]. . . . .	29
2.6	Vertical view of the pad chamber [33]. . . . .	30
2.7	The structure of the lead scintillator electromagnetic calorimeter [34]. . . . .	31
2.8	The structure of the lead glass calorimeter [34]. . . . .	32
3.1	A typical correlation function. On the top are the jet pairs. On the bottom are uncorrelated underlying backgrounds . . . . .	36
3.2	$\Delta\eta$ - $\Delta\phi$ correlation functions of trigger 2-3 GeV/c, partner 2-3 GeV/c, in p+p, Au+Au at 60-90% and 0-20%. (a): Correlation function before remove the combinatorial background; (b): conditional yield per trigger. . . . .	37
3.3	$v_2$ of the inclusive photon at centrality 0-20%. Red points (CHC) are measurement from this analysis; blue points (an518) are measurements from PHENIX preliminary results [51]. (a): 0-20%; (b): 20-40%; (c): 40-60%; . . . . .	42
3.4	$v_2$ of the inclusive charged hadron at centrality 0-20%. Red points (CHC) are measured in this analysis; blue points (an473) are from PHENIX preliminary results. [52]. (a): 0-20%; (b): 20-40%; (c): 40-60%; . . . . .	44

3.5	Probability distribution of $\pi^0$ generating a 2–3 GeV/c decay photon. . . . .	47
3.6	$\pi^0$ spectra (black) and the $\pi^0$ spectra weighted by the sharkfin (red) at centrality 0–20% . . . . .	48
3.7	$\Delta\eta$ – $\Delta\phi$ jet function of 2–3x1–2 GeV/c, centrality 0–20%, with $v_2$ modulated underlying event background subtracted. . . . .	51
3.8	$\Delta\phi$ correlation function of 2–3x1–2 GeV/c, centrality 0–20%, $0.0 <  \Delta\eta  < 0.7$ . . . . .	52
3.9	$\Delta\phi$ correlation function of 2–3x1–2 GeV/c, centrality 0–20%, $0.0 <  \Delta\eta  < 0.1$ . . . . .	52
3.10	$\Delta\phi$ correlation function of 2–3x1–2 GeV/c, centrality 0–20%, $0.1 <  \Delta\eta  < 0.3$ . . . . .	53
3.11	$\Delta\phi$ correlation function of 2–3x1–2 GeV/c, centrality 0–20%, $0.3 <  \Delta\eta  < 0.5$ . . . . .	53
3.12	$\Delta\phi$ correlation function of 2–3x1–2 GeV/c, centrality 0–20%, $0.5 <  \Delta\eta  < 0.7$ . . . . .	54
3.13	Left: correlation function with (black) and without pc3 veto cut (red). Right: the ratio of the correlation function of (without veto)/(veto). trigger $p_T = 2$ –3 GeV/c, partner $p_T = 1$ –2 GeV/c, and centrality = 0–90. . . . .	55
4.1	$\Delta\eta$ – $\Delta\phi$ correlation functions of trigger 2–3 GeV/c, partner 1–2 GeV/c, in p+p, Au+Au at 60–90% and 0–20%. (a): Correlation function before removing combinatorial background; (b): conditional yield per trigger. . . . .	57
4.2	$\Delta\eta$ – $\Delta\phi$ correlation functions of trigger 2–3 GeV/c, partner 2–3 GeV/c, in p+p, Au+Au at 60–90% and 0–20%. (a): Correlation function before remove the combinatorial background; (b): conditional yield per trigger. . . . .	58
4.3	Peripheral Au+Au (60–90%) and p+p conditional per trigger yield in different $\Delta\eta$ regions for trigger $p_T = 2.0 - 3.0$ GeV/c and partner $p_T = 1.0 - 2.0$ GeV/c. Au+Au (p+p) data are shown by solid circles (squares). . . . .	59
4.4	The same as Fig. 4.3, but for central Au+Au collisions (0–20%).	60
4.5	Near side $\Delta\eta$ correlations of Au+Au (circles) and p+p (squares). (a): various centralities for trigger $p_T = 2.0 - 3.0$ GeV/c, partner $p_T = 1.0 - 2.0$ GeV/c; (b): Au+Au at 0–20% and p+p for for various partner $p_T$ bins. . . . .	61

4.6	The Near side per trigger yields for various partner $p_T$ and in different regions $\Delta\eta$ versus $N_{part}$ . Trigger photon $p_T = 2.0 - 3.0$ GeV/c. Gray shade bands are the systematic errors from ZYAM and $v_2$ (Au+Au). The data points are shifted a bit to avoid overlap. . . . .	63
4.7	Jet broadening case, where the jet yield in the nearside is fixed and fit the jet width of the near side. Near side jet widths are plotted as a function of $N_{part}$ and partner $p_T$ . . . . .	66
4.8	Near side jet suppression case. The jet width in near side is unmodified and fit the nearside jet yield Near side jet yields, $N^{AB}$ are plotted as a function of $N_{part}$ and partner $p_T$ . . . . .	67
4.9	Ridge yields extracted by $Y_{ridge} = Y_{Au+Au,near} - Y_{p+p,near}$ for trigger $p_T = 2.0 - 3.0$ GeV/c and various partner $p_T$ in two different $\Delta\eta$ region ( $0 <  \Delta\eta  < 0.7$ and $0.5 <  \Delta\eta  < 0.7$ ). The brown lines apply to $0.5 <  \Delta\eta  < 0.7$ and is the systematic error due to physics assumptions regarding ridge/jet modification interplay described in the text . . . . .	68
4.10	The width of the head component (punch through jet), $\sigma^{head}$ , by fitting jet function with Eq. 4.5. trigger $p_T = 2.0 - 3.0$ GeV/c, partner $p_T = 1.0 - 2.0$ GeV/c. . . . .	70
4.11	The position of the shoulder, D, from fitting with Eq. 4.5. Trigger $p_T = 2.0-3.0$ GeV/c, partner $p_T = 1.0-2.0$ GeV/c . . . . .	71
4.12	Fitting of the per trigger yield in the away side. Trigger $p_T = 2.0-3.0$ GeV/c, partner $p_T = 1.0-2.0$ GeV/c, centrality 0-20% . . . . .	73
4.13	Per trigger yield of away side components: head, shoulder and total away side, vs $N_{part}$ . Trigger $p_T = 2.0 - 3.0$ GeV/c and various partner $p_T$ . Gray shaded band represents the combined systematic error from ZYAM and $v_2$ . . . . .	74
4.14	Punch through $I_{AA}$ for trigger $p_T = 2.0 - 3.0$ GeV/c and various partner $p_T$ vs $N_{part}$ . . . . .	76
4.15	Punch through $I_{AA}$ for trigger $p_T = 2.0 - 3.0$ GeV/c in various centrality vs partner $p_T$ . . . . .	77
4.16	Ratios of the ridge yield to the underlying event in near side as a function of $N_{part}$ for different partner $p_T$ bins. . . . .	78
4.17	Ratios of the shoulder yield to the underlying event in away side as a function of $N_{part}$ for different partner $p_T$ bins. . . . .	79
4.18	Ratios of the ridge (shoulder) yield to the underlying event as a function of $N_{part}$ for different partner $p_T$ bins. . . . .	79

4.19	Yields of ridge and shoulder vs. $N_{part}$ at trigger $p_T = 2.0 - 3.0$ GeV/c and various partner $p_T$ . The green lines are the estimated systematic error of the ridge yields due to physics assumptions regarding the jet contamination and modification discussed in the text. . . . .	81
4.20	Normalized ridge yield vs $N_{part}$ . The green lines are the estimated systematic error of the ridge yields due to physics assumptions regarding the jet contamination and modification discussed in the text . . . . .	82
4.21	Normalized shoulder yield vs $N_{part}$ in different partner $p_T$ . . .	82
4.22	Yields of ridge and shoulder vs. $N_{part}$ at trigger $p_T = 2.0 - 3.0$ GeV/c and partner $p_T = 1.0 - 2.0$ GeV/c. The brown lines are the estimated systematic error of the ridge yields due to physics assumptions regarding the jet contamination and modification discussed in the text. . . . .	83
4.23	Ratio of the yields of shoulder over ridge vs. $N_{part}$ at trigger $p_T = 2.0 - 3.0$ GeV/c and partner $p_T = 1.0 - 2.0$ GeV/c. The green lines are the estimated systematic error of the ridge yields due to physics assumptions regarding the jet contamination and modification discussed in the text. The average value of the ratio shown by the straight line is 1.29. . . . .	84
4.24	$p_T$ weighted yields of ridge and shoulder vs. $N_{part}$ at trigger $p_T = 2.0 - 3.0$ GeV/c and partner $p_T = 1.0 - 2.0$ GeV/c . . . . .	85
4.25	$p_T$ weighted yields of near and away side vs. $N_{part}$ . Trigger $p_T = 2.0 - 3.0$ GeV/c and partner $p_T = 1.0 - 2.0$ GeV/c . . . . .	87
4.26	$p_T$ weighted yields of near and away side vs. $N_{part}$ . Trigger $p_T = 2.0 - 3.0$ GeV/c and partner $p_T = 1.0 - 5.0$ GeV/c . . . . .	87
4.27	Spectra of ridge, shoulder and head for trigger $p_T = 2.0 - 3.0$ GeV/c. . . . .	90
4.28	Truncated mean $p_T$ of spectra of ridge, shoulder and head for trigger $p_T = 2.0 - 3.0$ GeV/c and partner $p_T = 1-5$ GeV/c. . .	91
5.1	Raw correlation strengths of the event planes for various detector combinations as a function of collision centrality. The event planes are measured with the following forward detectors: (a) RXN North, (b) BBC South, (c) MPC North, and (d) MPC South. . . . .	95
5.2	$v_n\{\Psi_n\}$ vs. $p_T$ measured via the event plane method. The curves are calculations from two hydrodynamic models: Alver <i>et al.</i> [67] and Schenke <i>et al.</i> [70]. . . . .	97



5.3	Correlation functions for trigger and partner at 0.5–0.6 GeV/c at various centralities. The blue curve is the sum of the Fourier spectra. . . . .	99
5.4	Correlation functions for trigger and partner at 1.5–2.0 GeV/c at various centralities. The blue curve is the sum of the Fourier spectra. . . . .	99
5.5	$c_n$ for trigger and partner at 1.5–2.0 GeV/c at various centralities.	100
5.6	$v_1$ of various $p_T$ as a function of $N_{part}$ . . . . .	101
5.7	$v_2$ of various $p_T$ as a function of $N_{part}$ . The dash lines are $v_2$ measurements from [19]. . . . .	102
5.8	$v_3$ of various $p_T$ as a function of $N_{part}$ . . . . .	102
5.9	$v_4$ of various $p_T$ as a function of $N_{part}$ . . . . .	103
5.10	$v_1$ of various centralities as a function of $p_T$ . . . . .	103
5.11	$v_2$ of various centralities as a function of $p_T$ . The dash lines are $v_2$ measurements from reference [19]. . . . .	104
5.12	$v_3$ of various centralities as a function of $p_T$ . . . . .	104
5.13	$v_4$ of various centralities as a function of $p_T$ . . . . .	105
5.14	Comparison between $v_2$ values from method 1 (symmetric $p_T$ , red) and method 2 (asymmetric $p_T$ , black). Centralities from 0–10% to 50–60%. The bottom panel shows the ratio between black and red (black/red-1). . . . .	107
5.15	Comparison between $v_3$ values from method 1 (symmetric $p_T$ , red) and method 2 (asymmetric $p_T$ , black). Centralities from 0–10% to 50–60%. The bottom panel shows the ratio between black and red (black/red-1). . . . .	108
5.16	Comparison between $v_2$ values from $\Delta\eta = 0.3$ (red) and $\Delta\eta = 0.5$ (black). Centralities from 0–10% to 50–60%. The bottom panel shows the percentage deviation from $\Delta\eta = 0.3$ . . . . .	109
5.17	Same as Fig. 5.16, but comparing $v_3$ . . . . .	110
5.18	Same as Fig. 5.16, but comparing $v_4$ . . . . .	111
5.19	$v_2$ in this analysis (black points) compared with $v_2$ measured by reaction plane method (dashline) [19]. Inclusive charged hadrons with $p_T = 0.5$ –0.8 GeV/c. . . . .	113
5.20	Ratio between $v_2\{2P\}$ value in this analysis and $v_2\{\psi_2^{MPC}\}$ , where the second event plane, $\psi_2$ , is determined by the Muon Piston Calorimeter (MPC) in [19]. . . . .	114
5.21	Ratio between $v_2\{2P\}$ value in this analysis and $v_2\{\psi_2^{RXNo}\}$ , where the second event plane, $\psi_2$ , is determined by the outer sector of the Reaction Plane Detector (RXNo) in [19]. . . . .	115

5.22	Ratio between $v_2\{2P\}$ value in this analysis and $v_2\{\psi_2^{RXNiO}\}$ in [19] with various centralities. . . . .	115
5.23	Same as Fig. 5.22, only the Y range is changed. . . . .	116
5.24	$v_2$ vs $p_T$ . The final $v_2$ curve is plotted in pink, along with 4 other methods. . . . .	117
5.25	$v_3$ vs $p_T$ . The final $v_3$ curve is plotted in pink, along with 4 other methods. . . . .	118
5.26	$v_2$ measured by this analysis, $v_2\{2P\}$ (red) and from reference [68], $v_2\{\psi_2\}$ (blue) with systematic error. . . . .	119
5.27	$v_3$ measured by this analysis, $v_3\{2P\}$ (red) and from reference [68], $v_3\{\psi_3\}$ (blue) with systematic error. . . . .	120
5.28	$v_2$ measurement in (a)Au+Au; (b)Cu+Cu; (c) $v_2$ scaled with $p_T$ integrated $v_2$ [18] . . . . .	122
5.29	An example of collision of two gold nuclei in Glauber model. The solid circles are nucleons participating the collision; the dash circles are spectators which do not participating the collision. The solid green (magenta) line is pointing to the direction of $\psi_2$ ( $\psi_3$ ). The dashlines are the 2 (3) fold symmetry directions of $\psi_2$ ( $\psi_3$ ). . . . .	124
5.30	Participant eccentricity $\varepsilon_2$ vs $N_{part}$ . . . . .	125
5.31	Participant eccentricity $\varepsilon_3$ vs $N_{part}$ . . . . .	125
5.32	Average participant eccentricity $\varepsilon_1$ to $\varepsilon_3$ as function of $N_{part}$ . . . . .	126
5.33	Participant eccentricity $\varepsilon_2$ compared with various systematic checks . . . . .	127
5.34	Ratios of Participant eccentricity $\varepsilon_2$ compared with various systematic checks. The green band is the final systematic errors . . . . .	128
5.35	Participant eccentricity $\varepsilon_3$ compared with various systematic checks . . . . .	128
5.36	Ratios of Participant eccentricity $\varepsilon_3$ compared with various systematic checks. The green band is the final systematic errors . . . . .	129
5.37	$v_2$ of various centralities as a function of $p_T$ . Dash lines are PPG098 measurement. . . . .	131
5.38	$v_2/(p_T$ integrated $v_2)$ vs $p_T$ in various centralities . . . . .	132
5.39	$v_2/(p_T$ integrated $v_2)$ vs $N_{part}$ in various $p_T$ bins. . . . .	132
5.40	$v_3$ of various centralities as a function of $p_T$ . . . . .	133
5.41	$v_3/(p_T$ integrated $v_3)$ vs $p_T$ in various centralities . . . . .	133
5.42	$v_3/(p_T$ integrated $v_3)$ vs $N_{part}$ in various $p_T$ bins. . . . .	134
5.43	$v_2/\varepsilon_2$ vs $p_T$ in various centralities. . . . .	136
5.44	$v_2/\varepsilon_2$ vs $N_{part}$ in different $p_T$ bins. . . . .	137
5.45	$v_3/\varepsilon_3$ vs $p_T$ in various centralities. . . . .	137

5.46	$v_3/\varepsilon_3$ vs $N_{part}$ in different $p_T$ bins. . . . .	138
6.1	Per trigger yield jet function of various centralities (black) are compared with Fourier expansion results (red). Trigger $p_T = 2.0-3.0$ GeV/c and partner $p_T = 1.0-2.0$ GeV/c . . . . .	141
6.2	Per trigger yield jet function of various centralities (black) are compared with Fourier expansion results (red). Trigger $p_T = 2.0-3.0$ GeV/c and partner $p_T = 3.0-5.0$ GeV/c . . . . .	141
6.3	Fourier spectra for various centrality in Au+Au collisions. Trigger $p_T = 2.0-3.0$ GeV/c and partner $p_T = 1.0-2.0$ GeV/c, with $v_2$ modulated background shape subtracted. . . . .	143
6.4	Fourier spectra for various centrality in Au+Au collisions. Trigger $p_T = 2.0-3.0$ GeV/c and partner $p_T = 3.0-5.0$ GeV/c, with $v_2$ modulated background shape subtracted. . . . .	144
6.5	Measurements of $v_2, v_3, v_4$ with respect to $\psi_n$ from [68]. . . . .	146
6.6	Correlation functions with different $v_n$ modulated underlying event background subtracted. The left column: $v_2$ modulation; middle column: $v_2$ and $v_3$ modulation; right column: $v_2, v_3$ and $v_4$ modulation. Top panel: correlation function with $v_n$ modulated underlying event background; middle panel: jet function with $v_n$ modulated background subtracted; bottom panel: Fourier spectra of the jet function. . . . .	149
6.7	Fourier Spectra in different simulated p+p like jet scenarios. Black: unmodified p+p jet; red: awayside jet yield is fully suppressed; green: awayside yield is suppressed by 50%; blue: awayside jet width is broadened by 50%; yellow: the awayside jet yield is suppressed by 50% and the jet width is broadened by 50%. . . . .	150
6.8	$C_0$ from Au+Au in different as a function of $N_{part}$ compare with two p+p references in different partner $p_T$ . . . . .	152
6.9	$C_2$ from Au+Au in different as a function of $N_{part}$ compare with two p+p references in different partner $p_T$ . . . . .	153
6.10	$C_3$ from Au+Au in different as a function of $N_{part}$ compare with two p+p references in different partner $p_T$ . . . . .	154
6.11	$C_4$ from Au+Au in different as a function of $N_{part}$ compare with two p+p references in different partner $p_T$ . . . . .	155
7.1	$v_2$ measurement in (a)Au+Au; (b)Cu+Cu; (c) $v_2$ scaled with $p_T$ integrated $v_2$ [18] . . . . .	159

7.2	(a) $v_2$ vs $p_T$ and (b) $v_2$ vs $KE_T$ of identified charged hadrons in min-bias Au+Au collisions [18]. STAR data from [79, 80] . . .	160
7.3	Quark number scaling of identified charged hadrons: (a) $v_2/n_q$ vs $p_T/n_q$ and (b) $v_2/n_q$ vs $KE_T/n_q$ [18]. STAR data from [79, 80] . . . . .	161
7.4	Flow calculations with different initial state conditions with various $\eta/s$ [83]. The data is from STAR [84] . . . . .	163
7.5	$v_2$ and $v_3$ compared with various theory calculations in Au+Au [68] . . . . .	165

## List of Tables

3.1	The reaction plane resolution, $\Delta$ , in various centrality . . . . .	41
3.2	$v_2$ of the inclusive photon in various centrality at $p_T = 2-3$ GeV/c	41
3.3	$v_2$ of the inclusive charged hadron in various centrality at $p_T =$ 1.0–1.5 GeV/c . . . . .	43
3.4	$v_2$ of the inclusive charged hadron in various centrality at $p_T =$ 1.5–2.0 GeV/c . . . . .	43
3.5	$v_2$ of the inclusive charged hadron in various centrality at $p_T =$ 1.0–2.0 GeV/c . . . . .	45
3.6	$v_2$ of the inclusive charged hadron in various centrality at $p_T =$ 2.0–3.0 GeV/c . . . . .	45
3.7	$v_2$ of the inclusive charged hadron in various centrality at $p_T =$ 3.0–5.0 GeV/c . . . . .	45
3.8	The average $p_T$ of $\pi^0$ which decays to a 2–3 GeV/c photon . .	47
3.9	Efficiency of AuAu and pp in various $p_T$ and centrality bins. .	50
4.1	$\chi^2$ table for different fitting method (Degrees of freedom = 5)	66
4.2	The p+p away side width in different partner $p_T$ bins. Trigger $p_T = 2-3$ GeV/c . . . . .	72
4.3	The shoulder displacement, $D(p_T)$ , in different partner $p_T$ bins at centrality 0–20. Trigger $p_T = 2-3$ GeV/c . . . . .	72
5.1	$\varepsilon_2$ measured via Glauber Monte Carlo simulations in different centralities. . . . .	130
5.2	$\varepsilon_3$ measured via Glauber Monte Carlo simulations in different centralities. . . . .	130
5.3	$p_T$ integrated $v_2$ values (0.5–3.0 GeV/c) from two particle cor- relation method in this analysis. . . . .	134
5.4	$p_T$ integrated $v_3$ values (0.5–3.0 GeV/c) from two particle cor- relation method in this analysis. . . . .	135

## Acknowledgements

PhD is a long journey, without help from people around me, this task will not be able to finish.

The first person I would like to thank is my thesis adviser, Prof. Barbara Jacak. Over the years, she always gave me useful suggestions and insightful comments on my work. All these point me to a clearer direction of analysis direction and sharper physics messages.

I would also like to thank Justin Frantz, who was a post-doc in the group during my first few years in group. With Justin's help, I can start my analysis rather smoothly, from a person who never wrote codes to be able to finish a big analysis.

People from the heavy ion group in Stony Brook always gave me all the supports. Professors Tom Hemmick, Axel Drees, and Abhay Deshpande all gave me helpful comments during my always never-ending presentations in group meetings.

Friends in the group are always fun to be with. I would like to thank Megan, who always listens to my complaints patiently. She also helps me corrects most of the English problems in most of my proceedings, which makes my writing much smoother. I'd like to thank Ali, she patiently read through this long thesis and gave me suggestions on English and physics messages.

Over the years, friends here and in Taiwan all give me all kinds of encouragement, either from email, instant messaging, or even Facebook. With all of you, even though I am working alone, I know I have a lot of friends surrounding me.

At the end, I would like to thank my parents. They just wait me patiently at home and give me support through phone calls and emails. The process is a bit long, but finally all this become fruitful. Without their understanding and support, I probably can not finish the study.

**Part I**  
**Introduction**

# Chapter 1

## Physics Introduction and Motivation

### 1.1 Quantum Chromodynamics

All stable matter in the current universe consists of protons and neutrons. Protons and neutrons combined together form all the elements we see today. In the viewpoint of the Standard Model of particle physics, protons and neutrons are not the fundamental building blocks. Instead, quarks and gluons are the most fundamental building blocks. Protons and neutrons are baryons, which consist of three quarks. There are six kinds of quarks: up (u), down (d), strange (s), charm (c), bottom (b), and top (t). Quarks have color, which is a quantum number: red (R), green (G), and blue (B). The interaction between quarks is mediated by exchanging gluons. The theory used to describe quark and gluons is called Quantum Chromodynamics (QCD).

The strength of the interaction between quarks is described by the coupling constant of the strong interaction,  $\alpha_s$ . The strength of  $\alpha_s$  as a function of the momentum transfer  $Q$  of the interaction is shown in Fig. 1.1 [1, 2]. The horizontal axis,  $Q$ , is the momentum exchange. Large  $Q$  is reached in the high energy interactions. At the same time, high energy also corresponds to short distance.

The running of the coupling constant,  $\alpha_s$ , with increasing  $Q$  leads to the phenomenon of “asymptotic freedom” [3, 4]. When the two quarks are separated by a large distance, the interaction strength will increase and tend to bring the two quarks together, which lowers the energy of the system. This is why quarks are bound inside the nucleon.



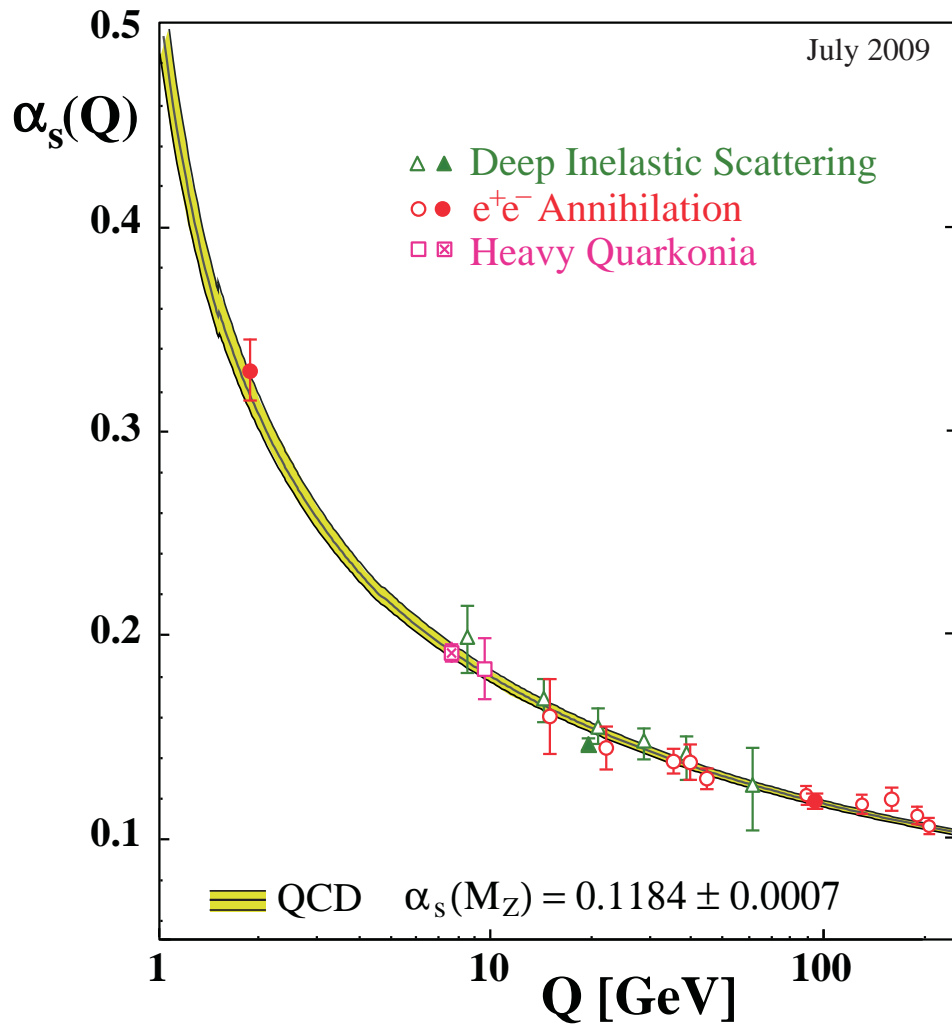


Figure 1.1: The QCD coupling constant,  $\alpha_s$ , as a function of the momentum exchange,  $Q$ . [1, 2].

## 1.2 The Quark Gluon Plasma

From Fig. 1.1, we know that the strength of the interaction between quarks varies with energy. One might imagine that when the coupling constant  $\alpha_s$  is small enough, quarks and gluons can move freely as gas.

There are two methods to achieve the condition of small  $\alpha_s$ . First, one can “heat up” the nucleon. Second, one can reduce the distance between the quarks, i.e. “squeeze” the nucleon. Both of these conditions can be achieved by colliding large nuclei at relativistic energies.

QCD predicts a phase transition from hadronic gas to quark gluon plasma. The calculation from lattice QCD, as shown in Fig. 1.2 [5], indicates that with the sudden increase of the ratio of the energy density over the fourth power of the temperature, there is indeed a phase transition when temperature,  $T$ , is around the critical temperature,  $T_c$ . The high temperature phase is known as “quark gluon plasma” [6, 7]

When  $T < T_C$ , and by assuming  $c = \hbar = k_B = 1$ , the energy density,  $\varepsilon$  (in units of  $[\text{GeV}]^4$ ), of the massless pion gas is given in Eq. 1.1

$$\varepsilon_\pi = 3d_\pi \frac{\pi^2}{90} T^4 \quad (1.1)$$

where  $d_\pi$  is the number of degrees of freedom of the pions, which can be calculated by Eq. 1.2:

$$d_\pi = N_f^2 - 1 \quad (1.2)$$

In the quark–gluon–plasma phase, we have the energy density

$$\varepsilon_{QGP} = 3d_{QGP} \frac{\pi^2}{90} T^4 + B \quad (1.3)$$

Here,  $d_{QGP}$  is number of degrees of freedom in the QGP phase, which is written as

$$d_{QGP} = d_g + \frac{7}{8}d_q \quad (1.4)$$

$$d_g = 2_{spin} \times (N_C^2 - 1) \quad (1.5)$$

$$d_q = 2_{spin} \times 2_{q\bar{q}} \times N_C \times N_f \quad (1.6)$$

For the case of three flavors of massless quarks, or  $N_f = 3$ , we have  $d_\pi = 3^2 - 1 = 8$ ,  $d_g = 2 \times (3^2 - 1) = 16$ ,  $d_q = 2 \times 2 \times 3 \times 3 = 36$ ,  $d_{QGP} = 8 + \frac{7}{8} \times 36 = 47.5$

So from hadron gas phase to QGP phase, there is a sudden increase of the number of degrees of freedom. This corresponds to the jump of  $\varepsilon/T^4$  at  $T = T_C$  in Fig. 1.2. Note that this is true for all three assumptions of quark type and masses in the figure.

For  $T > T_C$ ,  $\varepsilon/T^4$  is approximately constant with temperature. In Fig. 1.2, the values of the Stefan–Boltzmann limit,  $\varepsilon_{SB}/T^4$ , which corresponds to the noninteracting gluon gas are also plotted. But  $\varepsilon/T^4$  is below the energy density by assuming that the quarks and gluons are non–interacting, or the Boltzmann limit by about 20%. This is a hint that within quark–gluon plasma, quarks and gluons are strongly interacting.

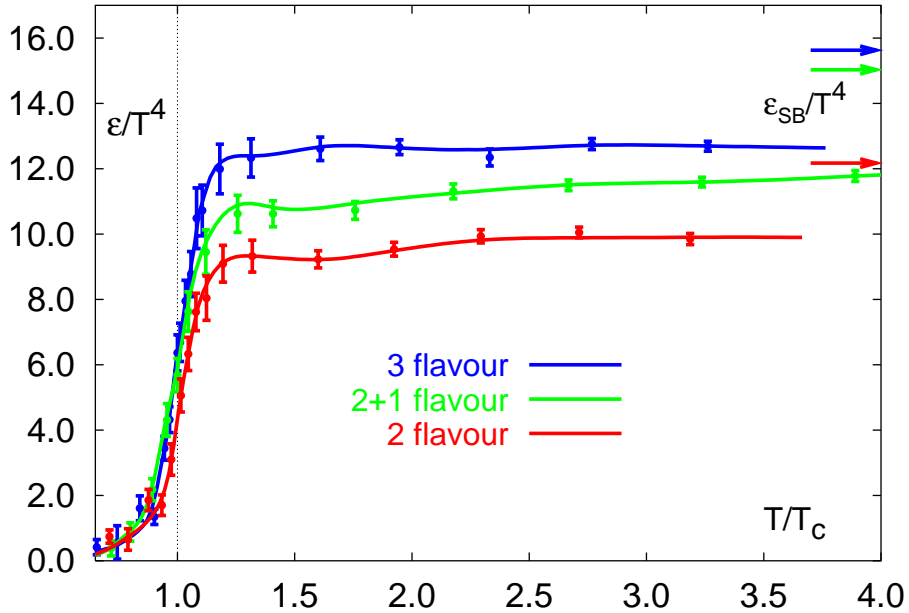


Figure 1.2: Energy density,  $\varepsilon$ , as a function of temperature from Lattice QCD calculations [5].  $\varepsilon_{SB}/T^4$  represent the Stefan–Boltzmann limit of non–interacting gluon gas.

### 1.3 Different Stages of Heavy Ion Collisions

The Relativistic Heavy Ion Collider (RHIC) at Brookhaven National Lab (BNL) collides gold nuclei and various nucleus systems at center of mass energies up to 200 GeV per nucleon pair ( $\sqrt{s_{NN}} = 200$  GeV). Under this condition,

a new type of hot dense matter, the quark–gluon plasma, is created. Here we describe the time history of the such collisions.

### 1.3.1 $0 < \tau < \tau_0$ , Pre–equilibrium and Thermalization

At the top RHIC energy, due to Lorentz contraction, the nuclei will have longitudinal size  $2R/\gamma_{cm}$ , where  $\gamma_{cm} = E_{cm}/2m_n \approx (200 \text{ GeV})/(2 \text{ GeV}) \approx 100$ , where  $m_n$  is the nucleon mass. When the two nuclei collide, the resulting collisions of constituent partons produce many semi–hard partons, or mini–jets. A lot of entropy is also created at this stage. These mini–jets form an equilibrated parton plasma and interact with other partons. At this stage, local thermalization is achieved and creates the hydrodynamical initial conditions for  $\tau > \tau_0$ , where  $\tau_0$  is the characteristic proper time of the QGP. At RHIC,  $\tau_0$  is less than 1 fm/c under perfect fluid hydrodynamical models [8].

### 1.3.2 $\tau_0 < \tau < \tau_f$ , Hydrodynamical Evolution and Freeze–out

At  $\tau_0$  the system is in local thermal equilibrium. The system expands both in longitudinal and transverse directions. This longitudinal expansion expands the volume of the system in the z direction (beam direction) and this process cools the system and decreases its temperature. When the temperature drops to the critical temperature,  $T_c$ , there will be a phase transition, the system will become a hot dense hadronic gas. After the phase transition, the hadron gas will still expand.

The relativistic hydrodynamics is used to describe the expansion of the system from the time that local thermal equilibrium is reached in the quark gluon plasma phase until freeze-out. . Under relativistic hydrodynamics, the energy–momentum is conserved, that is

$$\partial_\mu \langle T^{\mu\nu} \rangle = 0, \quad (1.7)$$

where  $T^{\mu\nu}$  is the energy–momentum tensor of the fluid. By assuming the system is a perfect fluid, the system can be described by the energy density,  $\varepsilon$ , and the local pressure, P, and  $T^{\mu\nu}$  can be written as

$$T^{\mu\nu}(x) = \begin{bmatrix} \varepsilon(x) & 0 & 0 & 0 \\ 0 & P(x) & 0 & 0 \\ 0 & 0 & P(x) & 0 \\ 0 & 0 & 0 & P(x) \end{bmatrix} \quad (1.8)$$

The energy density,  $\varepsilon$  and the local pressure,  $p$ , are linked by Equation of State, EoS. In the fluid, the number of baryon number is also conserved, where

$$\partial_\mu \langle j_B^\mu \rangle = 0. \quad (1.9)$$

and the baryon number current,  $j_B^\mu$  is given by

$$j_B^\mu(x) = n_B(x)u^\mu(x) \quad (1.10)$$

where  $n_B(x)$  is the baryon number density and  $u^\mu(x)$  is the four velocity. The evolution can then be calculated with proper initial conditions, starting from  $\tau = \tau_0$  to  $\tau = \tau_f$ , which is the freeze-out time, when the hadronic plasma stop interacting with each other.

### 1.3.3 $\tau_f < \tau$ , Freeze-out and Post-equilibrium

The freeze-out of the hadronic plasma happens at this stage,  $\tau_f < \tau$ . The freeze-out is defined as the time when local thermalization breaks, or the mean free path of the hadrons is larger than the size of the system. The hadron gas is still very dense and the hadrons still interact with each other in a non-equilibrium way, where the system may be described by transport theories, such as UrQMD [9, 10].

## 1.4 Definition of terms

In order to describe the heavy ion collisions, we define the following terms.

The transverse momentum of the particle,  $p_T$ , is the momentum in the transverse plane, which is perpendicular to the beam direction. The magnitude of  $p_T$  is  $p_T = |p| \sin \theta$ , where  $p$  is the magnitude of the momentum,  $\theta$  is the angle between the direction of the particle and the beam direction. The longitudinal momentum,  $p_L$  is the momentum along the beam direction.

The direction of the particle is typically described by two angles, the azimuthal angle on the transverse plane  $\phi$  and  $\theta$ . The pseudorapidity,  $\eta$ , is defined as  $\eta = -\ln[\tan(\theta/2)]$ , which is often used to describe the direction of  $\theta$ .

The geometry in heavy ion collisions is an important parameter, which describe how much matter is colliding. The geometry for head-on collisions and peripheral collisions is very different. When two nuclei collide, the nucleons which participate the collision are called “participants”, and the rest are called “spectators”. These participants form the collision region. The collisions are

typically categorized by different “centralities”. Centrality is defined by the total nuclei-nuclei inelastic cross section, which is strongly correlated with the number of participants. The 5% events which have the largest total inelastic cross section is defined as centrality of 0–5%. Experimentally, centrality is determined by the density of the charged particles produced from the collisions, or  $dN^{ch}/d\eta$ . For example, the centrality of 0–5% events produces the highest multiplicity.

The Glauber model [11] has been used to calculate the colliding geometry. The Glauber model breaks the nuclei–nuclei interaction into numerous nucleon–nucleon interactions. It assumes the nucleon moves in a straight trajectory and not deflected after the collisions. Using the Glauber model, we can calculate  $N_{part}$  for the average number of participant of the certain centrality. The number of binary collisions,  $N_{coll}$ , is also used extensively to describe heavy ion collisions. When the two nuclei collide, many partons within colliding region may interact. The total number of binary collisions is  $N_{coll}$ , which can also be estimated with a Glauber simulation, is used extensively to describe heavy ion collisions.

## 1.5 General Properties of QGP

At RHIC, quark–gluon plasma is routinely created in central Au+Au collisions. There are several interesting properties of this new type of matter.

### 1.5.1 Temperature of QGP

One of the most important questions at RHIC has been the temperature achieved. This has been determined by measuring thermal radiation. When the quark–gluon plasma is produced in heavy ion collisions, it will radiate thermal photons. By measuring the spectra of the thermal photons, we can extract the temperature of the medium.

The hot quark–gluon–plasma should emit thermal radiation [12]. The partonic phase is predicted to be the major source of direct photons at  $1 < p_T < 3$  GeV/c [13]. But at this  $p_T$  range, there is a large background of hadronic decay photons. Since any photon production can also emit virtual photons, which decay to electron-positron pairs, one can measure the virtual photons via di-electrons and require the mass of the electron pairs to be larger than the mass of the  $\pi^0$  to suppress the background. PHENIX has measured low mass di-electrons in Au+Au and p+p collisions ( $m_{e^+e^-} < 0.3$  GeV/c<sup>2</sup> and  $1 < p_T < 5$  GeV/c) [14]. After removing all the pairs from hadronic

decays, an excess yield is found in central Au+Au collisions compared to p+p, as shown in Fig. 1.3.

Fig. 1.3 shows the spectra of di-electrons which come from direct photons in p+p and Au+Au collisions. The spectrum from p+p is fit with a modified power law function  $[A_{pp}(1 + p_T^2/b)^{-n}]$ . The same di-electron spectrum is measured in different centralities in Au+Au and compared with the p+p spectrum scaled by the total inelastic nucleus-nucleus cross section. An excess yield for  $1 < p_T < 3$  GeV/c is found in central Au+Au collisions compared to p+p collisions. The low mass di-electrons excess in Au+Au is interpreted as coming from thermal radiation photons produced by the QGP. After fitting an exponential function,  $Ae^{-p_T/T}$ , to the spectra of the excess, or the thermal radiation, the slope of the exponential is extracted as  $T = 221 \pm 19^{stat} \pm 19^{syst}$  MeV. If the source of this excess is from thermal photons, the inverse slope, T, is related to the initial temperature,  $T_{ini}$ . From hydrodynamical calculations,  $T_{ini}$  is 1.5 to 3 times T due to the space-time evolution of the fireball [15]. Several hydrodynamical calculations can reproduce the central Au+Au data within a factor of 2. These models were  $T_{ini} = 300 - 600$  MeV, depending upon which thermalization time is assumed.  $\tau_0$  ranges from  $\tau_0 = 0.6 - 1.5$  fm/c [16]. From Lattice QCD, the critical temperature of the QGP is  $T_C = 170$  MeV [17]. This measurement clearly shows that the  $T_{ini}$  of the medium is above  $T_C$ , and we have indeed created quark-gluon plasma at RHIC.

## 1.5.2 Elliptic Flow

When two nuclei collide, most of the time the two nuclei do not overlap completely, but producing an almond-shape collision zone as shown in Fig. 1.4. The plane which connects the centers of the two nuclei is called the reaction plane, along the direction of the impact parameter of the collision. In order to study the spatial anisotropy of the collision, the particle azimuthal distribution,  $dN/d(\phi - \psi)$  is measured with respect with the direction of the reaction plane ( $\psi$ ). This distribution can be expanded as a Fourier series in  $\phi$ :

$$\frac{dN}{d(\phi - \psi)} \propto 1 + \sum (2v_n \cos n(\phi - \psi_n)) \quad (1.11)$$

The elliptic flow, defined as the second Fourier coefficient,  $v_2$ , of the particle distribution, is used to describe the azimuthal anisotropy of the particle distribution and has been measured extensively and precisely [18, 19]. Fig. 1.5 shows the  $v_2$  and  $v_4$  measured with respect to the second event plane,  $\psi_2$ , which is the estimation of the reaction plane. If the QGP is weakly interacting, the whole system should expand like a gas, i. e. homogeneously in all directions.

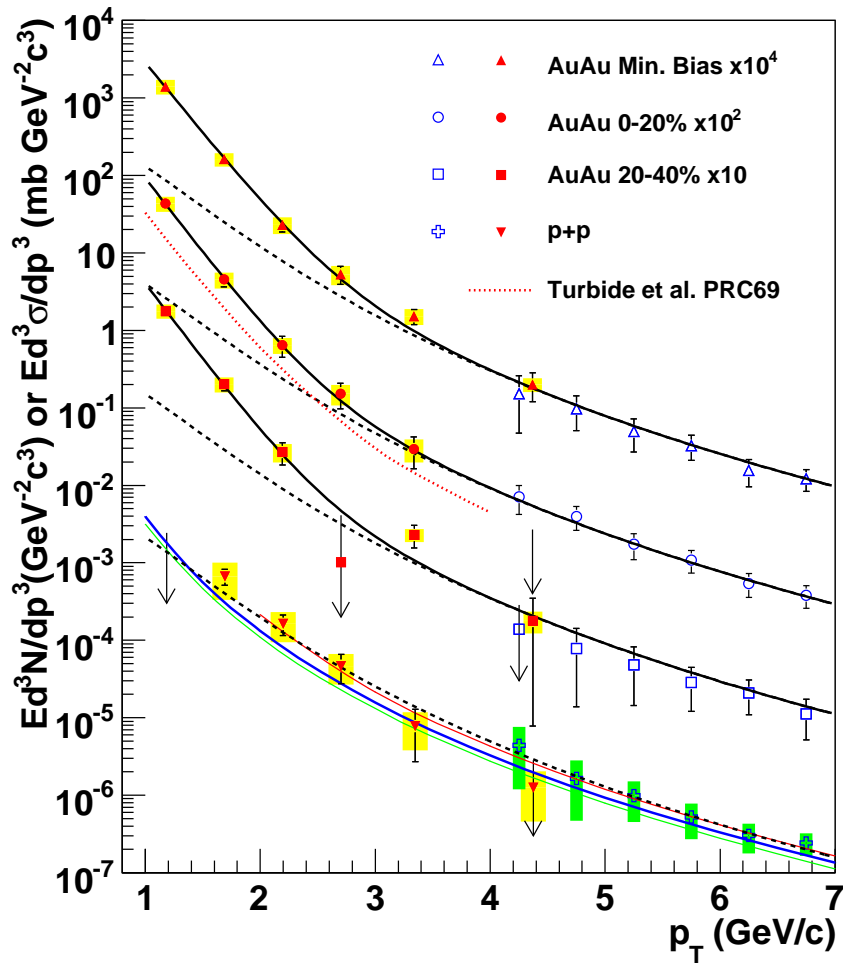


Figure 1.3: Invariant cross section (p+p) and invariant yield (Au+Au) of direct photons as a function of  $p_T$ . The black dashed curves are modified power law fit to the p+p data, scaled by the number of binary collisions. Low mass di-electrons excess in Au+Au shows the thermal radiation of QGP [14].



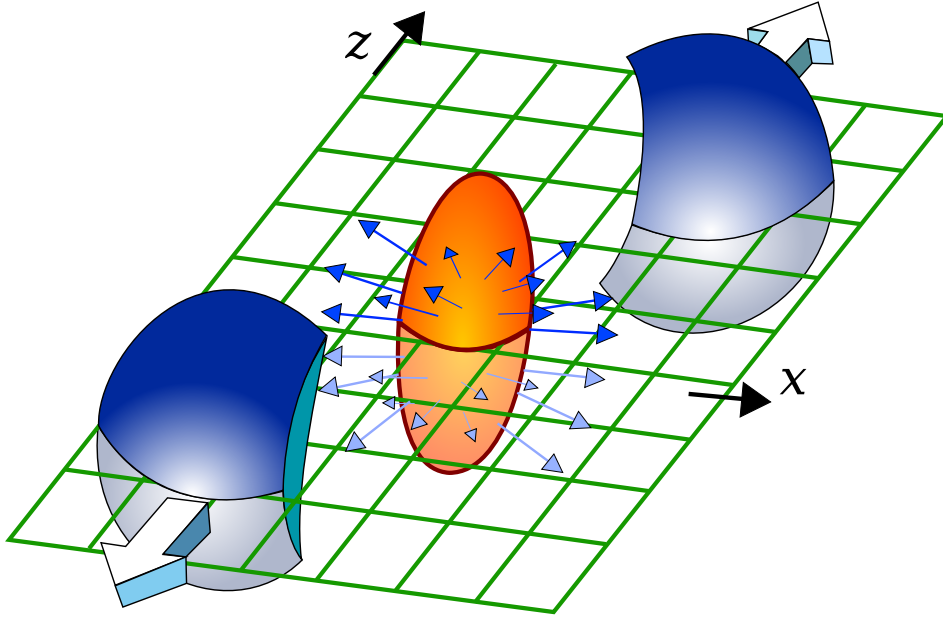


Figure 1.4: When two nuclei collide, the colliding area has an almond-like shape.

The large, non zero  $v_2$  in Fig. 1.5 indicates that the medium expands faster in the short direction (in-plane) and slower in the long direction (out-of-plane). This implies that the system has a large pressure gradient and experiences a fast thermalization. More detail will be discussed in Chapter 5 and Chapter 7.

### 1.5.3 Jet Quenching

When two nucleon collides, the partons within the nucleon may experience a hard scattering, which can be illustrated by Fig. 1.6. Fig. 1.6 shows two high energy protons collides (blue arrows). During the collision, the partons in protons scattered into a pair of high energy partons (red arrows) in opposite directions due to conservation of momentum. The partons will hadronized into high  $p_T$  particles or fragment into a shower of particles in a small cone in  $\phi$  and  $\eta$ , which become jets. In heavy ion collisions, this hard process happened in the early stage of the collisions, so the energetic parton will interact with the quark gluon plasma before the parton leaves the medium.

A key question in heavy ion collisions is how partons interact with the medium as they travel through. By measuring the properties of the high  $p_T$

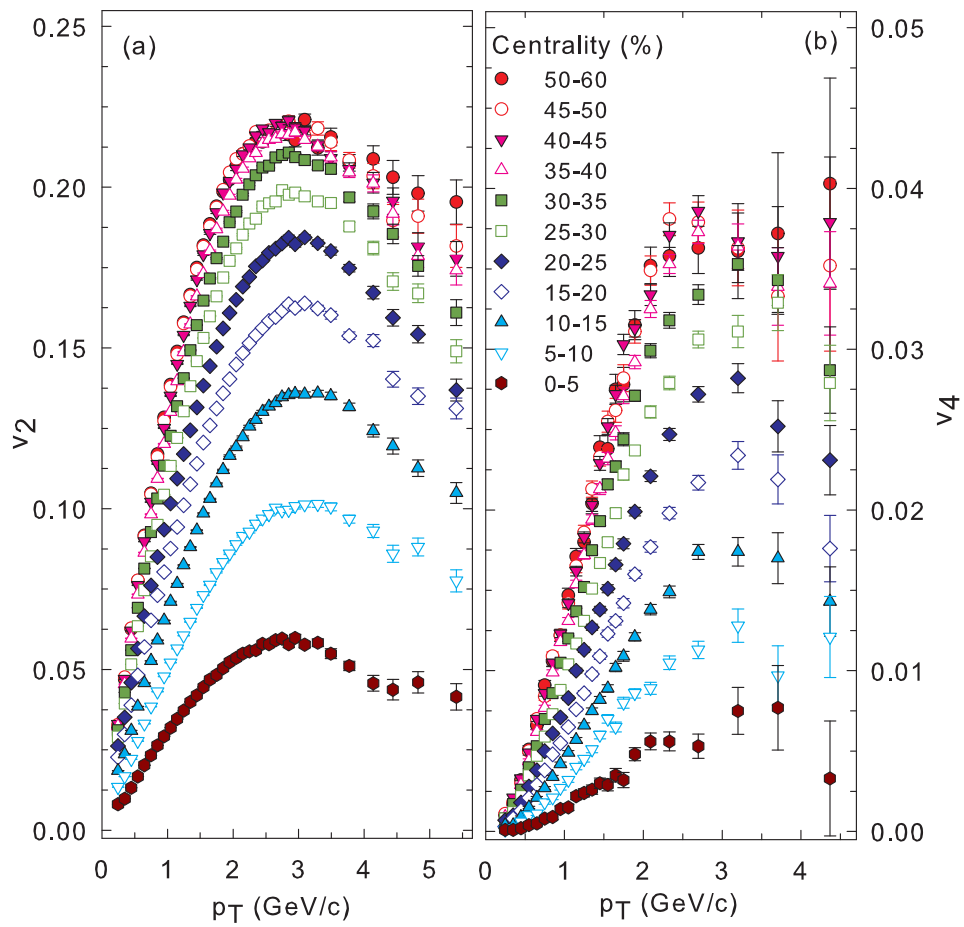


Figure 1.5:  $v_2$  and  $v_4$  of inclusive charged hadrons vs  $p_T$  of several centralities [19].

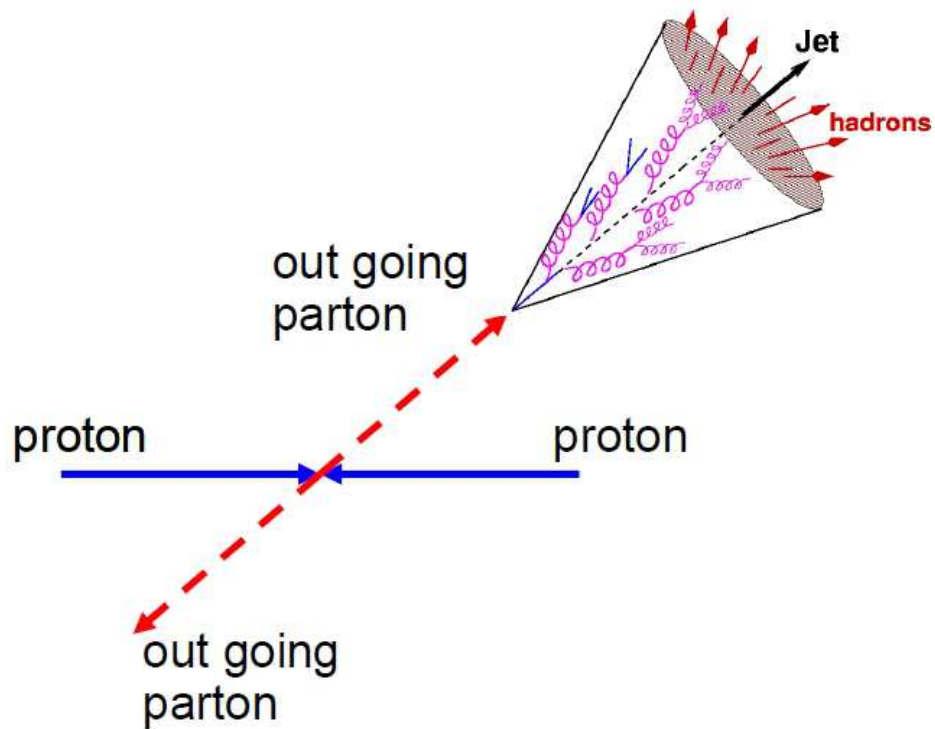


Figure 1.6: Hard scattering in a proton-proton collision. The blue arrows are the direction of the protons, the red arrows are the outgoing partons. The upper out going parton fragment into a jet.

particles or jets, we can have the information on how partons interact with the quark gluon plasma. By measuring the spectra of high  $p_T$  hadrons in Au+Au collisions, where the medium is produced, and comparing with p+p collisions, where there is no medium produced, we can gain some insight on the effect of the medium and the study the parton–medium interaction.

One parameter used to quantify the medium modification is the medium modification factor,  $R_{AA}$ , which is defined in Eq. 1.12:

$$R_{AA}(p_T) = \frac{d^2N^{AuAu}/dp_Td\eta}{N_{coll}d^2N^{pp}/dp_Td\eta} \quad (1.12)$$

where  $d^2N/dp_Td\eta$  is the particle spectrum in Au+Au/p+p, and  $N_{coll}$  is the total number of binary nucleon–nucleon collisions in Au+Au at a given impact parameter. If the particle spectrum in Au+Au is simply given by the spectrum in p+p scaled by the number of binary collisions in Au+Au, then  $R_{AA}$  should be equal to 1.  $R_{AA} < 1$  means the spectra in Au+Au are suppressed compared to p+p.

PHENIX has measured  $\pi^0$  spectra in Au+Au in various centralities and over a broad range of  $p_T$  [20]. The results are shown in Fig. 1.7. At  $p_T > 5$  GeV/c,  $R_{AA}$  in central collisions (0–10%) is about 0.2, which means the  $\pi^0$  yields are suppressed by a factor of 5. This is strong evidence that partons are losing energy in the medium. At higher  $p_T$ ,  $R_{AA}$  shows a weak rising trend with  $p_T$ . In Fig. 1.8,  $R_{AA}$  at  $p_T > 5$  GeV/c shows that  $R_{AA}$  decreases with increasing  $N_{part}$ , i.e. from peripheral to central collisions. This indicates that larger medium volume results in larger suppression.

## 1.6 Two Particle Correlations

### 1.6.1 The Definition of Two Particle Correlations

In section 1.5.3, hard partons will produce high  $p_T$  particles or jets. Jets are important probes for understanding the properties of the quark–gluon plasma. But in central heavy ion collisions, thousands of particles are produced, making jet finding an extremely difficult task. Instead, two particle azimuthal correlations are used as a proxy for studying properties of jets in the medium.

This correlation function method is a statistical method. When high energy partons are produced in hard collisions, they will fragment into hadrons which are confined to a cone of small  $\Delta\phi$  and  $\Delta\eta$ . So the idea of two particle correlations is to select a high  $p_T$  particle, known as the trigger particle, which is supposed to be fragment from a jet and roughly in the direction of the

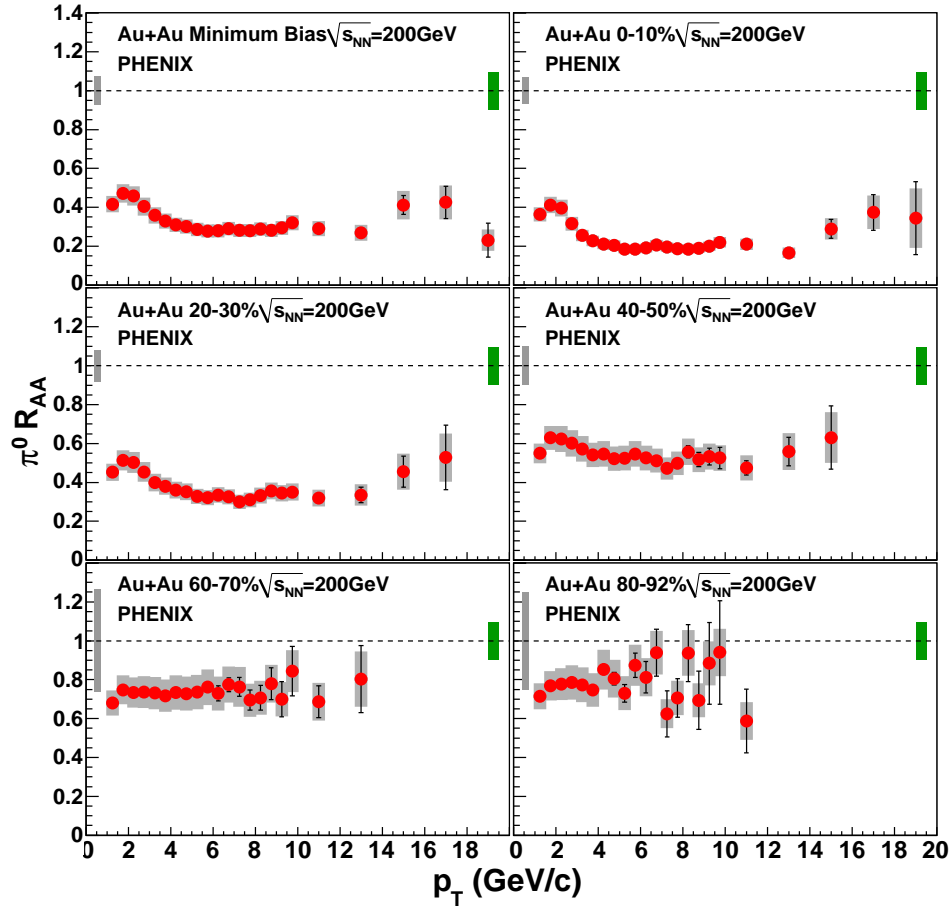


Figure 1.7:  $R_{AA}$  of  $\pi^0$  vs  $p_T$  in various centralities [20]. Error bars are statistical and  $p_T$ -uncorrelated errors, boxes around the points indicate  $p_T$ -correlated errors. Single box around  $R_{AA} = 1$  on the left is the error due to  $N_{coll}$ , whereas the single box on the right is the overall normalization error of the p+p reference spectrum.

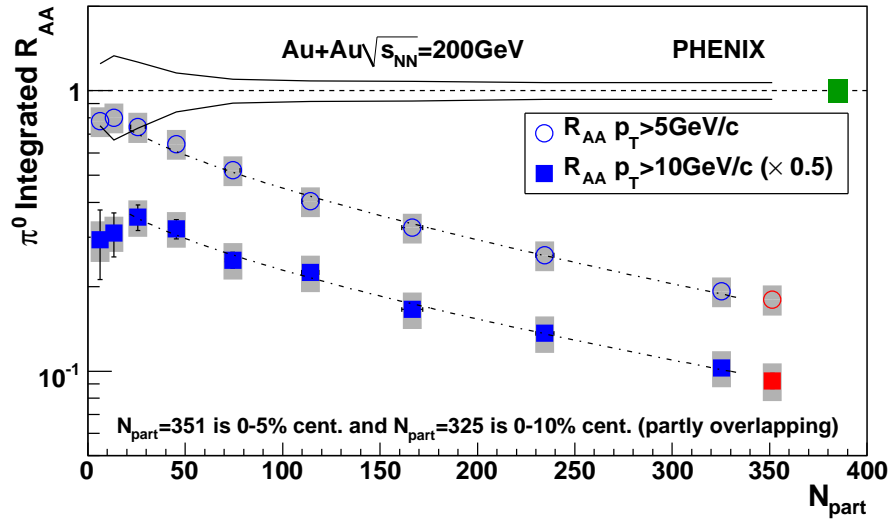


Figure 1.8: Integrated  $R_{AA}$  of  $\pi^0$  vs  $N_{part}$  [20]. The error bars/bands are the same as in Fig. 1.7. The two lines at unity show the errors on  $N_{coll}$ . The last two points correspond to partially overlapping centrality bins.

original parton, and correlate it with lower  $p_T$  associated particles in  $\phi$  or  $\eta$ . When the difference of the azimuthal angle between the trigger and associated particles is  $\Delta\phi \approx 0$ , this means both particles arise from the same jet. If  $\Delta\phi \approx \pi$ , this means the associated particle is coming from the opposing jet, which is due to the conservation of momentum.

A typical correlation function looks like Fig. 1.9. The two particle correlation function has two components: contributions from jet pairs and the underlying event. In order to extract the jet signal, we need to determine the level and also the shape of the underlying event background. After the shape and the level are properly determined, we can subtract the background and extract the jet signal. The peak at  $\Delta\phi = 0$  is the near side jet, which is the jet where the trigger particle comes from. The peak at  $\Delta\phi = \pi$  is the opposing jet. So with two particle correlations, we can study the properties of dijet events.

## 1.6.2 High $p_T$ Correlations

PHENIX has performed extensive studies with two-particle correlations [21, 22, 23]. Fig. 1.10 [24] shows the  $\pi^0$ -h correlations in central Au+Au collisions. When both particles are at high  $p_T$ , such as 7–9 GeV/c for trigger particles, and 3–5 GeV/c associated particles, the near side ( $\Delta\phi = 0$ ) in

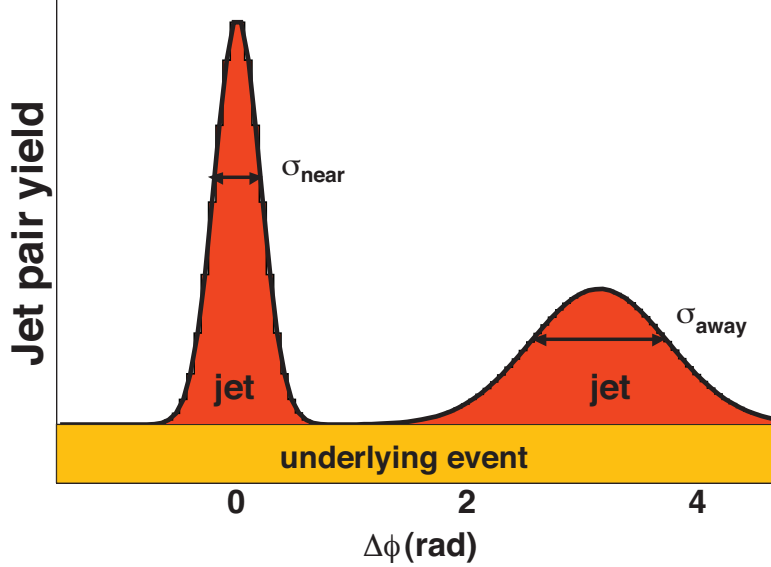


Figure 1.9: A typical correlation function. On the top are the jet pairs. On the bottom are uncorrelated underlying backgrounds

Au+Au (solid circles) behaves just like p+p (empty circles). However, on the away side ( $\Delta\phi = \pi$ ), the jet like structure in Au+Au is significantly suppressed compared to p+p, which is the evidence of jet quenching inside the medium at high  $p_T$ . At low partner  $p_T$ , the away side jet is modified and comprises more particle than p+p, as shown in upper left of Fig. 1.10. From the two-particle correlations shown in Fig. 1.10, we can clearly see that the suppression happens when the away side jet goes through the medium. By selecting the high  $p_T$  particle as the trigger, we are biased by selecting the trigger particles emitted from the surface, which suffers no or little energy loss. But the opposing jet had to pass through the medium, suffering energy loss. This is known as trigger bias.

### 1.6.3 Intermediate $p_T$ correlations

When the momentum range for both trigger and associated particles is decreased, interesting features come out. Fig. 1.11 [22] shows the jet function from Au+Au and Cu+Cu collisions at various centralities. In peripheral collisions, the correlation function looks like unmodified p+p, which shows peaks at 0 and  $\pi$  in  $\Delta\phi$ . In central collisions, we see the near side peak still sits at  $\Delta\phi = 0$ , but on the away side, instead of a peak at  $\Delta\phi = \pi$ , a dip appears,

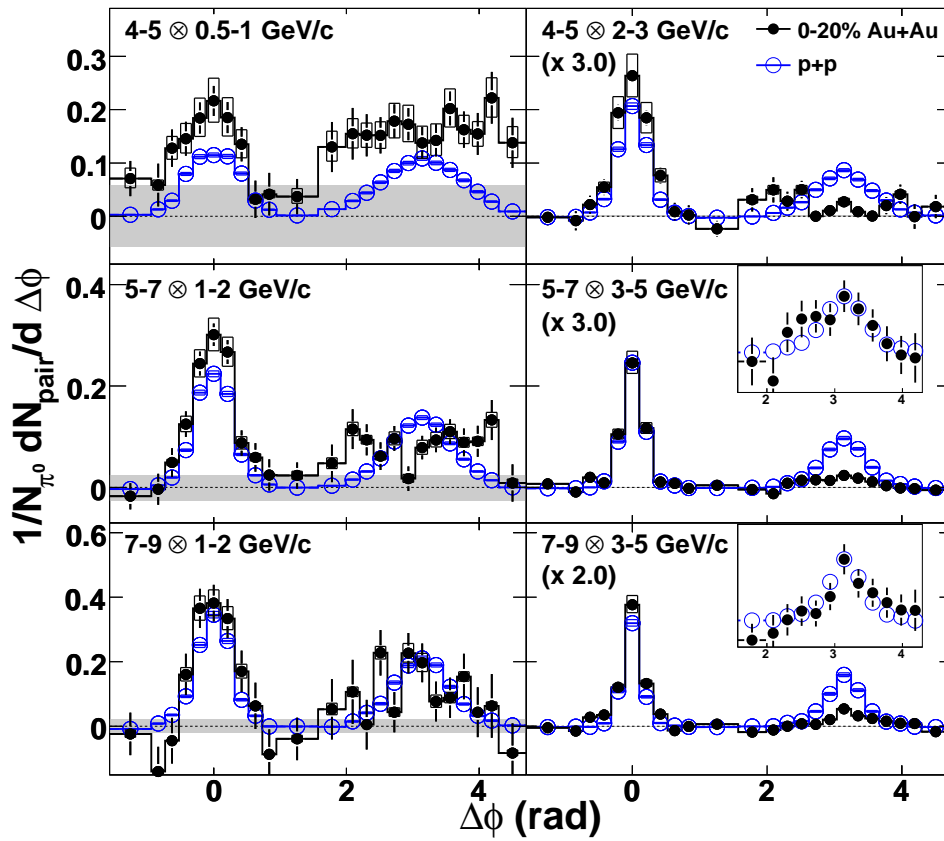


Figure 1.10: High  $p_T$   $\pi^0$ -h jet correlations in central Au+Au (0-20%) in solid circles and p+p collisions in empty circles [24].



and the peak shifts to  $\Delta\phi \approx 2$ . This strange shape is found in different colliding systems and different colliding energies, and the position of the away side peak, parametrized by  $D$ , is the same for all  $N_{part} > 50$ . Fig. 1.12 [22] summarizes the centrality dependence of the peak location,  $D$ , at the bottom, and shows how the peak shape changes on the top panel.

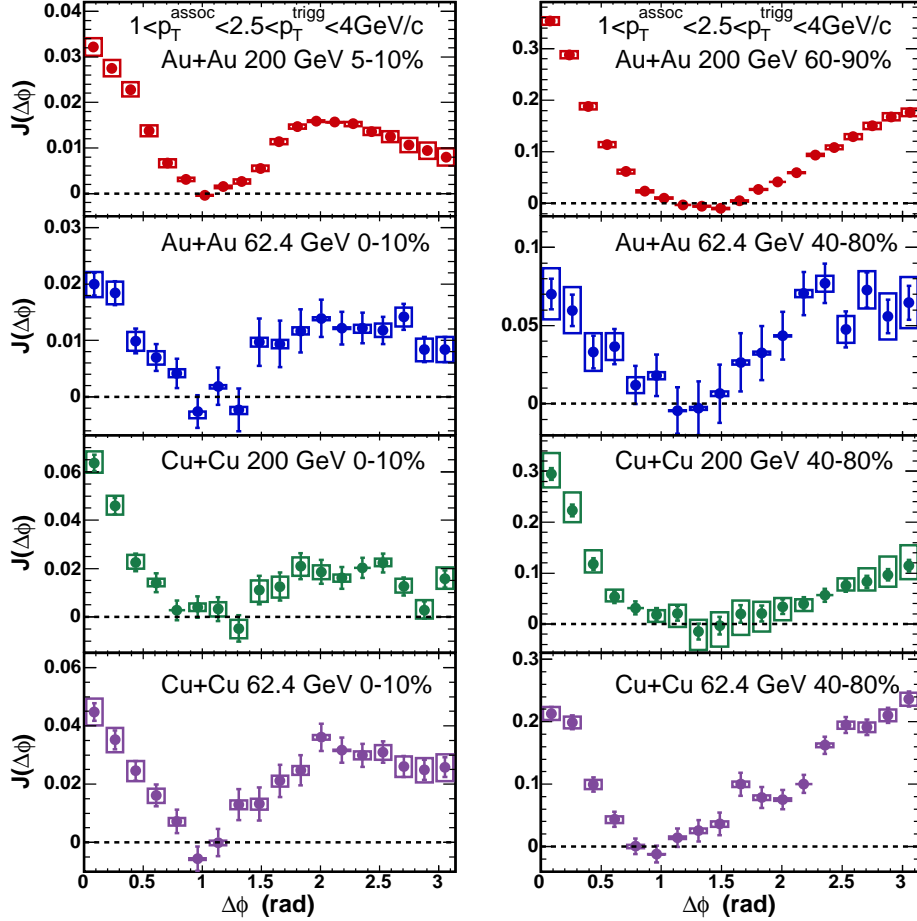


Figure 1.11: Shape of jet functions in Au+Au/Cu+Cu at  $\sqrt{S_{NN}} = 200/62.4$  GeV/c at intermediate  $p_T$  [22].

#### 1.6.4 $\Delta\eta$ - $\Delta\phi$ Correlations

The near side correlation is found to be modified not only in  $\Delta\phi$ , but also in  $\Delta\eta$ , which is defined as  $\eta = -\ln[\tan(\theta/2)]$ , where  $\theta$  is relative to the beam direction. Fig. 1.13(a) shows the  $\Delta\eta$ - $\Delta\phi$  correlation function in central

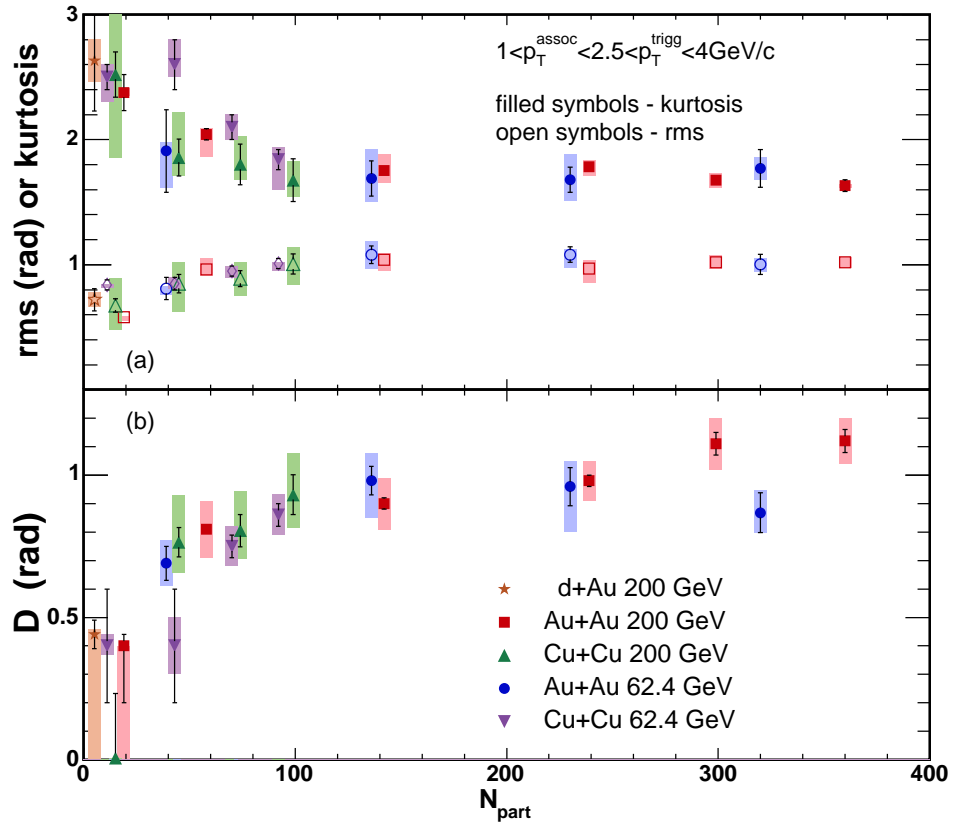


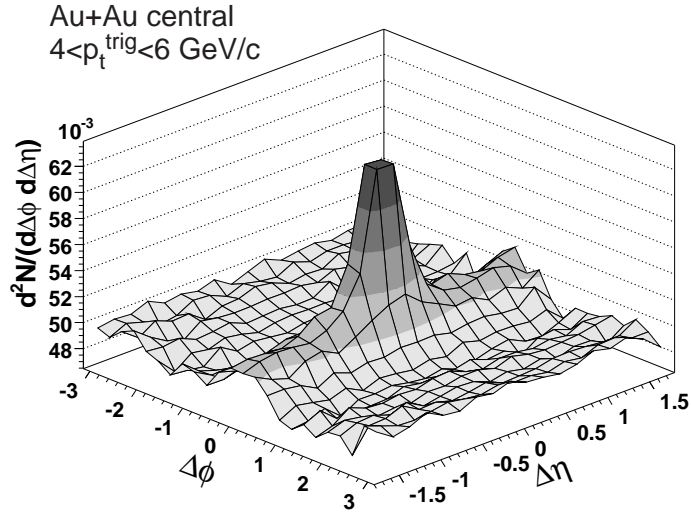
Figure 1.12: Shape parameters of jet functions in various colliding systems and energies [22]. RMS(kurtosis) in top panel describes the shape of the away side jet function.  $D$  in the bottom panel is used to describe the peak position of the double peak structure.

Au+Au collisions [25]. Fig. 1.13(b), shows the correlation function in d+Au collisions, which has no medium effect. Fig. 1.13(a) shows the correlation in central Au+Au, an enhancement along  $\Delta\eta$  at  $\Delta\phi \approx 0$  is found. This structure is called the “ridge”. Together with the cone-like double-peak structure, we see that the effect of the quark gluon plasma in Au+Au upon jets appears to be very complicated.

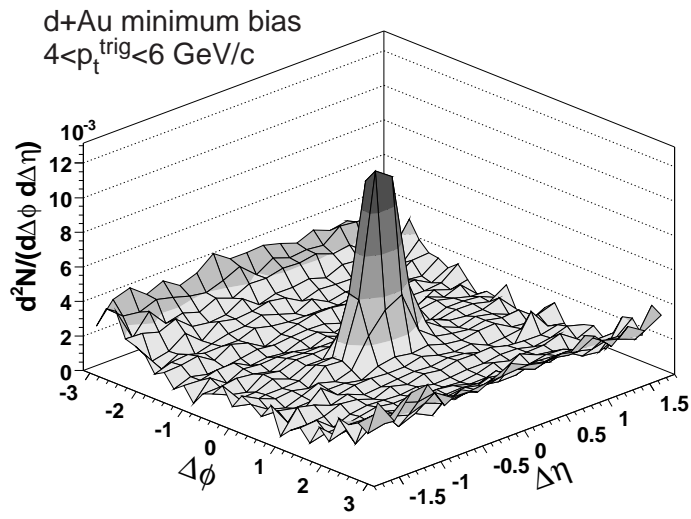
## 1.7 Motivation for this Dissertation Work

We have performed a study aimed at understanding the exotic structures seen in two particle correlations in heavy ion events, and using properties of the ridge in the near side and the double peak structure in the away side to learn about the response of the quark-gluon plasma to the energy deposited by fast partons. There are several theoretical interpretations of each structure, but very few theoretical approaches treat them together. Furthermore, new insights from higher harmonic Fourier coefficients have also triggered new interpretations of these structures.

In this analysis, we study the two particle correlations with the PHENIX detector. First, we extract the ridge and shoulder from the correlation functions and study their centrality and  $p_T$  dependence. In order to understand the effects of higher harmonics of the collective flow of the underlying event, we measured the higher harmonics in correlations of two low  $p_T$  particles, as well as for intermediate  $p_T$  particles, and applied those measurements back to the background subtraction in the correlation analysis to gain new insights into the source of the ridge and shoulder structures.



(a) Au+Au (0–12%)



(b) d+Au

Figure 1.13:  $\Delta\eta$ - $\Delta\phi$  jet function in central Au+Au (a) and in d+Au (b) [25].

## Chapter 2

### Experiment

#### 2.1 RHIC

From Sec. 1.2, we know the way to create the quark-gluon plasma is to create a high temperature, a high energy density state. In order to achieve this condition, the Relativistic Heavy Ion Collider (RHIC) at Brookhaven National Laboratory (BNL) [26] accelerates gold nuclei up to 100 GeV per nucleon along its 2.4 mile ring. When full energy gold nuclei collide, violent interactions happen. RHIC is capable of colliding various species of nuclei, such as gold, copper, deuteron and proton at various energies. This makes RHIC a unique machine to explore the properties of the QGP under different conditions.

These collisions are detected and have been studied extensively by four dedicated experiments: BRAHMS [27], PHOBOS [28], STAR [29] and PHENIX [30].

With good particle identification capability, the Broad RAnge Hadron Magnetic Spectrometers Experiment (BRAHMS) [27] at RHIC was designed to measure the identified charged hadron spectra over wide pseudorapidity and transverse momentum range. It consisted of two spectrometers. One at mid-rapidity was used to measure the low  $p_T$  particles. The other was at forward rapidity, where the momentum of the particle will be boosted. BRAHMS experiment started taking data in 2000 and completed data taking in 2006.

The PHOBOS experiment [28] focused on the global properties of the quark-gluon plasma, such as particle multiplicity distributions and elliptic flow. PHOBOS placed silicon sensors around the interaction region, allowing precision measurements of the number of particles and their angular distributions in Au+Au collisions. The PHOBOS experiment started taking data in 2000 and completed data taking in 2005.

The Solenoidal Tracker at RHIC (STAR) [29] is a multi purpose particle detector. The main component of STAR is a time projection chamber (TPC) which can track thousands of particles at the same time. The full azimuth and

large rapidity acceptance makes it ideal for studying the hadron production and global properties of the medium.

## 2.2 PHENIX

PHENIX stands for "Pioneering High Energy Nuclear Interaction Experiment" [30]. This is the detector used for this work. Fig. 2.1 is the detector configuration of PHENIX during the 2004 run. There are two central arm spectrometers covering pseudorapidity  $|\eta| < 0.35$ . These are optimized for measuring electrons, photons and charged hadrons with great precision. There are also two muon spectrometers ( $1.0 < |\eta| < 2.2$ ), which measure muons in the forward direction. The analysis in this thesis was done with the central arms only.

The coordinate system of the PHENIX follows the right hand rule. Z axis is along the beam direction, where the north is the positive direction. X direction points to west.

### 2.2.1 Beam Beam Counter and Zero Degree Calorimeter

The Beam–Beam counter (BBC) [31] is used to determine the position and timing of collisions. The BBC has two identical counters, sitting 144 cm away from the collision center in the north and south direction, called BBCN and BBCS. The position of the two BBC is equivalent to  $3.0 < |\eta| < 3.9$ . Each BBC consist of two arrays of Cerenkov detectors with quartz radiators and photomultiplier readouts. Each counter has 64 mesh–dynode photo–multiplier tubes with 1–inch diameter, with a 3 cm quartz radiator on the head of the photo–multiplier tube.

When a collision happens, prompt hadrons hit the BBCs. The average hit time at BBCN and BBCS are  $T_N$  and  $T_S$ . The average arrival time,  $T_0$ , is calculated for both BBCs. This is used as the start time of the Time of Flight and to determine the collision vertex position along the beam direction (ZVTX).

The Zero Degree Calorimeter (ZDC) [32] is used to measure the neutrons emitted during the heavy ion collisions. ZDCs are located on both sides of the beam direction and is 18 m away from the collision point. The coincidence between both ZDCs can be used for selection of minimum bias events. The information can also be used to determine the vertex of the collision.

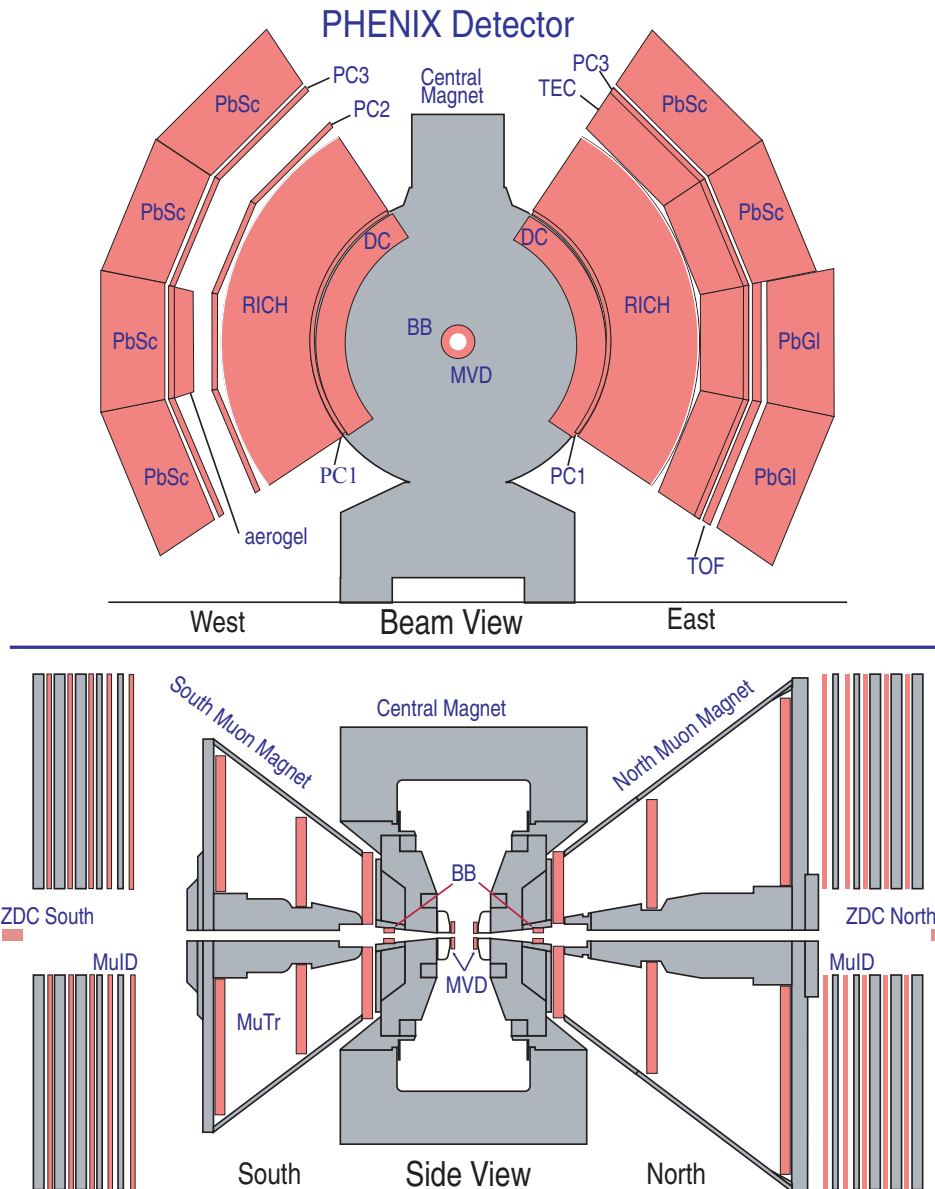


Figure 2.1: Detector configuration of PHENIX during the 2004 run. Top panel: Beam view; bottom panel: side view.

When combined with the ZDC, the centrality of the events can be determined. The centrality describes the degree of the overlap of the two nuclei during the collision. When the two nuclei collide, the nucleons which do not participate in the collision, or the spectators, will travel at forward angles. The the neutrons will be detected by ZDC. For central collisions, most nucleons participate the collision, which means the number of spectators seen at ZDC is small but the number of prompt hadrons hitting the BBC is large. By sorting the events with respect to the response of BBC and ZDC, the centrality of the events can be determined, as shown in Fig. 2.2

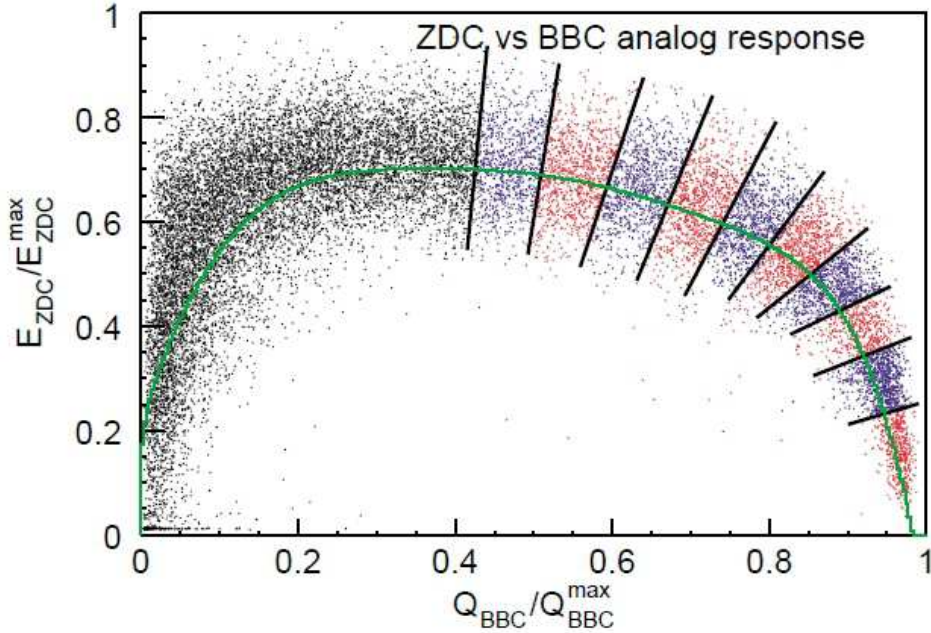


Figure 2.2: The correlations between the charge sum in BBC and the energy in ZDC. The line contains the centrality interval of 5%. The far right region corresponds to centrality 0–5%.

### 2.2.2 Central Arm

There are two central spectrometers in PHENIX [33], each covers  $|\eta| < 0.35$  and  $\pi/2$  in azimuth, as shown in Fig. 2.1. The central arms have layers of different detectors. The innermost layer is the drift chamber (DC) [33], followed by the first layer of pad chamber (PC) [33]. After the pad chamber is the ring imaging Cherenkov detector (RICH). In east arm, there are time



expansion chambers (TEC) and time of flight detector (TOF) in the east arm. In the west arm, there is a second layer of pad chamber behind the RICH. There are also aerogel detectors in the west arm. Both arms contain an additional layer of pad chambers in front of the electromagnetic calorimeters (EMCAL), which is the last layer of the central arm [34]. In this analysis, we use the information from the drift chamber and pad chamber to determine the direction and the momentum of the charged tracks and the electromagnetic calorimeter to measure the energy of the photon.

### Drift Chamber

The Drift chambers [33] are two cylindrically shaped detectors with titanium frames, as shown in Fig. 2.3. The locations of the drift chambers are between 2 to 2.4 m radially from the beam pipe. They extend 2m in the beam direction in both the east and west arm. Each drift chamber is used to measure the position of the tracks in the  $r$ - $\phi$  direction and to provide  $p_T$  information.

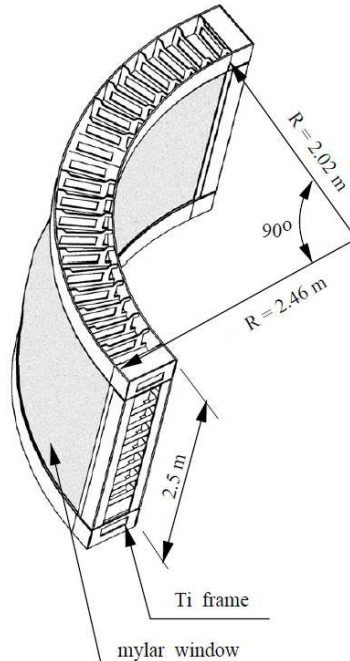


Figure 2.3: Shape of the frame of the drift chamber [33].

The draft chamber is filled with a mixture of 50% argon and 50% ethane gas. When charged tracks pass through the drift chamber, the gas mixture

will be ionized. The ionized electrons drift to the anode wires of the drift chamber and are registered as a hit. Each drift chamber has 20 sectors in the  $\phi$  direction. The layout of a sector is shown in the left hand side of Fig. 2.4. Each sector covers  $4.5^\circ$  in  $\phi$  and has 6 wire modules, which are X1, U1, V1, X2, U2 and V2. Each wire module has 4 anode planes, and has 4 cathode planes.

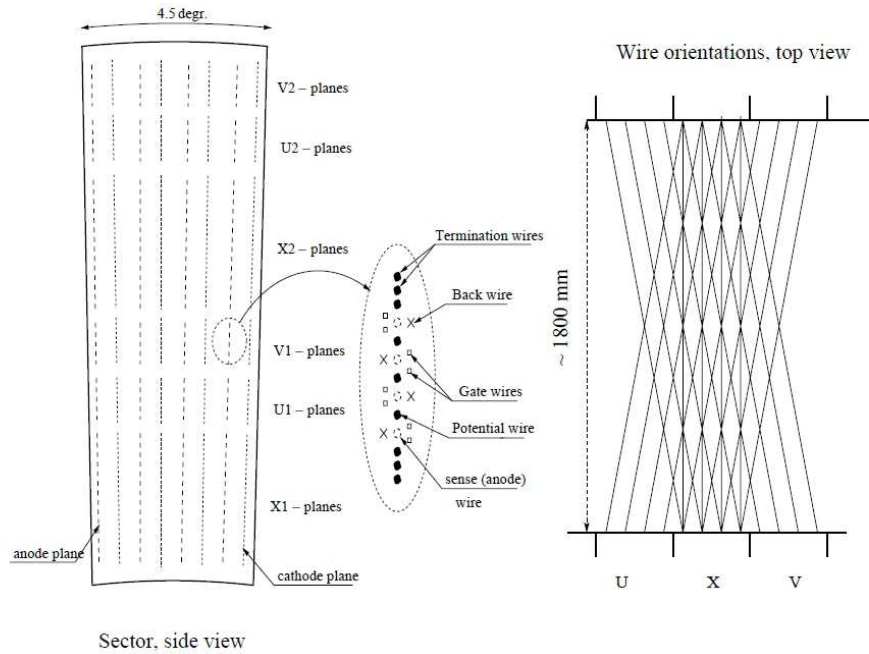


Figure 2.4: Left: Wire position of a sector of drift chamber. Also a map of the anode plane. Right: Top view of the wire orientation in a sector [33].

The position of the wire modules are the following. The wires in the X1 and X2 modules lie parallel to the beam direction, and are used to measure the direction in  $r-\phi$  precisely. The U1, U2, V1, V2 modules are inclined by  $6^\circ$  degrees with respect to X the modules, as shown in the right hand side of Fig. 2.4, in order to give information about the  $z$  position of the track. For each anode plane, there are 12 anode wires in the X modules and 4 anode wires in the U and V modules each. In total, there are about 6500 anode wires in each of the drift chamber arms.

The set up of each anode plane is shown in the right hand side of Fig. 2.4. The anode wires are separated by potential wires which have strong electric potentials. The potential wires separate the sensitive region of each anode wire. Each anode wire is surrounded by two gate wires and a back wire on

the opposite side of the gate wires. Gate wires help focus the ionized electrons drift toward the anode wire and minimize the track sample length to about 3 mm. The back wire has a relatively lower potential, which terminates most of the drift lines from the other direction and can avoid the left–right ambiguity.

To reconstruct the transverse momentum and direction of the track in the drift chamber, the technique “combinatorial Hough transform” is used. To use this method, one looks for tracks hit both the X1 and X2 plane, then the track can be reconstructed. Those tracks with hits in X1 and X2 modules are plotted in the  $x$ – $y$  plane. The polar angle,  $\phi$ , is defined from the center to the intersection of the track with the reference circle with a radius of 220 cm, which is close to the mid–point of the drift chamber. The inclination of the track relative to the intersection is defined as  $\alpha$ . All these features are shown in Fig. 2.5. With  $\phi$  and  $\alpha$ , the direction of the track is also defined. Since the tracks bend in the magnetic field, the inclination angle,  $\alpha$ , is proportional to the inverse of the transverse momentum. With the direction of the track, specified by  $\phi$  and  $\alpha$ , the  $p_T$  of the track can be determined.

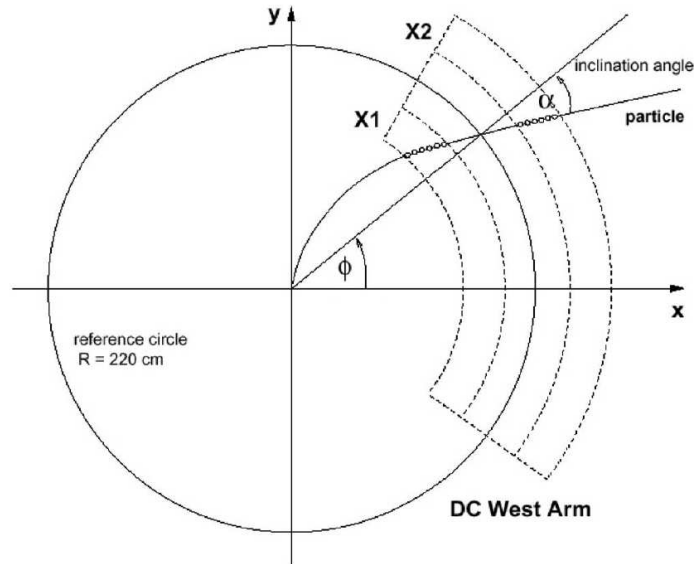


Figure 2.5: Illustration of the Hough transform parameters for drift chamber track reconstruction. The outline shows the drift chamber active volume. The circles represent drift chamber hits along the particle trajectory. [35].

## Pad Chamber

The pad chambers (PC) are three layers of multi-wire proportional chambers [33]. The positions of the pad chambers are shown in Fig. 2.1. The first layer of pad chambers (PC1) are located right behind the drift chambers. The second layer of pad chambers (PC2) are in the west arm, behind the RICH detector. The third layer of pad chambers (PC3) are in both arms, in front of the electromagnetic calorimeter. The combined information from DC and PC1 provides the  $z$  position information of the track, and gives the direction vectors to the RICH, which is crucial for electron identification. The PC2 and PC3 information is important to reject the particles produced from particle decays, which do not point back to the collision vertex. They also reject conversion electrons after or outside the DC acceptance.

Each pad chamber has a similar structure. The vertical structure of the pad chamber is shown in Fig. 2.6. It consists of an anode layer in the gas chamber and sandwiched by two cathode layers. One of the cathode layers is made of solid copper and the other is finely segmented into pixels. When the charged tracks pass through the chamber, the anode wire will start to avalanche, which causes charge to be induced on the pixels. This signal is read out through the readout electronics.

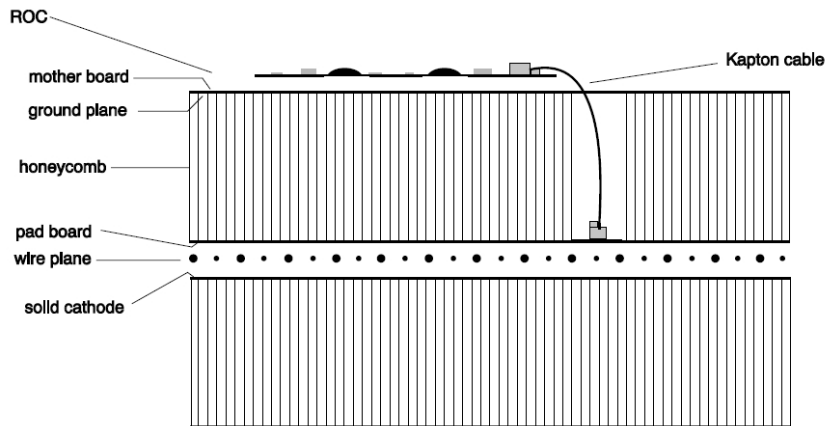


Figure 2.6: Vertical view of the pad chamber [33].

## Electromagnetic Calorimeter

Electromagnetic calorimeters (EMCal) are used to measure the energy and the position of photons and electrons. There are eight sectors of EMCal in the

central arms of PHENIX [34]. There are two different kinds of EMCal used in PHENIX. One is lead scintillator (PbSc), which has good timing resolution. The other is lead glass (PbGl), which has better energy resolution. In the west arm, there are four sectors of lead scintillator, while in east arm there are two lead scintillator and two lead glass sectors.

The lead scintillator electromagnetic calorimeter measures the energy by detecting the shower light coming from the deposited energy from the photons or the electrons. Lead scintillator calorimeter is a shashlik detector, which uses layers of lead as absorber and scintillator for calorimetry. When a photon or electron hits the lead absorber, it showers and is detected by the scintillator. The radiation length of lead scintillator is  $18X_0$  deep.

Each tower in the PbSc calorimeter contains 66 cells, each consisting of alternating layers of lead and plastic scintillator, with the edges covered with aluminum. Four towers are combined into a module, as shown in Fig. 2.7. In total, there are 15552 towers in the PbSc calorimeter. Every 36 modules will be walled by stainless steel to form a super module. Every 18 super modules are grouped as a sector.

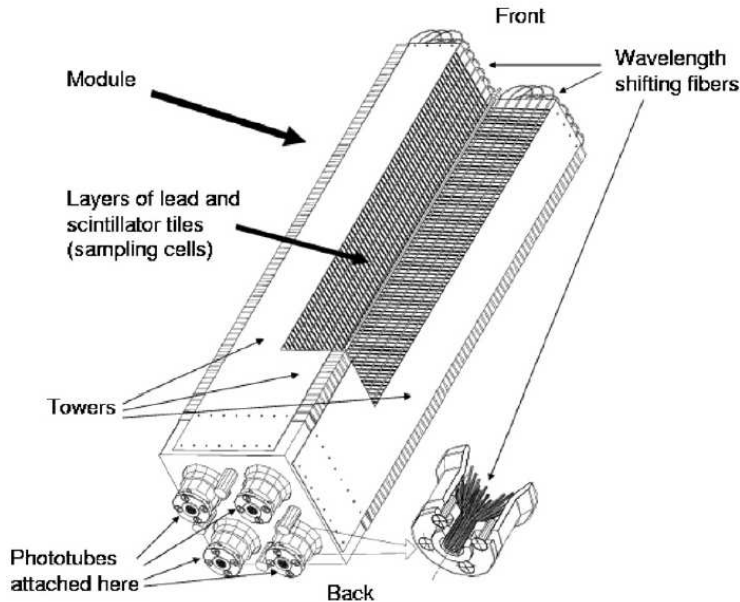


Figure 2.7: The structure of the lead scintillator electromagnetic calorimeter [34].

The lead glass calorimeter is a Cherenkov radiation detector. When photons or electrons pass through the calorimeter, Cherenkov radiation will be

generated and detected. Hadrons with momentum above the Cherenkov threshold also generate Cherenkov radiation, the threshold is 106 MeV/c for pions and 751 MeV/c for protons. Once the momentum of the hadron is below the threshold, the radiation light will be absent.

Each PbG1 module is 40mm x 40mm x 400mm in size. A group of 6x4 PbG1 Modules is a supermodule. For each sector, it has 16x12 supermodules as shown in Fig. 2.8.

When measuring photons with the calorimeter, we exclude the photon clusters which are identified as hot towers or unresponsive regions of the EMCAL. Each photon cluster also must pass shower shape cuts to remove showers from charged particles. The position information from PC3 is used to ensure that there are no charged particles in the cluster in the calorimeter. Time of flight of the particle is also used to remove neutral particles, such as neutrons.

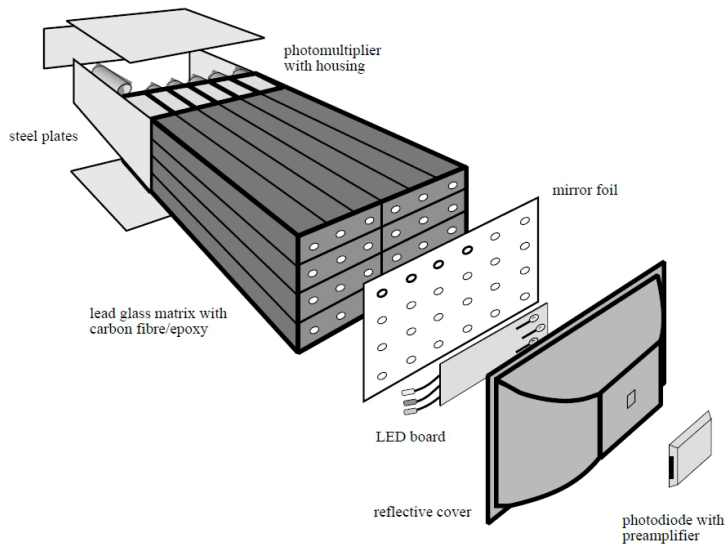


Figure 2.8: The structure of the lead glass calorimeter [34].

## Part II

### Analysis: correlation function

## Chapter 3

# Correlation Function

### 3.1 Introduction

Two particle azimuthal correlations have provided a lot of insight into how jets interact with the quark gluon plasma. In  $p+p$  collisions the azimuthal angular difference between two particles,  $\Delta\phi$ , shows jet fragmentation peaks at  $\Delta\phi = 0$  when both particles are from the fragmentation of the same jet, and at  $\Delta\phi = \pi$  when the particles arise from a back to back di-jet. In Au+Au collisions, high  $p_T$  ( $p_T > 7\text{GeV}/c$ ) back-to-back azimuthal correlations are suppressed, while the near side jet remains nearly unmodified from  $p+p$  collisions [36, 24]. At intermediate transverse momentum ( $2 < p_T < 5\text{GeV}/c$ ), in the transition region from soft (hydro) to hard (jet fragment), several new structures have been observed: the *ridge* [37, 25] and the *shoulder* [21, 22].

There have been several physical pictures proposed to explain the production of the ridge. Jet-medium interactions may result in a momentum kick to particles in the bulk medium, boosting their momentum and producing a correlation with a traversing fast parton [38]. A correlated emission model describes radiation of soft gluons by a parton penetrating the medium; these gluons and their resulting hadronic fragments are boosted by longitudinal flow of the medium [39]. The Glasma model treats the ridge as arising from the flux tube formed early in the collision; expansion of the quark gluon plasma along the longitudinal direction elongates the ridge in  $\eta$  [40]. The shoulder structure has been suggested to arise from passage of a sound wave as the medium responds to shocks deposited by jet energy loss [41, 42, 43]. However there is considerable debate as to whether it is possible to observe the resulting Mach cone-like structure [44, 45].

Until now, analyses of data have typically addressed properties of either the ridge or the shoulder. We address both the modification to the near side and to the away side in the same analysis. Theoretical investigations have



also considered the structures separately. While their origins might in fact be unrelated, they do both appear in the transition region from the low  $p_T$ , hydrodynamical region to the high  $p_T$  energy loss dominated region. Both phenomena could be sensitive to the same properties of the produced matter, or perhaps even be from related physical processes. Consequently, detailed comparison between the near and away side modifications, particularly their evolution with centrality is of prime interest. In this paper we present systematic data on the centrality and transverse momentum dependence of both the ridge and the shoulder.

## 3.2 Definition of Correlation Function

Jets are important probes to understand the properties of the quark–gluon plasma. But in central heavy ion collisions, thousands of particles are produced in the final state, making jet finding an extremely difficult task. Instead, two particle azimuthal correlations provide a simpler method to study the properties of jet in the medium.

This correlation function method is a statistical method to study two particle correlations. When jets are produced in hard collisions, they will fragment into high  $p_T$  particles which are confined to a small range of azimuthal angle  $\Delta\phi$  and pseudorapidity  $\Delta\eta$ , where  $\eta = -\ln(\tan(\theta/2))$  and  $\theta$  is the polar angle relative to the beam direction. The size of the jet cone,  $R = \sqrt{\Delta\phi^2 + \Delta\eta^2} \approx 0.3$ . So the idea of two particle correlations is to select a high  $p_T$  particle, known as the trigger particle, presumed to be a jet fragment, and correlate it with lower  $p_T$  particles (the partner or associated particle) in  $\phi$  or  $\eta$ . Then the pair distribution is plotted in the difference in azimuthal angle,  $\Delta\phi$ , and pseudorapidity,  $\Delta\eta$ , of trigger and associated particles. When the difference of the azimuthal angle between trigger and associated particles,  $\Delta\phi \approx 0$ , both particles are fragments of the same jet. If  $\Delta\phi \approx \pi$ , the associated particle comes from the opposing jet. By looking at these correlations, we can study the properties of the near ( $\Delta\phi \approx 0$ ) and away ( $\Delta\phi \approx \pi$ ) side jets statistically.

A typical correlation function looks like Fig. 3.1. The two particle correlation function has contributions from two sources: jet pairs and the underlying event. In order to extract the jet signal, we need to determine the level and also the shape of the underlying event background. After the shape and the level are properly determined, we can subtract out the background and extract the jet signal.

In this analysis, we measure the two particle  $\Delta\eta$ – $\Delta\phi$  correlations. We select a photon as the trigger particle and a charged hadron as the associated

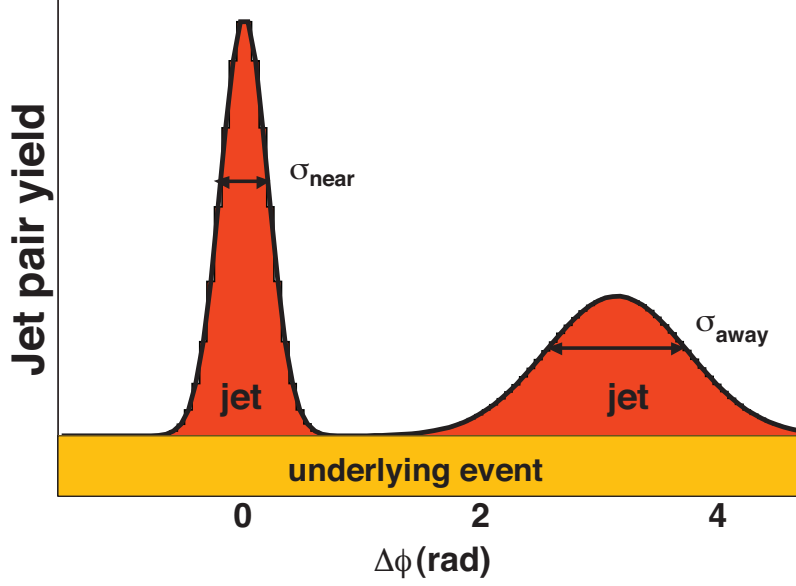


Figure 3.1: A typical correlation function. On the top are the jet pairs. On the bottom are uncorrelated underlying backgrounds

particle, and measure the difference between the trigger and associated particle azimuthal angles and pseudo-rapidities,  $\eta$ . The  $p_T$  range of the photons in this analysis is 2–3 GeV/c, which are primarily from the decay of  $\pi^0$  mesons. This also avoid the low  $\pi^0$  signal to background ratio of low  $p_T$   $\pi^0$ s due to huge combinatorial background. Using photon as a trigger particle provides the advantage of removing correlations coming from triggering baryons and anti-baryons which have less associated meson yields than associated meson yields in meson triggered collisions in central Au+Au collisions in this  $p_T$  range [46]. Due to the geometry of the PHENIX central arms, the acceptance is non uniform in both  $\Delta\phi$  and  $\Delta\eta$ . We use the shape of the mixed event background to correct the  $\Delta\phi$  and  $\Delta\eta$  acceptance. The idea of event mixing is that by forming pairs with trigger particles from one event and associated particles from another event, the two particles will be totally uncorrelated. Hence, the only effect which will change the shape of the mixed event distribution is the acceptance of the detector. By measuring the mixed event background properly, therefore we can correct for the acceptance in  $\Delta\eta$  and  $\Delta\phi$ .

We define the 2D correlation function,  $C(\Delta\eta, \Delta\phi)$ , as:

$$C(\Delta\eta, \Delta\phi) = \frac{N^{same}(\Delta\eta, \Delta\phi) \int N^{mixed}(\Delta\eta, \Delta\phi) d\Delta\eta d\Delta\phi}{N^{mixed}(\Delta\eta, \Delta\phi) \int N^{same}(\Delta\eta, \Delta\phi) d\Delta\eta d\Delta\phi} \quad (3.1)$$

where  $N^{same}(\Delta\eta, \Delta\phi)$  is for the measured correlated pairs, and  $N^{mixed}(\Delta\eta, \Delta\phi)$  is for the pairs from the mixed events.

The resulting  $C(\Delta\eta, \Delta\phi)$  is then both  $\Delta\eta$  and  $\Delta\phi$  acceptance corrected. A typical distribution is shown in Fig. 3.2(a).

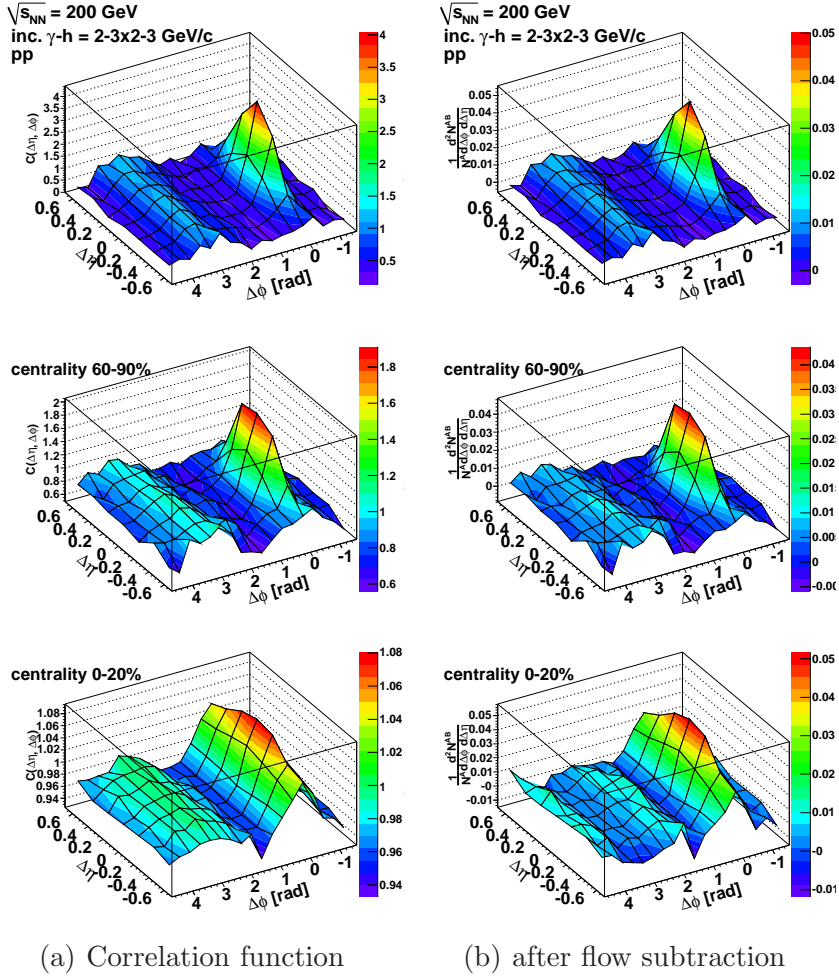


Figure 3.2:  $\Delta\eta$ - $\Delta\phi$  correlation functions of trigger 2–3 GeV/c, partner 2–3 GeV/c, in p+Au, Au+Au at 60–90% and 0–20%. (a): Correlation function before remove the combinatorial background; (b): conditional yield per trigger.

## 3.3 Data Selection

### 3.3.1 Data and Selection

In this analysis, we use the data taken during the 2004 and 2005 runs (Run4 and Run5). After quality assurance checks,  $8.8 \times 10^8$  events are used in Au+Au, and  $1.3 \times 10^9$  events are used in p+p.

All data has been calibrated. Events are removed if the vertex is more than 30 cm from the center, where the magnetic field is uniform within this region.

#### Single Particle Selection

We use the electro-magnetic calorimeter (EMCAL) to measure the photons. We remove the photon clusters that hit the hot towers and unresponsive regions of the EMCAL. Each photon cluster also must pass shower shape cuts to remove showers from charged particles. The position information from PC3 is used to ensure that there are no charged particles in the cluster. We also require a time of flight cut to remove the neutral particles, such as neutrons ( $\text{TOF} < 1.35$  ns).

For charged particles, we require  $|zed_{DC}| < 75$  cm to remove drift chamber edge effects. We also require a  $2\sigma$  PC3 matching cut in both  $z$  and  $\phi$ . We group charged particles in 5 different  $p_T$  bins, which are 1–1.5, 1.5–2, 1–2, 2–3, 3–5 GeV/ $c$ .

### 3.3.2 Analysis Scheme

In this analysis, we use the standard mixing scheme of PHENIX, which is called “CabanaBoy”. In two particle correlation analysis, the signal, or the foreground, is formed by pairing trigger and partner particles in the same event. The mixed event background is formed by pairing trigger particles from one event and partner particles from another event. Since the two events are independent, this mixed event describes the uncorrelated event shape and detector acceptance. In order to apply the same cuts to both foreground and background, we apply the same pair cuts in mixed events. In CabanaBoy, we group the events into 20 centrality bins (0–100%, 5% per bin), 12  $z$  vertex bins ( $-30 < z < 30$  cm, 5 cm per bin). We do the mixing for events which have similar centrality and  $z$ -vertex.

The centrality bins used in this analysis are 0–5%, 5–10%, 10–20%, 20–40%, 40–60%, 60–90%. The most central bins are merged into 0–20% for

more statistics. Trigger  $p_T = 2\text{--}3$  GeV/c, partner  $p_T = 1\text{--}1.5, 1.5\text{--}2, 2\text{--}3, 3\text{--}5$  GeV/c. The same  $p_T$  bins also applied to p+p analysis.

### 3.4 Background Subtraction

In order to estimate the yield of the jet-induced pairs in the correlation functions, we assume a two component model [21]. The two component model assumes that the measured pairs are either from jet fragments or combinatorial background from the underlying event.

For the underlying events, we must correct for the correlations created by the collective flow described before. To do this, we assume the distributions of both trigger and partner particle are proportional to  $1 + 2 \langle v_2 \rangle \cos 2(\phi - \psi_{RP})$ , where  $\psi_{RP}$  is the angle of the reaction plane. The uncorrelated pairs in the underlying events are then proportional to  $1 + 2 \langle v_2^A v_2^B \rangle \cos(2\Delta\phi)$ , where A and B correspond to trigger and associated particles, respectively. Based on the results of PHOBOS [47] and PHENIX [48], the  $v_2$  of inclusive photons and charged hadrons are treated as constant along the  $\eta$  direction, within the PHENIX central arm  $\eta$  acceptance ( $|\eta| < 0.35$ ).

In the two source model, the correlation function,  $CF(\Delta\eta, \Delta\phi)$  can be rewritten as

$$CF(\Delta\eta, \Delta\phi) = b_0(1 + 2 \langle v_2^A v_2^B \rangle \cos(2\Delta\phi)) + JF(\Delta\eta, \Delta\phi) \quad (3.2)$$

where  $JF(\Delta\eta, \Delta\phi)$  is the correlation of the jet pairs, or the jet function. The  $b_0$  determines the level of the underlying events.

The  $v_2$  of inclusive photons and charged hadrons used in this analysis are measured by the standard reaction-plane method. Details will be presented in the following sections.

In order to determine the contribution from the jet,  $J(\Delta\eta, \Delta\phi)$ , we need to determine  $b_0$ . We apply the ‘‘Zero Yield at Minimum’’ or ZYAM method [23], which assumes that after subtraction the yield is zero at the minimum of the jet function. This technique determines the maximum possible background level. The point where the yield is zero is called the ZYAM point. Since  $v_2$  is constant along  $\eta$  within the PHENIX acceptance, then the combinatorial background should also be flat within the PHENIX acceptance. Since the single particle distribution in  $\eta$ ,  $dN/d\eta$ , is uniform with the PHENIX  $\eta$  acceptance [49], we assume the ZYAM level,  $b_0$ , is constant within the PHENIX  $\Delta\eta$  acceptance. We project the correlation function,  $C(\Delta\eta, \Delta\phi)$ , on the  $\Delta\phi$  direction to maximize the statistics, and then determine the ZYAM level. This ZYAM level is applied to the whole  $\Delta\eta$  range.

The result of the subtracted correlation function is shown in Fig. 3.2(b). The detail of the subtracted correlation function will be described in Chapter 4.

### 3.5 Measurement of $v_2$

In this analysis, we measured  $v_2$  of inclusive photons and inclusive charged hadrons, to ensure precise values in the centrality and  $p_T$  bins for which we construct correlation functions. The results are compared with other existing PHENIX analysis.

We use the event plane method [50] to measure the azimuthal anisotropy. The definition of  $v_2$  is Eq. 3.3

$$v_2 = \langle \cos(2\phi - \psi_{RP}) \rangle \quad (3.3)$$

where  $\psi_{RP}$  is the direction of the reaction plane. Experimentally we can not measure  $\psi_{RP}$  precisely. We define the event flow vector  $\vec{Q}_n = (Q_x, Q_y)$ . Then the event plane  $\psi_n$  for the  $n$ -th harmonic is defined as

$$Q_x \equiv |\vec{Q}_n| \cos(n\psi_n) = \sum_i^M w_i \cos(n\phi_i), \quad (3.4)$$

$$Q_y \equiv |\vec{Q}_n| \sin(n\psi_n) = \sum_i^M w_i \sin(n\phi_i), \quad (3.5)$$

$$\psi_n = \frac{1}{n} \tan^{-1} \left( \frac{Q_y}{Q_x} \right), \quad (3.6)$$

where  $M$  is the number of particles used to determine the event plane,  $\phi_i$  is the azimuthal angle of each particle, and  $w_i$  is the weight to optimize the reaction plane resolution. From Eq. 3.6, we can reconstruct the event plane  $\psi_2$  event by event. This is known as the event plane for the second harmonic. The event plane for higher harmonics will not necessarily be exactly the same.

After determining  $\psi_2$ ,  $v_2$  can be measured as

$$v_2 = \frac{v_2^{obs}}{\Delta} = \frac{\langle \cos(2(\phi - \psi_2)) \rangle}{\langle \cos(2(\psi_2 - \psi_{RP})) \rangle} \quad (3.7)$$

where

$$\Delta = \langle \cos(2(\psi_2 - \psi_{RP})) \rangle \quad (3.8)$$

is the resolution of the reaction plane.

### 3.5.1 Reaction plane resolution, $\Delta$

We measured the reaction plane resolution,  $\Delta$ , using the beam–beam counter (BBC). The systematic error is the difference in the resolution given by BBC north and BBC south. The values of  $\Delta$  used in this analysis are listed in Table 3.1.

Table 3.1: The reaction plane resolution,  $\Delta$ , in various centrality

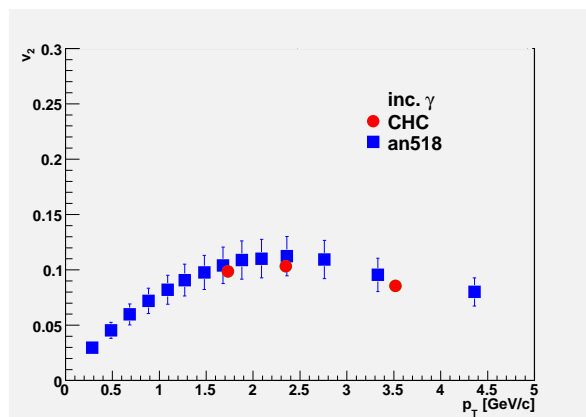
Centrality	$\Delta$	stat. err	sys. err
0–5	0.2109	0.0005	0.0011
5–10	0.3094	0.0004	0.0038
10–20	0.3852	0.0002	0.0067
20–40	0.3867	0.0001	0.0067
40–60	0.2580	0.0002	0.0020
60–90	0.0909	0.0005	0.0015
0–10	0.2649	0.0003	0.0022
0–20	0.3310	0.0002	0.0042

### 3.5.2 $v_2$ of Inclusive Photons

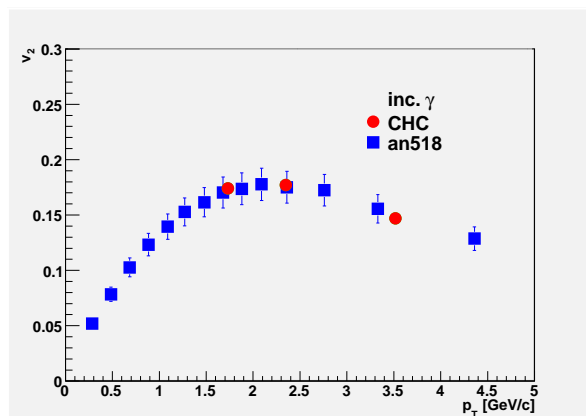
We measured the  $v_2$  of inclusive photons using the event plane method described above. The measured results in this analysis are shown as red points (CHC) and compared with with PHENIX preliminary Run4 result (shown as blue points, AN518) [51] as shown in Fig 3.3(a), Fig 3.3(b) and Fig 3.3(c). The  $v_2$  of inclusive photons used in this analysis are listed in Table 3.2. The systematic error for the photon  $v_2$  is dominated by the reaction plane resolution.

Table 3.2:  $v_2$  of the inclusive photon in various centrality at  $p_T = 2\text{--}3$  GeV/c

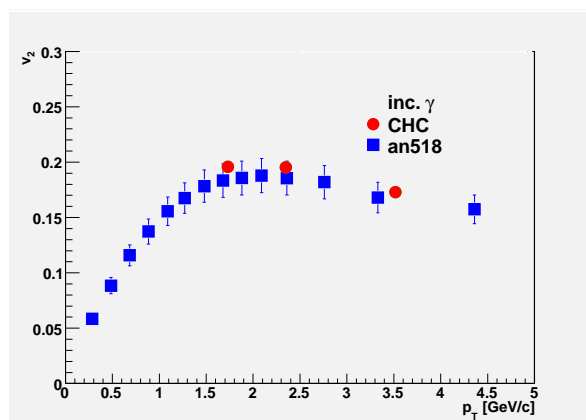
Centrality	$v_2$	stat. err	sys. err
0–5	0.0618	0.0015	0.0003
5–10	0.0950	0.0011	0.0012
10–20	0.1346	0.0007	0.0023
20–40	0.1780	0.0006	0.0031
40–60	0.1966	0.0014	0.0015
60–90	0.1825	0.0069	0.0030
0–10	0.0783	0.0008	0.0007
0–20	0.1038	0.0005	0.0013



(a) 0–20%



(b) 20–40%



(c) 40–60%

Figure 3.3:  $v_2$  of the inclusive photon at centrality 0–20%. Red points (CHC) are measurement from this analysis; blue points (an518) are measurements from PHENIX preliminary results [51]. (a): 0–20%; (b): 20–40%; (c): 40–60%;



### 3.5.3 $v_2$ of inclusive charged hadron

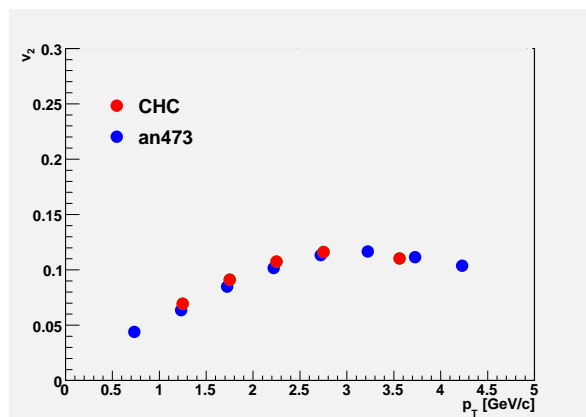
We measured the  $v_2$  of the inclusive charged hadrons with the event plane method described in Sec. 3.5.1. The particle selection cuts are consistent with the cuts used in the correlation analysis. The measured values are compared with PHENIX preliminary 2004 result [52]. Selected comparisons are shown in Fig 3.4(a) to Fig 3.4(c). The  $v_2$  measurement in this analysis is in good agreement with the PHENIX preliminary results. The  $v_2$  of inclusive charged hadrons used in this analysis are listed in Table 3.3 to Table 3.7. The systematic error on this measurement is again dominated by the reaction plane resolution.

Table 3.3:  $v_2$  of the inclusive charged hadron in various centrality at  $p_T = 1.0\text{--}1.5$  GeV/c

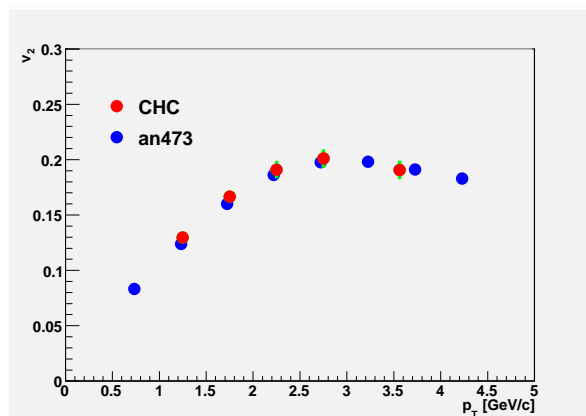
Centrality	$v_2$	stat. err	sys. err
0–5	0.0419	0.0002	0.0019
5–10	0.0627	0.0002	0.0016
10–20	0.0915	0.0001	0.0034
20–40	0.1296	0.0001	0.0045
40–60	0.1558	0.0002	0.0029
60–90	0.1613	0.0014	0.0063
0–10	0.0520	0.0001	0.0010
0–20	0.0695	0.0001	0.0021

Table 3.4:  $v_2$  of the inclusive charged hadron in various centrality at  $p_T = 1.5\text{--}2.0$  GeV/c

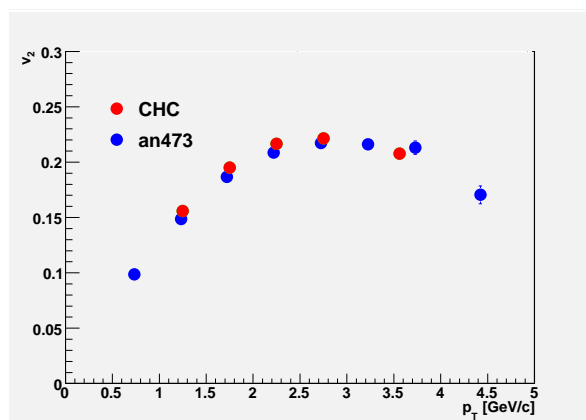
Centrality	$v_2$	stat. err	sys. err
0–5	0.0543	0.0004	0.0017
5–10	0.0821	0.0003	0.0021
10–20	0.1198	0.0002	0.0045
20–40	0.1666	0.0002	0.0059
40–60	0.1950	0.0004	0.0032
60–90	0.1982	0.0023	0.0108
0–10	0.0680	0.0002	0.0013
0–20	0.0912	0.0001	0.0028



(a) 0–20%



(b) 20–40%



(c) 40–60%

Figure 3.4:  $v_2$  of the inclusive charged hadron at centrality 0–20%. Red points (CHC) are measured in this analysis; blue points (an473) are from PHENIX preliminary results. [52]. (a): 0–20%; (b): 20–40%; (c): 40–60%;

Table 3.5:  $v_2$  of the inclusive charged hadron in various centrality at  $p_T = 1.0\text{--}2.0$  GeV/c

Centrality	$v_2$	stat. err	sys. err
0–5	0.0448	0.0002	0.0019
5–10	0.0672	0.0002	0.0017
10–20	0.0981	0.0001	0.0037
20–40	0.1382	0.0001	0.0048
40–60	0.1647	0.0002	0.0029
60–90	0.1694	0.0013	0.0072
0–10	0.0557	0.0001	0.0010
0–20	0.0745	0.0001	0.0022

Table 3.6:  $v_2$  of the inclusive charged hadron in various centrality at  $p_T = 2.0\text{--}3.0$  GeV/c

Centrality	$v_2$	stat. err	sys. err
0–5	0.0654	0.0006	0.0014
5–10	0.0992	0.0004	0.0026
10–20	0.1424	0.0003	0.0053
20–40	0.1934	0.0002	0.0067
40–60	0.2177	0.0006	0.0036
60–90	0.2151	0.0035	0.0073
0–10	0.0823	0.0004	0.0017
0–20	0.1095	0.0002	0.0034

Table 3.7:  $v_2$  of the inclusive charged hadron in various centrality at  $p_T = 3.0\text{--}5.0$  GeV/c

Centrality	$v_2$	stat. err	sys. err
0–5	0.0643	0.0017	0.0028
5–10	0.0989	0.0012	0.0025
10–20	0.1438	0.0008	0.0060
20–40	0.1907	0.0007	0.0070
40–60	0.2078	0.0016	0.0041
60–90	0.2052	0.0085	0.0123
0–10	0.0817	0.0010	0.0013
0–20	0.1104	0.0006	0.0035

## 3.6 Photon Distribution

Inclusive photons with  $2 < p_T < 3$  GeV/c are dominated by decay photons from  $\pi^0$ s. It is important to know the  $p_T$  distribution of the parent  $\pi^0$ s.

The method used here is similar to the “shark fin” method used in direct  $\gamma$ -h analyses in PHENIX [53]. The idea is to calculate the probability of a  $\pi^0$  with the momentum at  $p_T^{\pi^0}$  has a decay photon which has transverse momentum  $p_T^\gamma$ . We use an analytic approach to directly calculate the probability of a  $\pi^0$  with transverse momentum  $p_T^{\pi^0}$ , decaying to a photon with  $p_T^\gamma$  between 2 and 3 GeV/c.

The probability of a photon parent with  $p_T^{\pi^0}$ ,  $\text{Prob}(p_T^{\pi^0})$  is

$$\begin{aligned}
 \text{Prob}(p_T^{\pi^0}) &= 0, \text{ if } p_T^{\pi^0} < p_T^\gamma|_{low} \\
 &= 2 \frac{p_T^{\pi^0} - p_T^\gamma}{p_T^{\pi^0}}, \text{ if } p_T^\gamma|_{low} < p_T^{\pi^0} < p_T^\gamma|_{high} \\
 &= 2 \frac{p_T^{\pi^0} - p_T^\gamma|_{high}}{p_T^{\pi^0}}, \text{ if } p_T^\gamma|_{high} < p_T^{\pi^0}
 \end{aligned} \tag{3.9}$$

Here the  $p_T^\gamma$  is between 2–3 GeV/c. The resulting decay probability distribution is shown in Fig 3.5. As an example, for a 3 GeV  $\pi^0$ , the probability to have a 2–3 GeV/c decay photon is about 0.66.

This probability distribution is weighted by the  $\pi^0$  spectra from p+p [54], and Au+Au in various centralities [20]. The  $\pi^0$  spectra in [20] are measured mainly in 10% centrality bins, and properly combined to be consistent with the centrality bins used in this analysis. We only consider  $\pi^0$   $p_T$  below 10 GeV/c, since the yields for high  $p_T$   $\pi^0$  are several orders of magnitude smaller and have essentially no contributions in the yields of the decay photons. When  $p_T$  of  $\pi^0$  is below 2 GeV/c, the  $\pi^0$  has no contribution to decay photons between 2–3 GeV/c.

We use the  $\pi^0$  spectrum of Au+Au at 0–20%, Fig 3.6, as an example. Fig 3.6 has two spectra. The black spectrum is the measured  $\pi^0$  spectrum in Au+Au [20]. The red points show the measured spectrum weighted by the probability in Fig 3.5. It is clear that in the weighted spectra (red), 2–3 GeV/c  $\pi^0$ s are still the dominant source of photons at 2–3 GeV/c.

From these weighted spectra, we can measure the average  $p_T$  of the parent  $\pi^0$ s, which is tabulated in Table 3.8. For comparison, we also list the mean  $p_T$  of  $\pi^0$ s at  $p_T$  2–3 GeV/c. The overall trend is that the mean  $p_T$  of the parent  $\pi^0$ s is higher than the mean  $p_T$  from the unweighted  $\pi^0$  spectra.

Table 3.8: The average  $p_T$  of  $\pi^0$  which decays to a 2–3 GeV/c photon

Centrality	mean parent $\pi^0$ $p_T$ [GeV/c]	mean $\pi^0$ $p_T$ at 2–3 GeV/c
0-5	2.60729	2.34511
5-10	2.62896	2.35626
10-20	2.64737	2.35876
20-40	2.66607	2.36175
40-60	2.69527	2.36674
60-90	2.71375	2.3706
0-10	2.61747	2.35025
0-20	2.63031	2.35382
p+p	2.71317	2.36951

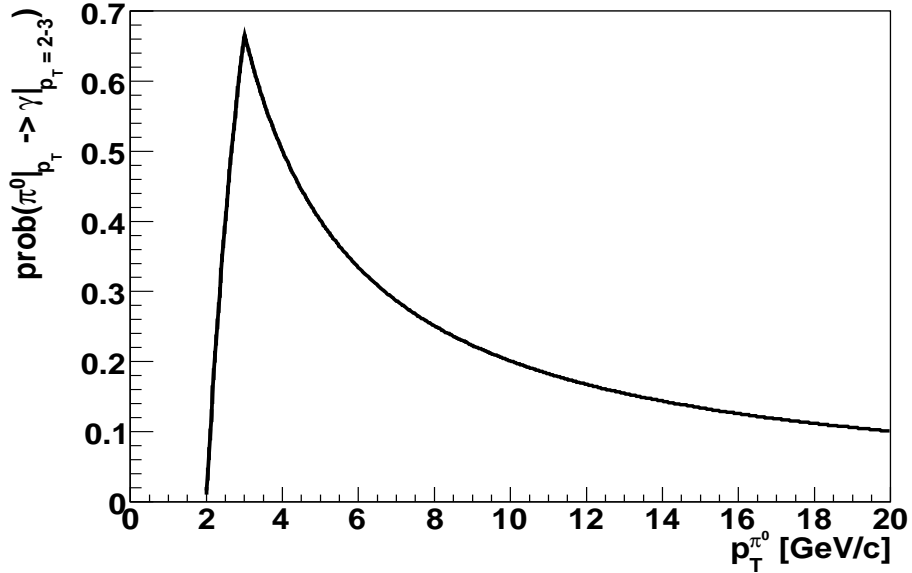


Figure 3.5: Probability distribution of  $\pi^0$  generating a 2–3 GeV/c decay photon.

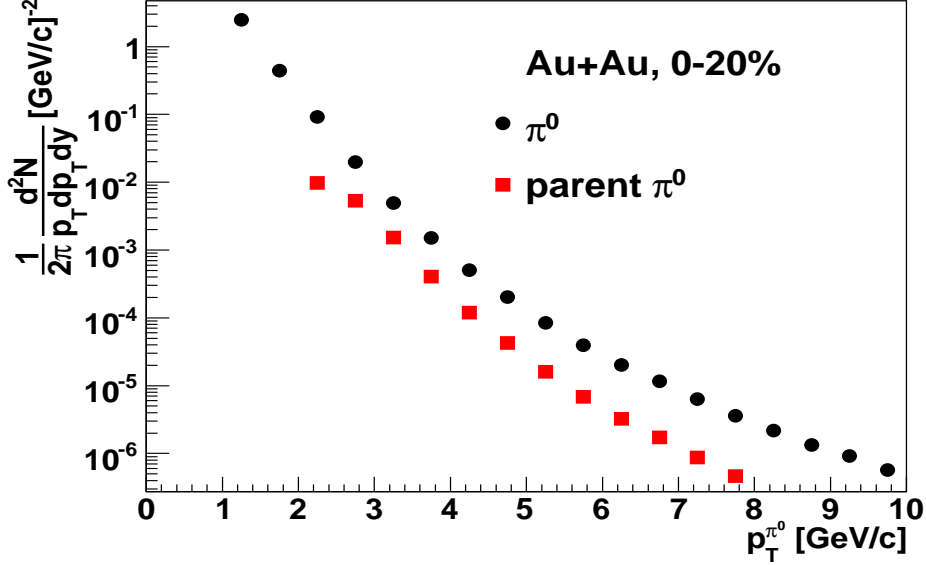


Figure 3.6:  $\pi^0$  spectra (black) and the  $\pi^0$  spectra weighted by the sharkfin (red) at centrality 0–20%

### 3.7 Normalization

For standard two particle azimuthal  $\Delta\phi$  correlations, the conditional yield is an important quantity which measures the number of associated particles when there exists a trigger particle. This conditional yield is also called the “per trigger yield”. Eq. (3.10) is used to calculate this per trigger yield:

$$\frac{1}{N^A} \frac{dN^{AB}(\Delta\phi)}{d(\Delta\phi)} = \frac{1}{\epsilon_B} \frac{N_{Real}^{AB}}{N_{Real}^A} \frac{1}{\int d(\Delta\phi)} J(\Delta\phi) \quad (3.10)$$

In Eq. (3.10),  $\epsilon_B$  is the single particle efficiency of the associated particles.  $N_{Real}^{AB}$  (and  $N_{Real}^A$ ) is the true number of pairs (triggers) measured in the analysis.

For  $\Delta\phi$  correlations, the integral  $\int d(\Delta\phi)$  is  $\pi$  ( $2\pi$ ) if the  $\Delta\phi$  is from 0 to  $\pi$  ( $2\pi$ ). This is because  $\Delta\phi$  is a cyclic function.

To get the per trigger yield of in  $\Delta\eta$ - $\Delta\phi$  correlation functions, we extend Eq. (3.10):

$$\frac{1}{N^A} \frac{d^2N^{AB}(\Delta\eta, \Delta\phi)}{d(\Delta\eta)d(\Delta\phi)} = \frac{1}{\epsilon_B} \frac{N_{Real}^{AB}}{N_{Real}^A} \frac{1}{\int d(\Delta\eta) \int d(\Delta\phi)} J(\Delta\eta, \Delta\phi) \quad (3.11)$$

In this analysis,  $\Delta\phi$  is from  $-\pi/2$  to  $3\pi/2$ , so  $\int \Delta\phi$  is  $2\pi$ , which is the same as the one-dimensional case.

In the  $\Delta\eta$  direction, both the trigger and the partner distributions are flat within the PHENIX  $\eta$  acceptance ( $|\eta| < 0.35$ ). If we convolve two flat distribution between  $|\eta| < 0.35$ , we can find a simple triangular shape for the  $\Delta\eta$  acceptance,  $acc(\Delta\eta) = (0.7 - |\Delta\eta|)/0.7$  [55]. This means we only have 50% pair efficiency in the  $\Delta\eta$  direction. In Eq. (3.11),  $\int d(\Delta\eta)$  should be written as  $\int_{-0.7}^{0.7} acc(\Delta\eta)d(\Delta\eta) = 0.7$ .

Similarly, if both trigger and partner distributions are flat in  $\phi$  from 0 to  $2\pi$ , we can show that  $acc(\Delta\phi) = 1$ .

The equation to calculate the per trigger yield in 2D  $\Delta\eta$   $\Delta\phi$  correlation, or Eq. (3.11), should be re-written in the form of

$$\frac{1}{N^A} \frac{d^2 N^{AB}(\Delta\eta, \Delta\phi)}{d(\Delta\eta)d(\Delta\phi)} = \frac{1}{\epsilon_B} \frac{N^{AB}}{N^A} \frac{1}{\int acc(\Delta\eta)d(\Delta\eta) \int acc(\Delta\phi)d(\Delta\phi)} J(\Delta\eta, \Delta\phi) \quad (3.12)$$

where  $\int_{-0.7}^{0.7} acc(\Delta\eta)d(\Delta\eta) = 0.7$  and  $\int_{-\pi/2}^{3\pi/2} acc(\Delta\phi)d(\Delta\phi) = 2\pi$ .

### 3.8 Efficiency Correction

In order to obtain the per trigger yield of the correlation function, we need to know the efficiency of detecting the associated charged hadrons,  $\epsilon_B$ , in Eq. 3.11. We determine this efficiency by comparing the measured charged particle spectra in this analysis with the published spectra [56], which has been corrected for the detector acceptance and all the efficiencies.

In [56], PHENIX published the spectra for inclusive charged hadrons,  $\frac{(h^+ + h^-)}{2}$ , in units of  $\frac{1}{2\pi p_T N_{evt}} \frac{dN^2}{dp_T d\eta}$ . In order to get the corrected number of particles inside the PHENIX central arm  $\eta$  acceptance, we convert the spectrum to the number of particles expected in a certain  $p_T$  bin in this measurement. To do this, we multiply  $2\pi$ ,  $p_T$  and  $dp_T$  for each  $p_T$  bin in the spectrum. We then apply  $d\eta = 0.7$ , a factor of 2 for  $h^+$  and  $h^-$ , and the number of events,  $N_{evt}$ , in our measurement.

Using the number of particles expected from the published spectra,  $N^{publish}$ , and number of particles we measured,  $N^{measured}$ , we can calculate the associated particle efficiency,  $\epsilon$ , for this measurement, defined as

$$\epsilon = \frac{N^{measured}}{N^{publish}} \quad (3.13)$$

For p+p, the inclusive charged hadron spectra is taken from PHENIX paper [57]. By comparing the measured spectra with the published ones in [57], we can determine the efficiency in p+p. The spectrum in [57] is absolutely normalized; we use Eq.( 3.14) to convert the cross section to number of particles:

$$E \frac{d^3 \sigma_x^{unbiased}}{d^3 p} = \sigma_x^{unbiased} \frac{1}{2\pi} \frac{1}{p_T} \frac{1}{N_X^{TotalUnbiased}} \frac{d^2 N_X^{Unbiased}}{dp_T dy} \quad (3.14)$$

$\sigma_x^{unbiased} = 42.5$  mb is the total p+p inelastic cross section at  $\sqrt{s} = 200$  GeV. There is also a BBC trigger bias effect, which is  $N_x^{unbiased} = C_{p+p}^{BBC} N_x^{totalbiased}$ . The value of  $1/C_{p+p}^{BBC} = 0.75$ . With all the parameters, we can calculate  $N_x^{totalbiased}$ . From Eq.( 3.14), we transform the cross section of inclusive charged particles to an invariant yield.

The efficiency in our measurement in Au+Au and p+p is shown in Table 3.9.

Table 3.9: Efficiency of AuAu and pp in various  $p_T$  and centrality bins.

centrality	partner $p_T$ [GeV/c]				
	1.0 – 1.5	1.5 – 2.0	1.0 – 2.0	2.0 – 3.0	3.0 – 5.0
0–5	0.1954	0.2011	0.1966	0.2143	0.2522
5–10	0.2033	0.2097	0.2048	0.2236	0.2535
10–20	0.2158	0.2241	0.2177	0.2371	0.2618
20–40	0.2297	0.2399	0.2320	0.2531	0.2758
40–60	0.2469	0.2608	0.2499	0.2745	0.2971
60–90	0.2589	0.2773	0.2627	0.2986	0.3187
0–10	0.1986	0.2047	0.2000	0.2180	0.2520
0–20	0.2057	0.2129	0.2073	0.2258	0.2563
p+p	0.2061	0.2172	0.2082	0.2299	0.2610

### 3.9 Multiplicity Cross Check

To make sure that we applied the correct factor when calculating the per trigger yield, we perform a multiplicity crosscheck. The idea is that the total multiplicity obtained from  $\Delta\eta$ - $\Delta\phi$  correlation should be the same as from  $\Delta\phi$  correlations times the  $\Delta\eta$  bin width. Since we applied the same method in all centrality and  $p_T$  bins, we only select one particular example here.

We use trigger  $p_T = 2$ –3 GeV/c, partner  $p_T = 1$ –2 GeV/c, centrality 0–20% as an example. When we integrate the  $\Delta\eta$ - $\Delta\phi$  correlation function, Fig 3.7,



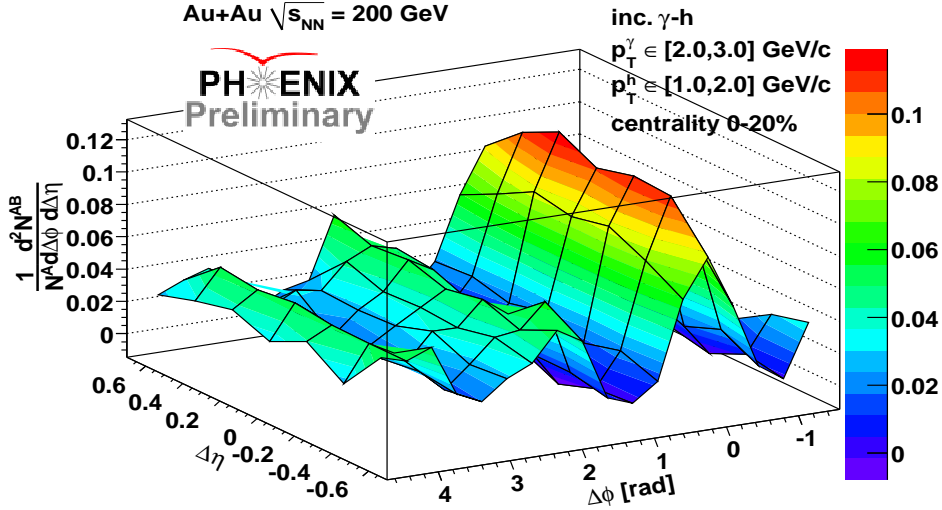


Figure 3.7:  $\Delta\eta$ - $\Delta\phi$  jet function of 2–3x1–2 GeV/c, centrality 0–20%, with  $v_2$  modulated underlying event background subtracted.

times the bin width in  $\Delta\phi$  and  $\Delta\eta$ , the total multiplicity is 0.660 pairs per trigger. Integrating the correlation function along  $\Delta\phi$  for the  $0.0 < |\Delta\eta| < 0.7$ , Fig 3.8, yield the total multiplicity of  $0.471 * 1.4 = 0.660$ , showing that the two results are consistent.

We also check in finer  $\Delta\eta$  bins. Integrating 4  $\Delta\eta$  bins separately and summing  $0.0 < |\Delta\eta| < 0.1$ ,  $0.1 < |\Delta\eta| < 0.3$ ,  $0.3 < |\Delta\eta| < 0.5$ , and  $0.5 < |\Delta\eta| < 0.7$ , (Fig 3.9, Fig 3.10, Fig 3.11 and Fig 3.12), then the total multiplicity of  $0.495 * 0.2 + 0.481 * 0.4 + 0.494 * 0.4 + 0.427 * 0.4 = 0.660$ . This verifies that the result is consistent between 1D  $\Delta\phi$  and 2D  $\Delta\eta$ - $\Delta\phi$  correlation functions.

### 3.10 Systematic Error

In this analysis, systematic errors arise from four different sources:  $v_2$ , ZYAM, hadron efficiency, and hadron contamination of the photon trigger.

The shape of the underlying event background is  $b_0(1 + 2c_2 \cos(2\Delta\phi))$ , where  $b_0$  is the level of the background, and  $c_2$  is the modulation defined as  $c_2 = v_2^{trig} \times v_2^{part}$ . The  $v_2$  systematic error of the subtracted jet function is by fixing background level,  $b_0$  and varying the  $v_2$  by the  $1\sigma$  systematic error.

The ZYAM error is the uncertainty of the ZYAM level, or  $b_0$ . To estimate

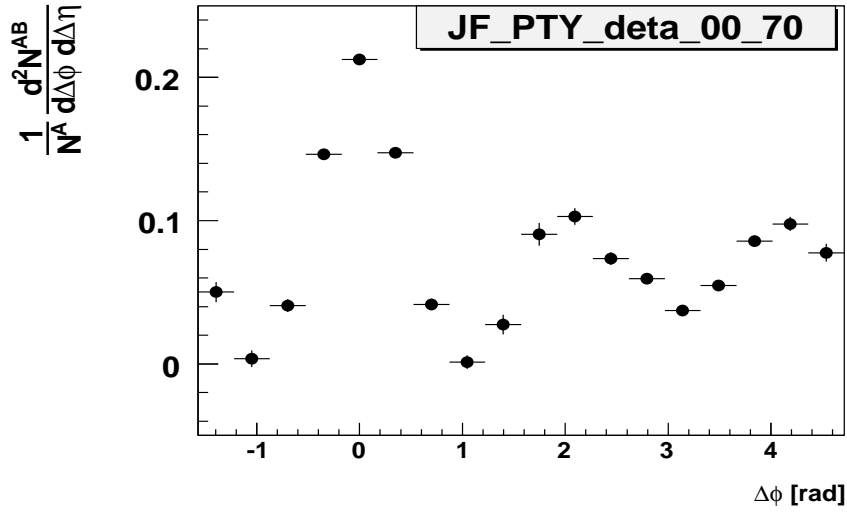


Figure 3.8:  $\Delta\phi$  correlation function of 2–3x1–2 GeV/c, centrality 0–20%,  $0.0 < |\Delta\eta| < 0.7$

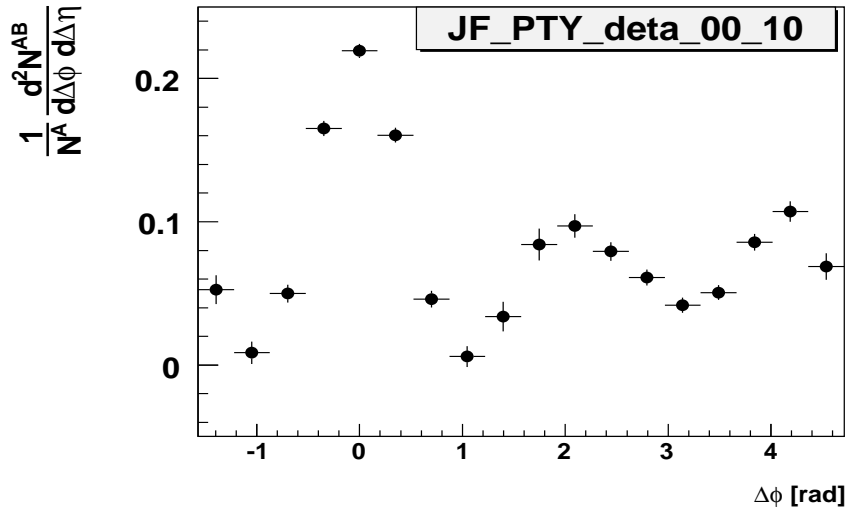


Figure 3.9:  $\Delta\phi$  correlation function of 2–3x1–2 GeV/c, centrality 0–20%,  $0.0 < |\Delta\eta| < 0.1$

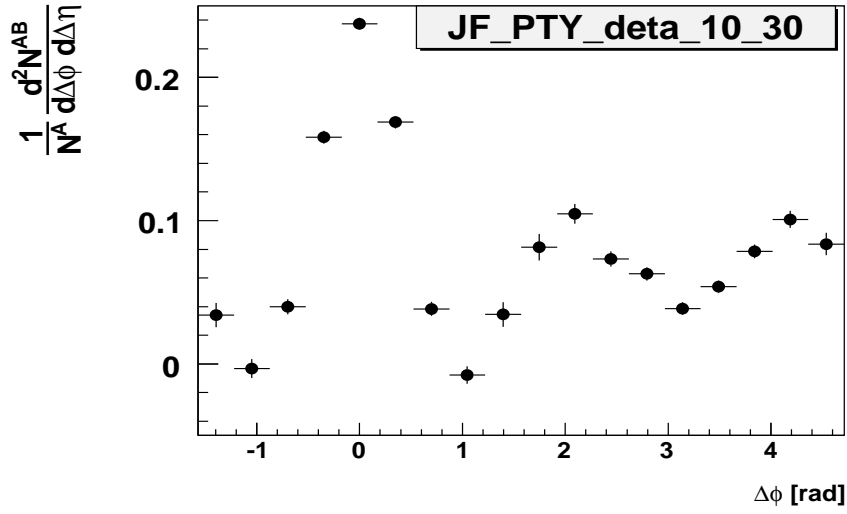


Figure 3.10:  $\Delta\phi$  correlation function of 2–3x1–2 GeV/c, centrality 0–20%,  $0.1 < |\Delta\eta| < 0.3$

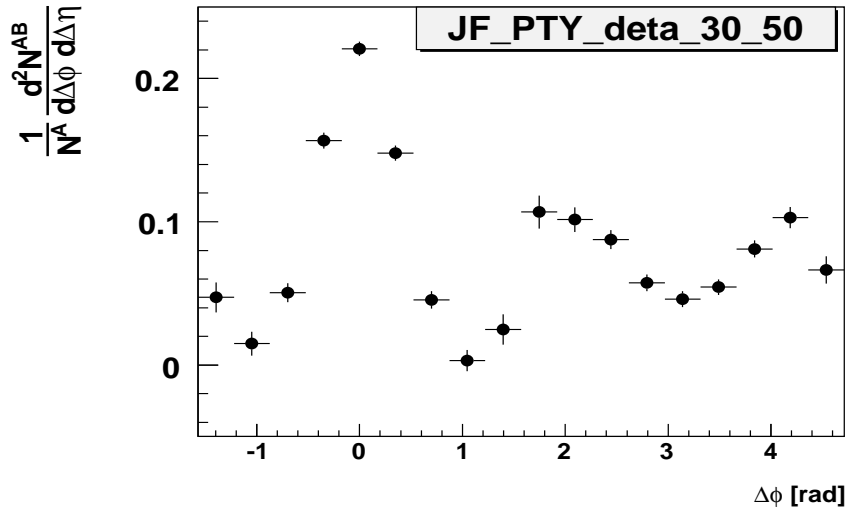


Figure 3.11:  $\Delta\phi$  correlation function of 2–3x1–2 GeV/c, centrality 0–20%,  $0.3 < |\Delta\eta| < 0.5$

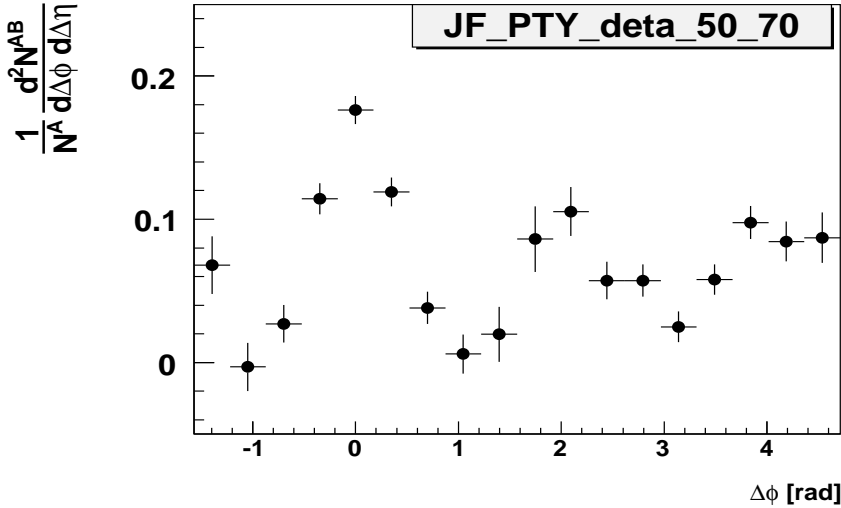


Figure 3.12:  $\Delta\phi$  correlation function of 2–3x1–2 GeV/c, centrality 0–20%,  $0.5 < |\Delta\eta| < 0.7$

this value, use a Monte Carlo simulation by varying the data points of the correlation function by their statistical errors. The ZYAM error is determined by the the variation of the ZYAM level.

The systematic error due to the hadron efficiency comes from comparing the measured inclusive hadron spectra with the published spectra. This value is between 7.1% – 9.4%, depending on centrality and partner  $p_T$ .

In order to estimate the hadron contamination of the trigger, we removed the PC3 veto cut. in Fig. 3.13, we compare the correlation function with and without veto cut. by comparing the per trigger yield after removing the PC3 veto cut, we can estimate the effect of the hadron contamination in the trigger photons. The level of the contamination is about 5%

All four different systematic are summed in quadrature.

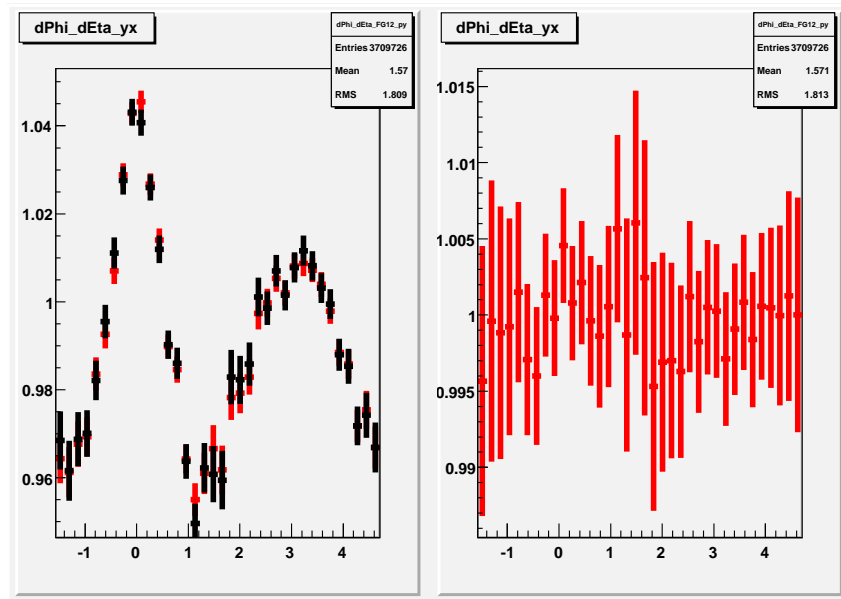


Figure 3.13: Left: correlation function with (black) and without pc3 veto cut (red). Right: the ratio of the correlation function of (without veto)/(veto). trigger  $p_T = 2-3$  GeV/c, partner  $p_T = 1-2$  GeV/c, and centrality = 0-90.

## Chapter 4

# Decomposing the Correlation Functions

### 4.1 Introduction

In this chapter, we assume the collective flow induced modulation of the underlying background is described by  $v_2(\cos 2\Delta\phi)$ . Effects of higher harmonics will be discussed in Chapter 5 and 6. After subtracting the underlying events, we study the  $\Delta\eta$ - $\Delta\phi$  correlation functions in detail. We decompose the jet functions by fitting the different components to extract the yield of the pp-like away side jet and the shoulder, which corresponds to the possible medium modification. The shoulder is also compared with the ridge in the nearside.

### 4.2 $\Delta\eta$ - $\Delta\phi$ Correlation Functions

$\Delta\eta$ - $\Delta\phi$  correlations are measured for various centralities in Au+Au collisions and in p+p. By applying the normalization and the efficiency correction discussed in Chapter 3, and the ZYAM method, we obtain the  $\Delta\eta$ - $\Delta\phi$  conditional yields of the associated particles per photon trigger.

In left hand side of Fig. 4.1 and Fig. 4.2, we present correlation functions from p+p, peripheral and central Au+Au collision before removing the combinatorial background. Before subtracting the underlying event background, the p+p correlation function has a clear peak on the nearside ( $\Delta\phi \approx 0$  and  $\Delta\eta \approx 0$ ). There is an awayside peak at  $\Delta\phi \approx \pi$  which extends along  $\Delta\eta$ . This extension along  $\Delta\eta$  is due to  $k_T$  smearing. The correlation function in the 60–90% centrality range looks like that in p+p. In central Au+Au collisions, an enhancement is seen along the  $\Delta\eta$  direction on the near side ( $\Delta\phi \approx 0$ ), this is the ridge which is significantly different from peripheral Au+Au or p+p cases. .

The right hand side of Fig. 4.1 and Fig. 4.2 show the correlation functions after subtraction of the flow modulated background. Both p+p and peripheral Au+Au collisions (60–90%) show similar dijet structure. In 0–20%, the near-side enhancement along  $\Delta\eta$  in nearside is significant. This ridge was reported by STAR [25] and PHOBOS [37] previously. On the awayside, where  $\Delta\phi \approx \pi$ , p+p peaks at  $\Delta\phi = \pi$ , but central Au+Au shows a local minimum. The peaks shift to  $\Delta\phi \approx \pi \pm 1$  and extend along  $\Delta\eta$ . This double peak structure, the shoulder, is consistent with previous PHENIX results [21, 22, 23].

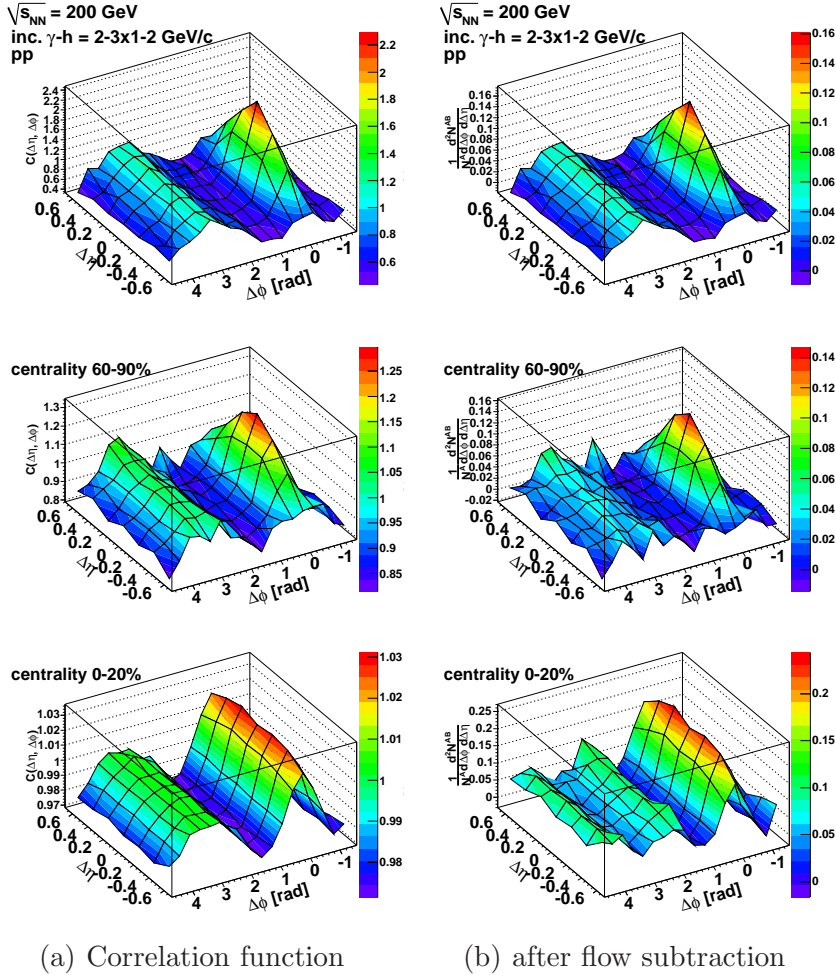


Figure 4.1:  $\Delta\eta$ - $\Delta\phi$  correlation functions of trigger 2–3 GeV/c, partner 1–2 GeV/c, in p+p, Au+Au at 60–90% and 0–20%. (a): Correlation function before removing combinatorial background; (b): conditional yield per trigger.

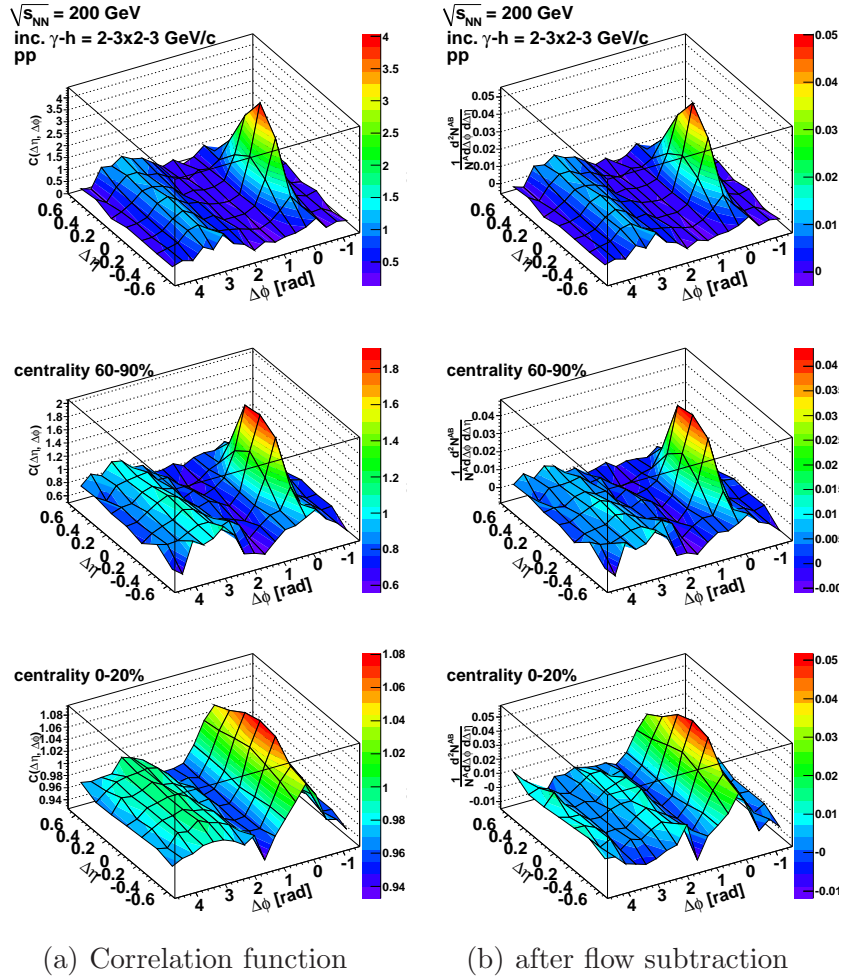


Figure 4.2:  $\Delta\eta$ - $\Delta\phi$  correlation functions of trigger 2-3 GeV/c, partner 2-3 GeV/c, in p+p, Au+Au at 60-90% and 0-20%. (a): Correlation function before remove the combinatorial background; (b): conditional yield per trigger.



### 4.2.1 $\Delta\phi$ Correlation Functions in Different $\Delta\eta$ Region

In order to trace the modification from p+p to Au+Au collisions, we slice the  $\Delta\phi$  correlation in 4  $\Delta\eta$  ranges:  $|\Delta\eta| = 0-0.1$ ,  $0.1-0.3$ ,  $0.3-0.5$  and  $0.5-0.7$ . In peripheral Au+Au collisions (60–90%), shown in Fig.4.3, the  $\Delta\phi$  shape is consistent with p+p collisions for all 4  $\Delta\eta$  regions. The near side yield decreases as the  $\Delta\eta$  slice moves from  $\Delta\eta = 0$  to larger  $\Delta\eta$ , which is consistent with the fact that the nearside jet has a Gaussian shape in the  $\Delta\eta$  direction and peaks at  $\Delta\eta = 0$ . In contrast, the away side peak remains roughly the same in all  $\Delta\eta$  regions.

However, in central Au+Au collisions at large  $\Delta\eta$  on the near side, we see a clear difference from p+p, as shown in Fig.4.4. In the rapidity range  $0.5 < |\Delta\eta| < 0.7$ , substantial yield is seen in Au+Au, while in p+p there is very little yield on the near side. At smaller  $\Delta\eta$  in Au+Au collisions there is also some enhancement compared to the jet peak in p+p. In all measured  $\Delta\eta$  regions on the away side, the double peak structure away from  $\Delta\phi \approx \pi$  is clearly seen in central Au+Au, in contrast to the single peak in p+p collisions. This is consistent with previous observations [21].

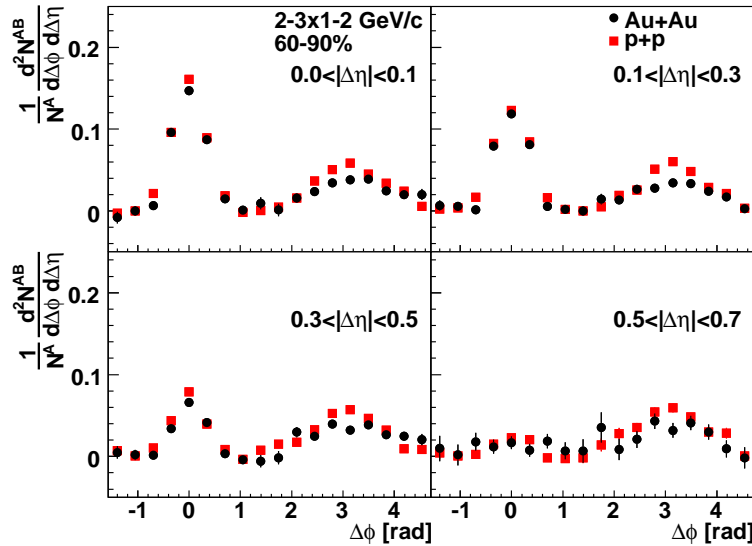


Figure 4.3: Peripheral Au+Au (60–90%) and p+p conditional per trigger yield in different  $\Delta\eta$  regions for trigger  $p_T = 2.0 - 3.0$  GeV/c and partner  $p_T = 1.0 - 2.0$  GeV/c. Au+Au (p+p) data are shown by solid circles (squares).

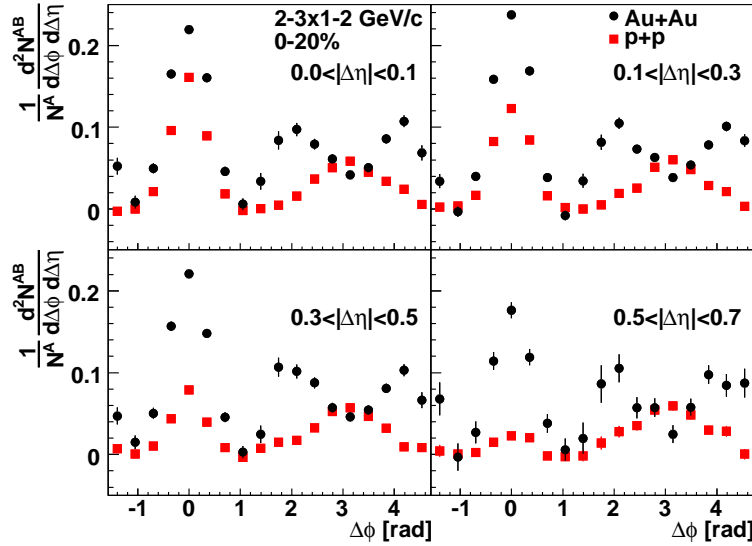


Figure 4.4: The same as Fig. 4.3, but for central Au+Au collisions (0–20%).

### 4.3 Near Side Projection along $\Delta\eta$ Direction

To focus on the modification of the near side yield along  $\Delta\eta$  in Au+Au, the two-particle  $\Delta\eta$ - $\Delta\phi$  correlation function is integrated in  $|\Delta\phi| < 7\pi/18$  and is projected in the  $\Delta\eta$  direction, shown in Fig. 4.5(a). We choose  $|\Delta\phi| < 7\pi/18$  because in p+p, this is the size of the near side jet. In central Au+Au collisions the near side is wider along  $\Delta\eta$  and is enhanced compared to p+p. Moving from central to peripheral Au+Au collisions, the near side enhancement along  $\Delta\eta$  decreases, and the peak becomes more consistent with the jet-like shape in p+p. This indicates that the yield of the ridge strongly correlates with the size of the medium.

To investigate the partner  $p_T$  dependence, we present the  $\Delta\eta$  projections for four partner  $p_T$  ranges in the most central Au+Au (0–20%) collisions in Fig. 4.5(b). The effect of the ridge is the strongest in central collisions compared to p+p. At partner  $p_T$  below 3 GeV/c, the enhancement is significant in Au+Au, and the peak is wider than in p+p. At larger partner  $p_T = 3$ –5 GeV/c, there is no obvious enhancement in Au+Au and the Au+Au shape is consistent with p+p. Therefore near side enhancement along  $\Delta\eta$  decreases significantly for high partner  $p_T$ . The ridge is most significant at partner  $p_T$  below 3 GeV/c.

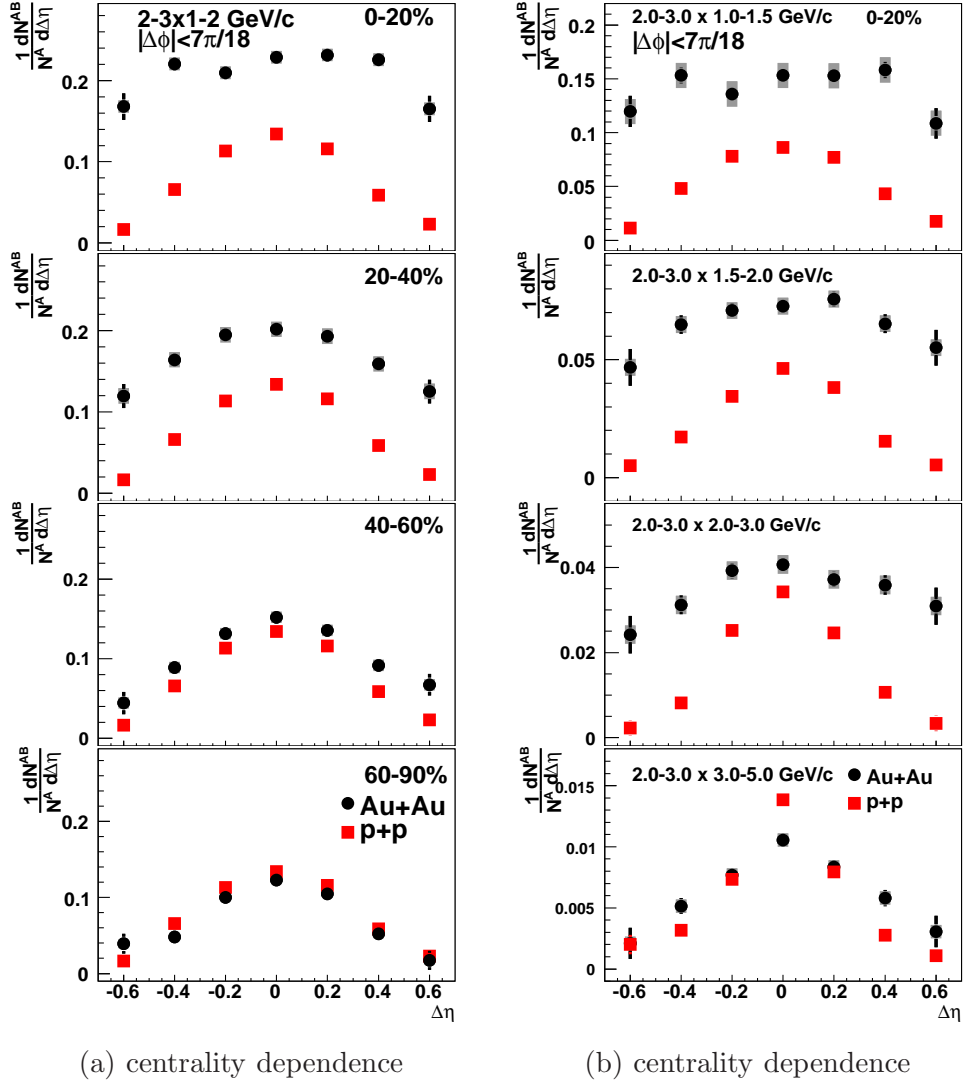


Figure 4.5: Near side  $\Delta\eta$  correlations of Au+Au (circles) and p+p (squares). (a): various centralities for trigger  $p_T = 2.0 - 3.0$  GeV/c, partner  $p_T = 1.0 - 2.0$  GeV/c; (b): Au+Au at 0-20% and p+p for for various partner  $p_T$  bins.

## 4.4 Extracting the Near Side Yield

In Fig. 4.6, the near side per trigger yield is plotted as a function  $N_{part}$ , which is the number of nucleons participating the collisions, for different partner  $p_T$ . Since we are using the ZYAM method to determine the background level, it is natural to use ZYAM point to separate the near and away side. In this analysis, we adapt the idea of the ZYAM point, but more closely follow previous PHENIX analysis [23]. We define the near side within a fixed  $\Delta\phi$  region as  $|\Delta\phi| < 7\pi/18$ . The selection of this  $\Delta\phi$  range is due to the bin width in the correlation function histogram. However, it is consistent with the previous result using the ZYAM point to separate the near and away side. The systematic error of the nearside yield is coming from the determination of the ZYAM level and from the  $v_2$  modulations.

Different symbols correspond to sequential slices in  $|\Delta\eta|$ . The p+p near side yields are plotted as the left most symbols and serve as a baseline measurement. In p+p collisions, the yield decreases gradually for ranges from  $|\Delta\eta| = 0-0.1$  to  $0.5-0.7$ . This is consistent with a typical jet structure, which peaks at  $\Delta\eta \approx 0$  and decreases at larger  $\Delta\eta$ . In the range of  $0.5 < |\Delta\eta| < 0.7$  the yield in p+p is very small.

For partner  $p_T$  below 3 GeV/c, the conditional yield monotonically increases with  $N_{part}$  up to  $N_{part} \approx 240$  in all  $\Delta\eta$  regions. For Au+Au collisions the largest enhancement relative to p+p collisions is seen in the  $0.5 < |\Delta\eta| < 0.7$  region where the p+p yield (from jets) is small. This enhancement is clear evidence of the ridge. At  $N_{part}$  larger than 240, the yield at  $0.5 < |\Delta\eta| < 0.7$  levels off. For partner  $p_T$  above 3 GeV/c the yield does not change with  $N_{part}$  within the errors.

## 4.5 Ridge Extraction

### 4.5.1 Definition of Ridge in PHENIX

From Fig. 4.5(a) and Fig. 4.5(b), we know that the near side correlation consists of a jet-like correlation which peaks at  $\Delta\phi = 0$ , and a ridge like correlation which is flat in  $\Delta\eta$ . The ridge is flat along the  $\Delta\eta$  direction to 4 units of pseudorapidity [37]. In two particle correlation analysis, the width of the near side jet when fitting with a Gaussian function is about 0.3 in  $\Delta\phi$  direction. Assume the jet shape is symmetric in  $\Delta\eta$  and  $\Delta\phi$  direction, then the width in  $\Delta\eta$  is about 0.3. However, since the PHENIX  $\Delta\eta$  acceptance is limited ( $|\Delta\eta| \sim 0.7$ , which contains more than 95% of the near side jet) there

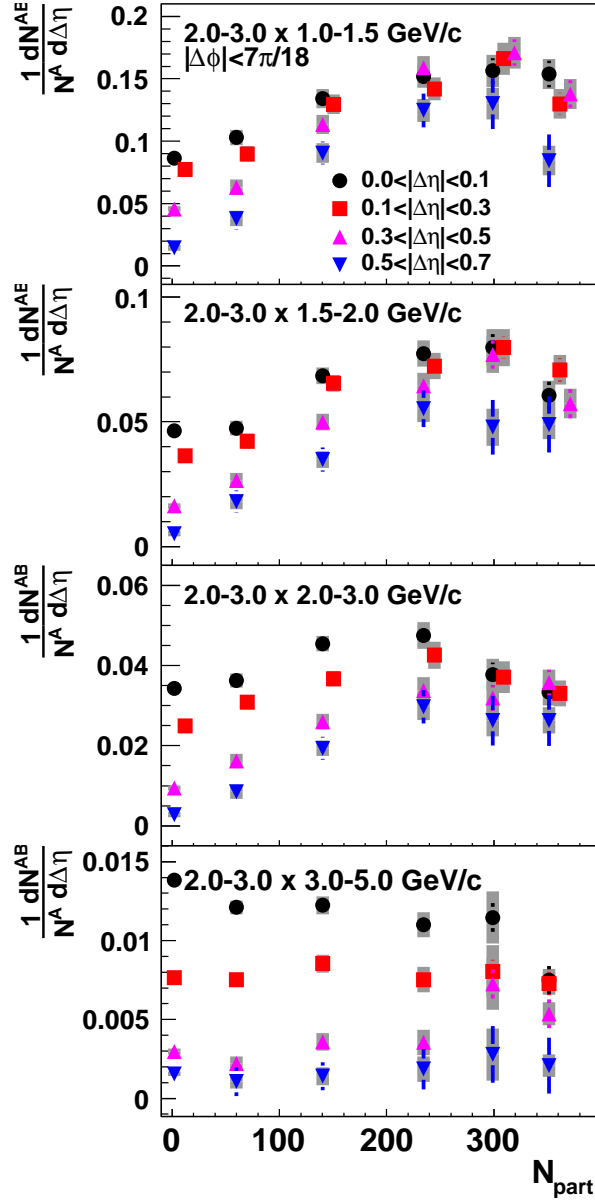


Figure 4.6: The Near side per trigger yields for various partner  $p_T$  and in different regions  $\Delta\eta$  versus  $N_{part}$ . Trigger photon  $p_T = 2.0 - 3.0 \text{ GeV}/c$ . Gray shade bands are the systematic errors from ZYAM and  $v_2$  (Au+Au). The data points are shifted a bit to avoid overlap.

is always a non-negligible jet contamination. The level of jet contamination to any ridge characterization of the enhancement can be estimated from the non-zero yield in p+p at the same  $\Delta\eta$  region, which is quite small in the outermost  $0.5 < |\Delta\eta| < 0.7$  bin. Thus in what follows, we define our ridge yield as the excess of the near side yield in Au+Au compared to p+p for  $0.5 < |\Delta\eta| < 0.7$ :

$$Y_{ridge} = Y_{AuAu}^{near} |_{0.5 < |\Delta\eta| < 0.7} - Y_{pp}^{near} |_{0.5 < |\Delta\eta| < 0.7} \quad (4.1)$$

The potential effect of an interplay between near side jet modification and ridge yield is investigated, and an extra systematic uncertainty from this source is assigned to  $Y_{ridge}$ . To do this, different possible scenarios for the near side are assumed, including (i) jet broadening, (ii) jet suppression, and (iii) dilution—meaning a lowering of the per-trigger yield by the presence of the ridge or other non-jet trigger particles.

Here we discuss these three possible scenarios separately. The first is when the near side jet interacts with the medium, the number of associated particles in the jet-like correlation in Au+Au is the same as in p+p, but with a wider Gaussian width in  $\Delta\eta$ ; we call this situation as “jet broadening”. The second case assumes that the jet medium interaction does not change the shape of the jet, but the yield is modified. This is the case of near side jet suppression. We can simply write this as:

$$Y_{AuAu} = xY_{pp} + Y_{ridge} \quad (4.2)$$

where  $Y_{AuAu}$  is the total near side yield in Au+Au,  $Y_{pp}$  is the jet like yield in p+p and  $Y_{ridge}$  is the ridge yield. The factor  $x$  is the suppression in Au+Au, which is a function of centrality. In p+p collisions, Eq. 4.2 automatically leads to  $x = 1$  and  $Y_{ridge} = 0$ . The third case is near side jet dilution. In this analysis, the  $p_T$  of our trigger particle is between 2–3 GeV/c, where the medium response dominates, so some of our trigger particles may not come from jets, but instead arise the ridge. If the trigger particle is from the jet, then associated particles will come from both jet and ridge. If the trigger particle is from the ridge, then the associated particle will come from ridge only. We define this situation as jet dilution, which indicates the trigger from the jet is ‘diluted’ by triggers from the ridge. Since we report per trigger yields, we assume that  $x$  triggers are from jets, which carry  $x$  times  $(Y_{pp} + Y_{ridge})$ . There will be  $(1-x)$  triggers from the ridge, with associate particles  $(1-x)$  times  $Y_{ridge}$ . So the over all effect is

$$\begin{aligned} Y_{AuAu} &= x \times (Y_{pp} + Y_{ridge}) + (1 - x) \times Y_{ridge} \\ &= xY_{pp} + Y_{ridge} \end{aligned} \quad (4.3)$$

By comparing Eq. 4.2 and Eq. 4.3, we see that the jet dilution effect is equivalent to jet suppression. We will treat the two situations as one scenario. We fit the jet function to evaluate the yield of the ridge. The  $\Delta\eta$  correlation functions are fitted by Eq. 4.4:

$$Y_{AuAu}(\Delta\eta) = \frac{Y_{jet}}{\sqrt{2\pi}\sigma_{jet}} \exp\left(-\frac{(\Delta\eta)^2}{2\sigma_{jet}^2}\right) + Y_{ridge} \quad (4.4)$$

There are three parameters in Eq. 4.4: the yield of jet like correlation,  $Y_{jet}$ , the jet width in the  $\Delta\eta$  direction,  $\sigma_{jet}$ , and the yield of ridge,  $Y_{ridge}$ . The first step is to fit the p+p correlation with Eq. 4.4 by fixing  $Y_{ridge} = 0$ , as there is no ridge in p+p collisions at RHIC. Then we can extract the yield and Gaussian width in  $\Delta\eta$  of p+p collisions.

In order to consider the scenarios of jet broadening and jet suppression, we use Eq. 4.4 to fit the  $\Delta\eta$  correlation, but must fix different parameters according to different assumptions. In the jet broadening case, we fixed the jet yield to be equal to the yield in p+p, or  $Y_{jet} = Y_{pp}$ , and leave the jet width and ridge yield as free parameters. In the jet suppression case, we fix the jet  $\Delta\eta$  width to p+p (i.e.  $\sigma_{jet} = \sigma_{pp}$ ), and let the jet yield and ridge yield as free parameters.

$\Delta\eta$  correlation functions in various associated particle  $p_T$  and centrality bins such as Fig. 4.5(a) and Fig. 4.5(b) are fitted using Eq. 4.4. When testing the jet broadening scenario, where we fix the jet yield to p+p, the near side jet width increases with  $N_{part}$  as shown in Fig. 4.7. On the other hand, if we fit with the jet suppression scenario, where we fix the jet width to p+p, the near side jet yield in Au+Au decreases when increasing  $N_{part}$ , as shown in Fig. 4.8. The  $\chi^2$  of two different assumptions are tabulated in Table 4.1. From Table 4.1, the assumption of jet broadening generally gives smaller  $\chi^2$  value. But both assumptions give reasonable  $\chi^2$  values. So it is hard to say which assumption is better than the other. More important, either method gives a substantial ridge yield in central collisions, providing supporting evidence that the ridge has been observed in PHENIX.

In addition to the two extreme cases mentioned above, we also estimate the ridge yield through another method. We assume that the  $Y_{Au+Au,near} = Y_{p+p,near} + Y_{ridge}$ , or  $Y_{ridge} = Y_{Au+Au,near} - Y_{p+p,near}$ , which assumes that near side Au+Au is simply a p+p like jet yield plus a ridge yield which is flat  $\Delta\eta$ . The ridge yield is simply the excess in Au+Au compare to p+p in different  $\Delta\eta$  region.

This systematic uncertainty coming from this physical assumptions describes previously is included in Fig. 4.9 and other figures as the thin solid

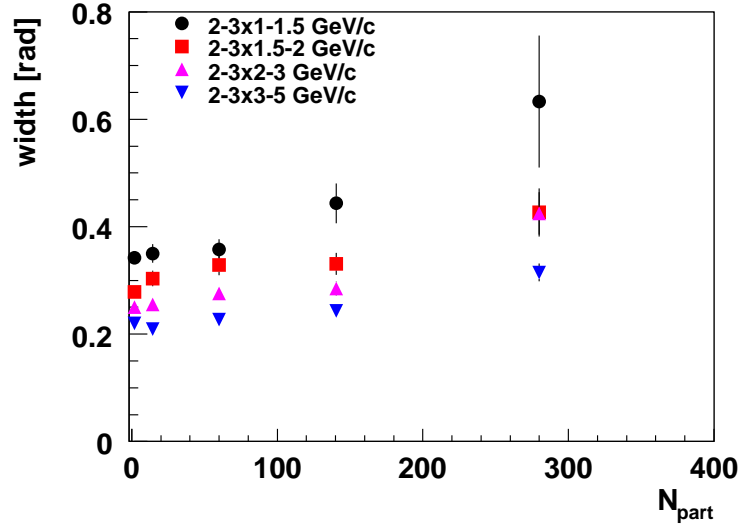


Figure 4.7: Jet broadening case, where the jet yield in the nearside is fixed and fit the jet width of the near side. Near side jet widths are plotted as a function of  $N_{part}$  and partner  $p_T$

Table 4.1:  $\chi^2$  table for different fitting method (Degrees of freedom = 5)

assoc. $p_T$	Centrality	jet broadening	jet suppression
1.0–1.5	Cent–00–20	15.94	17.26
1.0–1.5	Cent–20–40	1.75	2.40
1.0–1.5	Cent–40–60	2.67	2.67
1.0–1.5	Cent–60–90	3.98	3.73
1.5–2.0	Cent–00–20	3.83	5.99
1.5–2.0	Cent–20–40	3.14	4.91
1.5–2.0	Cent–40–60	1.50	1.70
1.5–2.0	Cent–60–90	7.57	7.40
2.0–3.0	Cent–00–20	4.05	5.05
2.0–3.0	Cent–20–40	6.55	5.39
2.0–3.0	Cent–40–60	3.14	4.53
2.0–3.0	Cent–60–90	10.22	10.17
3.0–5.0	Cent–00–20	4.40	4.78
3.0–5.0	Cent–20–40	2.12	1.57
3.0–5.0	Cent–40–60	10.77	9.48
3.0–5.0	Cent–60–90	4.33	4.39



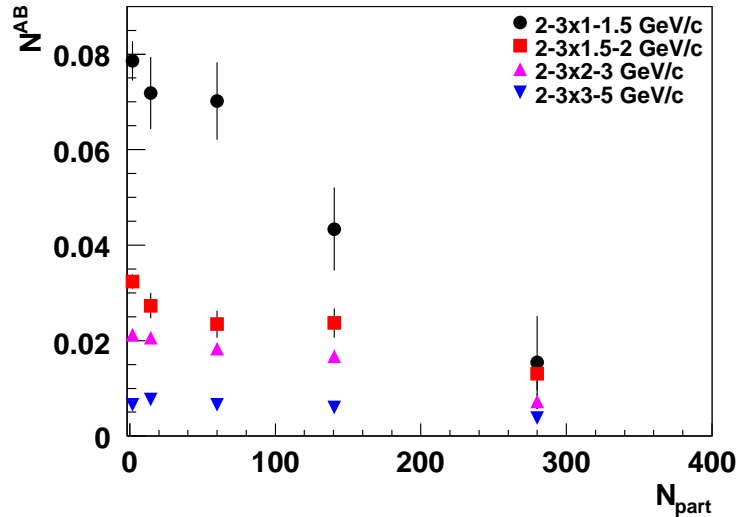


Figure 4.8: Near side jet suppression case. The jet width in near side is unmodified and fit the nearside jet yield Near side jet yields,  $N^{AB}$  are plotted as a function of  $N_{part}$  and partner  $p_T$

brown lines which bracket the  $Y_{ridge}$  ( $0.5 < |\Delta\eta| < 0.7$ ) data points.

The ridge yield defined by Eq. 4.1 can also be applied to the entire  $\Delta\eta$  range,  $0.0 < |\Delta\eta| < 0.7$ . While the  $0.5 < |\Delta\eta| < 0.7$  p+p jet like contribution is relatively small, the  $\Delta\eta$  region  $0.0 < |\Delta\eta| < 0.7$  contains approximately the full near side jet. The ridge yield per unit  $\Delta\eta$  extracted in the  $\Delta\eta$  regions ( $|\Delta\eta| = 0.5-0.7$  and  $0-0.7$ ) are compared in Fig. 4.9. The ridge yield extracted from the two different  $\Delta\eta$  regions are consistent with each other, indicating that the ridge yield is relatively flat in  $\Delta\eta$  around  $\Delta\eta = 0$ .

## 4.5.2 Results

The final results of the ridge yield as a function of  $N_{part}$  in different partner  $p_T$  bins are shown in Fig. 4.9. At partner  $p_T$  below 3 GeV/c, the ridge yield is consistent with 0 at  $N_{part} \approx 14$ . The ridge yield increases with  $N_{part}$  up to  $N_{part} \approx 250$ . When  $N_{part} > 250$ , the ridge yield is constant, or even decreasing with increasing with  $N_{part}$  for the most central collisions. Similar trends in  $N_{part}$  have been observed previously by PHENIX [21]. At partner  $p_T > 3$  GeV/c, the ridge yield is consistent with zero.

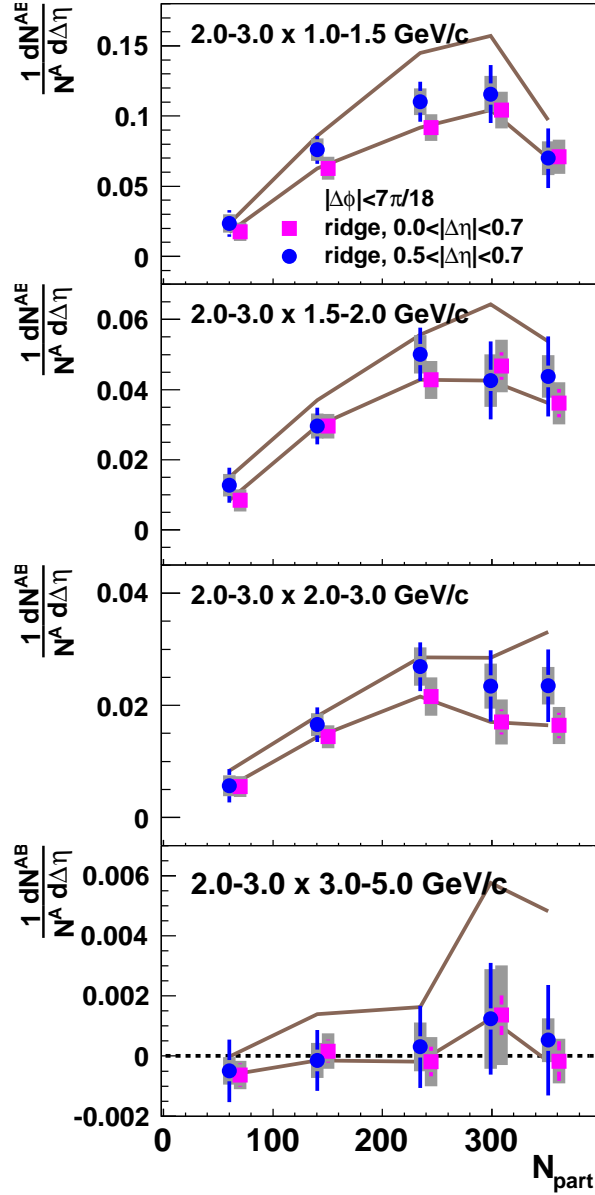


Figure 4.9: Ridge yields extracted by  $Y_{ridge} = Y_{Au+Au, near} - Y_{p+p, near}$  for trigger  $p_T = 2.0 - 3.0$  GeV/c and various partner  $p_T$  in two different  $\Delta\eta$  region ( $0 < |\Delta\eta| < 0.7$  and  $0.5 < |\Delta\eta| < 0.7$ ). The brown lines apply to  $0.5 < |\Delta\eta| < 0.7$  and is the systematic error due to physics assumptions regarding ridge/jet modification interplay described in the text .

## 4.6 Extracting the Away Side Yields

### 4.6.1 Decomposing Different Components

We fit the jet functions to extract the contribution of different components of the away side correlation. This allows separating the two components, which we refer to as the *head* of the jet at  $\Delta\phi = \pi$  and *shoulder* at  $\Delta\phi \approx 2$  rad.

Eq. 4.5 is used to fit the full  $\Delta\phi$  jet correlation function:

$$\begin{aligned}
 J(\Delta\phi) = & \frac{Y_n}{\sqrt{2\pi}\sigma_n} \exp\left(-\frac{(\Delta\phi)^2}{2\sigma_n^2}\right) \\
 & + \frac{Y_s}{\sqrt{2\pi}\sigma_s} \exp\left(-\frac{(\Delta\phi - \pi - D)^2}{2\sigma_s^2}\right) \\
 & + \frac{Y_s}{\sqrt{2\pi}\sigma_s} \exp\left(-\frac{(\Delta\phi - \pi + D)^2}{2\sigma_s^2}\right) \\
 & + \frac{Y_h}{\sqrt{2\pi}\sigma_h} \exp\left(-\frac{(\Delta\phi - \pi)^2}{2\sigma_h^2}\right)
 \end{aligned} \tag{4.5}$$

Eq. 4.5 has four terms. The first term describes the near side jet. The second and third term describe the shoulder, which has been considered a possible medium response due to the jet. These two terms peak at  $\Delta\phi = \pi \pm D$ . The last term is motivated by [24, 58], where the away side jet reappears at large  $p_T$  at  $\Delta\phi = \pi$ . We assume there is a remnant of a p+p like away side jet, which is called the “head”.

In Eq. 4.5, we assume each component has a Gaussian shape.  $Y_n$ ,  $Y_s$ , and  $Y_h$  ( $\sigma_n$ ,  $\sigma_s$ , and  $\sigma_h$ ) are the yield (width of the Gaussian) of the near side, shoulder and head respectively.  $D$  is the position of the shoulder to describe the displacement of the peak.

In order to reduce the number of fit parameters, we checked whether the width of the head could be fixed. We use Eq. 4.5 to fit the jet function in Au+Au to extract the width of the head component,  $\sigma^{head}$ . The result is shown in Fig. 4.10. We see the extracted width in Au+Au is consistent with p+p. Consequently, we fix the width of the head component to the width of the away side jet in the corresponding  $p_T$  bin in p+p collisions. The p+p away side width is tabulated in Table 4.2.

After fixing the width of the head component, we also tried to fix the position of the shoulder, parametrized by  $D$  in Eq. 4.5. After fixing the head width, we fit the correlation function to obtain the  $D$  in Eq. 4.5. In Fig. 4.11,  $D$  is plotted as a function of  $N_{part}$  at trigger  $p_T = 2-3$  GeV/c, partner  $p_T$

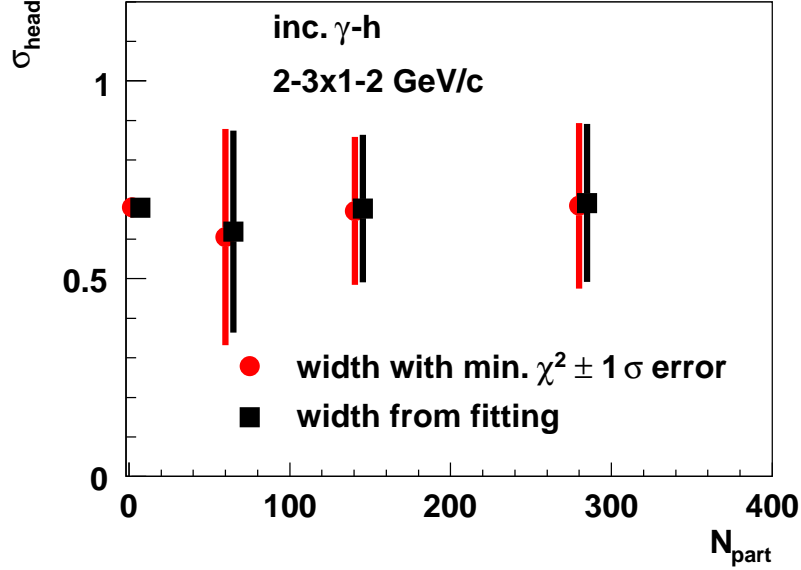


Figure 4.10: The width of the head component (punch through jet),  $\sigma^{head}$ , by fitting jet function with Eq. 4.5. trigger  $p_T = 2.0 - 3.0$  GeV/c, partner  $p_T = 1.0 - 2.0$  GeV/c.

= 1–2 GeV/c. The D does not vary significantly with  $N_{part}$ . Similar results are also found in other  $p_T$  bins. Based upon this study, we fix the position of the shoulder, D, to that obtained in the 0–20 % centrality bin, where the modification is most statistically significant. The values of D used in this analysis is tabulated in Table 4.3

Now we can fix the head width and the position of the shoulder, we are able to decompose the away side associated particle yields.  $\Delta\phi = 7\pi/18$  is used as the separation point between the near and the away side. In the away side decomposition, fit only in between  $7\pi/18 < \Delta\phi < (2 - 7/18)\pi$ . The jet function of different centrality and  $\Delta\eta$  bins is fitted by Eq. 4.5 without the term describing the near side:

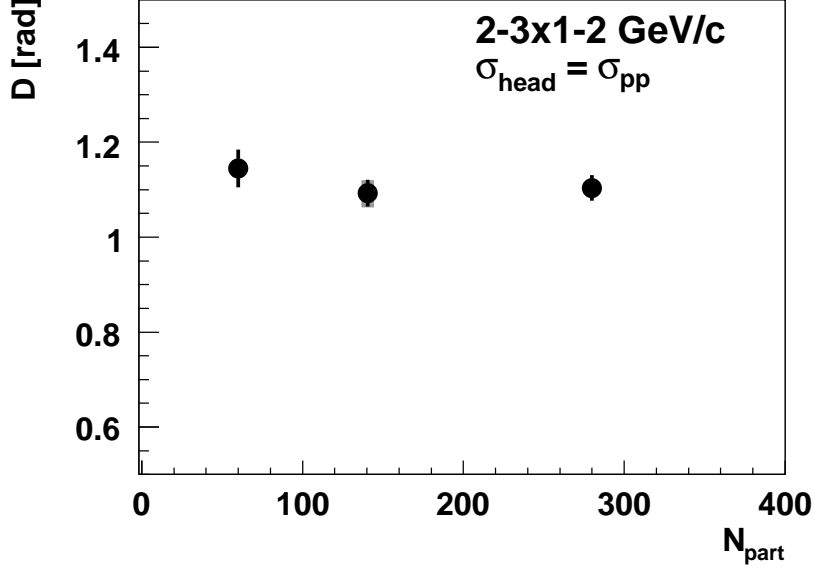


Figure 4.11: The position of the shoulder,  $D$ , from fitting with Eq. 4.5. Trigger  $p_T = 2.0\text{--}3.0$  GeV/ $c$ , partner  $p_T = 1.0\text{--}2.0$  GeV/ $c$

$$\begin{aligned}
J(\Delta\phi) = & \frac{Y_s}{\sqrt{2\pi}\sigma_s} \exp\left(-\frac{(\Delta\phi - \pi - D)^2}{2\sigma_s^2}\right) \\
& + \frac{Y_s}{\sqrt{2\pi}\sigma_s} \exp\left(-\frac{(\Delta\phi - \pi + D)^2}{2\sigma_s^2}\right) \\
& + \frac{Y_h}{\sqrt{2\pi}\sigma_h} \exp\left(-\frac{(\Delta\phi - \pi)^2}{2\sigma_h^2}\right)
\end{aligned} \tag{4.6}$$

Eq. 4.6 is used to fit both Au+Au and p+p jet functions. When used to fit p+p,  $Y_s$  is fixed to 0 because this structure is not observed in p+p. As previously described, the width of the head region is fixed to the away side width in p+p, and the position of the shoulder is fixed by  $D$  in Table 4.2 and Table 4.3. Finally, there are only 3 free parameters in the fitting function: the yield of the head region, the yield of the shoulder region, and the width of the shoulder. We do not set any limit on these parameters.

A typical fit is shown in Fig 4.12. The left hand side of the plot shows a fit to the full  $\Delta\phi$  range ( $-\pi/2$  to  $3\pi/2$ ) with Eq. 4.5, while the right hand side

Table 4.2: The p+p away side width in different partner  $p_T$  bins. Trigger  $p_T = 2-3$  GeV/c

partner $p_T$ [GeV/c]	width [rad]
1.0–1.5	$0.702 \pm 0.025$
1.5–2.0	$0.622 \pm 0.031$
1.0–2.0	$0.679 \pm 0.019$
2.0–3.0	$0.581 \pm 0.031$
3.0–5.0	$0.532 \pm 0.028$

Table 4.3: The shoulder displacement,  $D(p_T)$ , in different partner  $p_T$  bins at centrality 0–20. Trigger  $p_T = 2-3$  GeV/c

partner $p_T$ [GeV/c]	D [rad]
1.0–1.5	$1.125 \pm 0.030$
1.5–2.0	$1.030 \pm 0.068$
1.0–2.0	$1.104 \pm 0.027$
2.0–3.0	$1.166 \pm 0.047$
3.0–5.0	$1.274 \pm 0.132$

shows a fit to the away side only, from  $7\pi/18$  to  $29\pi/18$ , with Eq. 4.6. The magenta curve is the complete fit function, the red curve is the head, the blue is the shoulder, and the green is the near side. On left hand side, p1 is the near side yield, p2 is the near side width, p3 is the yield of one shoulder, p5 is the width of shoulder, and p6 is the yield of head. For right hand side, p3 is the yield of one shoulder, p5 is the width of shoulder, and p6 is the yield of the head, which has the same definition as left hand side. After fitting, we obtain the yield of head, shoulder and total away side yield by integrating the fitting function. The statistical error for these yield is obtained from the error matrix. The systematic error of the away side yield is coming from the determination of the ZYAM level and from the  $v_2$  modulations.

## 4.6.2 Results

In Fig. 4.13 the two components of the away side yield along with the total yield are plotted versus  $N_{part}$ . As a crosscheck, the away side yield was also measured via direct integration over  $|\Delta\phi| > 7\pi/18$ . The result is consistent with the away side yield determined from the fits. The centralities used in the fitting analysis are 0–20%, 20–40% and 40–60%.

In Fig. 4.13, when the partner  $p_T$  is below 3 GeV/c, the total away side

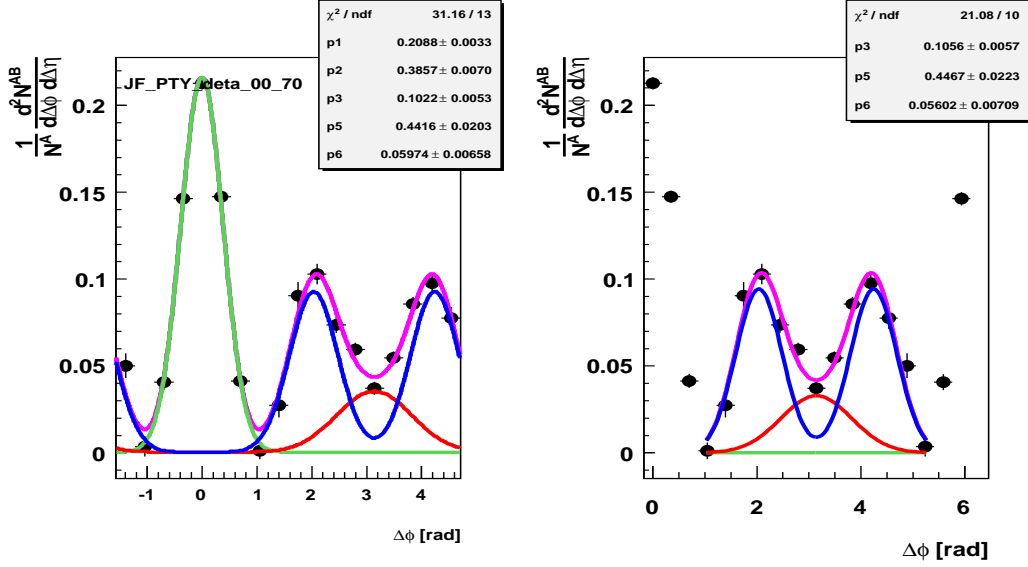


Figure 4.12: Fitting of the per trigger yield in the away side. Trigger  $p_T = 2.0\text{--}3.0$  GeV/c, partner  $p_T = 1.0\text{--}2.0$  GeV/c, centrality 0–20%

yield increases with  $N_{part}$ . This happens to be the  $p_T$  region where the shoulder is significant. There is also an obviously different trend in shoulder and head region versus  $N_{part}$ .

The decreasing trend of the head with increasing  $N_{part}$ , discussed above, is generally interpreted as the away side jet becoming more and more quenched inside the formed matter as the size of the medium increases [23, 58, 59, 60]. Similarly, the appearance of the shoulder has also been commonly attributed to this process, as the jet is quenched, particles appear at larger angle with respect to the jet axis to form the shoulder

For associated particles with  $p_T > 3$  GeV/c, the total away side yield in Au+Au collisions is smaller than in p+p. This unambiguous suppression of the total away side yield in heavy ion collision is due to the the overwhelming domination of the jet-like "head" correlation with increasing  $p_T$ , and thus is another confirmation of the jet quenching effect.

## 4.7 Punch Through $I_{AA}$

$I_{AA}$  is defined as the ratio of the yield between Au+Au and p+p jet yields [23]. The key drawback of  $I_{AA}$  is that it does not account for the crosstalk between

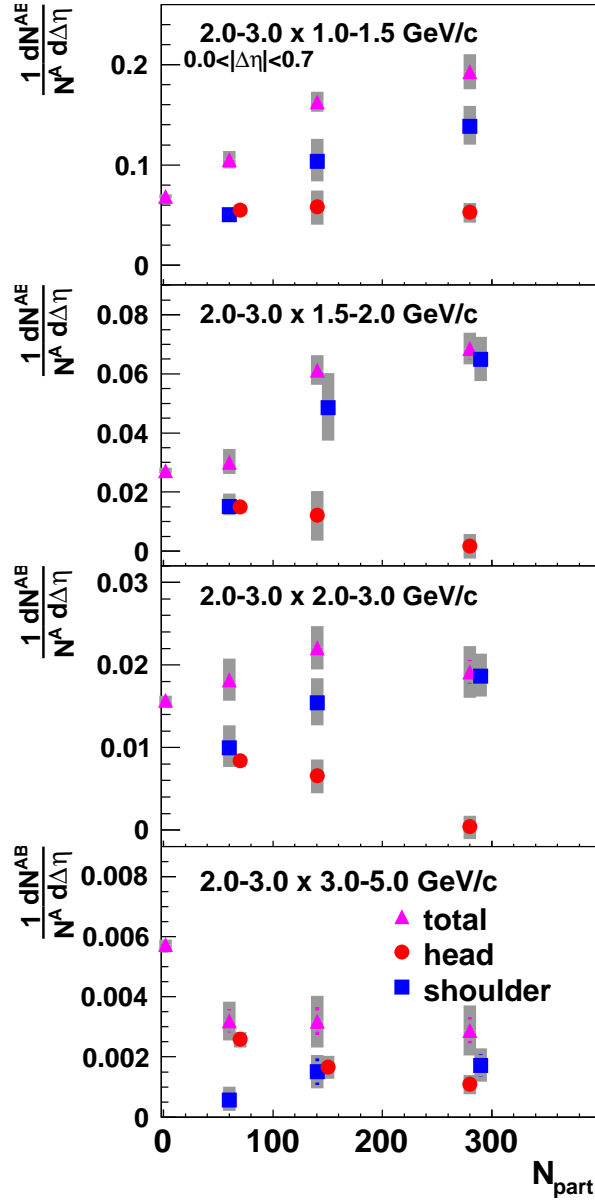


Figure 4.13: Per trigger yield of away side components: head, shoulder and total away side, vs  $N_{part}$ . Trigger  $p_T = 2.0 - 3.0$  GeV/c and various partner  $p_T$ . Gray shaded band represents the combined systematic error from ZYAM and  $v_2$ .



the head and shoulder properly. To quantify the suppression of the punch through jet, we introduce a new parameter, the ‘‘punch through  $I_{AA}$ ’’. The idea of the punch through  $I_{AA}$  is to quantify the suppression of the punch through jet, or head, in the medium. It is defined as

$$I_{AA,punch} = Y_{AuAu}^{head} / Y_{pp}^{away-side} \quad (4.7)$$

Fig. 4.14 shows the punch through  $I_{AA}$  as a function of  $N_{part}$  for different partner  $p_T$  bins. Punch through  $I_{AA}$  decreases from mid central to central Au+Au collisions. This indicates that increasing the medium increases the suppression of the punch through jet. To compare the suppression level, the  $\pi^0 R_{AA}$  (defined by Eq. eq:RAA) [20] for same  $p_T$  range (same as partner  $p_T$ ) is plotted as well.

We also plot the punch through  $I_{AA}$  as a function of partner  $p_T$  in different centralities in Fig. 4.15. Here the punch through  $I_{AA}$  decreases with increasing partner  $p_T$ . The higher the partner  $p_T$ , the more suppression in the punch through jet.

## 4.8 Comparison of the Ridge, the Shoulder and the Underlying Event Background

In Fig. 4.6, at partner  $p_T < 3.0$  GeV/c, the near side yield in Au+Au collisions is significantly larger than that in p+p collisions for rapidity  $0.5 < |\Delta\eta| < 0.7$ , due to the existence of the ridge. On the away side, the shoulder is also a sign of jet–medium interaction.

In two particle correlations, the combinatorial background increases with the number of participants. In order to extract the jet signal, this background needs to be removed, leading one to wonder whether the ridge and shoulder structures arise from artifacts in the combinatorial background subtraction.

If the ridge is part of the combinatorial background, then the ridge yield should scale with the particle multiplicity in the underlying events. We study this via the ratio of the ridge yield to the yield of the combinatorial background integrated over the same  $\Delta\phi$  range between the ZYAM points. Fig. 4.16 shows the ratio between the ridge yield and the yield of the underlying event, plotted as a function of  $N_{part}$  for different partner  $p_T$ . The ridge yield constitutes only a few percent of the underlying event. Furthermore, the ratio decreases at  $N_{part} > 240$ , which means the combinatorial background in the underlying event increases faster than multiplicity, or  $N_{part}$ . Therefore the non–flatness of the ratio means that the ridge yield is not produced by unsubtracted com-

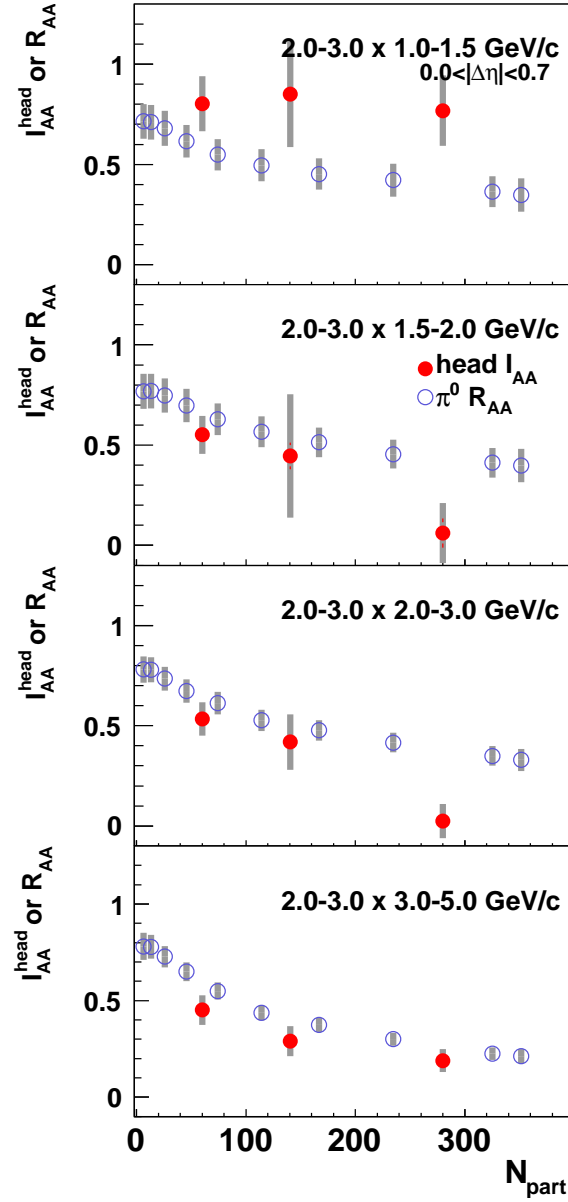


Figure 4.14: Punch through  $I_{AA}$  for trigger  $p_T = 2.0 - 3.0$  GeV/c and various partner  $p_T$  vs  $N_{\text{part}}$

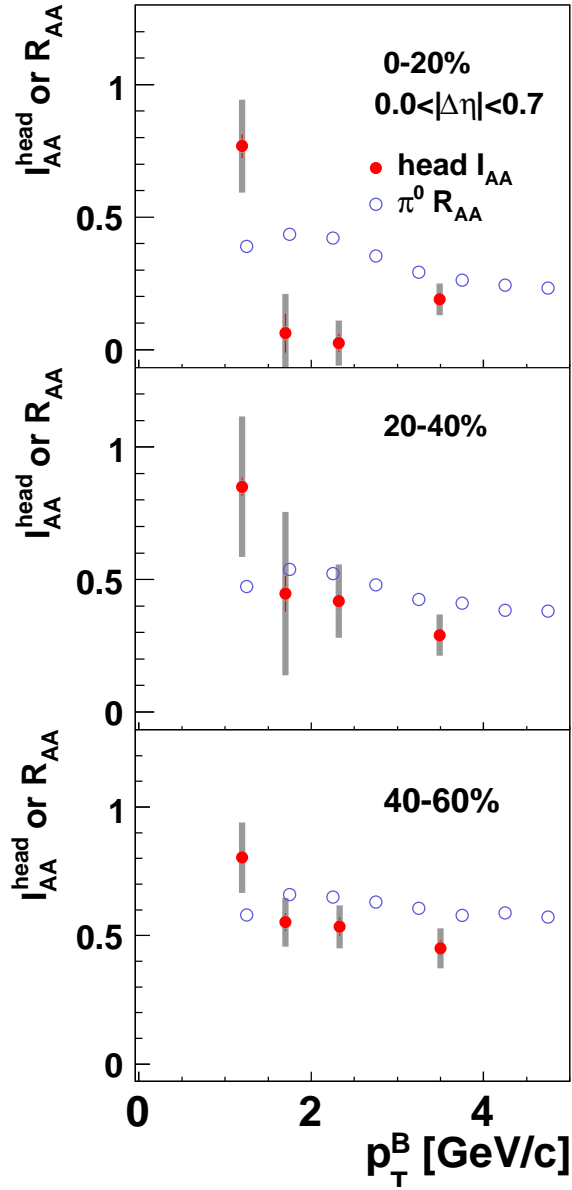


Figure 4.15: Punch through  $I_{AA}$  for trigger  $p_T = 2.0 - 3.0$  GeV/c in various centrality vs partner  $p_T$

binatorial background in the underlying event. We also observe that this ratio increases with partner  $p_T$ . This does not follow the particle spectrum, which decreases with momentum in the underlying event. From these observations it is clear that the ridge cannot simply be due to uncorrelated combinatorial background.

Similar procedures have been applied to the shoulder. The ratios of the shoulder to the combinatorial background on the away side are plotted as a function of  $N_{part}$  for different partner  $p_T$ , as shown in Fig. 4.17. The ratio decreases with increasing  $N_{part}$ , and increases with partner  $p_T$ , as was seen for the ridge.

We compare the two ratios together, as shown in Fig. 4.18. At partner  $p_T$  below 2 GeV/c, the two ratios are consistent with each other. At  $p_T$  larger than 2 GeV/c, the ratio of the shoulder to background is smaller than the ratio of the ridge at large  $N_{part}$ .

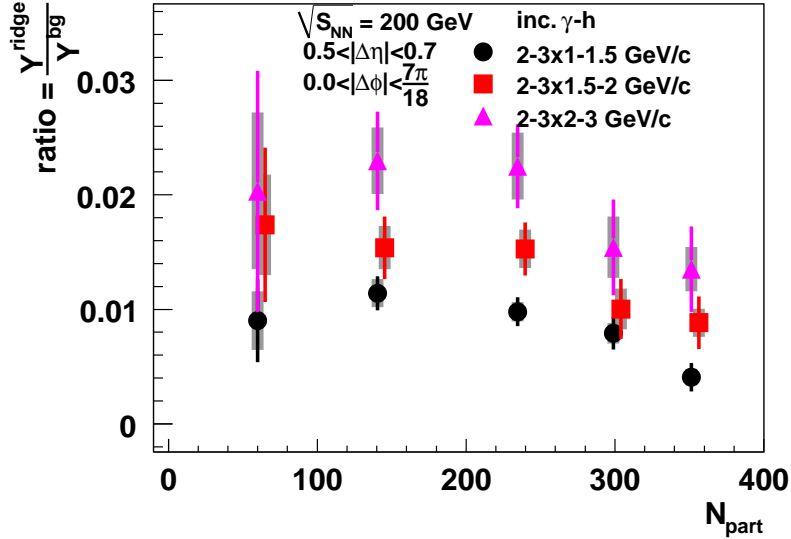


Figure 4.16: Ratios of the ridge yield to the underlying event in near side as a function of  $N_{part}$  for different partner  $p_T$  bins.

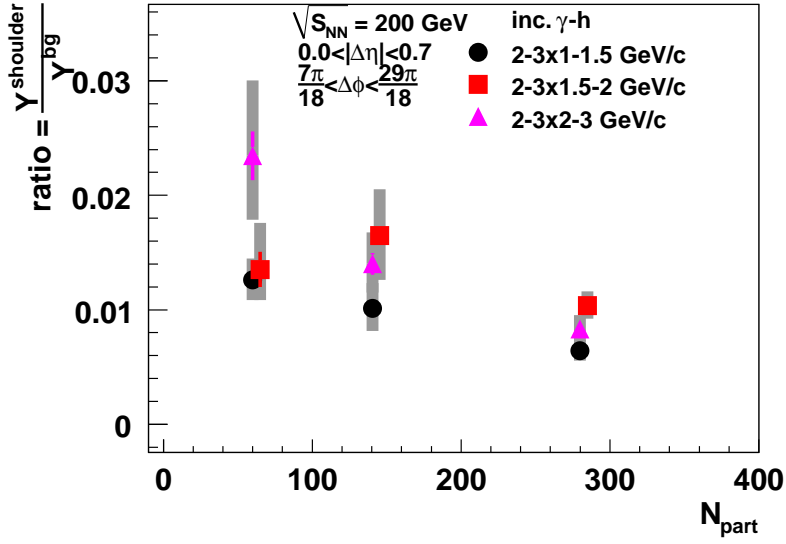


Figure 4.17: Ratios of the shoulder yield to the underlying event in away side as a function of  $N_{part}$  for different partner  $p_T$  bins.

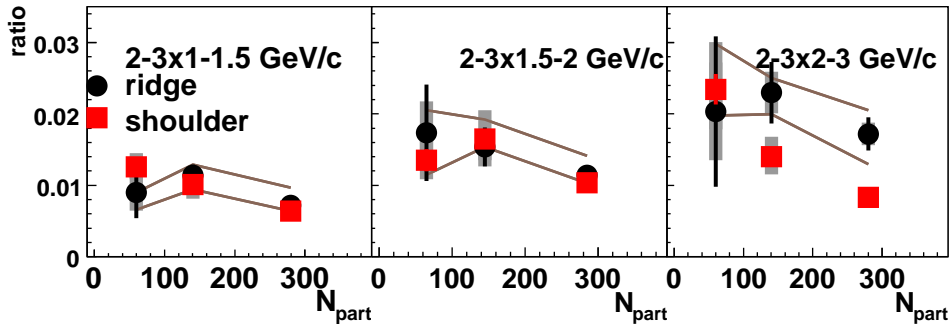


Figure 4.18: Ratios of the ridge (shoulder) yield to the underlying event as a function of  $N_{part}$  for different partner  $p_T$  bins.

### 4.8.1 Medium Modification and Comparison of Near-side and Away-side

The decomposition of the away-side allows comparison of the two jet induced modifications: ridge in the near-side and shoulder in the away-side. The two phenomena share many qualitative features. For example, as discussed above, the ridge appears to be constant over  $\Delta\eta$ . Fig. 4.4 suggests this is true for the shoulder as well. In fact, both of the preceding statements have been confirmed over much larger  $\Delta\eta$  ranges by other experiments [25, 37]. Thus, the two phenomena seem to share this feature, as also previously noted in [61]. They are both "exotic" (compared to elementary collisions) and appear in similar  $p_T$  and centrality ranges. Thus it is very natural to look for more quantitative connections between the two phenomena.

Fig. 4.19 compares the yields of the ridge and shoulder as a function of  $N_{part}$ , in various partner  $p_T$  bins. When normalized per unit pseudo-rapidity, the yields are similar, both rising in the most central collisions to the level of about 0.2 charged particles above 1 GeV/c (integrating over all  $p_T$  bins shown) per trigger. At partner  $p_T$  below 2 GeV/c, the yield of the shoulder is larger than the ridge, but still consistent with the ridge, within systematic uncertainty. At partner  $p_T$  larger than 2 GeV/c, the two yields are even consistent numerically but uncertainties are increasing. At the highest partner  $p_T$ , 3–5 GeV/c, the ridge and shoulder are compatible within large systematic uncertainties, although the yield of ridge is approximately consistent with zero.

To further investigate the partner  $p_T$  dependence, we investigate the  $p_T$  and centrality trends of the ridge and shoulder separately. In Fig. 4.20, we normalized the ridge yield to that in the most central collisions, 0–5%. The normalized ridge yields are plotted as a function of  $N_{part}$  for different partner  $p_T$  bins. The centrality dependence of the ridge yield vs  $N_{part}$  is consistent from 1 to 3 GeV/c. This indicates that the centrality trend scales almost the same way for all  $p_T$  bins. A similar plot for shoulder yield is shown in Fig. 4.21. In this case, the  $N_{part}$  dependence is approximately the same over the whole  $p_T$  range, albeit with fewer centrality selections to reliably examine all three  $p_T$  bins.

At lower partner  $p_T$ , better statistics allows for the fitting decomposition in the away-side in finer centrality bins, especially in the most central collisions. Since the previous plots show no dependence on  $p_T$ , we compare the ridge and shoulder yields as a function of  $N_{part}$  at partner  $p_T = 1\text{--}2$  GeV/c in Fig. 4.22. The most central collisions corresponds to 0–5% centrality. The two yields are numerically close and show a very similar  $p_T$  trend for  $N_{part}$  up to 250. At  $N_{part} \approx 250$ , the trend of the two yields start to deviate—the yield of the

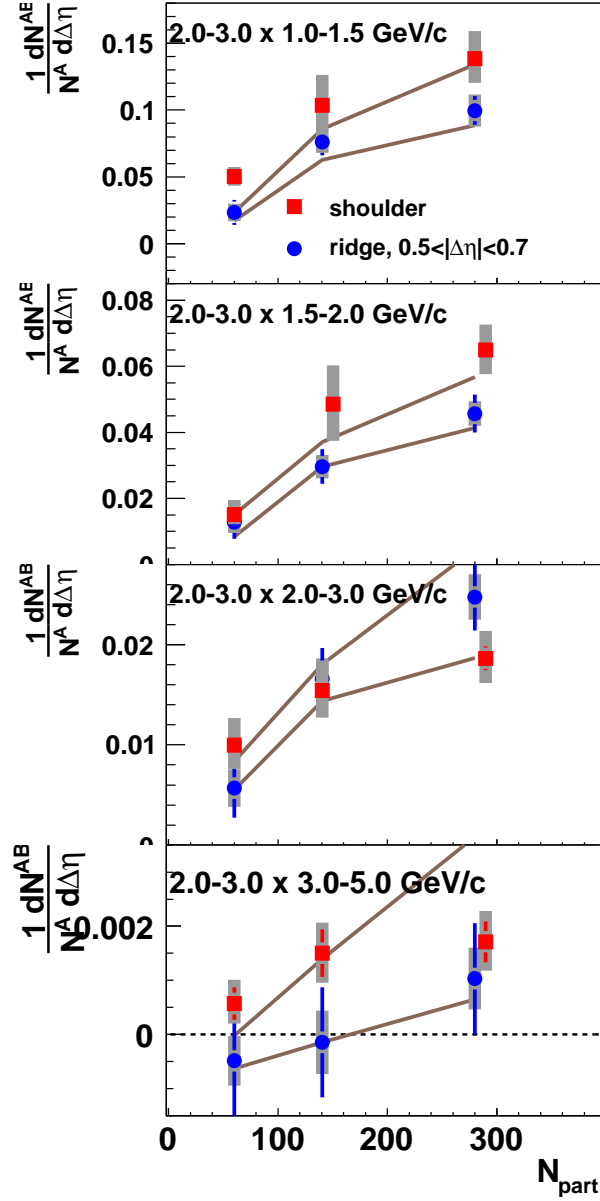


Figure 4.19: Yields of ridge and shoulder vs.  $N_{part}$  at trigger  $p_T = 2.0 - 3.0$  GeV/c and various partner  $p_T$ . The green lines are the estimated systematic error of the ridge yields due to physics assumptions regarding the jet contamination and modification discussed in the text.

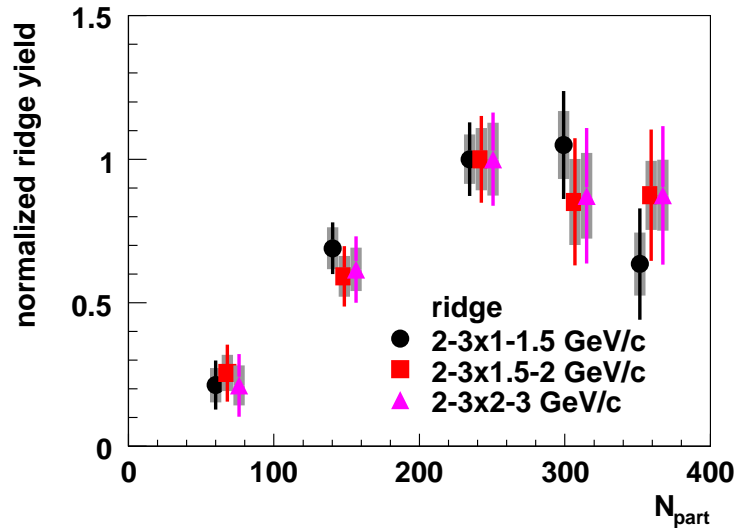


Figure 4.20: Normalized ridge yield vs  $N_{part}$ . The green lines are the estimated systematic error of the ridge yields due to physics assumptions regarding the jet contamination and modification discussed in the text

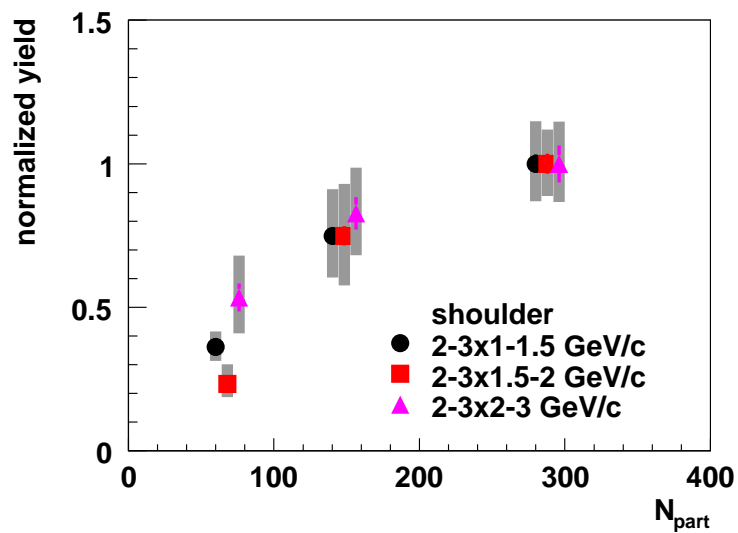


Figure 4.21: Normalized shoulder yield vs  $N_{part}$  in different partner  $p_T$



shoulder keeps increasing while the yield of ridge shows hints (within the larger extra systematic) of flattening or even decreasing. However, this effect hinges on the single 0–5% point, where in other observables such as the baryon excess [62], deviations from an otherwise monotonic increase with centrality have also been observed.

Finally, by taking the ratio between the yield of shoulder and ridge which also cancels part of the systematic errors, we can best examine whether or not the two modifications scale the same way with centrality. The result is shown in Fig. 4.23. Although hinting at more complex behavior, the ratio is consistent with being constant in centrality within systematic uncertainties. The average value of the ratio across all centralities is  $1.29 \pm 0.08$  (stat. only). So, although numerically close, they are not exactly the same—the shoulder yield is about 30% higher on average than that of the ridge across all centralities. It should be noted that given the discussion above about the  $\Delta\eta$  independence of both phenomena, this ratio value is not specific to the PHENIX acceptance.

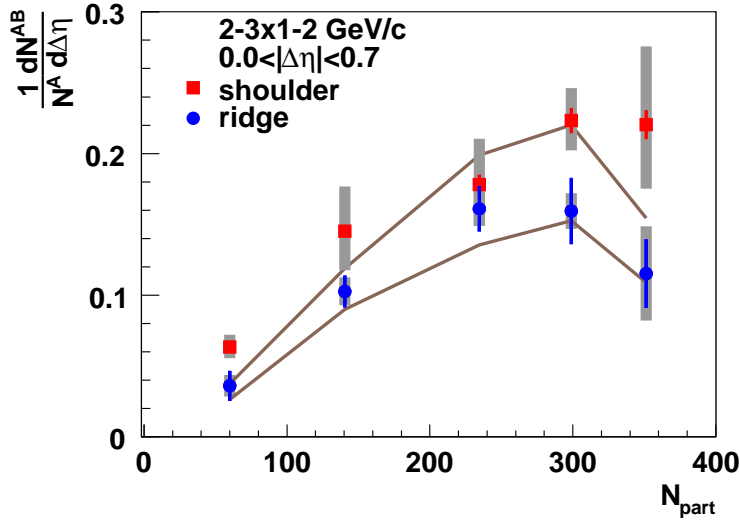


Figure 4.22: Yields of ridge and shoulder vs.  $N_{part}$  at trigger  $p_T = 2.0 - 3.0$  GeV/c and partner  $p_T = 1.0 - 2.0$  GeV/c. The brown lines are the estimated systematic error of the ridge yields due to physics assumptions regarding the jet contamination and modification discussed in the text.

In Fig. 4.24, we calculate the average per-trigger transverse momentum by integrating the per trigger yield weighted by the transverse momentum,

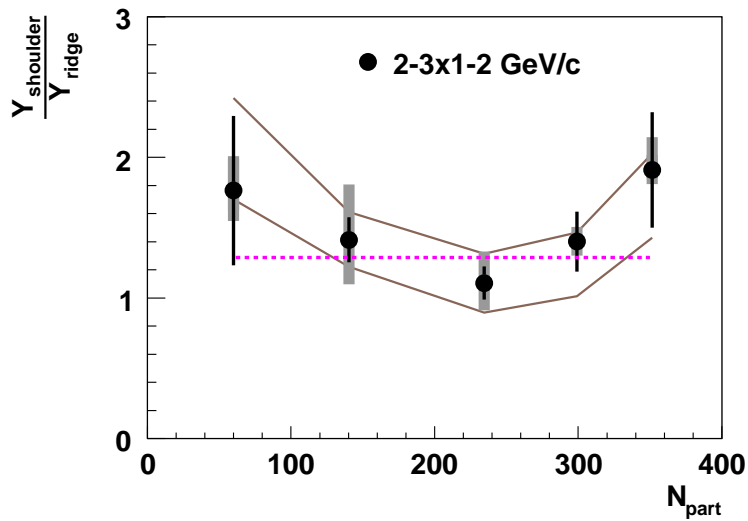


Figure 4.23: Ratio of the yields of shoulder over ridge vs.  $N_{part}$  at trigger  $p_T = 2.0 - 3.0$  GeV/c and partner  $p_T = 1.0 - 2.0$  GeV/c. The green lines are the estimated systematic error of the ridge yields due to physics assumptions regarding the jet contamination and modification discussed in the text. The average value of the ratio shown by the straight line is 1.29.

relative to the direction of the trigger particle. A weight factor of  $p_T^B \cos \Delta\phi$  is used, where  $\Delta\phi$  is the azimuthal angular difference between trigger and partner particle and the weighted yields are then integrated over  $p_T$  and  $\Delta\phi$ :

$$\frac{1}{N^A} \frac{d\langle p_T \rangle}{d\Delta\eta} = \int \frac{dN}{dp_T^B} p_T^B \cos \Delta\phi d\Delta\phi dp_T^B \quad (4.8)$$

By weighting with  $p_T$ , one can see how much transverse momentum is carried by the ridge and shoulder respectively. After weighting with  $p_T$ , the relative strength between the ridge and shoulder is changed. The  $p_T$  carried by shoulder is consistently *lower* than the  $p_T$  carried by ridge. The most important reason for this change is because the shoulder peaks at  $\Delta\phi \approx 1.1$ , so after weighting with a factor of  $\cos \Delta\phi$ , the contribution is more suppressed. Furthermore, one might argue that the  $p_T$  of the trigger itself should be added to the ridge total, and thus the imbalance could presumably be even larger.

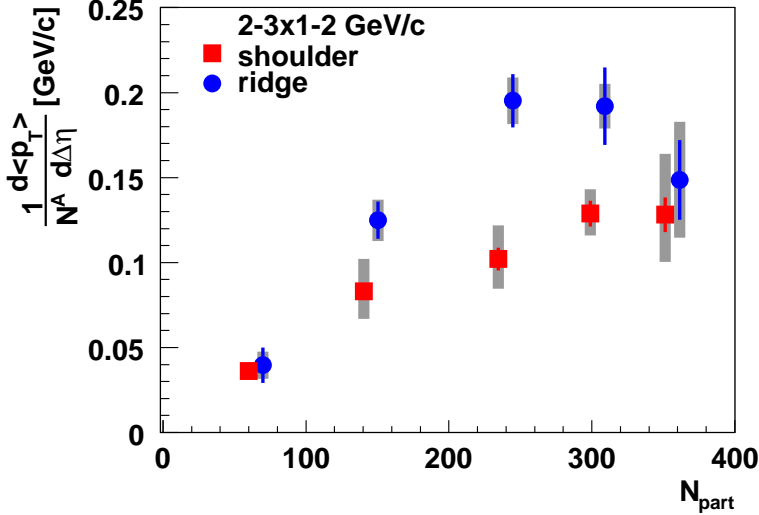


Figure 4.24:  $p_T$  weighted yields of ridge and shoulder vs.  $N_{part}$  at trigger  $p_T = 2.0 - 3.0$  GeV/c and partner  $p_T = 1.0 - 2.0$  GeV/c

## 4.8.2 Transverse Momentum in Near and Away side

In Fig. 4.13, the away side yield is suppressed at partner  $p_T > 3$  GeV/c and is enhanced below 3 GeV/c. This leads to a fundamental question: where does

the energy lost by those high  $p_T$  particles go and does that energy reappear as the enhancement of the lower  $p_T$  particles?

In order to answer this question, we again use transverse momentum as our observable. In hard scattering, transverse momentum is a conserved quantity. In reality, it is impossible to collect all the particles. But we can use p+p collisions as a reference for the collisions without medium effects, and see how much transverse momentum is carried in both the near and away side in a certain  $p_T$  range. When the hard scattering happens inside the medium, the jet-medium interaction may redistribute the transverse momentum. Comparing the transverse momentum in the near and away side between Au+Au and p+p in the same  $p_T$  range may offer more information about the medium.

The per trigger yields in Fig. 4.6 and Fig. 4.13 were weighted with the mean partner  $p_T$  along the direction of the trigger particles of each  $p_T$  bin according to Eq. 4.8. We first look at partner  $p_T$  between 1–2 GeV/c in Fig. 4.25. The transverse momentum in both near and away side are plotted as a function of  $N_{part}$ . In the left panel, we see, as expected, that the mean  $p_T$  carried in the near side in heavy ion collisions is significantly larger than in p+p. This enhancement is mostly due to the existence of the ridge.

In the right panel, the awayside is plotted with its different components, where the head corresponds to the jet like correlation, the shoulder represents the medium modification, and the sum of the two is the total transverse momentum in the away side within the  $p_T$  range. We see that the  $p_T$  carried in the head region decreases with increasing  $N_{part}$ , which means the  $p_T$  carried by the head region is lost inside the medium. This is consistent with the jet suppression observed in previous measurements. For the shoulder region, the trend of the transverse momentum is similar to the ridge yields, which increases with  $N_{part}$ .

Adding the  $p_T$  carried in head and shoulder together gives the  $p_T$  carried in total away side. The transverse momentum carried in the away side increases with  $N_{part}$ . This indicates that in this partner  $p_T$  range, 1–2 GeV/c, even though the  $p_T$  carried in the head region is suppressed, the  $p_T$  lost in the head region apparently reappears in the shoulder region. The excess of total away side momentum in central Au+Au collisions also indicates that the away side may even pick up additional momentum from the medium. Another possibility for the enhancement may be that the momentum lost by high  $p_T$  particles due to jet quenching reappears in the lower  $p_T$  region.

In Fig. 4.13, at partner  $p_T$  of 3–5 GeV/c, the away side is suppressed. In order to see if the lost momentum at high  $p_T$  reappears as the transverse momentum enhancement at low  $p_T$ , we summed over partner  $p_T$  between 1–5 GeV/c, which also includes the  $p_T$  region where the away side is suppressed

and the result is plotted as a function of  $N_{part}$  in Fig. 4.26. The trends in Fig. 4.25 all hold here. The near side carries more  $p_T$  in Au+Au than in p+p. On the away side, the total transverse momentum in central Au+Au collisions is larger than p+p. Even though the momentum in the away side is smaller than p+p at  $p_T = 3-5$  GeV/c due to jet quenching, the total away side transverse momentum in away side is still larger than p+p when summed over 1-5 GeV/c.

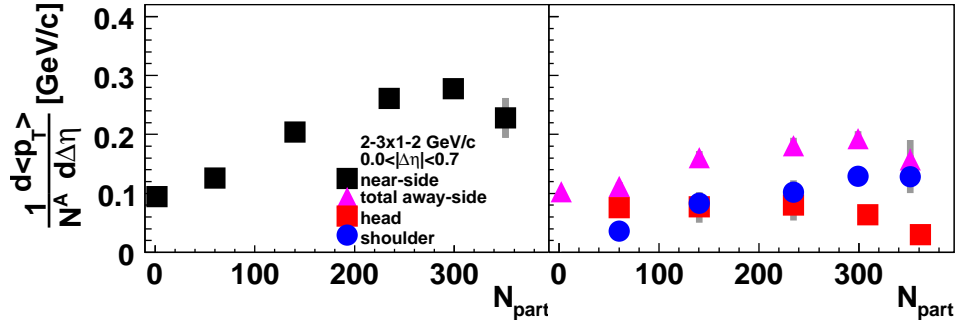


Figure 4.25:  $p_T$  weighted yields of near and away side vs.  $N_{part}$ . Trigger  $p_T = 2.0 - 3.0$  GeV/c and partner  $p_T = 1.0 - 2.0$  GeV/c

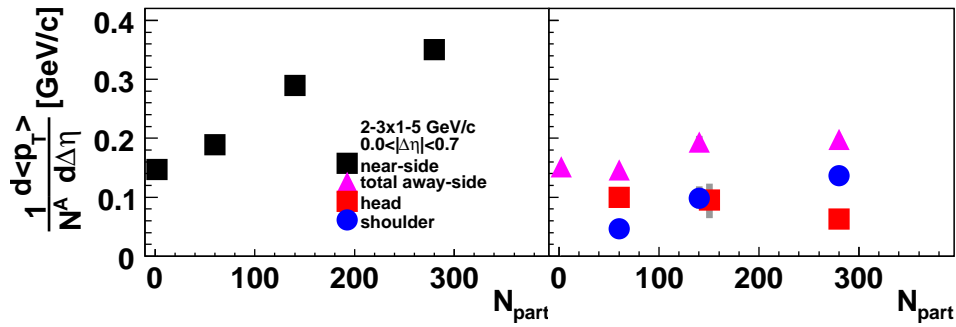


Figure 4.26:  $p_T$  weighted yields of near and away side vs.  $N_{part}$ . Trigger  $p_T = 2.0 - 3.0$  GeV/c and partner  $p_T = 1.0 - 5.0$  GeV/c

Thus the  $p_T$  lost by the head appears to be recovered as the  $p_T$  gained in the shoulder. This could be the first evidence of a direct connection between the awayside jet correlation and the shoulder enhancement, such that the quenched jet  $p_T$  is pushed or redirected into the shoulder, as would be the case in many of the speculated enhancement sources [42, 63, 64, 65, 66].

On the other hand, since the total transverse momentum summed over 1–5 GeV/c in the away side is enhanced in Au+Au compared to p+p, this implies that the momentum enhancement in low partner  $p_T$  is more than the transverse momentum lost in the away side at high partner  $p_T$ . Since the momentum lost at high  $p_T$  can not account for the enhancement of transverse momentum at low  $p_T$ , this suggests that the jet may also carry out some particles from the medium.

In this analysis, the partner  $p_T$  range is 1–5 GeV/c. Even though we did not include the full possible  $p_T$  range, the result does not change if we extend the measured  $p_T$  range. In [23], for partner  $p_T$  above 5 GeV/c, the conditional yield is about 2 orders of magnitude smaller than the conditional yields at 1 GeV/c, so even weighted with momentum, the contribution to the total transverse momentum is negligible. Also in [23], for partner  $p_T$  below 1 GeV/c, the away side yield in Au+Au is consistently larger than in p+p. When we weighting with  $p_T$ , the away side in Au+Au still carries more  $p_T$  than p+p. So this does not change the conclusion that the total transverse momentum in away side in Au+Au is larger than in p+p.

## 4.9 Spectra and Truncated Mean $p_T$

The spectra of the ridge, head and shoulder are measured and plotted in Fig. 4.27. In order to measure the trend of the spectra, we use the truncated mean  $p_T$ ,  $\langle p'_T \rangle$  to describe the shape of the spectra. The truncated mean  $p_T$  is defined as

$$\langle p'_T \rangle = \frac{\sum_{p_T^{min}}^{p_T^{max}} p_T \frac{dN}{dp_T} dp_T}{\sum_{p_T^{min}}^{p_T^{max}} \frac{dN}{dp_T} dp_T} - p_T^{min} \quad (4.9)$$

Here the partner  $p_T$  range is 1–5 GeV/c. The truncated mean  $p_T$  as a function of  $N_{part}$  for each component is shown in Fig. 4.28. Both the near and away-side yield for p+p are measured as well as a reference for the hard scattering. The truncated mean  $p_T$  of the inclusive hadrons is used to represent the medium. Within the large ridge uncertainties, ridge and shoulder are consistent as is expected from previous discussions. Despite the large uncertainties, it appears that the most probable value for the ridge  $\langle p'_T \rangle$  is in fact the same as the shoulder. Both are consistently softer than their p+p counter part, which likely means neither comes purely from hard scattering processes. But when comparing with the spectra of the inclusive charged hadrons, the shoulder is slightly harder while the ridge is consistent with the inclusive charged

hadrons. This is in contrast to the the head region, where in central collisions,  $\langle p'_T \rangle$  is even lower than inclusive charged hadrons. As in [23], this should be interpreted as the punch through jet being so suppressed that the yield is in fact close to completely gone. Going from central to peripheral, the  $\langle p'_T \rangle$  rises, which is consistent with decreasing suppression.

## 4.10 Summary

In this analysis, we present the inclusive photon–hadron two particle  $\Delta\eta$ – $\Delta\phi$  correlations measured in Au+Au collisions at  $\sqrt{s_{NN}} = 200$  GeV. We decompose correlation function in  $\Delta\eta$  and  $\Delta\phi$  to disentangle contributions from the medium and the punch–through and trigger jets. Upon correcting the underlying event for elliptic flow, the ridge is observed for associated particle  $p_T$  below 3 GeV/c; it is broad in rapidity and narrow in  $\Delta\phi$ . The away side correlated particle yield is enhanced in central collisions. The yield of particles in the shoulder grows with centrality while the away side punch–through jet is suppressed. Remarkably, the ridge closely resembles the shoulder in the centrality dependence of particle yield and spectra. The truncated mean  $p_T$  of the ridge and shoulder are also consistent with the inclusive charged hadrons from the medium, which indicates the two structures are strongly related with the medium. With more understanding of the shape of the underlying event background, the shape of the subtracted correlation function may be changed as well, and so does our understanding of jet–medium interaction.

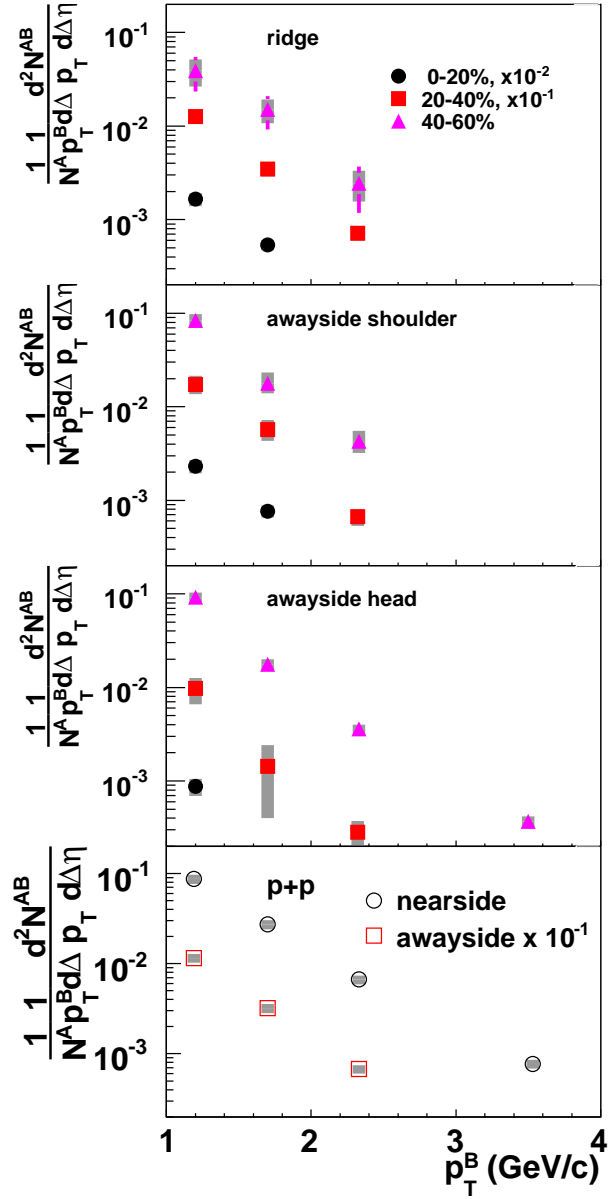


Figure 4.27: Spectra of ridge, shoulder and head for trigger  $p_T = 2.0 - 3.0$  GeV/c.



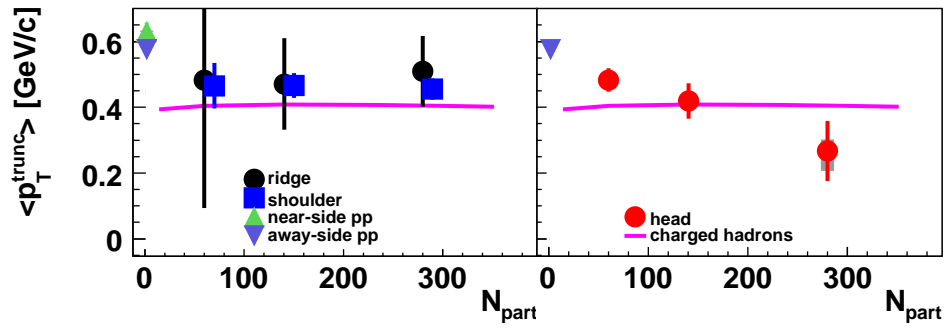


Figure 4.28: Truncated mean  $p_T$  of spectra of ridge, shoulder and head for trigger  $p_T = 2.0 - 3.0$  GeV/c and partner  $p_T = 1-5$  GeV/c.

## Part III

**Analysis:**  $v_n$

## Chapter 5

# Measurement of Effects on Higher Harmonics of the Collective Flow Correlations

### 5.1 Introduction

There are several explanations for the ridge and shoulder structures (see Sec. 3.1. However, higher harmonics of the collective flow have recently attracted a lot of attention [67].  $v_3$  is the third harmonic of the particle angular distribution, which corresponds to  $\cos 3\Delta\phi$ .  $v_3$  has an intrinsic three peak structure over  $2\pi$ , so it is natural to link  $v_3$  with both the ridge and shoulder [67].

In a collision between two identical nuclei, by definition, at mid-rapidity there should be no odd harmonics in the particle distributions due to left-right symmetry. But in reality, the shape of the nuclei are not perfectly spherical. The fluctuations of the shape breaks the left right symmetry, the odd moments of the harmonics, such as  $v_3$  become possible. Elliptic flow, or  $v_2$ , has become a standard measure of collective flow.  $v_2$  is measured with respect to the direction of the reaction plane,  $\psi$ , with the forward detectors, such as the Reaction Plane Detector (RXN), Beam Beam Counter (BBC), or Muon Piston Calorimeter (MPC), which is a forward electromagnetic calorimeter located at  $3.1 < |\eta| < 3.7$ . Then we can measure the particle azimuthal angular distribution with respect to the reaction plane and extract the  $v_2$  [19].

One way to measure  $v_3$  is to measure the orientation of the third event plane,  $\psi_3$ , then follow a similar method to that used to measure  $v_2$  [68]. Two particle correlations provide another way to measure  $v_n$ . The two particles come from the same event, so must share the same reaction plane direction  $\psi$ . By taking the relative azimuthal angle of the two particles, the direction of the reaction plane cancels out automatically. So there is no need to measure the direction of the reaction plane. The Fourier analysis of the correlation

function yields explicitly all n-th order Fourier coefficients. This method was first applied in early PHENIX  $v_2$  measurements [69]. We have now applied Fourier expansions on two particle correlations to extract the first four flow coefficients,  $v_1$ ,  $v_2$ ,  $v_3$  and  $v_4$ .

## 5.2 $v_n$ in Event Plane Method

As mentioned above, there are two major methods to measure  $v_n$ : by reconstructing the event plane and by analysis of two particle correlations. Here we briefly describe  $v_n$  measurements with the event plane method. This is a well established approach to extract  $v_2$  [48, 18, 19], as described in Sec. 3.5. PHENIX now extends the event plane method to higher harmonics. The event plane has been determined with the Reaction Plane Detector (RXN,  $1 < |\eta| < 2.8$ , the Beam-Beam Counter (BBC,  $3.1 < |\eta| < 3.9$ ) and the Muon Piston Calorimeter (MPC,  $3.1 < |\eta| < 3.7$ ). The n<sup>th</sup> event plane is determined by the following relation

$$Q_x \equiv |\vec{Q}_n| \cos(n\psi_n) = \sum_i^M w_i \cos(n\phi_i), \quad (5.1)$$

$$Q_y \equiv |\vec{Q}_n| \sin(n\psi_n) = \sum_i^M w_i \sin(n\phi_i), \quad (5.2)$$

$$\psi_n = \frac{1}{n} \tan^{-1} \left( \frac{Q_y}{Q_x} \right), \quad (5.3)$$

which is the same as Eq. 5.16. The  $v_n$  with respect of the event plane  $\psi_n$  can be measured as

$$v_n(\psi_n) = \frac{\cos(n[\phi - \psi_n])}{\Delta\{\psi_n\}} \quad (5.4)$$

where  $\Delta\{\psi_n\}$  is the event plane resolution.

The correlation strength,  $\langle \cos(j[\psi_n^A - \psi_m^B]) \rangle$  between various forward detectors are measured as a function of centrality. Here A, B are sub-events in forward detectors in different directions, separated by at least 5 units of pseudorapidity. The results are displayed in Fig. 5.1. Fig. 5.1(a) and (b) are cases where  $m = n$ . Strong correlations are found in all those cases. Note for  $n = 1$ , there is a anti-correlation, which is expected as a result of conservation of momentum in transverse direction.

The results are shown for  $n \neq m$  in Fig. 5.1(c) and (d). We see that the first and second event planes are correlated with each other. The second and fourth planes have similar correlations, but with smaller strength. This agrees with our understanding that the even harmonics are strongly correlated with each other because the shape of the colliding region is close to an almond shape, for which  $\psi_2$  and  $\psi_4$  should line up together if the shape is perfectly symmetric. But when correlating the with second and third plane, which is shown in Fig. 5.1(d) and the correlation strengths are scaled by a factor of 20, we find that the second and third plane are basically uncorrelated. This shows that  $\psi_3$  does not correlate with  $\psi_2$ , since the origin of  $\psi_3$  is from fluctuations.

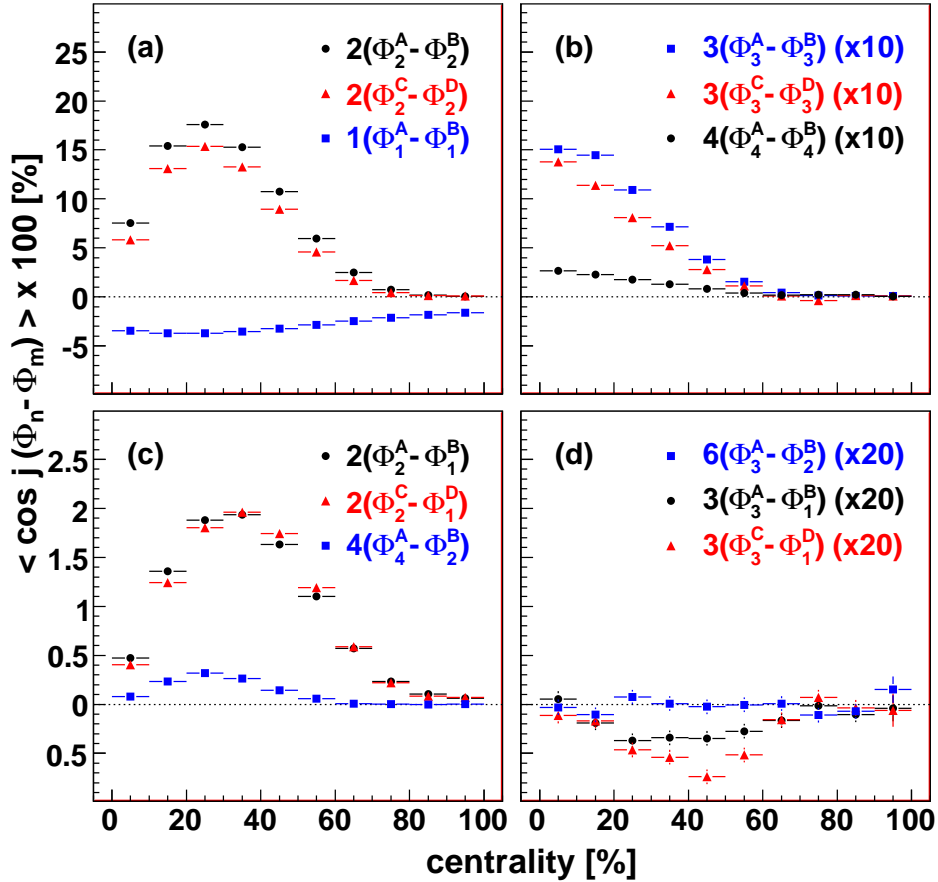


Figure 5.1: Raw correlation strengths of the event planes for various detector combinations as a function of collision centrality. The event planes are measured with the following forward detectors: (a) RXN North, (b) BBC South, (c) MPC North, and (d) MPC South.

The results of  $v_2(\psi_2)$ ,  $v_3(\psi_3)$  and  $v_4(\psi_4)$  as a function of  $p_T$  in various centralities are shown in Fig. 5.2. Here the event plane is determined with the Reaction Plane Detector (RXN). We see a significant non-zero values for  $v_3$  and  $v_4$ , increasing with  $p_T$ , similar to  $v_2$ . For  $v_2$  and  $v_4$ , the values increase from central to mid-peripheral collisions, as expected from increasing shape anisotropy.  $v_3$  does not show a similar trend. The value of  $v_3$  in all centralities is very similar. The measured  $v_2$  and  $v_3$  are compared with two hydrodynamic models [67] and [70]. These models will be described in detail in Chapter 7. Both models agrees with data very well, especially for  $p_T$  below 1 GeV/c.

## 5.3 Analysis

The data is taken from the 2007 run (run7) with Au+Au at  $\sqrt{s_{NN}} = 200$  GeV. Some special runs such as zero field runs, converter runs are removed. We also remove runs which has fewer than 1 million events. The event selection is similar to previous studies, which require the event centralities between 0–92% and the  $z$ -vertex measured by BBC is within 30 cm. For this two particle correlation measurement, both particles are charged hadrons.

We also applied  $\Delta\eta$  cuts between particle pairs. From previous analysis, we know in the  $\eta$  acceptance of the PHENIX central arms ( $|\eta| < 0.35$  or  $|\Delta\eta| < 0.7$ , there is a strong jet contribution at this  $\eta$  region. In order to remove the jet contributions as much as possible while still keeping enough singles, the  $\eta$  difference between the pairs with  $\Delta\eta < 0.3$  are removed.

## 5.4 $v_n$ from Correlation Function Method

### 5.4.1 Fourier Expansion

In a typical elliptic flow analysis, the particle distribution is written as Eq. 5.5

$$f(\phi) = \frac{dN(p_T)}{d\phi} = b_0 \sum (1 + 2v_n \cos(n(\phi - \psi_n))) \quad (5.5)$$

, where  $\psi_n$  is the direction of the reaction plane. Here  $v_n$  is defined as

$$\langle e^{in\phi} \rangle = \int f(\Delta\phi) e^{in\phi} d\phi = v_n e^{i\psi_n} \quad (5.6)$$

For particle pairs, where  $\phi_1 = \phi$ ,  $\phi_2 = \phi + \Delta\phi$ , the distribution is sensitive to  $v_n$ , where

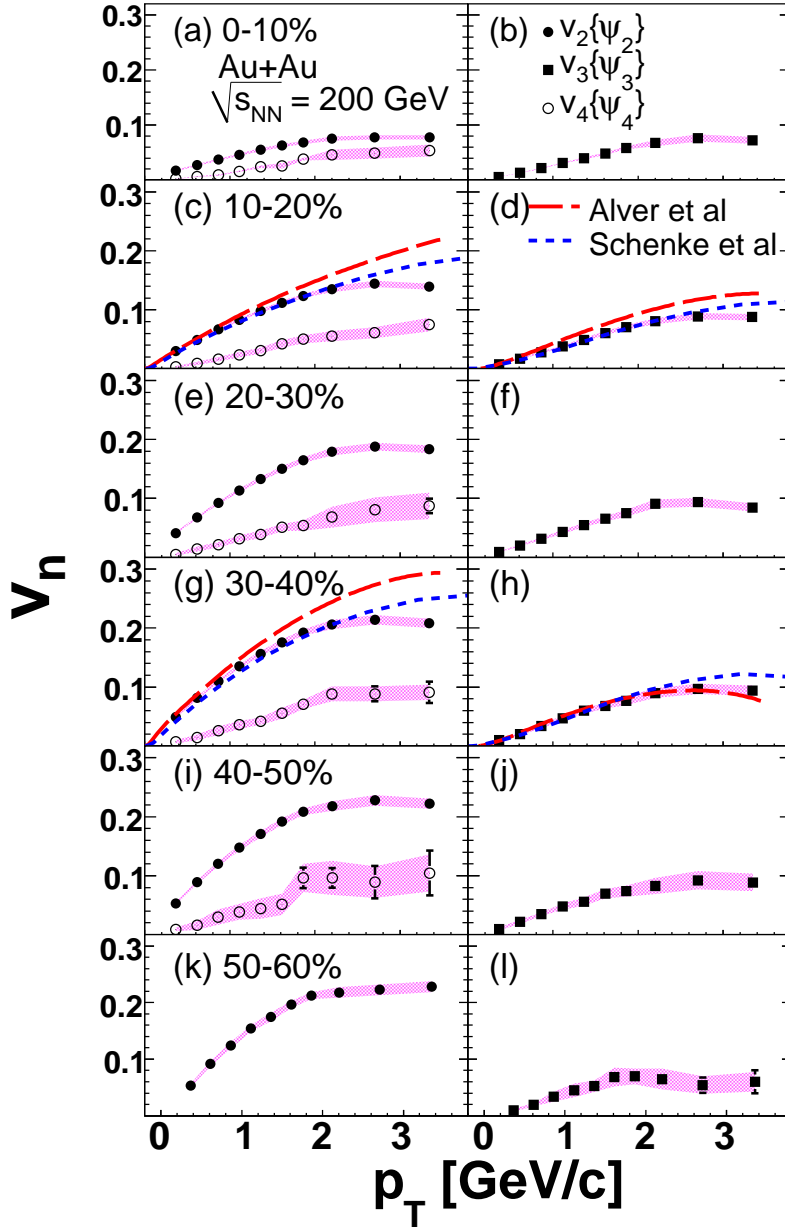


Figure 5.2:  $v_n\{\Psi_n\}$  vs.  $p_T$  measured via the event plane method. The curves are calculations from two hydrodynamic models: Alver *et al.* [67] and Schenke *et al.* [70].

$$\langle e^{in\Delta\phi} \rangle = \langle e^{in\phi_1} e^{-in\phi_2} \rangle = \langle e^{in\phi_1} \rangle \langle e^{-in\phi_2} \rangle = (v_n)^2 \quad (5.7)$$

When both trigger and partner particles are below 1 GeV/c, the contribution from jet particle correlations can be ignored. And the two particle azimuthal correlations can be expanded as

$$\frac{dN^{pair}(p_T)}{d\Delta\phi} \propto \sum (1 + 2c_n \cos(n\Delta\phi)) \quad (5.8)$$

From Eq. 5.8, it is clear that there is no need to determine the direction of the reaction plane,  $\psi$ , when using the correlation function method. This simplification is because both particles are from the same event, and therefore share the same reaction plane. When calculating the difference of the azimuthal angle of the two,  $\psi$  cancels out naturally.

In standard two particle correlation analyses in PHENIX [21, 22, 23, 24], the combinatorial background is assumed to be factorisable, that is

$$c_2(p_T^a, p_T^b) = v_2(p_T^a) \times v_2(p_T^b) \quad (5.9)$$

We follow the same assumption, for the higher harmonics,

$$c_n(p_T^a, p_T^b) = v_n(p_T^a) \times v_n(p_T^b) \quad (5.10)$$

When the  $p_T$  of the trigger is the same as the partner  $p_T$ , then Eq. 5.10 can be reduced to Eq. 5.11

$$c_n(p_T^a, p_T^a) = v_n^2(p_T^a) \quad (5.11)$$

Upon extracting the Fourier Coefficients of the correlation functions at low  $p_T$ , we obtain  $v_n$ .

The analysis is constructed in the following order:

- measure the correlation functions in various  $p_T$  and centrality bins
- extract the Fourier coefficients,  $c_n$
- obtain the  $v_n$  coefficients

## 5.4.2 Correlation Functions

The Correlation functions are constructed for particle  $p_T$  from 0.5 to 3.0 GeV/c, in six centrality bins from 0–10% to 50–60%. Some of the correlation functions are shown as examples in Fig. 5.3 and Fig. 5.4. The two plots are for particle  $p_T$  between 0.5–0.6 and 1.5–2.0 GeV/c in six centralities.



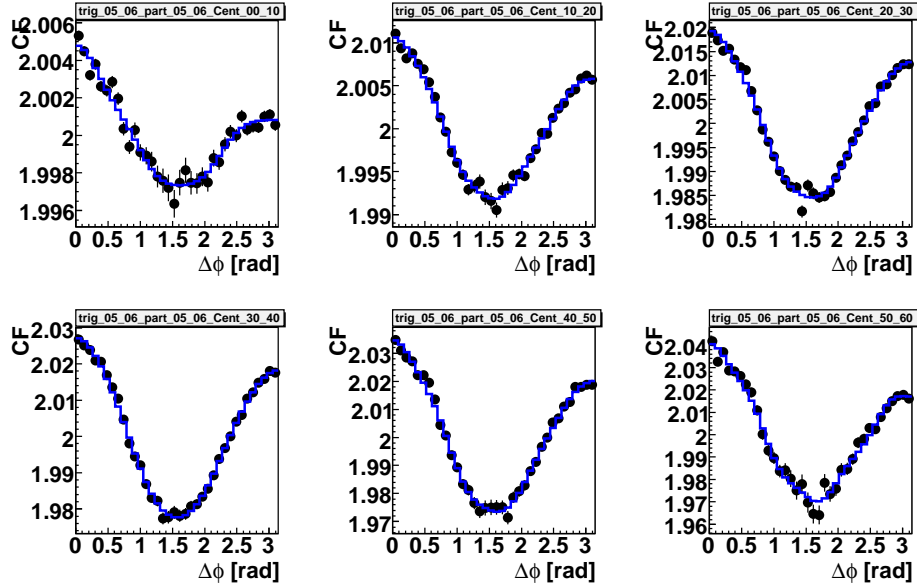


Figure 5.3: Correlation functions for trigger and partner at 0.5–0.6 GeV/c at various centralities. The blue curve is the sum of the Fourier spectra.

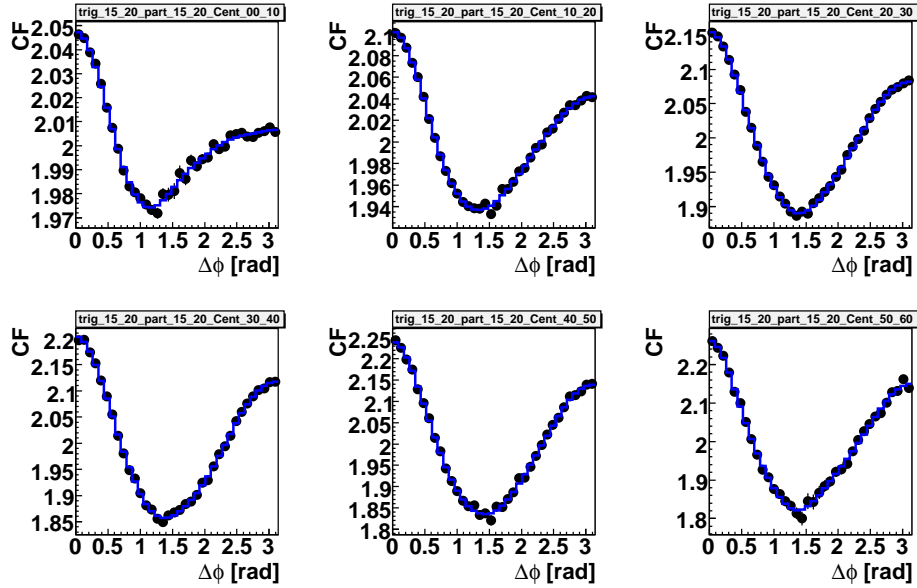


Figure 5.4: Correlation functions for trigger and partner at 1.5–2.0 GeV/c at various centralities. The blue curve is the sum of the Fourier spectra.

### 5.4.3 Extracting $c_n$

For the correlation functions shown in Fig. 5.3 and Fig. 5.4, we use Eq. 5.8 to extract the Fourier coefficients,  $c_n$ . Typical results for  $c_n$  are shown in Fig. 5.5, where the horizontal axis indicates the  $n^{\text{th}}$  Fourier Coefficients. In these plots, we see that the second Fourier coefficients, which are equivalent to  $v_2$ , are significantly larger than the other coefficients. However the first and third components are also significant.

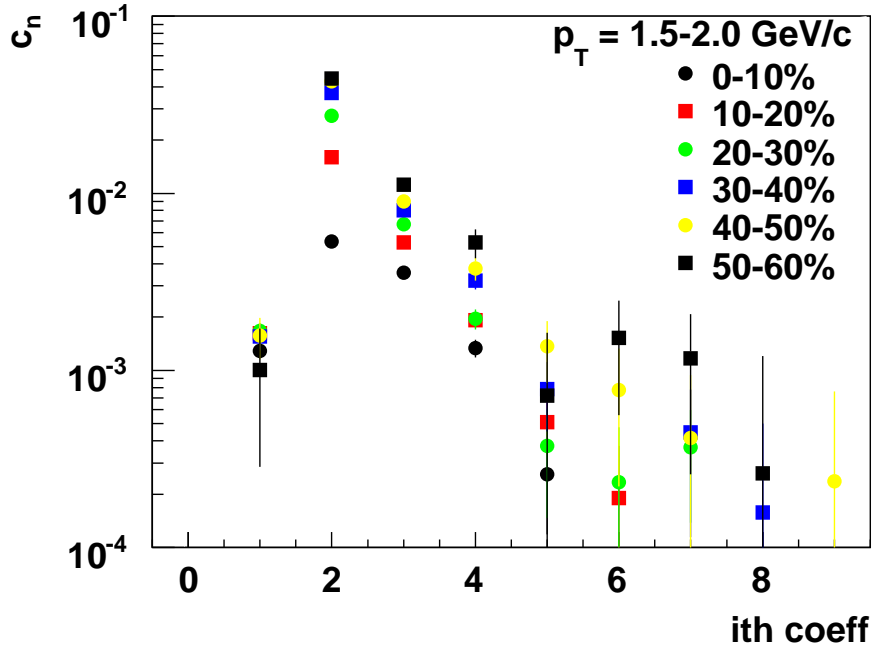


Figure 5.5:  $c_n$  for trigger and partner at 1.5–2.0 GeV/c at various centralities.

### 5.4.4 Extracting $v_n$

Since the correlation functions used to obtain  $c_n$  are symmetric in trigger and partner  $p_T$ , we can apply Eq. 5.11 to go from  $c_n$  to  $v_n$ . We will focus on the first four Fourier moments,  $v_1$ ,  $v_2$ ,  $v_3$  and  $v_4$ .

We plot each  $v_n$  as a function of  $N_{part}$  and  $p_T$ . The results of  $v_n$  vs  $N_{part}$  are shown as Figures 5.6 to 5.9.  $v_1$  shown in Fig. 5.6, is independent of  $p_T$  and decreases when going from peripheral to central collisions. For  $v_2$  shown

in Fig. 5.7, the results are compared with previous PHENIX measurements [19] and shows good agreement. Fig. 5.8 shows a non-zero value of  $v_3$  for all centralities and all  $p_T$ . The general trend here is (i)  $v_3$  decreases with increasing  $N_{part}$ ; (ii)  $v_3$  increases with  $p_T$ . For  $v_4$  (Fig. 5.9), due to statistics,  $v_4$  fluctuates much more than lower  $v_n$ s. And because some of the  $c_4$  values are negative, we set them to be zero to avoid taking the square root of a negative value.

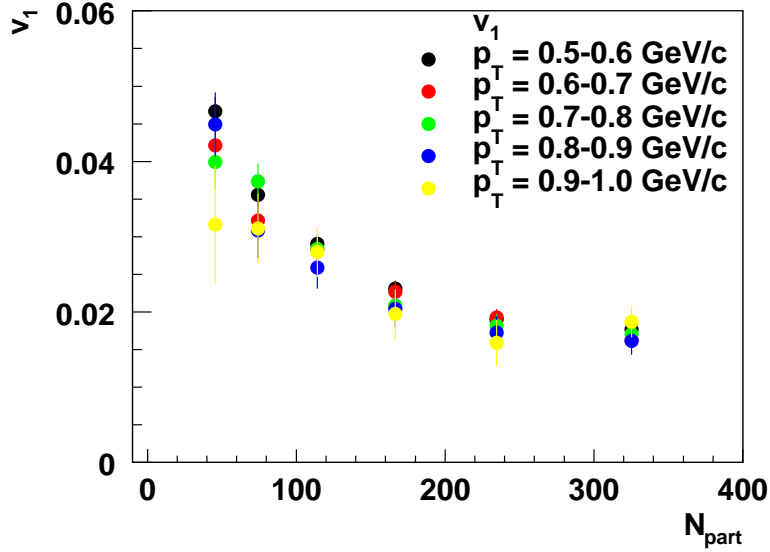


Figure 5.6:  $v_1$  of various  $p_T$  as a function of  $N_{part}$ .

In Fig. 5.10 to Fig. 5.13, we plot the  $v_n$  as a function of  $p_T$ . Fig. 5.10 shows the trend of  $v_1$ . The  $v_1$  is flat below 1 GeV, and increases with  $p_T$  at  $p_T > 1$  GeV/c. There is no obvious difference between different centralities at  $p_T > 1$  GeV/c. Fig. 5.11 plots  $v_2$  vs  $p_T$ . The result is also compared with previous PHENIX measurement, which is measured by reaction plane method [19]. Both measurement agrees well at  $p_T < 1$  GeV/c. At  $p_T > 1$  GeV/c, there  $v_2$  from two particle correlation method are slightly larger than the reaction plane method. The deviation increases from central to mid-peripheral collisions. The larger deviation at mid-peripheral and high  $p_T$  may come from the larger jet contamination. The result of  $v_3$  is shown in Fig. 5.12.  $v_3$  is non-zero and increases with  $p_T$ .  $v_3$  also increases from central (centrality 0–10%) to mid-peripheral (centrality 50–60%) collisions. The  $v_4$  measurement shown in Fig. 5.13 is similar to  $v_2$ , which also increases with  $p_T$ .

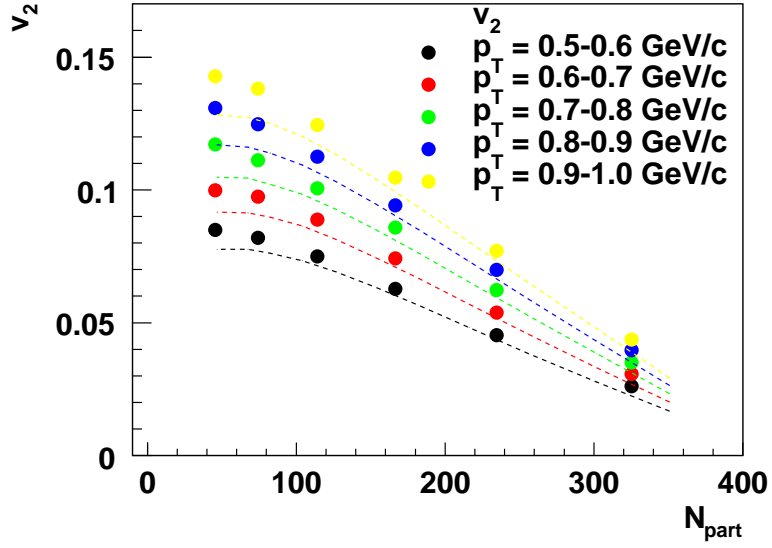


Figure 5.7:  $v_2$  of various  $p_T$  as a function of  $N_{part}$ . The dash lines are  $v_2$  measurements from [19].

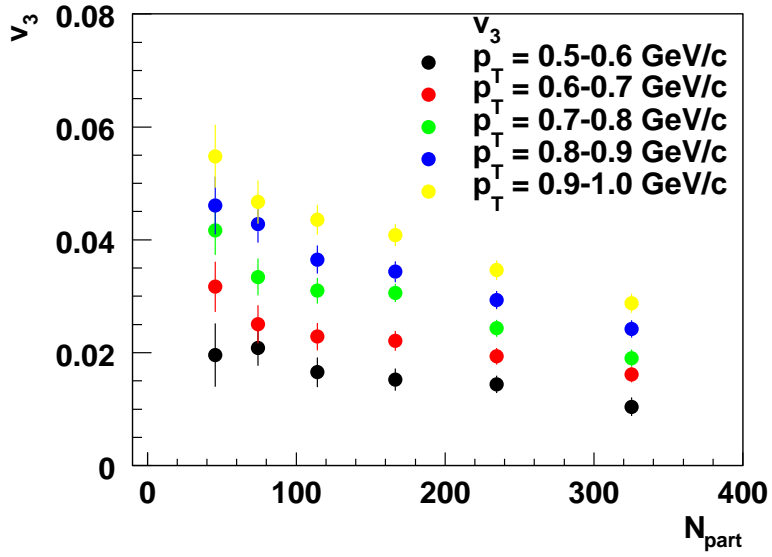


Figure 5.8:  $v_3$  of various  $p_T$  as a function of  $N_{part}$ .

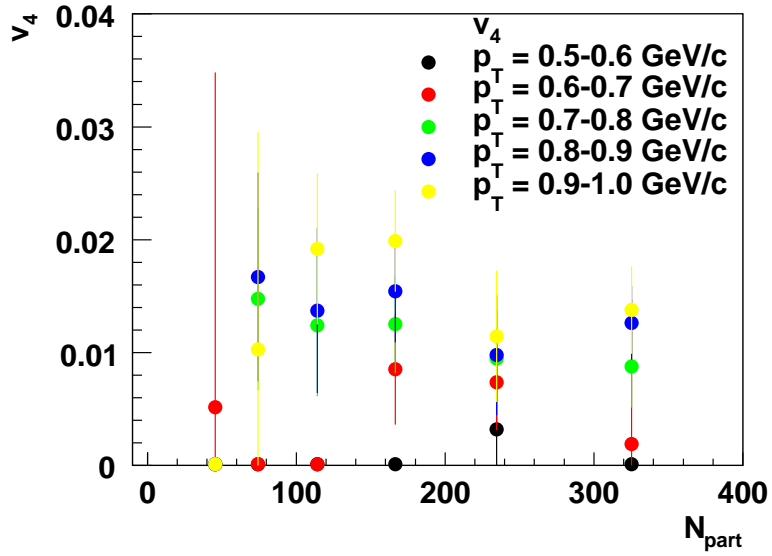


Figure 5.9:  $v_4$  of various  $p_T$  as a function of  $N_{part}$ .

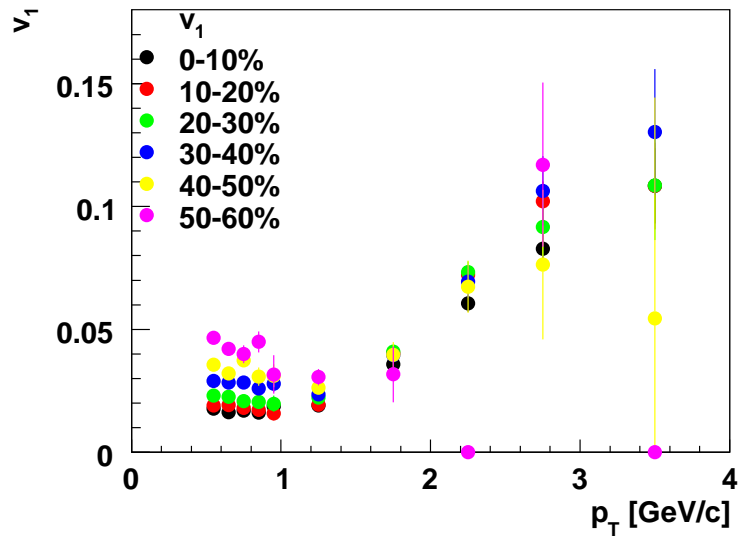


Figure 5.10:  $v_1$  of various centralities as a function of  $p_T$ .

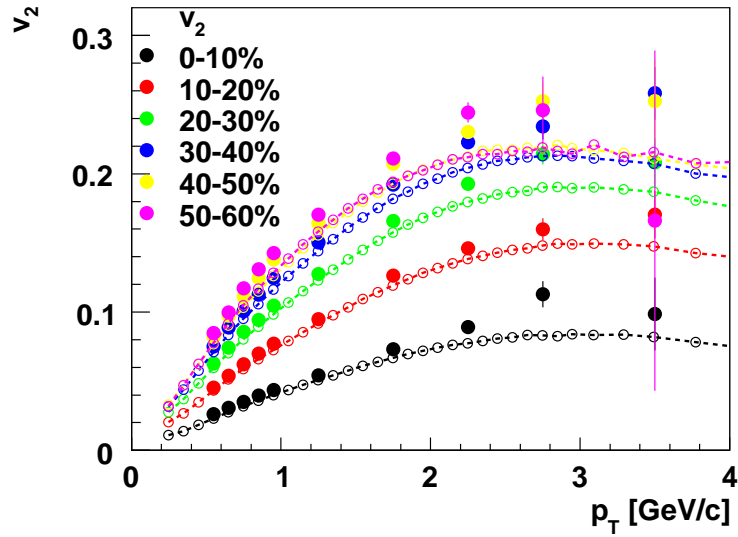


Figure 5.11:  $v_2$  of various centralities as a function of  $p_T$ . The dash lines are  $v_2$  measurements from reference [19].

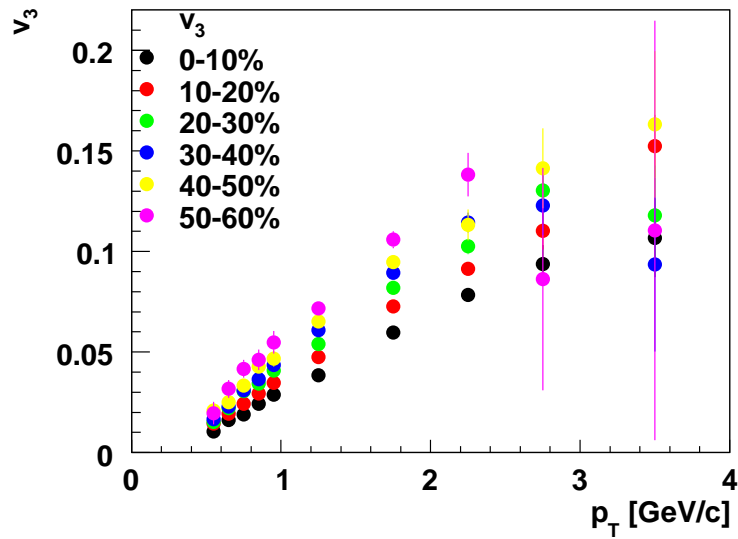


Figure 5.12:  $v_3$  of various centralities as a function of  $p_T$ .

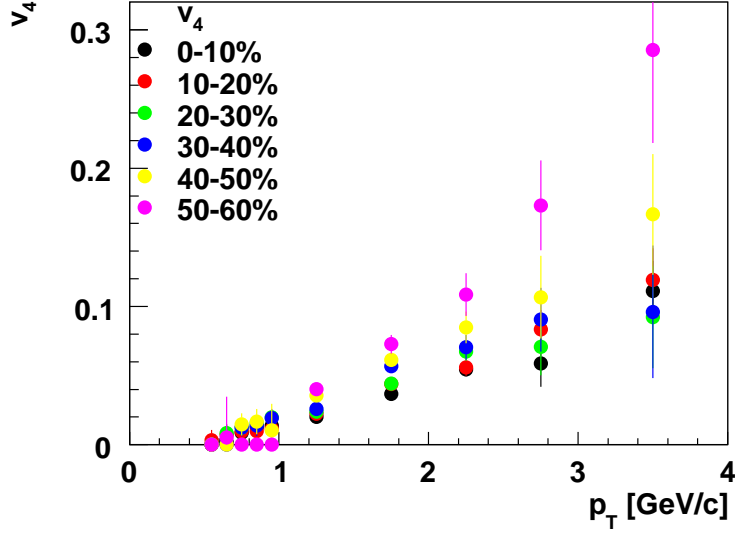


Figure 5.13:  $v_4$  of various centralities as a function of  $p_T$

## 5.5 Factorization of $v_n$

In the previous section, we made an assumption that

$$c_n(p_T^{trig}, p_T^{part}) = v_n(p_T^{trig}) \times v_n(p_T^{part}) \quad (5.12)$$

So when the trigger and the associated particle are at the same  $p_T$ , Eq. 5.12 can be reduced to

$$c_n(p_T) = v_n(p_T)^2 \quad (5.13)$$

Here we directly test this assumption. Eq. 5.13 is called the symmetric  $p_T$  method and Eq. 5.12 is the asymmetric  $p_T$  method. For the symmetric  $p_T$  method, both the trigger and the associated particles have the same  $p_T$ . In the case of the asymmetric  $p_T$  method, the  $p_T$  of the trigger particle is fixed at 0.5–1.0 GeV/c and the correlation function is measured with the associated particle in various  $p_T$  bins.

The  $v_2$  and  $v_3$  values of both the symmetric and asymmetric  $p_T$  methods are presented in Fig. 5.14 for  $v_2$  and Fig. 5.15 for  $v_3$  respectively. The top panel of Fig. 5.14 compares the  $v_2$  measured by the symmetric (asymmetric)  $p_T$  method in red (black) in six different centrality bins. Both methods show

good agreement. The value  $(v_2^{asymmetric}/v_2^{symmetric})-1$  is plotted in the lower panel. This ratio shows the two measurements agree within better than 1% at low  $p_T$  and deviate at the 5% level at highest  $p_T$ . Similar comparison for  $v_3$  is shown in Fig. 5.15. Both methods agree well at  $p_T < 2.5$  GeV/c. The deviation is the largest at 50–60% and at  $p_T > 2.5$  GeV/c.

## 5.6 $\Delta\eta$ dependence

In two particle azimuthal correlations, the  $\Delta\eta$  separation between the particle pairs is important. At particle  $p_T$  below 1 GeV/c, the  $\Delta\eta$  cut can help remove the HBT peak.

At higher particle  $p_T$ , the jet start to contribute in two particle correlations. The nearside jet has a Gaussian jet cone size about 0.3 in  $\Delta\eta$  and  $\Delta\phi$  direction. By requiring the particle pairs separate by 0.3 units of pseudorapidity, we can remove about 67% of the correlated near side pairs which are coming from jets. On the other hand, the ridge is constant along the  $\eta$  direction, so it will not be effected by the  $\eta$  cut.

For the awayside, the awayside jet swings along the full  $\Delta\eta$  acceptance of PHENIX central arm,  $|\Delta\eta| < 0.7$ , as shown in Fig. 4.1(b). So the  $\Delta\eta$  cut can not remove the awayside jet contributions, which will bias the  $v_n$  measurement.

In the current analysis, we require the two particles are separated by 0.3 unit in  $\Delta\eta$ , or  $|\Delta\eta| > 0.3$ . We vary the  $\Delta\eta$  cut to 0.5 to further reduce the contribution of the nearside jet. Fig. 5.16, Fig. 5.17 and Fig. 5.18 show good agreement between  $v_n$  values from two  $\Delta\eta$  cuts, which indicates we have removed a significant amount of nearside jet pairs with  $|\Delta\eta| > 0.3$  cut.

## 5.7 Comparison with $v_2$ measurements from PHENIX

The  $v_2$  measurement in this analysis, or the two particle correlation method, is compared with the latest  $v_2$  measurement from PHENIX [19]. In [19], PHENIX uses the reaction plane method to measure  $v_2$ .

### 5.7.1 $p_T$ vs $N_{part}$

We compare the  $v_2$  measured via two particle correlations with the  $v_2$  measurement from Fig. 2 in [19] as a function of  $N_{part}$ . The  $p_T$  bin used here is 0.5–0.8 GeV/c, and with various centralities from 0–5% up to 40–50%, or



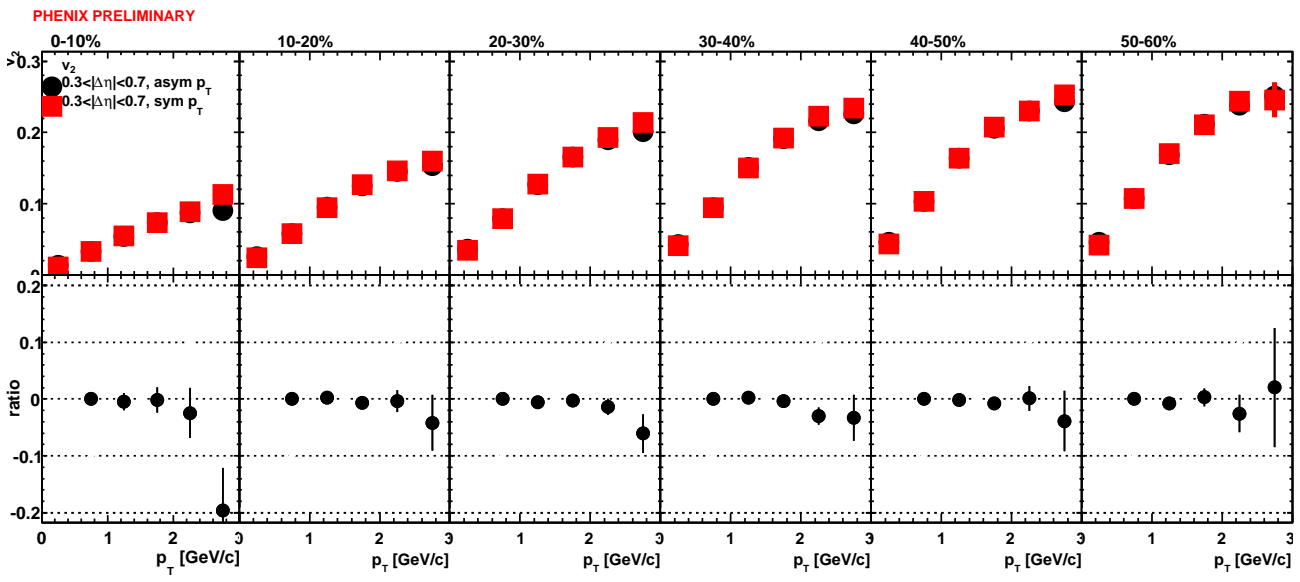


Figure 5.14: Comparison between  $v_2$  values from method 1 (symmetric  $p_T$ , red) and method 2 (asymmetric  $p_T$ , black). Centralities from 0–10% to 50–60%. The bottom panel shows the ratio between black and red (black/red-1).

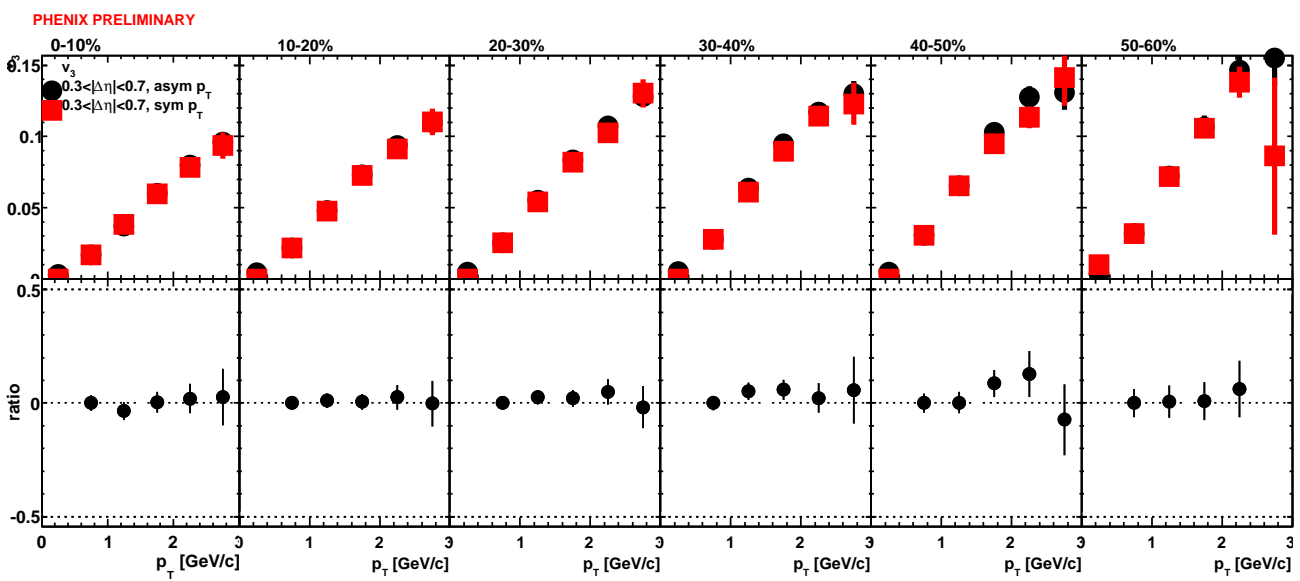


Figure 5.15: Comparison between  $v_3$  values from method 1 (symmetric  $p_T$ , red) and method 2 (asymmetric  $p_T$ , black). Centralities from 0–10% to 50–60%. The bottom panel shows the ratio between black and red (black/red-1).

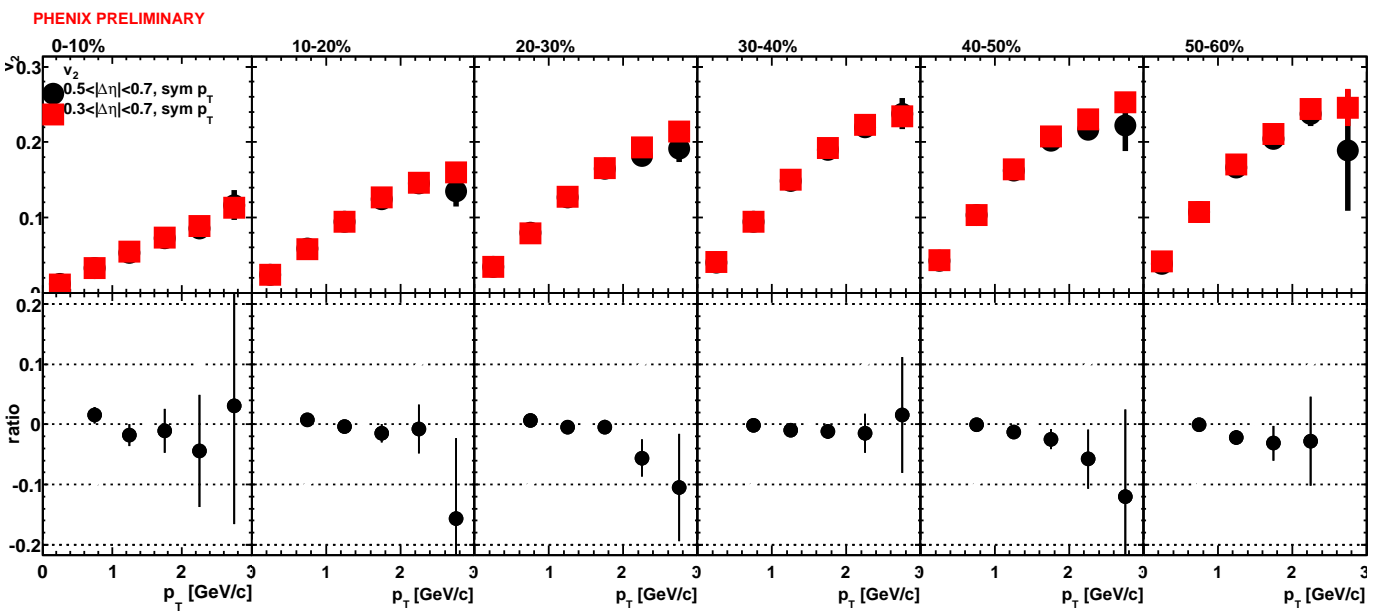


Figure 5.16: Comparison between  $v_2$  values from  $\Delta\eta = 0.3$  (red) and  $\Delta\eta = 0.5$  (black). Centralities from 0–10% to 50–60%. The bottom panel shows the percentage deviation from  $\Delta\eta = 0.3$ .

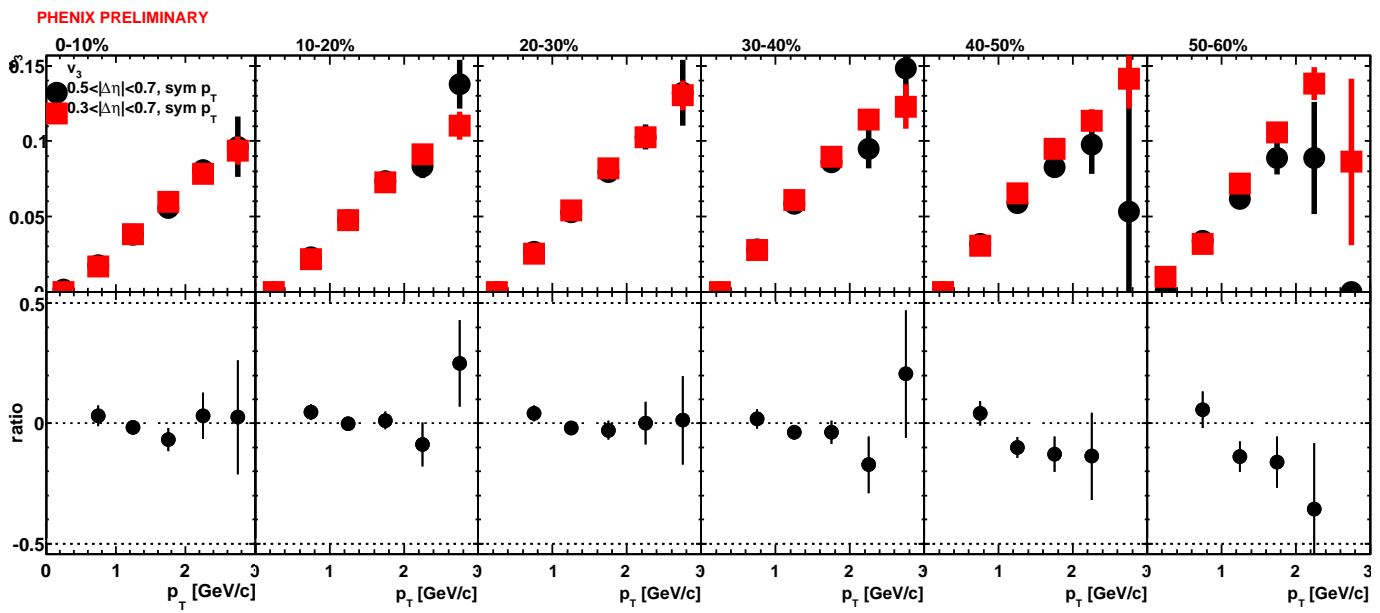


Figure 5.17: Same as Fig. 5.16, but comparing  $v_3$ .

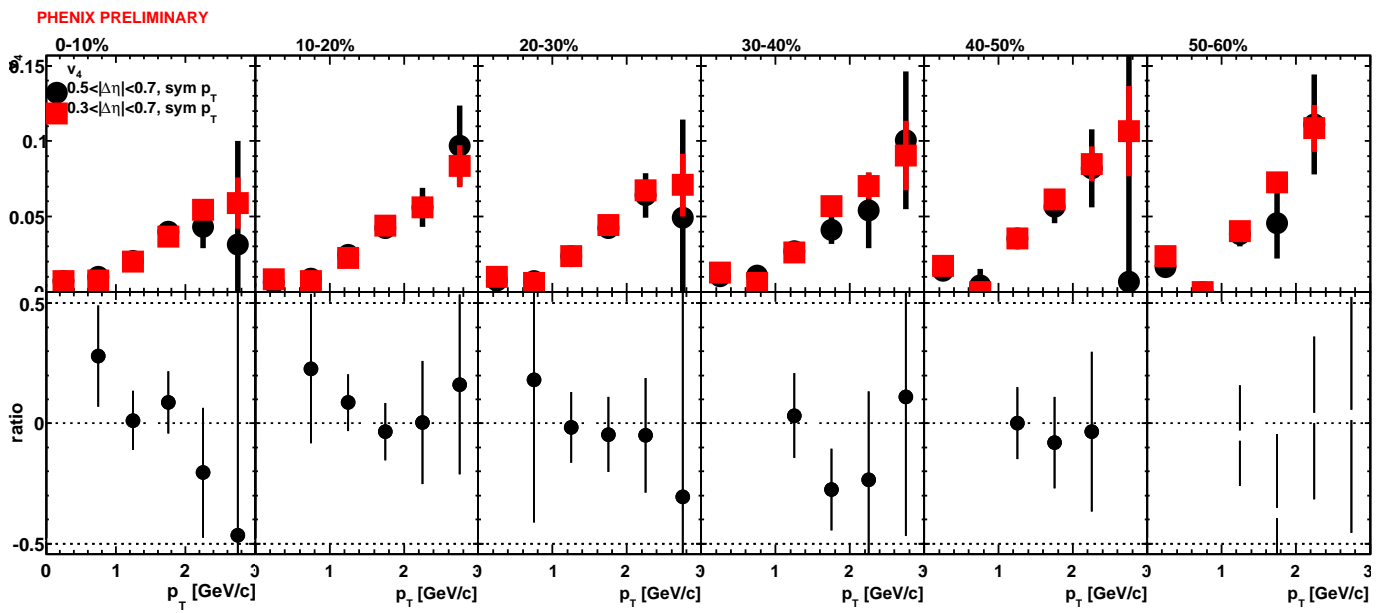


Figure 5.18: Same as Fig. 5.16, but comparing  $v_4$ .

$N_{part} \approx 60$ . The comparison is shown in Fig. 5.19. The  $v_2$  in this analysis is consistent with  $v_2$  values from [19] for  $N_{part} > 140$ . When  $N_{part}$  decreases from 140, we see  $v_2$  values are larger than data from [19].

In [19], the reaction plane is determined by several different detectors. Then the  $v_2$  is measured with respect to each of these reaction planes. We compare our results with the  $v_2$  obtained using the Muon Piston Calorimeter (MPC) and the outer layer of the Reaction Plane Detector (RXNo). The MPC covers  $\eta$  from 3.1–3.7, while RXNo has an  $\eta$  from 1–1.5. When determining the reaction plane  $\psi_2$ , the  $\eta$  position of the forward detector matters. This is because at smaller  $\eta$ , there is a stronger influence from jet particles which will bias the measurement of the reaction plane. This bias is known as the “non-flow” effect. Consequently, reaction plane determined at smaller  $\eta$  tend to have higher  $v_2$  values.

We take the ratio between the  $v_2$  measured in this analysis via the two particle correlation method,  $v_2\{2P\}$ , and  $v_2$  determined with the MPC,  $v_2\{\psi_2^{MPC}\}$ . The results are shown in Fig. 5.20. Fig. 5.21 is a similar plot comparing with  $v_2$  determined with RXNo,  $v_2\{\psi_2^{RXNo}\}$ . We see that for  $N_{part}$  below 260,  $v_2\{2P\}$  is larger than  $v_2\{\psi_2^{MPC}\}$  ( $v_2\{\psi_2^{RXNo}\}$ ) by 6 (2)%. The largest difference is for most central collisions, where the deviation is 25 (12)%. In two particle correlation measurements, both particles are detected within the PHENIX central arms, where the maximum  $\Delta\eta$  separation is  $\Delta\eta = 0.7$ . On the other hand, when using a forward detector to determine the reaction plane and correlated with charged particles in central arm, the  $\eta$  separation is larger than 1. So with smaller  $\eta$  separation, we expect a somewhat higher  $v_2$  value in the two particle correlation case.

### 5.7.2 $v_2$ vs $p_T$

We also compare the centrality dependence of  $v_2$  vs  $p_T$  with previous results [19], using the same centrality bins as in Fig. 3 of Reference [19]. The  $p_T$  range used in the comparison is from 0.5–1.0 GeV/c. We take the ratio between the measurements and values from [19]. The results are plotted in Fig. 5.22. Fig. 5.23 is the same plot as Fig. 5.22, the only difference is the range of the Y axis is adjusted to focus the range between 0.98–1.15. The ratio is very flat with  $p_T$ . The largest deviation is for 0–5% central collisions, which has about a 20–30% higher  $v_2$  than in [19]. For other centralities, the ratios are near 5 to 7%, except at 50–60% centrality, where the difference is about 10%. This shows that at low  $p_T$ , the  $v_2$  from the two particle correlation method is consistent with  $v_2$  from the reaction plane method.

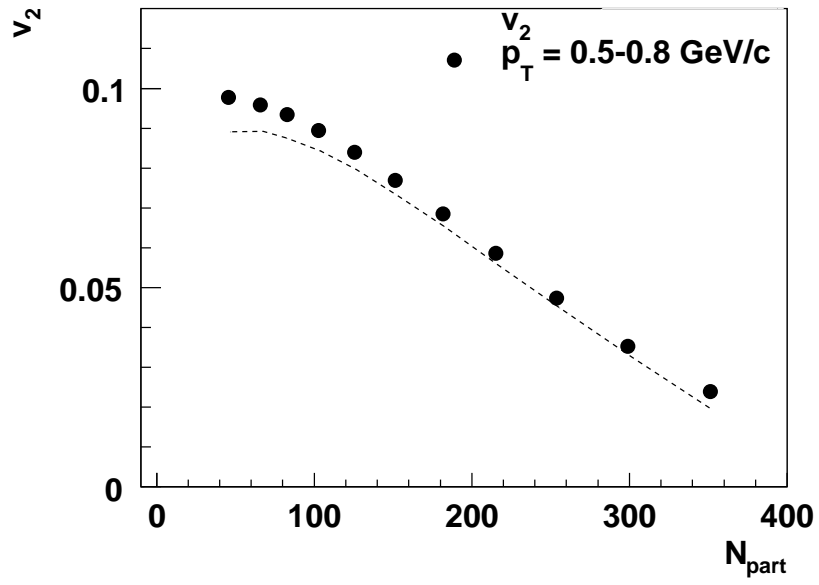


Figure 5.19:  $v_2$  in this analysis (black points) compared with  $v_2$  measured by reaction plane method (dashline) [19]. Inclusive charged hadrons with  $p_T = 0.5-0.8 \text{ GeV}/c$ .

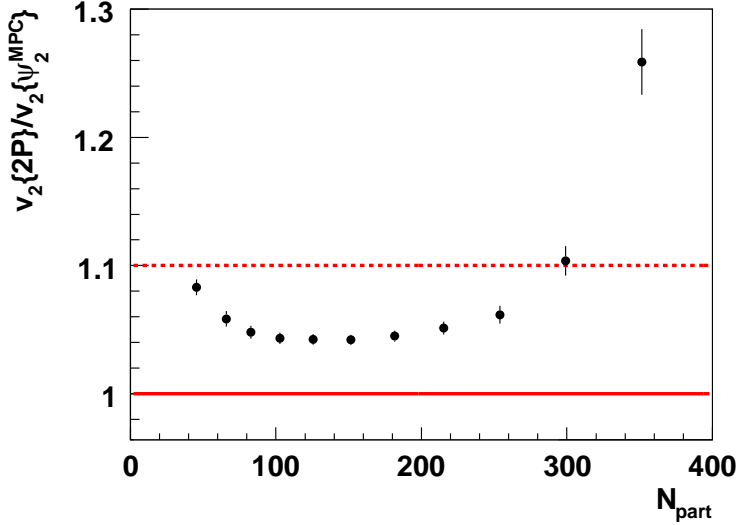


Figure 5.20: Ratio between  $v_2\{2P\}$  value in this analysis and  $v_2\{\psi_2^{\text{MPC}}\}$ , where the second event plane,  $\psi_2$ , is determined by the Muon Piston Calorimeter (MPC) in [19].

### 5.7.3 Systematic Uncertainties of $v_n$

In the previous discussion, we used two particle correlations to measure  $v_n$  where  $n = 1, 2, 3, 4$ . However, there are four different variations. We have two different  $|\Delta\eta|$  cuts (0.3 and 0.5), as well as symmetric and asymmetric  $p_T$  pairs. We use these four measurements to get our  $v_n$  and the corresponding systematic error. The the mean  $v_n$  is the average of the four measurements. The statistical error is the larger of the symmetric and asymmetric pairs, for the  $\Delta\eta$  cut of 0.3. We use this instead of  $\Delta\eta = 0.5$ , because the statistics between the two is almost a factor of 10. The highest and lowest non-zero points are used to determine the systematic error. The final  $v_2$  and  $v_3$  values are plotted in Fig. 5.24 and Fig. 5.25.

### 5.7.4 $v_n\{2P\}$ vs $v_n\{\psi_n\}$

We also compared with the PHENIX published result [68], as shown in Fig. 5.26 and Fig. 5.27.

In general, the measurement is higher than results from [68] but still consistent within the systematic error.



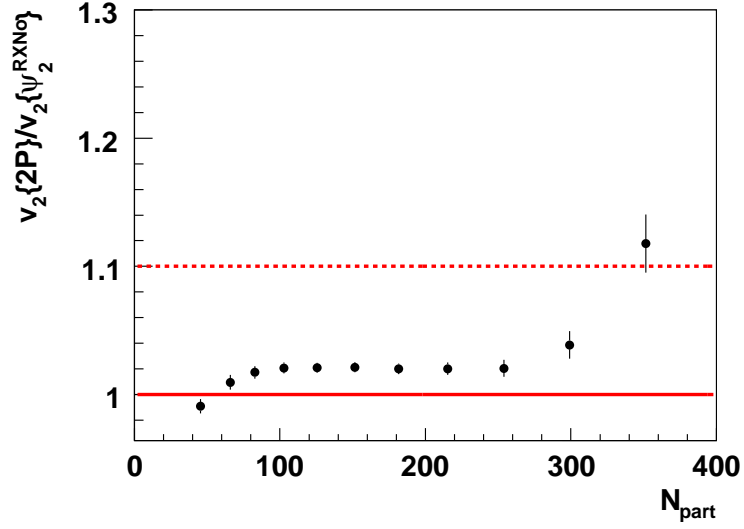


Figure 5.21: Ratio between  $v_2\{2P\}$  value in this analysis and  $v_2\{\psi_2^{RXNo}\}$ , where the second event plane,  $\psi_2$ , is determined by the outer sector of the Reaction Plane Detector (RXNo) in [19].

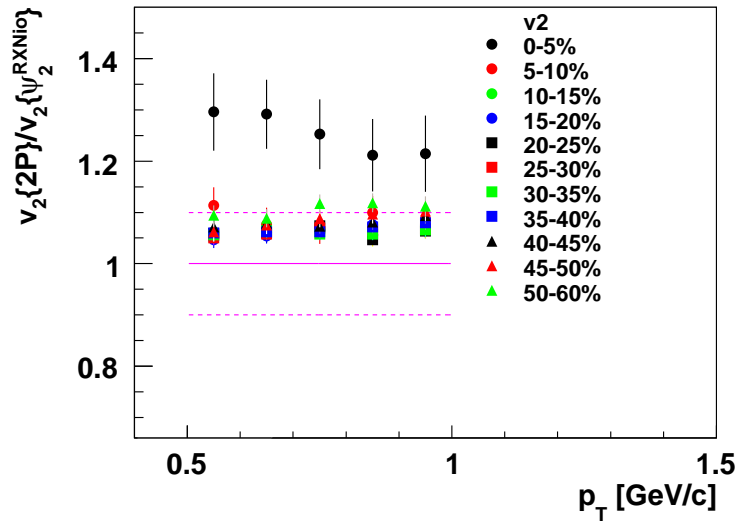


Figure 5.22: Ratio between  $v_2\{2P\}$  value in this analysis and  $v_2\{\psi_2^{RXNo}\}$  in [19] with various centralities.

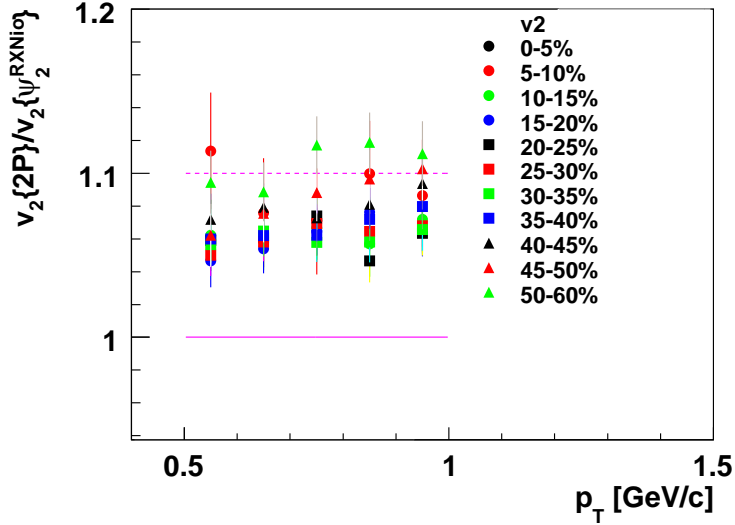


Figure 5.23: Same as Fig. 5.22, only the Y range is changed.

$v_2$  from this analysis,  $v_2\{2P\}$ , with the result from reference [68] as  $v_2\{\psi_2\}$ , which is shown in Fig. 5.26. For points with  $p_T$  from 0.5–1.0 GeV/c in all centralities, the measurements agree within 5%. As  $p_T$  goes up, the two methods begin to deviate significantly by as much as 10% in mid–central collisions and more than 20% at central collisions at 3 GeV/c.

We are not surprised by this result for several reasons. At  $p_T > 1$  GeV/c, the jet contribution starts to increase. In the current analysis, we only have an  $\eta$  cut, which removes particle pairs with  $|\Delta\eta| < 0.3$ . This pair cut removes some of the jet, or ”non–flow” pairs, but there is still a significant contribution from non–flow which is not being removed. Reference [19], showed that when the reaction plane is determined with detectors at smaller  $\eta$ , the  $v_2$  value becomes slightly larger.

Fig. 5.27 compares  $v_3\{2P\}$  values from this analysis with values from [68],  $v_3\{\psi_3\}$ , at  $p_T = 0.5$ –3.0 GeV/c. The two measurement agree within 5%, but deviate to about 20% at high  $p_T$ . We know that at high  $p_T$ , the jet contribution is significant in two particle correlations [23]. Furthermore, jet suppression will increase the third harmonic, since it decreases the correlation strength at  $\Delta\phi = \pi$ .

This comparison demonstrate two things. First, in the low  $p_T$  region,  $p_T = 0.5$ –1.0 GeV/c,  $v_2$  and  $v_3$  measured by the reaction plane method,  $v_n\{\psi_n\}$ , and

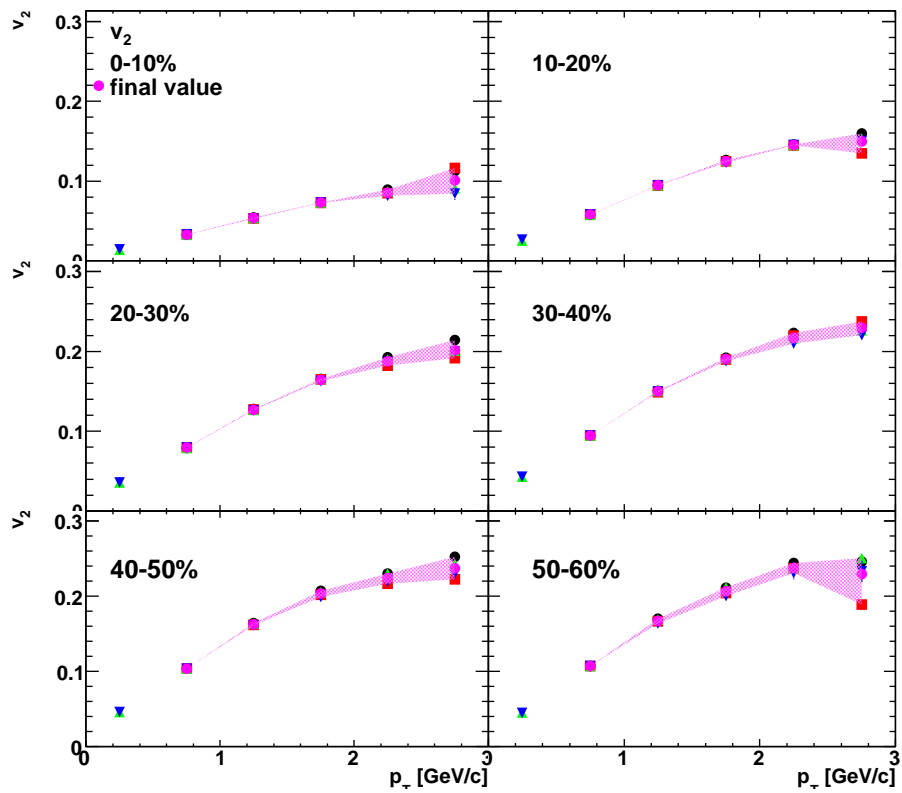


Figure 5.24:  $v_2$  vs  $p_T$ . The final  $v_2$  curve is plotted in pink, along with 4 other methods.

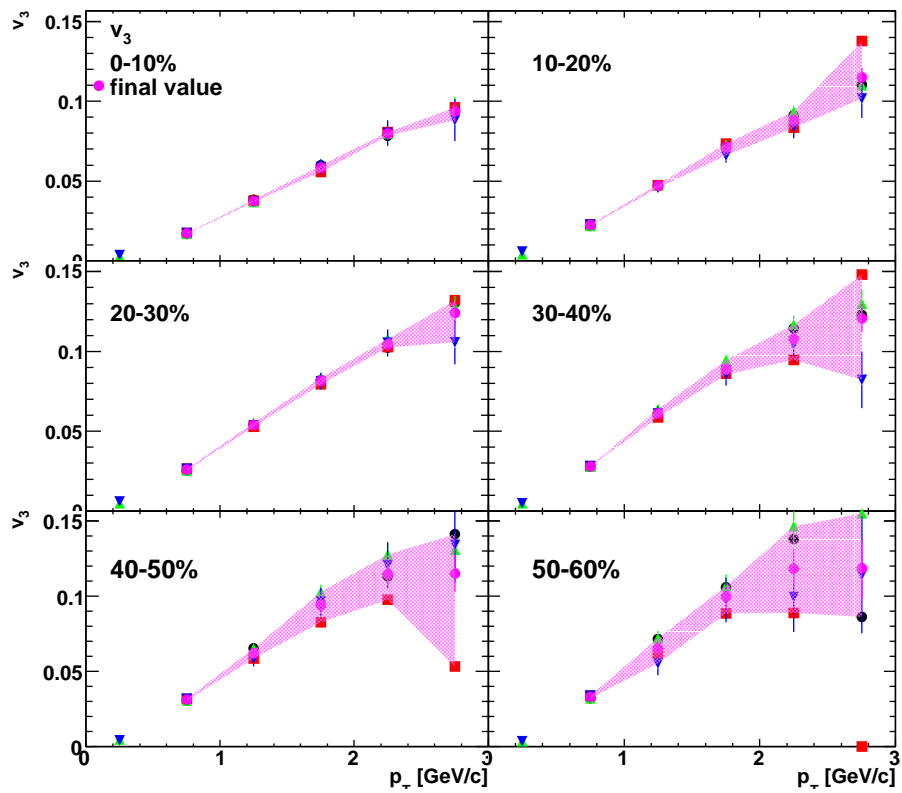


Figure 5.25:  $v_3$  vs  $p_T$ . The final  $v_3$  curve is plotted in pink, along with 4 other methods.

two particle correlation method,  $v_n\{2P\}$ , are consistent in all centralities from 0–10% to 50–60%. Second, at particle  $p_T$  above 1 GeV/c, since jet fragments are not completely removed, larger  $v_n\{2P\}$  values compared to reaction plane methods,  $v_n\{\psi_n\}$ , however the methods still agree within systematic errors. This also indicates the jet contributions at high  $p_T$  needs proper treatment.

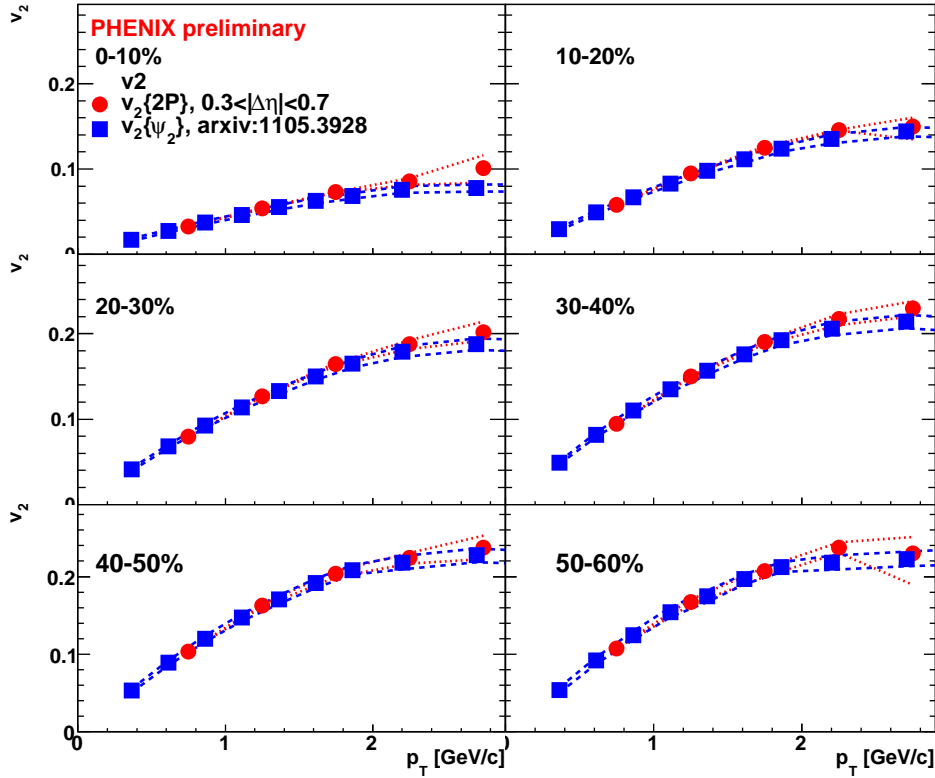


Figure 5.26:  $v_2$  measured by this analysis,  $v_2\{2P\}$  (red) and from reference [68],  $v_2\{\psi_2\}$  (blue) with systematic error.

## 5.8 Glauber Monte Carlo Simulation

In relativistic hydrodynamic models, the elliptic flow comes from the pressure gradient due to geometrical anisotropy or eccentricity,  $\varepsilon_2 = \langle y^2 - x^2 \rangle / \langle y^2 + x^2 \rangle$ . One of the important prediction is  $v_2/\varepsilon_2$ , which takes out the geometrical effect, should be independent on centrality [71]. Previously, PHENIX has shown that there is a  $v_2/\varepsilon_2$  scaling as shown in Fig. 5.28 [18]. When  $v_2/\varepsilon_2$

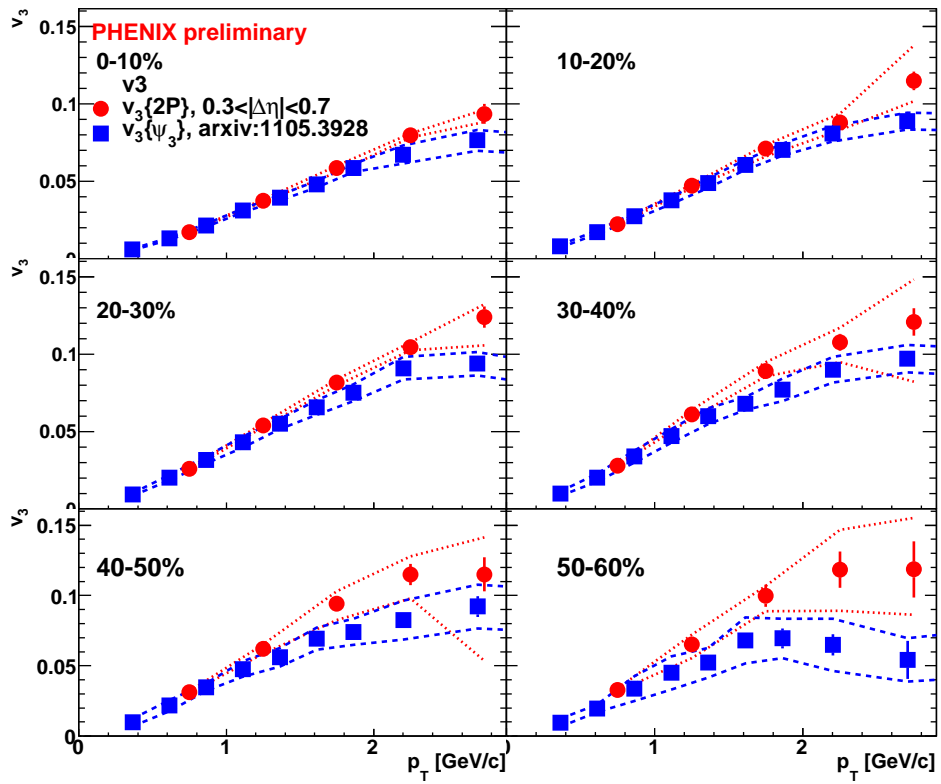


Figure 5.27:  $v_3$  measured by this analysis,  $v_3\{2P\}$  (red) and from reference [68],  $v_3\{\psi_3\}$  (blue) with systematic error.

is plotted as a function of  $p_T$ , all curves are following a universal curve independent of colliding systems and centralities. Along this line, there are several predictions which extend similar trend into  $v_3$  [67, 72]. In order to test the prediction of  $v_n/\varepsilon_n$  scaling, we use Glauber Monte Carlo simulations to calculate the eccentricity ( $\varepsilon_2$ ) or triangularity ( $\varepsilon_3$ ).

### 5.8.1 Eccentricity and Triangularity

There are two kinds of eccentricity. The first kind is the “standard eccentricity”,  $\varepsilon_2^{standard}$ , where the x-axis is along the direction of the impact parameter, and the y-axis goes through the origin, which is defined as the center of the impact parameter.  $\varepsilon_2^{standard}$  is defined as

$$\varepsilon_2 = \frac{\langle y^2 - x^2 \rangle}{\langle y^2 + x^2 \rangle} \quad (5.14)$$

There is another kind of eccentricity, the “participant eccentricity”, where the origin is shifted to the center of the mass makes  $\langle x \rangle = 0$  and  $\langle y \rangle = 0$ . Eq. 5.14 can be written as Eq. 5.15:

$$\varepsilon_2 = \frac{\sqrt{\langle r^2 \cos(2\phi_{part}) \rangle^2 + \langle r^2 \sin(2\phi_{part}) \rangle^2}}{\langle r^2 \rangle} \quad (5.15)$$

where  $r$  and  $\phi_{part}$  are the polar coordinates of the participant nucleons, nucleons involved in the collision, relative to the center of the mass. The short axis of the ellipse,  $\psi_2$  is pointing to the direction

$$\psi_2 = \frac{\tan^{-1}\left(\frac{\langle r^2 \sin(2\phi_{part}) \rangle}{\langle r^2 \cos(2\phi_{part}) \rangle}\right) + \pi}{2} \quad (5.16)$$

Since the pressure gradient is the largest in the direction of short axis, or direction of  $\psi_2$ , the strength of the collective flow should also be the largest in this direction.

In order to test the prediction of the scaling property  $v_3/\varepsilon_3$ , we need to calculate the triangularity,  $\varepsilon_3$ . We adopt the definition of  $\varepsilon_3$  used in [67], which is the natural extension of Eq. 5.15.  $\varepsilon_3$  is defined as

$$\varepsilon_3 = \frac{\sqrt{\langle r^2 \cos(3\phi_{part}) \rangle^2 + \langle r^2 \sin(3\phi_{part}) \rangle^2}}{\langle r^2 \rangle} \quad (5.17)$$

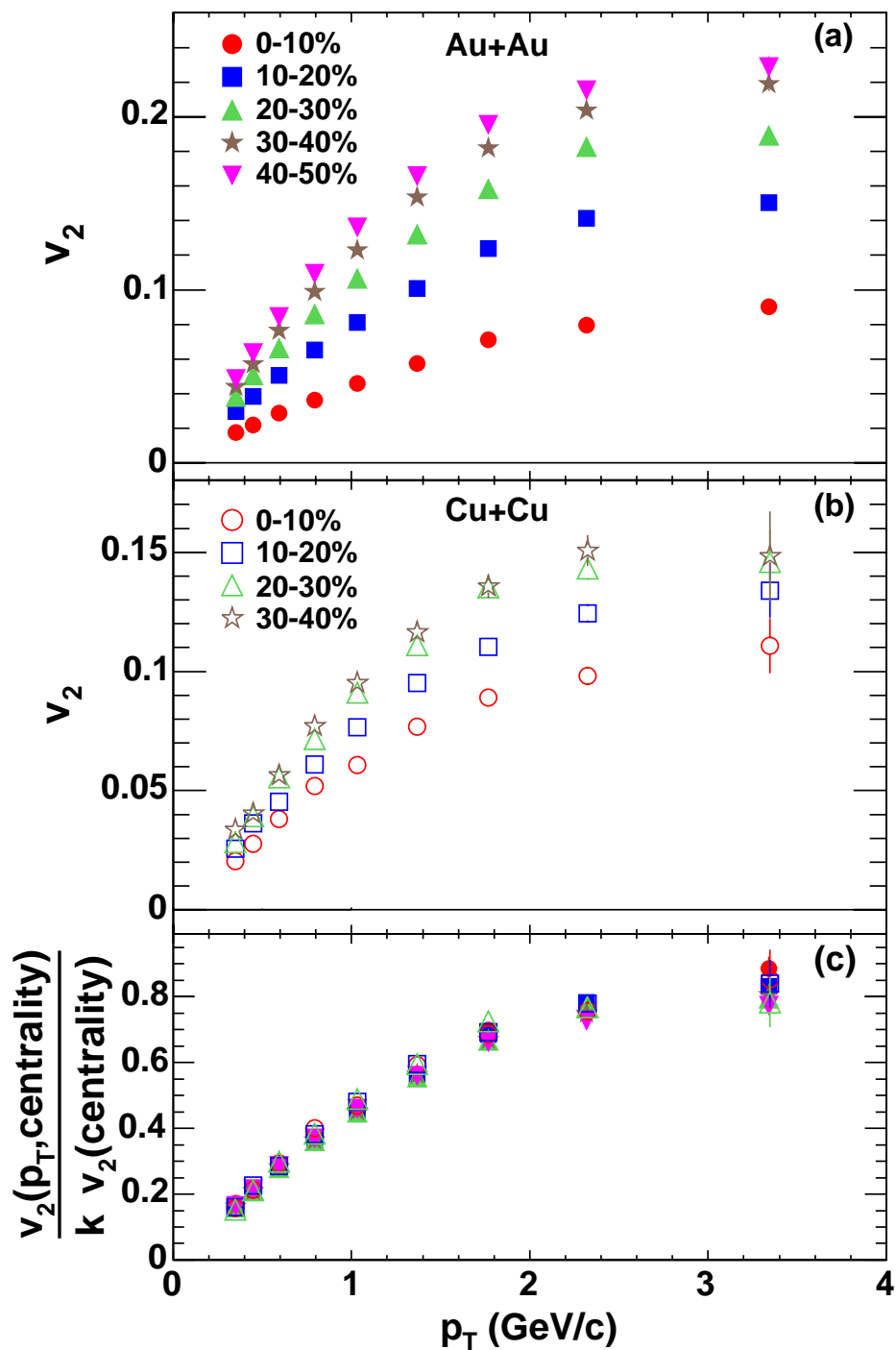


Figure 5.28:  $v_2$  measurement in (a) Au+Au; (b) Cu+Cu; (c)  $v_2$  scaled with  $p_T$  integrated  $v_2$  [18]



We can also define the direction of the event plane for the  $n$ -th moment,  $\psi_n$ . The general equation of  $\psi_n$  is an generalized form of Eq. 5.16, which is defined as Eq. 5.18:

$$\psi_n = \frac{\tan^{-1}\left(\frac{\langle r^2 \sin(n\phi_{part}) \rangle}{\langle r^2 \cos(n\phi_{part}) \rangle}\right) + \pi}{n} \quad (5.18)$$

## 5.8.2 Glauber Monte Carlo Simulation

Glauber model is used to calculate the geometrical related quantities, such as  $\varepsilon_2$ ,  $\varepsilon_3$ ,  $\psi_2$  and  $\psi_3$ . Glauber model assumes the nuclei consists of individual nucleons. Each nucleon is distributed randomly within the radius of the nucleus. This introduces shape fluctuations naturally. In order to estimate the initial collision geometrical parameters, we run Monte Carlo simulations event-by-event and measure these quantities statistically. In this analysis, we use the PHOBOS Glauber Monte Carlo Simulation [73] to measure the eccentricity and triangularity. We simulated 600,000 events. Some key parameters are listed below

- The inelastic nucleon–nucleon cross section at 200 GeV is  $\sigma_{NN} = 42$  mb
- The minimum nucleon separation distance = 0.4 fm
- The nuclear charge density is described by a Woods–Saxon function in the form with three parameters:  $\rho(r) = \rho_0 \frac{1+w(\frac{r}{R})^2}{1+\exp\frac{r-R}{a}}$ , where  $\rho_0$  is the nuclear density,  $R$  is the nuclear radius,  $a$  is the skin depth and  $w$  is the shape deviation from a spherical shape. For Au nuclei,  $R = 6.38$  fm,  $a = 0.535$  fm,  $w = 0$

A typical example of a Au+Au collision in Glauber simulations is shown in Fig. 5.29. The number of participants and number of binary nucleon–nucleon collisions are calculated for each event. The direction of the  $n$ -th event plane  $\psi_n$ ,  $\varepsilon_2$  and  $\varepsilon_3$  are also calculated with Eq. 5.15, Eq. 5.17 and Eq. 5.18. From this example, it is clear to see that the nuclei consists of randomly distributed nucleons. The colliding area is not a perfect almond shape. The direction of  $\psi_2$  is roughly long the direction of the impact parameter.  $\psi_3$  is pointing to a random direction which is because the origin of  $\psi_3$  is due to geometrical fluctuations.

With 600000 events, Fig. 5.30 and Fig. 5.31 are the participant eccentricity  $\varepsilon_2$  and  $\varepsilon_3$  plotted as a function of  $N_{part}$ . In both cases, even though the events

have the same  $N_{part}$ , but because of the event-by-event nucleon distribution fluctuations, we have a distribution of  $\varepsilon_2$  and  $\varepsilon_3$ .

We also calculated the average  $\varepsilon_1$ ,  $\varepsilon_2$  and  $\varepsilon_3$  as function of  $N_{part}$ , shown in Fig. 5.32. We see all three  $\varepsilon_n$  are the smallest at highest  $N_{part}$ . This is because at this situation, the two nuclei collide almost completely, which the collision region is almost like a circular shape. When  $N_{part}$  decreases, all  $\varepsilon$  increases, because the anisotropy of the colliding area becomes larger. We also note the  $\varepsilon_2$  is consistently larger than  $\varepsilon_3$ , because  $\varepsilon_2$  is mostly due to the geometrical shape, but  $\varepsilon_3$  comes from fluctuations.

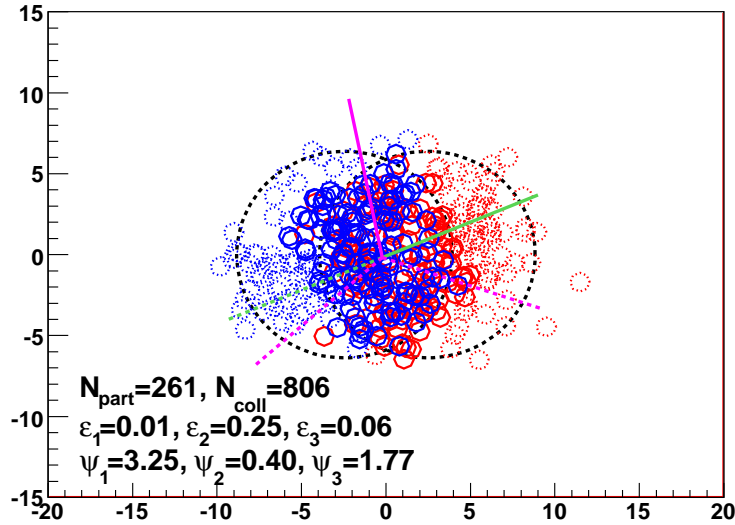


Figure 5.29: An example of collision of two gold nuclei in Glauber model. The solid circles are nucleons participating the collision; the dash circles are spectators which do not participating the collision. The solid green (magenta) line is pointing to the direction of  $\psi_2$  ( $\psi_3$ ). The dashlines are the 2 (3) fold symmetry directions of  $\psi_2$  ( $\psi_3$ ).

### 5.8.3 Calculating Eccentricity from Glauber Simulation

Here we extract average eccentricity in different centralities. Here the centrality is defined by the distribution of number of participants. The most central 5% collisions or 0–5% centrality is defined as top 5% of events which has the largest number of participants. Then we can use this distribution to

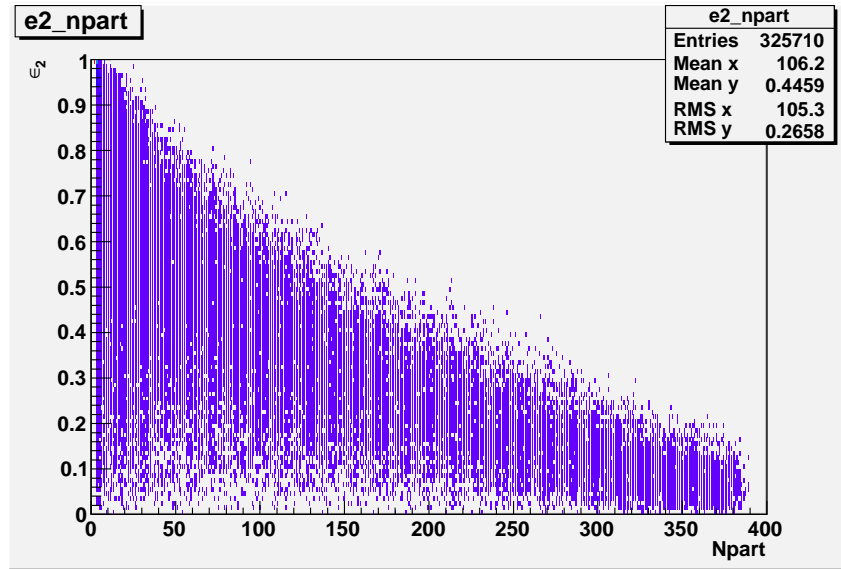


Figure 5.30: Participant eccentricity  $\varepsilon_2$  vs  $N_{part}$

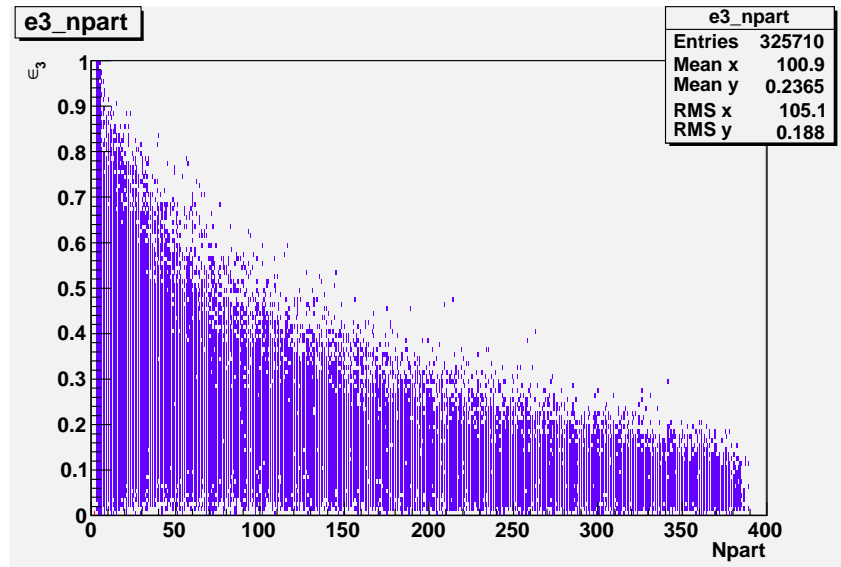


Figure 5.31: Participant eccentricity  $\varepsilon_3$  vs  $N_{part}$

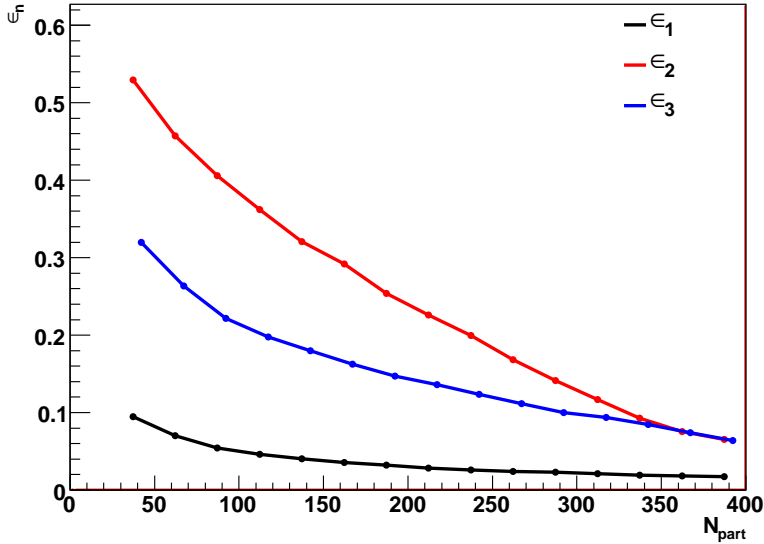


Figure 5.32: Average participant eccentricity  $\epsilon_1$  to  $\epsilon_3$  as function of  $N_{part}$ .

determine the centrality binning. The central value of the eccentricity is the average eccentricity in the centrality bin.

The  $\epsilon_2$  and  $\epsilon_3$  as a function of centrality are calculated from Fig. 5.30 and Fig. 5.31, and are tabulated in Table 5.1 and Table 5.2. Values in Table 5.1 are consistent with internal PHENIX measurements.

#### 5.8.4 Systematic Error of $\epsilon_n$

We estimate the systematic error of  $\epsilon_2$  and  $\epsilon_3$  by varying the following parameters:

- Change the nucleon–nucleon cross section from 42 mb to 39 mb.
- Change the nucleon–nucleon cross section from 42 mb to 45 mb.
- Change the Woods–Saxon function parameters from  $R = 6.38$  fm,  $a = 0.535$  fm to  $R = 6.65$  fm,  $a = 0.55$  fm
- Change the Woods–Saxon function parameters from  $R = 6.38$  fm,  $a = 0.535$  fm to  $R = 6.25$  fm,  $a = 0.53$  fm
- Change the minimum distance between nucleons from 0.40 fm to 0.36 fm

- Change the minimum distance between nucleons from 0.40 fm to 0.44 fm

The comparison of these systematic checks are shown in Fig. 5.33 and Fig. 5.35. The ratio between the systematic checks and the default value shows that the systematic error due to the description of the nuclear geometry of  $\varepsilon_2(\varepsilon_3)$  is about 2–4%(2–6%).

The final systematic error of  $\varepsilon_2(\varepsilon_3)$  for the given centrality is the quadratic sum of all differences compare to the values from default parameters. Systematic errors in both directions are calculated separately, and the larger of the two is used as the final systematic errors. The results are listed in Table 5.1 and Table 5.2.

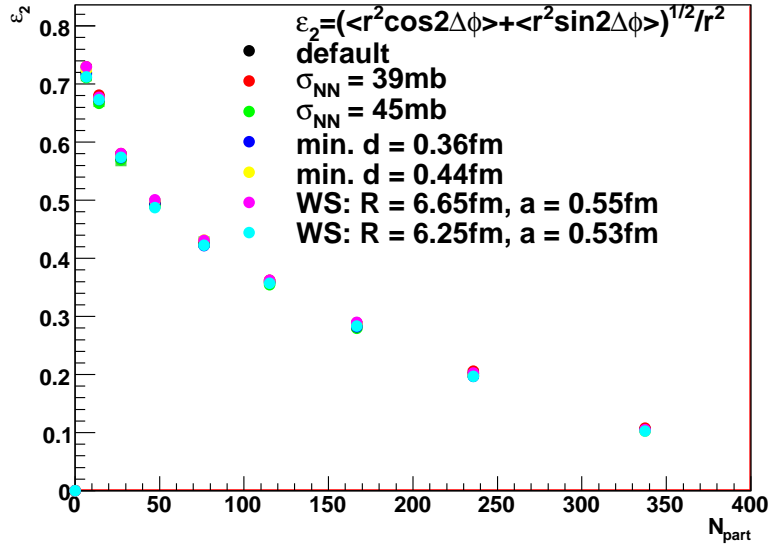


Figure 5.33: Participant eccentricity  $\varepsilon_2$  compared with various systematic checks

## 5.9 Scaling

When assuming there is no shear viscosity, ideal hydrodynamic calculation predicts when  $v_2$  scales with eccentricity, that is  $v_2/\varepsilon_2$  as a function of  $p_T$  is a universal curve, which is independent of centrality and collision species [71]. This relation can be written as

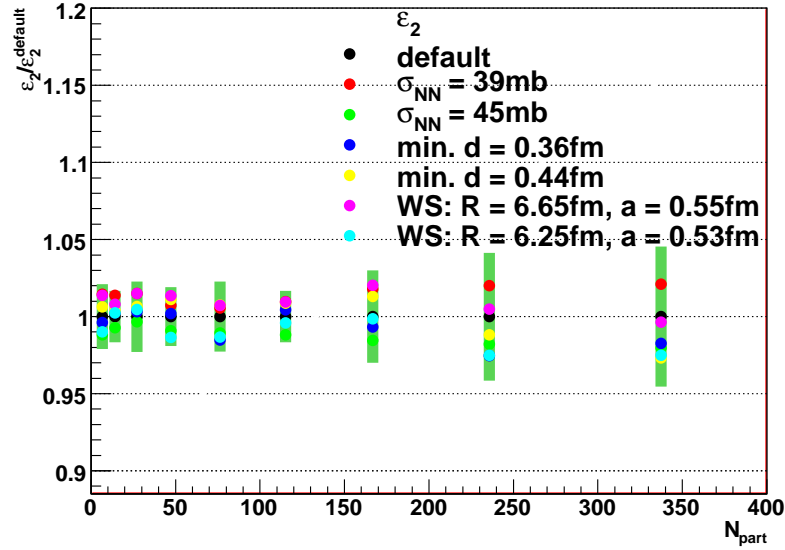


Figure 5.34: Ratios of Participant eccentricity  $\epsilon_2$  compared with various systematic checks. The green band is the final systematic errors

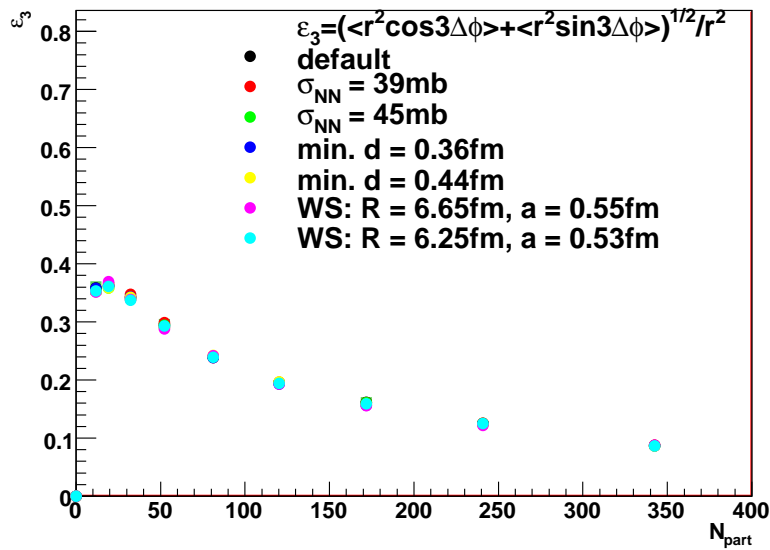


Figure 5.35: Participant eccentricity  $\epsilon_3$  compared with various systematic checks

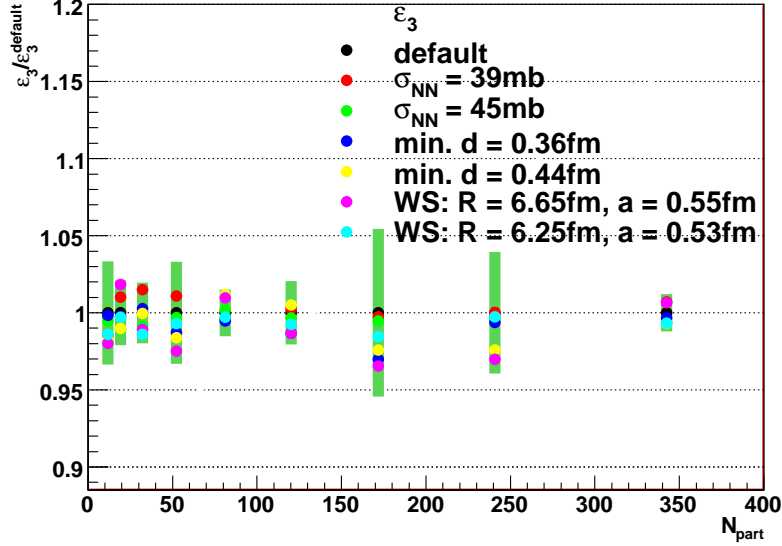


Figure 5.36: Ratios of Participant eccentricity  $\varepsilon_3$  compared with various systematic checks. The green band is the final systematic errors

$$v_2(\text{cent}, p_T) = \varepsilon \times v_2(p_T) \quad (5.19)$$

where  $v_2(\text{cent}, p_T)$  is the centrality and  $p_T$  dependent  $v_2$ , and  $v_2(p_T)$  only depends on  $p_T$ . From Eq. 5.19, if we integrated over  $p_T$ , what remains should be proportional to the eccentricity,  $\varepsilon$ .

This property has been shown in previous PHENIX measurement of  $v_2$  [18]. In [18], eccentricity is not calculated explicitly. In hydro predictions, the eccentricity is proportional to the  $p_T$  integrated  $v_2$  ( $\varepsilon = v_2 \times k$ ). So, reference [18] uses  $p_T$  the integrated  $v_2$  times a factor of  $k = 3.1$  as a proxy for the eccentricity. In reference [18], when  $v_2$  is rescaled by  $\varepsilon$  or  $p_T$  integrated  $v_2$  times a constant factor of  $k = 3.1$ , all  $v_2$  vs  $p_T$  curves follow an universal trend.

In various hydrodynamical calculations [67, 72, 74], the  $v_3$  value should be proportional to the magnitude of the triangularity or the  $\varepsilon_3$ . Therefore a trend similar to  $v_2/\varepsilon_2$  for  $v_3$  has also been shown, which says that  $v_3/\varepsilon_3$  also follows a similar scaling. Or  $v_3(p_T, \text{centrality}) = \varepsilon_3 \times v_3(p_T)$ .

Following the methods described in [18], we test the  $v_2/(\text{int. } v_2)$  scaling and extend the study to  $v_3/(\text{int } v_3)$ . We also use the  $\varepsilon_2$  and  $\varepsilon_3$  value from the Glauber Monte Carlo described in the previous section to search for the existence of scaling. In this scaling analysis, we use the  $v_n$  values from

Table 5.1:  $\varepsilon_2$  measured via Glauber Monte Carlo simulations in different centralities.

centrality	$\varepsilon_2$	variance	sys. error
0–10%	0.105499	0.0582523	0.0048
10–20%	0.20173	0.0855551	0.0084
20–30%	0.283996	0.106145	0.0085
30–40%	0.358557	0.131047	0.0060
40–50%	0.428096	0.15094	0.0098
50–60%	0.494127	0.172629	0.0094
60–70%	0.571483	0.199686	0.013
70–80%	0.671808	0.207904	0.011
80–90%	0.719405	0.221362	0.015

Table 5.2:  $\varepsilon_3$  measured via Glauber Monte Carlo simulations in different centralities.

centrality	$\varepsilon_3$	variance	sys. error
0–10%	0.0870931	0.047212	0.0010
10–20%	0.125344	0.0659116	0.0049
20–30%	0.161643	0.0837192	0.0088
30–40%	0.195772	0.101686	0.0040
40–50%	0.239647	0.12418	0.0036
50–60%	0.295354	0.14581	0.0098
60–70%	0.342285	0.169247	0.0067
70–80%	0.362377	0.183709	0.0077
80–90%	0.358197	0.215002	0.012

Chapter 5.7.3.

### 5.9.1 Scaling with $p_T$ Integrated $v_n$

The  $p_T$  integrated  $v_n$  is calculated by Eq. 5.20:

$$int.v_n = \frac{\int v_n(p_T) \frac{dN}{dp_T} dp_T}{\int \frac{dN}{dp_T} dp_T} \quad (5.20)$$

$v_2$  and  $v_3$  is summed over 0.5–3.0 GeV/c. The spectra for inclusive charged hadrons,  $dN/dp_T$ , are obtained from the published charged hadron spectra measured by PHENIX [56]. The integrated  $v_2$  ( $v_3$ ) are listed in Table 5.3 and Table 5.4.



Fig. 5.37 shows  $v_2$  as function of  $p_T$  in different centralities as measured in this analysis. The dash lines are  $v_2$  measurements from PHENIX ???. The agreement between the two measurement are good. We rescale the  $v_2$  by the  $p_T$  integrated  $v_2$ , which is tabulated in Table 5.3. The result is shown in Fig. 5.38, clearly that all six centrality bins, from 0–10% to 50–60%, follow a universal trend. The universality is also visible in Fig. 5.39, where the scaled  $v_2$  is plotted vs  $N_{part}$ . The flatness of the curves show the consistency of the scaled  $v_2$ . This suggest the system is locally thermalized rapidly.

Similar properties are also found in  $v_3$ . Fig. 5.40 is  $v_3$  vs  $p_T$  in six centrality bins. After scaled with  $p_T$  integrated  $v_3$ , as shown in Fig. 5.41, all  $v_3/(p_T$  integrated  $v_3)$  curves again lined up together as the  $v_2$  case shown in Fig. 5.38. Same trend is also seen when scaled  $v_3$  is plotted vs  $N_{part}$  as plotted in Fig. 5.42.

This analysis shows that if we assume  $v_2(cent, p_T)$  ( $v_3(cent, p_T)$ ) all follows a universal curve,  $v_2(p_T)$  ( $v_3(p_T)$ ), which is modulate by the centrality dependent eccentricity (triangularity).

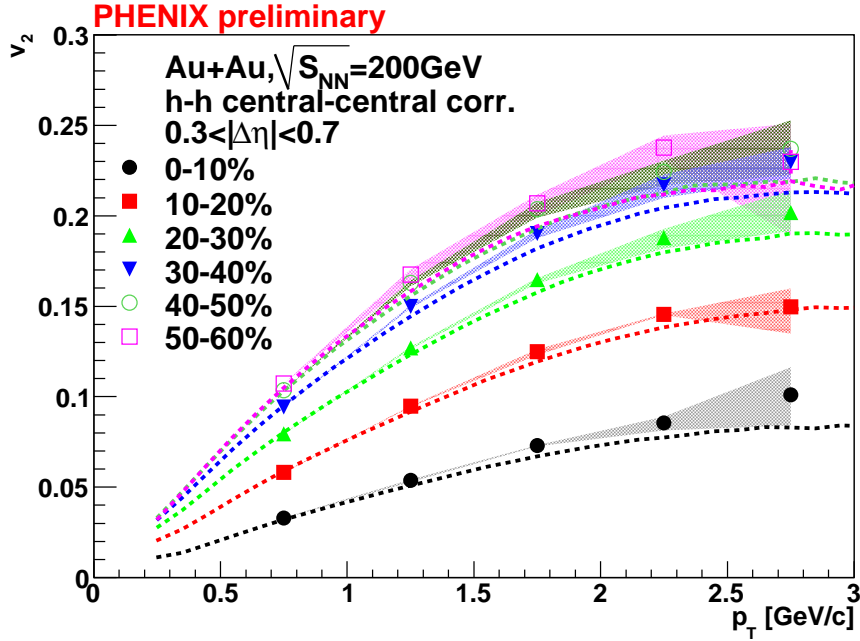


Figure 5.37:  $v_2$  of various centralities as a function of  $p_T$ . Dash lines are PPG098 measurement.

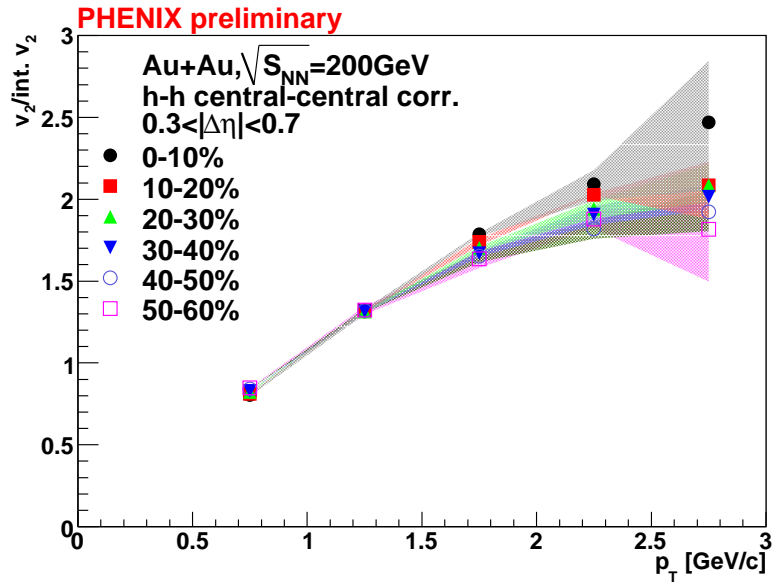


Figure 5.38:  $v_2/(p_T \text{ integrated } v_2)$  vs  $p_T$  in various centralities

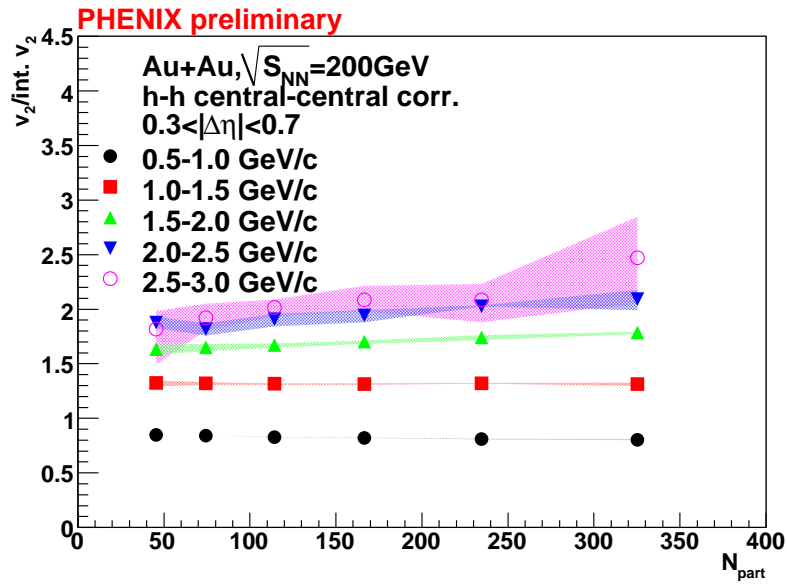


Figure 5.39:  $v_2/(p_T \text{ integrated } v_2)$  vs  $N_{part}$  in various  $p_T$  bins.

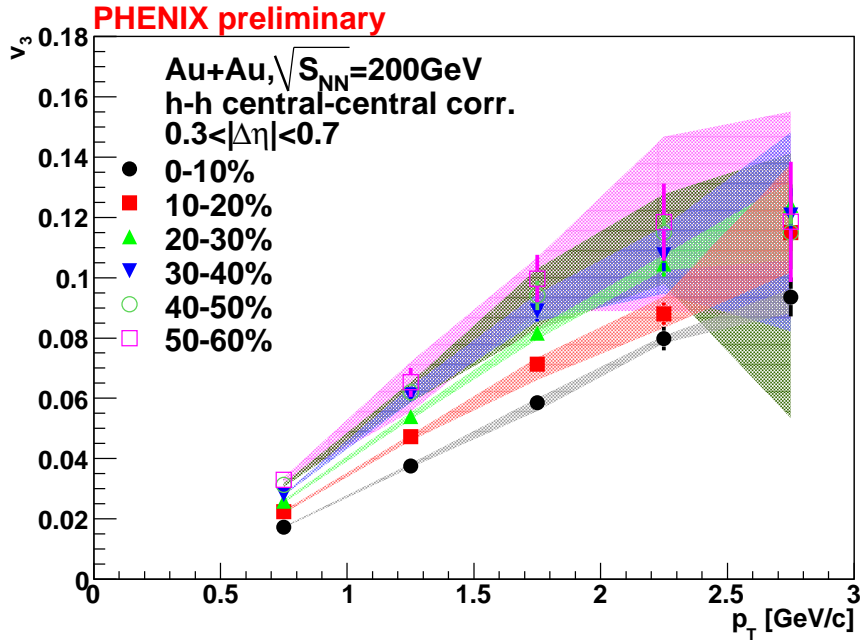


Figure 5.40:  $v_3$  of various centralities as a function of  $p_T$ .

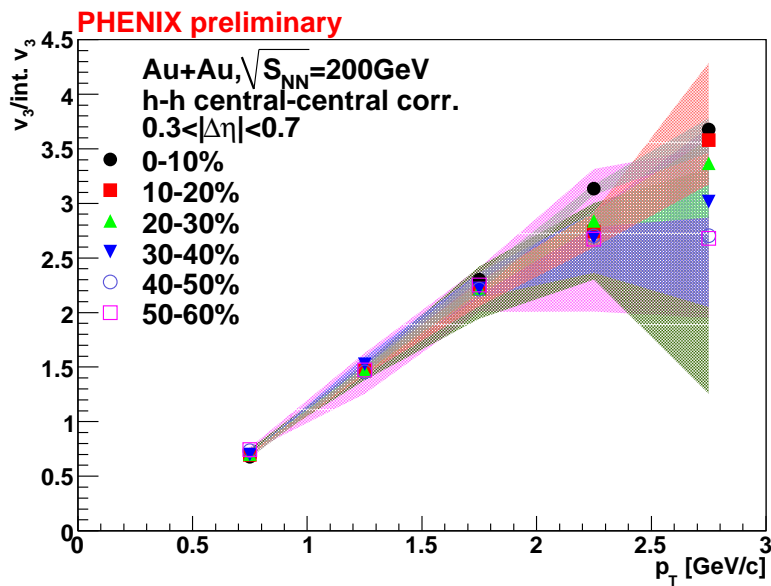


Figure 5.41:  $v_3/(p_T \text{ integrated } v_3)$  vs  $p_T$  in various centralities

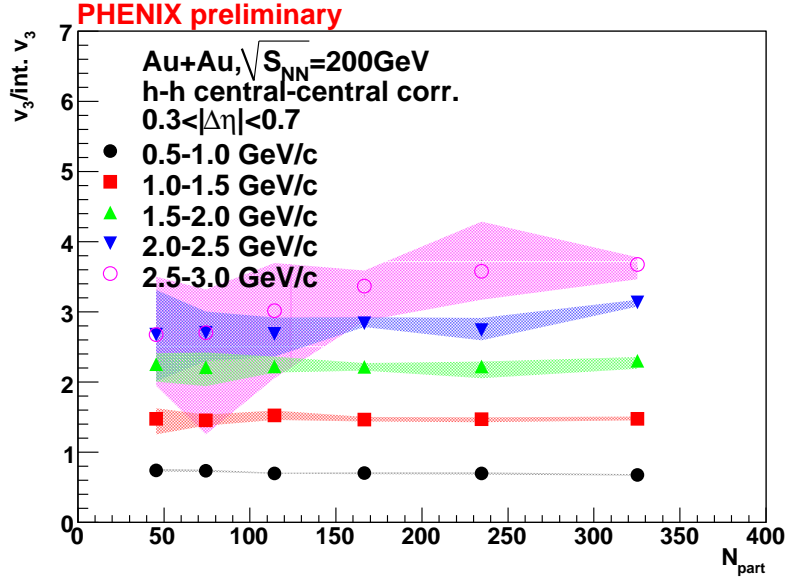


Figure 5.42:  $v_3/(p_T \text{ integrated } v_3)$  vs  $N_{part}$  in various  $p_T$  bins.

### 5.9.2 Scaling with Glauber $\varepsilon_2$ and $\varepsilon_3$

We use the  $\varepsilon_2$  and  $\varepsilon_3$  measured by Glauber Monte Carlo simulations listed in Table 5.1 and Table 5.2 as an alternative way to study scaling by plotting  $v_n/\varepsilon_n$ . The results are shown in Fig. 5.43, Fig. 5.44 ( $v_2$ ), and Fig. 5.45, Fig. 5.46 ( $v_3$ ).

$v_2/\varepsilon_2$  as a function of  $N_{part}$  is plotted in Fig. 5.44. Scaling would be indicated by a flat distribution of  $v_2/\varepsilon_2$ . The scaling holds approximately at low  $p_T$  when  $N_{part}$  is larger than 100, but not for the most central collisions

Table 5.3:  $p_T$  integrated  $v_2$  values (0.5–3.0 GeV/c) from two particle correlation method in this analysis.

centrality	int. $v_2$	stat err
0–10%	0.0409	0.0003
10–20%	0.0717	0.0002
20–30%	0.0967	0.0002
30–40%	0.1139	0.0002
40–50%	0.1233	0.0003
50–60%	0.1265	0.0005

Table 5.4:  $p_T$  integrated  $v_3$  values (0.5–3.0 GeV/c) from two particle correlation method in this analysis.

centrality	int. $v_3$	stat err
0–10%	0.0255	0.0005
10–20%	0.0321	0.0005
20–30%	0.0368	0.0006
30–40%	0.0401	0.0010
40–50%	0.0425	0.002
50–60%	0.0443	0.002

(0–10% or  $N_{part} \approx 330$ ). When  $p_T$  increases, this scaling does seem to work. The scaled  $v_2$  also increases with  $N_{part}$ . This is not exactly the same as we see in [18] or Fig. 5.38. But a similar trend has been seen by [75], where the scaling holds between  $N_{part} = 100$  and 300.

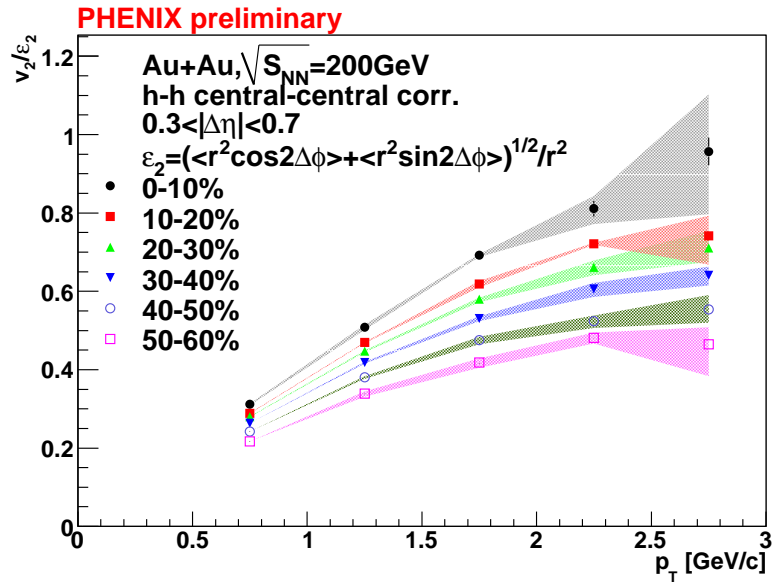


Figure 5.43:  $v_2/\epsilon_2$  vs  $p_T$  in various centralities.

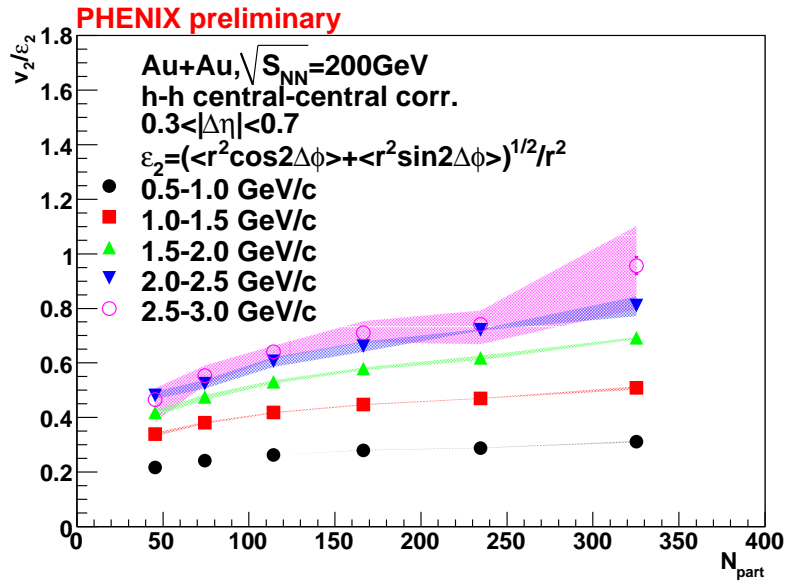


Figure 5.44:  $v_2/\varepsilon_2$  vs  $N_{part}$  in different  $p_T$  bins.

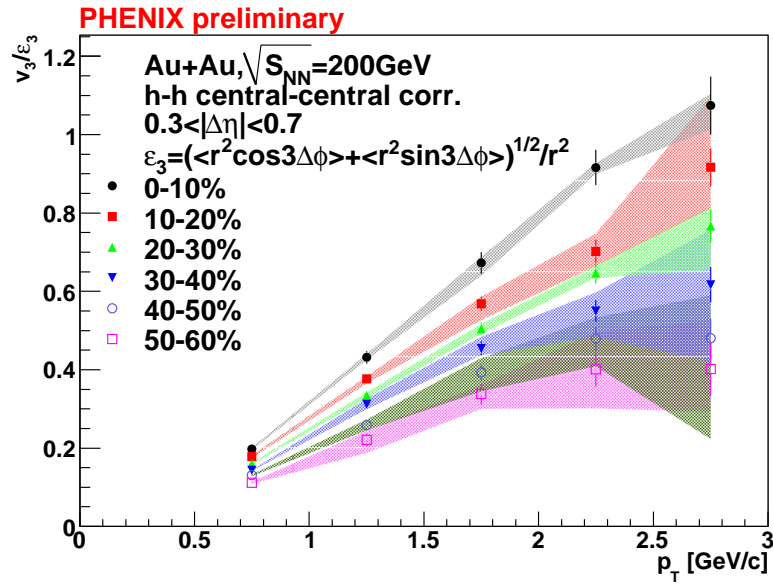


Figure 5.45:  $v_3/\varepsilon_3$  vs  $p_T$  in various centralities.

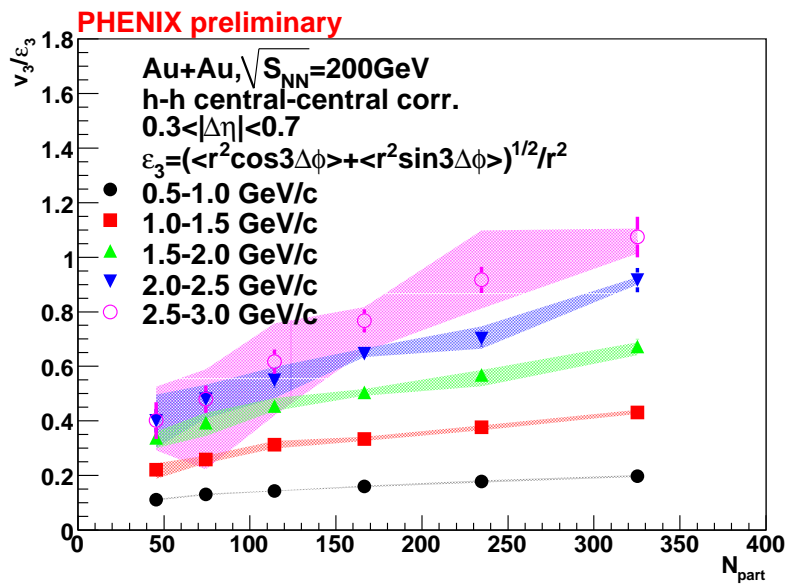


Figure 5.46:  $v_3/\varepsilon_3$  vs  $N_{part}$  in different  $p_T$  bins.



## Chapter 6

# Fourier Spectra and Jet Quenching

### 6.1 Introduction

The exotic structures of the ridge and shoulder are discussed in detail in previous chapters, and several theories have been proposed to explain these phenomena. One explanation is that these two structures have nothing to do with jets, and are due to the presence of the third harmonic of collective flow,  $v_3$  [67]. This  $v_3$  proposal has a natural appeal, since it provides three separate peaks, and the peak location ( $\Delta\phi = 0, 2\pi/3$  and  $4\pi/3$  roughly correspond to the locations of the ridge ( $\Delta\phi = 0$ ) and shoulder ( $\Delta\phi \approx \pi \pm 1$ ). Furthermore, this explains the similarity of the  $p_T$  spectra of the the ridge and shoulder and the bulk. The question then is whether evidence for jet modification remains.

In this chapter, we use an approach which is different from the fitting decomposition described in the previous chapter. We take the higher order harmonics  $v_3$  and  $v_4$  measured by PHENIX [68] and include those in the background subtraction, to have a better description of the shape of the background. Since those  $v_n$  are Fourier coefficients of the underlying background, we can further use the Fourier series of the correlation function to study the jet modification and gain more insight.

To study what, if any, evidence remains of jet modification, we now modulate the uncorrelated background with higher harmonics beyond  $v_2$ . After subtracting this background, we study the jet function by Fourier analysis. In the resulting Fourier spectra, all jet structures will be mixed together. There is no way to separate the near and away side jets, ridge and shoulder using the Fourier power spectra, so we compare to the power spectrum by Fourier analysis of p+p collisions. In central Au+Au collisions, the situation is further complicated by away-side jet quenching.

In order to understand the Fourier spectra in Au+Au, we make the following assumption. The correlation function in Au+Au can be separated into

two parts: p+p-like jet structures and possible jet-medium interactions.

From both PHENIX [24] and STAR [58], we know that the near-side jet is consistent with the nearside jet in p+p, with very little modification. We also know that the away-side jet is suppressed in Au+Au. But the problem is that we don't really know the level of suppression of the away-side jet. To describe the p+p like jet in Au+Au, we consider two extreme case scenarios. The first is that the p+p like jet is unmodified in Au+Au. This can be represented by the p+p jet correlation function, where there is no medium modification at all. The second is that the away-side jet is fully quenched in the medium. To mimic this situation, we set all points on the away side of the p+p jet function to zero. This can be regarded as equivalent to fully quenching the away side jet in Au+Au with no other structures present.

The true away-side jet in Au+Au should be in between these two cases. When the Fourier spectra of the Au+Au correlation function is measured, the spectra are compared with these two baselines. Any Fourier coefficients beyond the description of these two cases must come from sources more complicated than unmodified or fully absent jets.

## 6.2 Measuring the Fourier Coefficients of the Correlation Function

### 6.2.1 Fourier Coefficients and Correlation Function

We transform the efficiency corrected jet functions from this analysis to determine the Fourier spectra. We use the  $\Delta\eta$  range from 0–0.7, which is the full  $\Delta\eta$  acceptance of the PHENIX. The reason for using this  $\Delta\eta$  range, instead of 0.5–0.7 is that this range includes the full near side jet, which is important for studying jet physics.

First, we analyze the jet function obtained by subtracting out the underlying events modulated only by  $v_2$ . The resulting jet function is expanded in a Fourier series by the following:

$$J(\Delta\phi) = \sum C_n \cos(n\Delta\phi) \tag{6.1}$$

The Fourier coefficients are measured from the zeroth term up to the ninth term ( $C_0$  to  $C_9$  in Eq. 6.1). Fig. 6.1 and Fig. 6.2 compare the correlation functions with the Fourier expansion results in various centralities. The 10 terms of Fourier expansion describe the data very well.

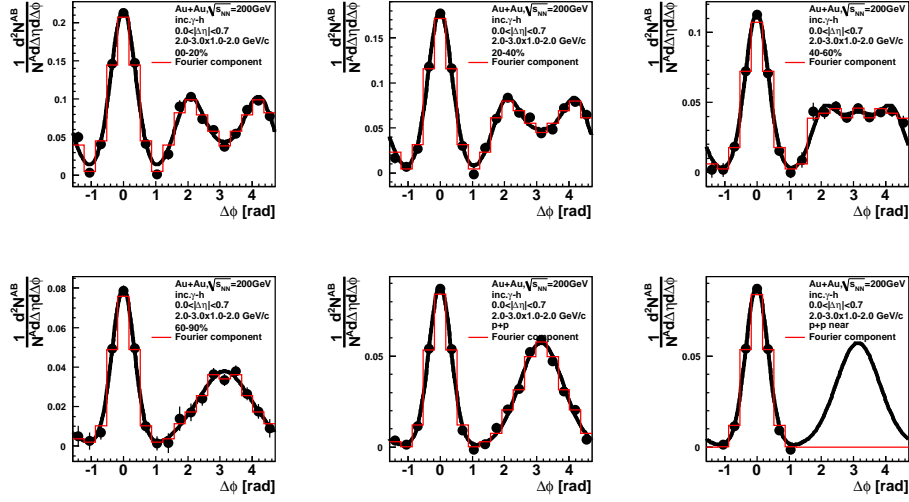


Figure 6.1: Per trigger yield jet function of various centralities (black) are compared with Fourier expansion results (red). Trigger  $p_T = 2.0\text{--}3.0$  GeV/ $c$  and partner  $p_T = 1.0\text{--}2.0$  GeV/ $c$

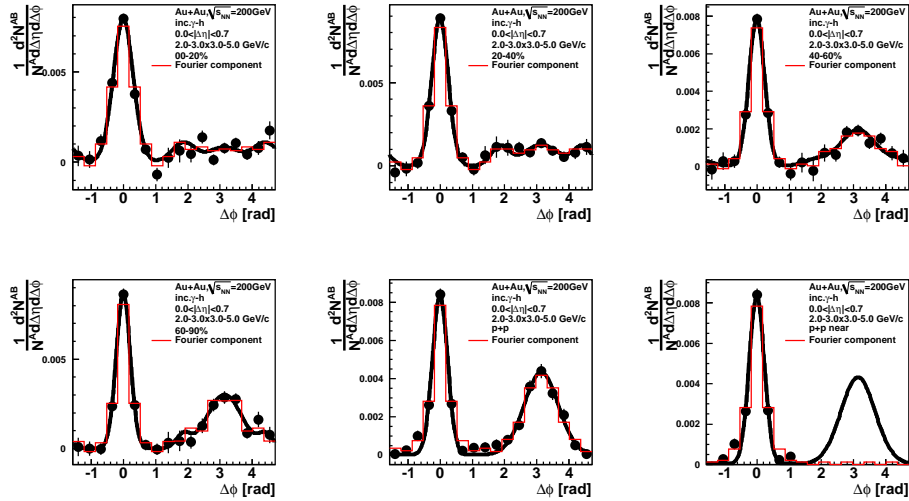


Figure 6.2: Per trigger yield jet function of various centralities (black) are compared with Fourier expansion results (red). Trigger  $p_T = 2.0\text{--}3.0$  GeV/ $c$  and partner  $p_T = 3.0\text{--}5.0$  GeV/ $c$

## 6.2.2 Fourier Spectra of the Jet Function

Fig. 6.3 show the Fourier coefficients of jet function in various centralities extracted from Fig. 6.1. The solid line in the figure is the Fourier spectrum of pp jets. The green dashed line represents the case will fully quenching the awayside of pp-like jets. In this case, we observed that for the even terms ( $C_0$ ,  $C_2$ ,  $C_4$ ), the full pp jet has larger coefficients than the fully quenched awayside pp-jet, since these even terms have peaks at  $\Delta\phi = \pi$ . On the other hand, the odd terms ( $C_1$ ,  $C_3$ ) in the full pp jet are smaller than the fully quenched awayside pp-jet, as these odd terms are negative at  $\Delta\phi = \pi$ . So jet quenching itself will increase the value of odd harmonic components.

Next, we look at the centrality dependence. For the Fourier coefficients larger than  $C_5$ , the values are very small in all centralities, indicating lesser importance of the higher harmonics.

The zeroth coefficient,  $C_0$ , is equivalent to the total yield integrated over  $2\pi$ . At low associated particle  $p_T$ , where most central Au+Au collisions have higher yield than pp. Consquently,  $C_0$  from Au+Au should exceed that for p+p. This can be seen clearly in Fig. 6.1. When moving from central to peripheral collisions, the total yield drops and approaches to the pp value.

The  $C_1$  value of the most central collisions is closer to the fully quenched jet. With increasing centralities,  $C_1$  is approaching the full p+p jet. This is consistent with the general picture that the more central the collision is, the more the jet is quenched.

In  $C_2$ , since we use ZYAM to remove most of the combinatorial background in Au+Au, what is left in the jet function should contain a significant portion of the jet.  $C_2$  is very similar to  $C_2$  observed in p+p collisions.

The third harmonic,  $C_3$ , shows strong enhancement in central collisions. The coefficients decrease with increasing centrality. It should be noted that, as described above, fully quenched away side jets cause the magnitude of the  $C_3$  to increase comparing to unmodified p+p jets.  $C_3$  in central collisions is much larger than the expectation from jet quenching, which means that there must be some other process causing an enhancement. A similar enhancement is observed in the fourth harmonic,  $C_4$ , but is less significant compared to  $C_3$ .

In Fig. 6.4, where associated particle  $p_T = 3 - 5$  GeV/c, the situation is a little bit different. The  $C_0$  term here is between that for full pp jets and awayside quenched pp jets. We know there is a strong jet quenching in this associated particle  $p_T$  region. (See Fig. 6.2). For this region, the structures from the medium effects such as ridge and shoulder are not strong, and the distribution is mostly dominated by jet quenching. Nevertheless, we still see some enhancement of  $C_3$  in the 0–20% and 20–40% centrality bins.

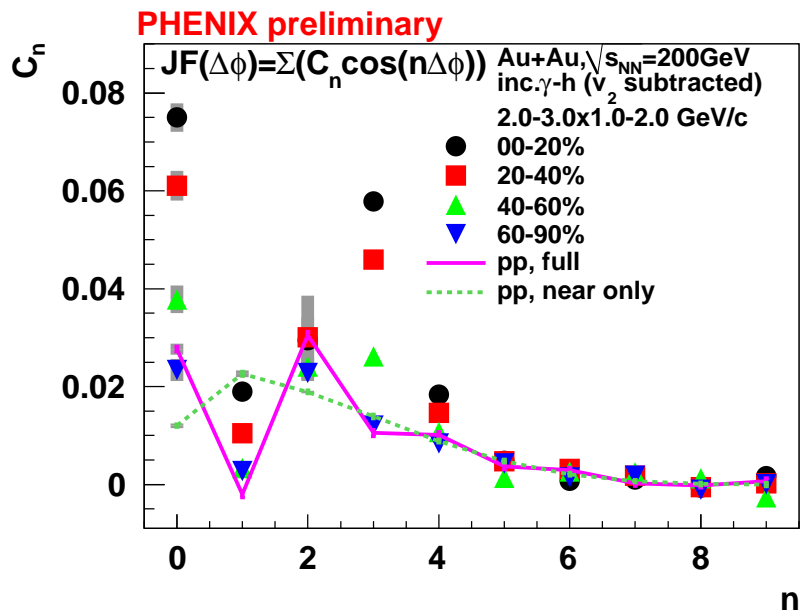


Figure 6.3: Fourier spectra for various centrality in Au+Au collisions. Trigger  $p_T = 2.0\text{--}3.0 \text{ GeV}/c$  and partner  $p_T = 1.0\text{--}2.0 \text{ GeV}/c$ , with  $v_2$  modulated background shape subtracted.

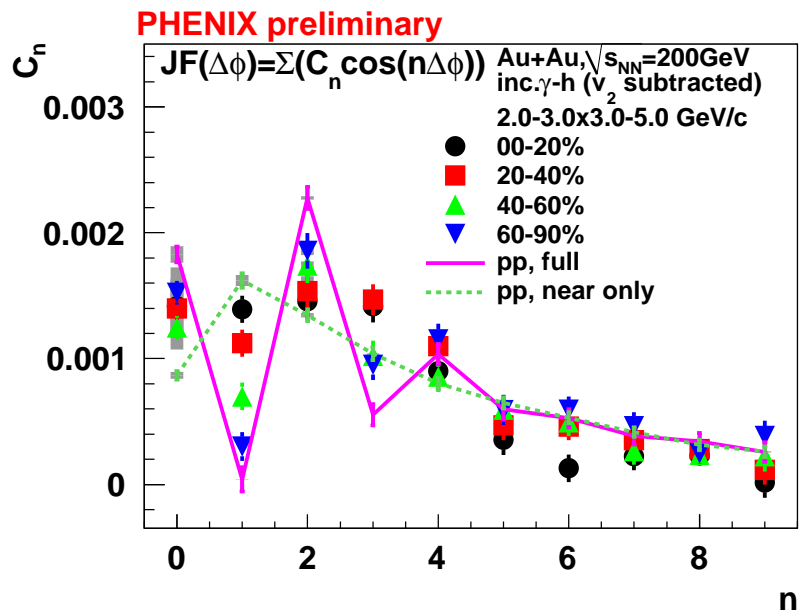


Figure 6.4: Fourier spectra for various centrality in Au+Au collisions. Trigger  $p_T = 2.0-3.0 \text{ GeV}/c$  and partner  $p_T = 3.0-5.0 \text{ GeV}/c$ , with  $v_2$  modulated background shape subtracted.

## 6.3 Background Subtraction with Modulations from Higher Harmonics

From the previous chapter, we learned that there are higher harmonic components of collective flow. PHENIX has measured  $v_n$  with respect to  $\psi_n$  for low  $p_T$  particles arising from the flowing bulk, which forms the underlying event for this analysis [68]. Those  $v_n$  values are now used to better describe the background shape in two particle correlations. The reason to use  $v_n$  values from [68] instead of  $v_n$  from two particle correlation methods is to avoid the non-flow contribution in  $v_n$  when both particles are measured at mid-rapidity.

To demonstrate the effect of higher harmonics in the underlying event, we take the following steps. First we rescale the correlation function (without background subtraction) so the y-axis is the per trigger yield. Then we subtract out the flow background with the shape described by Eq. 6.2. The background level,  $b_0$ , is determined by absolute normalization (ABS) [76]. The absolute normalization method assumes the level of the uncorrelated underlying event pairs is proportional to the particle production rate of the trigger and associated particles with a centrality dependent factor. Unlike ZYAM, ABS determines the background level independent from the shape of the background, which is important since we only change the shape, but not the level of the background. We add  $v_n$  one by one to Eq. 6.2, to see how each term changes the shape of the subtracted correlation function. The correlation function is then compared with the jet function in p+p, which represents the unmodified jet-function. The last step is to measure the Fourier spectrum of the subtracted Au+Au jet function, and compare to the Fourier spectra of the two p+p baselines (unmodified and away-side fully quenched), thus allowing us to quantify how the jet function is modified.

The full underlying event background shape is defined as

$$FL(\Delta\phi) = b_0(1 + 2c_2 \cos(2\Delta\phi) + 2c_3 \cos(3\Delta\phi) + 2c_4 \cos(4\Delta\phi)) \quad (6.2)$$

where

$$c_n = v_n^{trig}(\psi_n)v_n^{part}(\psi_n) \quad (6.3)$$

The details of how Eq. 6.2 is obtained are described in Appendix A. The  $v_n$  used here are from [68], as shown in Fig. 6.5. For this analysis, the trigger particle is inclusive photons with  $p_T$  at 2–3 GeV/c, which is mainly the  $\pi^0$  decay photon. The parent  $\pi^0$  mean  $p_T$  is about 2.6 GeV/c, so as a proxy, we use the inclusive charged hadron at 2.5–3.0 GeV/c as a proxy for the inclusive photon  $v_3$  and  $v_4$ .

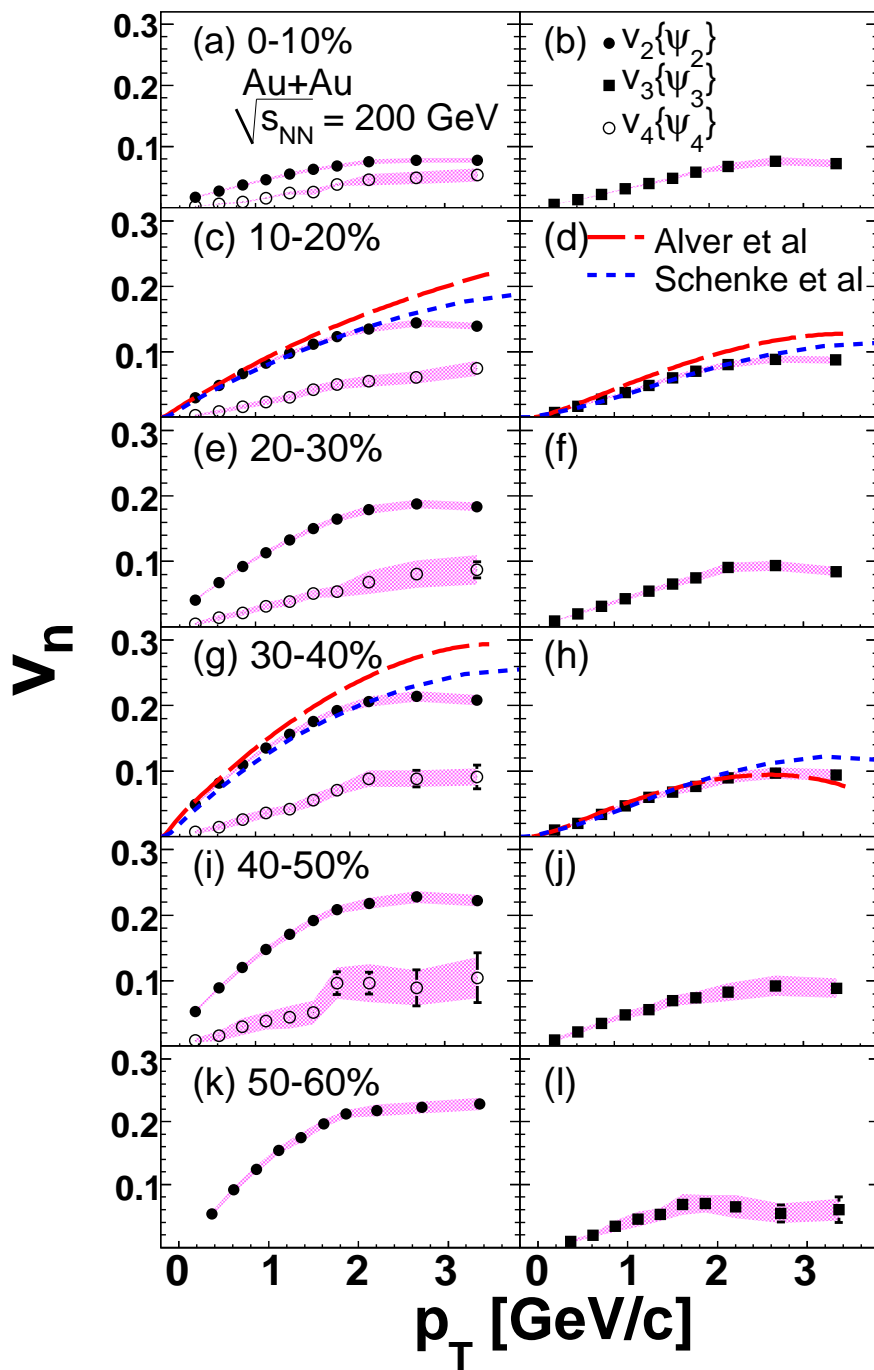


Figure 6.5: Measurements of  $v_2$ ,  $v_3$ ,  $v_4$  with respect to  $\psi_n$  from [68].



We use Fig. 6.6 as an example of the result of the background subtraction. Inclusive photon triggers at 2–3 GeV/c are associated with inclusive charged hadron at 1–2 GeV/c. The centrality is 0–20%. The left column includes  $v_2$  modulation of the background shape; the middle column is modulated by  $v_2$  and  $v_3$ , and right column is  $v_2$ ,  $v_3$  and  $v_4$ . Adding in background  $v_n$  one by one shows the effect of each  $v_n$ .

The left column uses the standard  $v_2$  modulated background only. The first row shows the per trigger yield Au+Au correlation function, with the blue curve representing the underlying event background to be subtracted. Using Eq. 6.5, the jet function is calculated and plotted in the second row as black points. The red points are the p+p correlation function as a reference. With  $v_2$  modulated background subtraction, the double peak structure is clearly seen. The third row shows the Fourier spectra of the Au+Au jet function (plotted in black points) and compared with the two different p+p cases. The solid red line represents the unmodified p+p and red dashed line represents p+p with away-side jets fully quenched.

Moving to the second column,  $v_3$  modulation is included in the background. The top panel shows that the background function has a different shape compared to the  $v_2$  only case. The jet function after subtraction in the second row shows that the double peak structure is significantly reduced, and there is a pedestal under the jet correlation function. This should be expected, since adding in those terms modulating the background function leave the total jet yield, re[resembled by  $C + 0$  imcjanged/ Ot os pm;u tje sja[e pf tje ket fimctopm wjocj cjages/

The Fourier spectrum in the third row shows that the third harmonic in the jet function is significantly reduced, which is not surprising since we now include  $v_3$  in the flow background. As a crosscheck, the  $C_0$  term in both cases ( $v_2$  and  $v_2 + v_3$ ) are the same, which is because adding in another  $v_n$  contribution in Eq. 6.2 will only change the shape of the jet function, not the total yield integrated over  $2\pi$ .

In the right column of Fig. 6.6, we also include the  $v_4$  modulation. The subtracted jet function in the second panel does not have a clear double peak structure. It looks more like a broadened and suppressed jet sitting on a flat pedestal.

The pedestal structure can be understood as follows. In all three different background cases shown in Fig. 6.6, the background level,  $b_0$ , is fixed to the same value determined by absolute normalization. Since adding in extra  $v_n$  terms do not change the total background, but only changes the shape, this means the total yield of the jet function is also the same with different  $v_n$  background shape. This is verified in the Fourier spectra that  $C_0$  is the same in all three

cases. Since the yield does not change, but the shape of the jet function does, the enhancement seen as ridge and shoulder for background with  $v_2$  only is redistributed when higher harmonics are included in the background. This redistribution of the extra yield recovers the ridge and shoulder and leads to the pedestals seen in the second and third columns of Fig. 6.6.

## 6.4 Motivation and Verification of the p+p reference

From the standard two particle correlation analysis, we know that the correlation function can be written as

$$CF(\Delta\phi) = JF(\Delta\phi) + FL(\Delta\phi) \quad (6.4)$$

or we can rewrite Eq. 6.4 as

$$JF(\Delta\phi) = CF(\Delta\phi) - FL(\Delta\phi) \quad (6.5)$$

We assume after removing the flowing background contributions,  $FL(\Delta\phi)$  in Eq. 6.5, what's left should resemble a p+p-like jet. This is inspired by the high  $p_T$  correlation function studies from PHENIX [23] and [24].

In the previous sections, we use unmodified p+p jets and awayside fully quenched p+p jets as two baselines. We claim that the Fourier spectra of any awayside-modified p+p like jets should lie in between the Fourier spectra of these two baselines. We tested several scenarios of jet modifications to see if the claim holds. In Fig. 6.7, several scenarios are illustrated. We have black(red) curves which represented the unmodified (awayside fully quenched) p+p jet. The Fourier spectra are plotted in the right hand side with the same color. We then varied the shape and yield of awayside jet. The first case is shown in green where the width of the awayside is unchanged, but the awayside yield is suppressed by 0.5. In the second case, the yield of the awayside is unchanged, but the width is broadened by 50%, which is shown in blue. The last case has awayside width broadened by 50% and yield suppressed by 50%, plotted in yellow.

The right hand side of Fig. 6.7 show that the Fourier spectra of the three jet scenarios all fall between the black and red points, thus support the use of these two extreme cases for comparison with Au+Au which are the two extreme case we used here. The awayside fully quenched case can be thought of as an awayside jet that is extremely broad. As visible in blue, even if the awayside yield is unchanged, once the width is broader, the Fourier spectrum starts to approach the fully quenched awayside case.

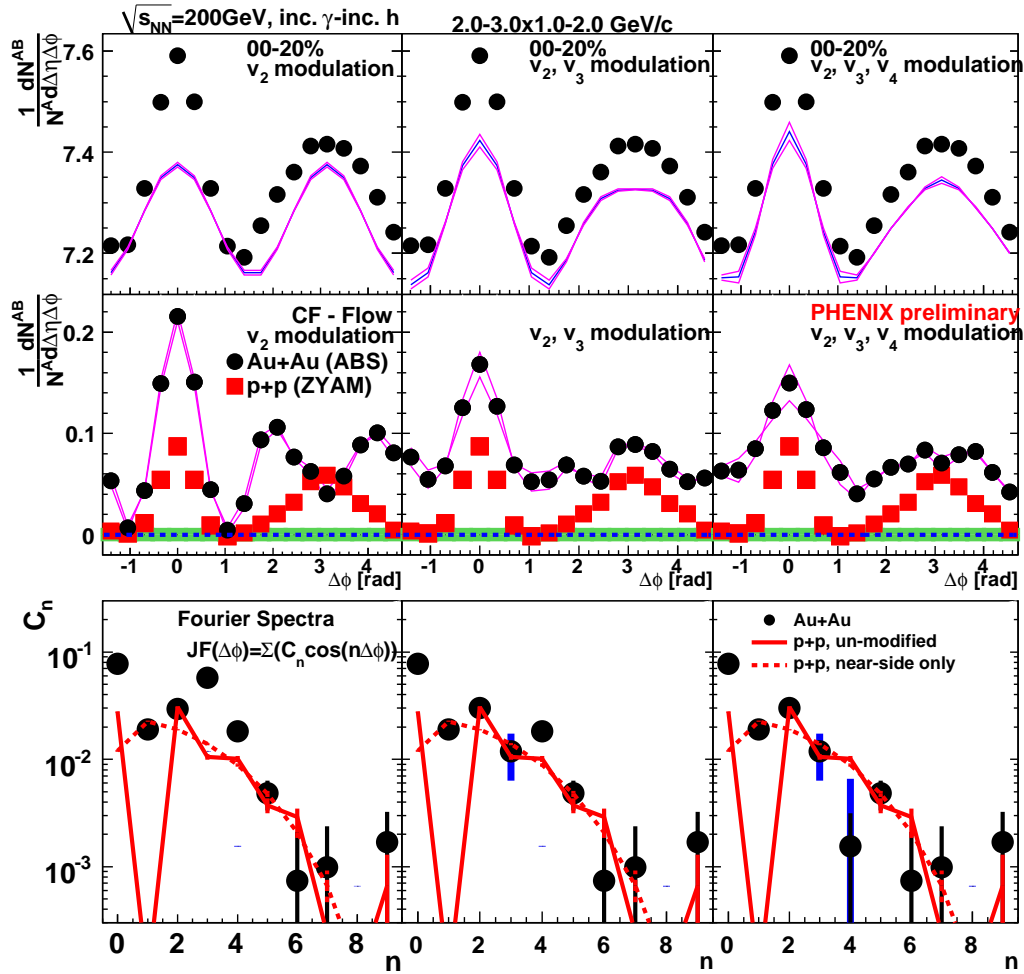


Figure 6.6: Correlation functions with different  $v_n$  modulated underlying event background subtracted. The left column:  $v_2$  modulation; middle column:  $v_2$  and  $v_3$  modulation; right column:  $v_2$ ,  $v_3$  and  $v_4$  modulation. Top panel: correlation function with  $v_n$  modulated underlying event background; middle panel: jet function with  $v_n$  modulated background subtracted; bottom panel: Fourier spectra of the jet function.

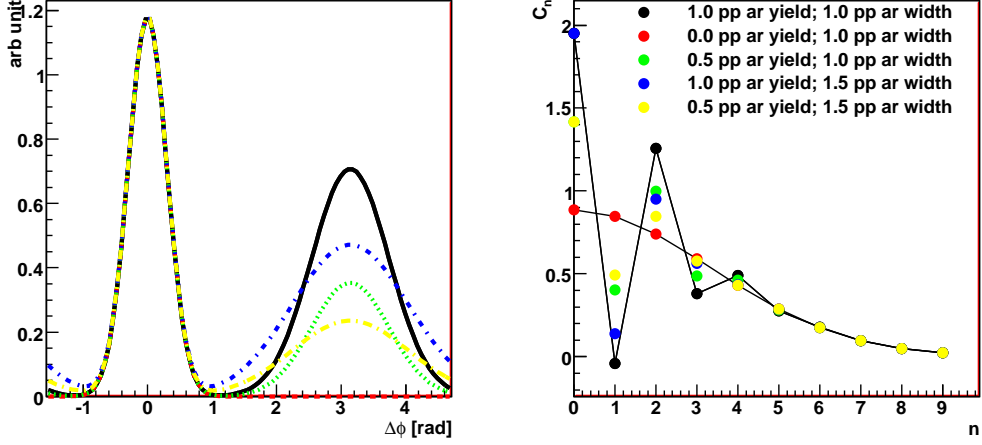


Figure 6.7: Fourier Spectra in different simulated p+p like jet scenarios. Black: unmodified p+p jet; red: awayside jet yield is fully suppressed; green: awayside yield is suppressed by 50%; blue: awayside jet width is broadened by 50%; yellow: the awayside jet yield is suppressed by 50% and the jet width is broadened by 50%.

## 6.5 Au+Au Compared with p+p

In this section, we start with the Fourier spectra and see the effect in the  $v_n$  subtraction.

To study the  $v_n$  effect, we first transform all the correlation functions in Eq. 6.4 in to Fourier spectra, say

$$CF(\Delta\phi) = \sum C_n^{CF} \cos(n\Delta\phi) \quad (6.6)$$

$$FL(\Delta\phi) = \sum C_n^{FL} \cos(n\Delta\phi) \quad (6.7)$$

$$JF(\Delta\phi) = \sum C_n^{JF} \cos(n\Delta\phi) \quad (6.8)$$

So for each Fourier coefficient,  $C_n$ , Eq. 6.4 can be written to be as

$$C_n^{CF} = C_n^{FL} + C_n^{JF} \quad (6.9)$$

or we can rearrange the equation

$$C_n^{JF} = C_n^{CF} - C_n^{FL} \quad (6.10)$$

From Eq. 6.2, we only use  $v_2$ ,  $v_3$ , and  $v_4$  and a constant term in the flow underlying background. When doing the subtraction shown in Eq. 6.10, only  $C_0$ ,  $C_2$ ,  $C_3$ ,  $C_4$  will be modified. The rest of the harmonics are untouched.

After we did the subtraction, we compare  $C_n$  in Au+Au with the corresponding term  $C_n$  from the two p+p reference baseline. If after  $v_n$  background subtraction, what's left in Au+Au falls in between the two p+p reference, we can assume the jet component left in Au+Au should be a "p+p-like jet shape". If what's left is beyond the two p+p reference, then this will indicate some extra contributions other than the bulk and jet contribution exists.

Fig. 6.8 is the  $C_0$  term.  $C_0$  corresponds to the total per trigger yield integrated over  $2\pi$ . We see all the Au+Au points are significantly above the p+p reference lines here. This is not surprising since we know at low partner  $p_T$ , there are more particles in Au+Au than in p+p, as seen in this analysis and reported by PHENIX earlier [23]. This extra yield was originally the ridge and shoulder, these structures are no longer observed. Nevertheless, the total particle yield in Au+Au correlations is higher than the totally uncorrelated underlying events (which is determined by absolute normalization) and unmodified jet can provide

In Fig. 6.9, after removing the uncorrelated  $v_2$  terms from the underlying event, the remaining  $C_2$  due to jets in Au+Au lies in between the two p+p references. This suggests that  $C_2$  in Au+Au can be explained by the p+p like jet; for  $C_2$ , there is only bulk and jet.

In Fig. 6.10, the  $C_3$  the central values still fall between the two p+p references, but the systematic error bar is large enough to cover the two reference curves. This plot suggests that the third harmonic could be described by the bulk  $v_3$  and the normal jet contribution only. If this is true, then the three peak structure (ridge plus two shoulders) is due to the bulk  $v_3$ , since after subtraction, only the jet-like structure remains.

The  $v_4$  case, shown Fig. 6.11, is different. We applied  $v_4$  obtained [68] and the result is surprising. Unlike Fig. 6.9 and Fig. 6.10, all the Au+Au points are below the p+p references, and are consistent with 0, except for the associated particle  $p_T = 3-5$  GeV/c. This is very surprising, since if  $C_4$  is consistent with 0, then it indicates that the bulk  $v_4$  describe everything in Au+Au collisions, and the jet component has no contribution to the fourth harmonic at all. We don't have good explanation for this at this moment.

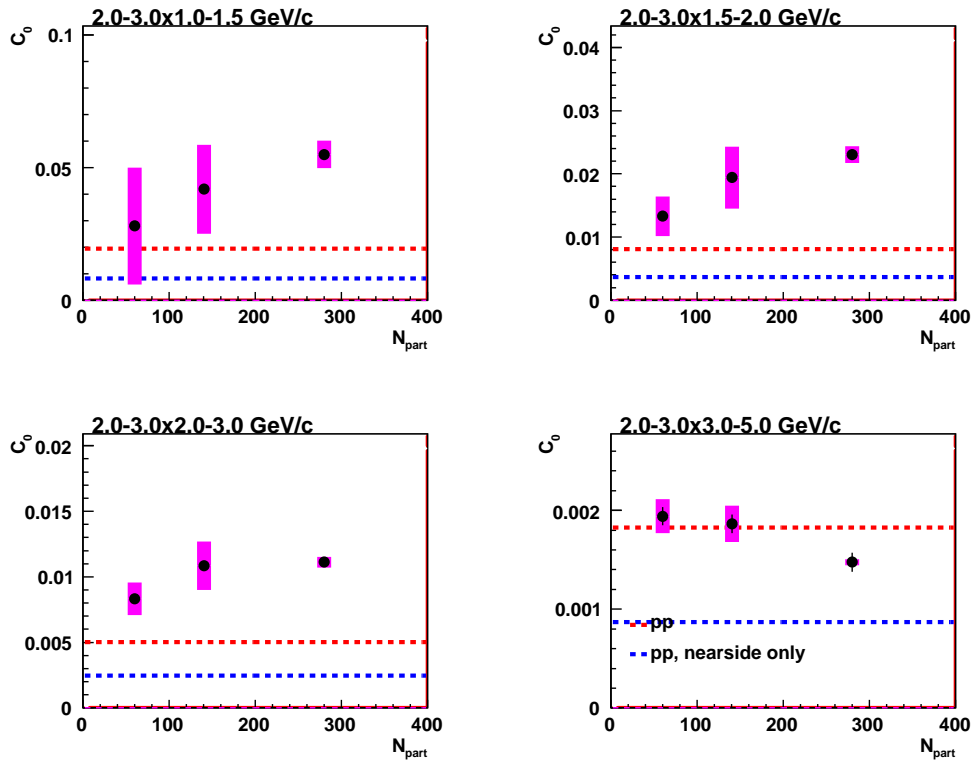


Figure 6.8:  $C_0$  from Au+Au in different as a function of  $N_{part}$  compare with two p+p references in different partner  $p_T$ .

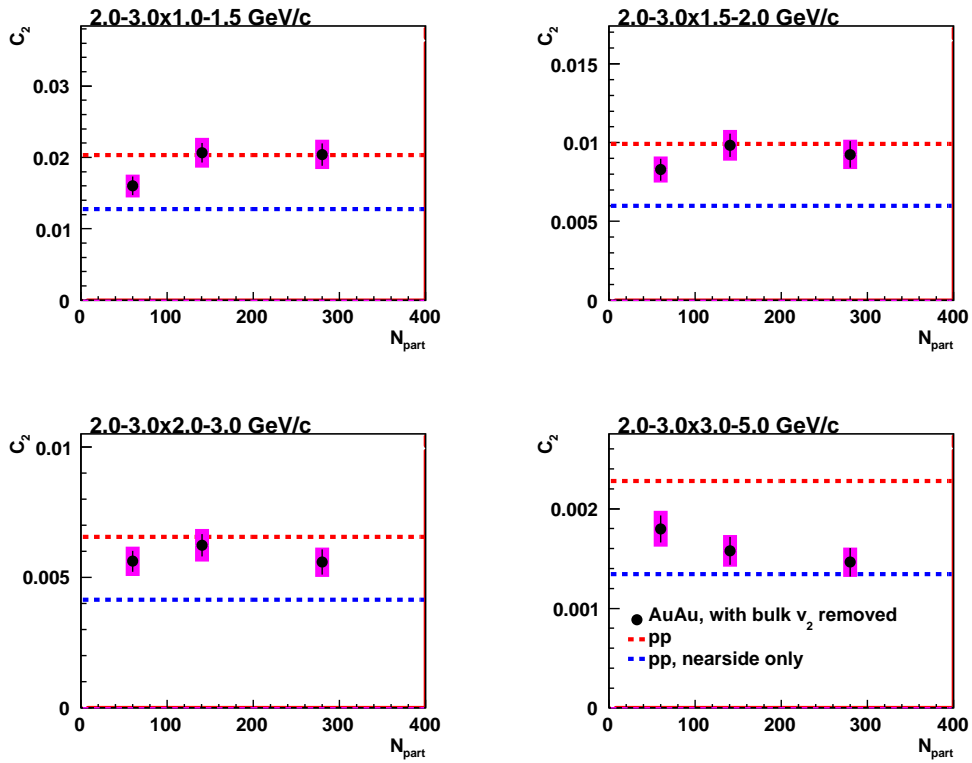


Figure 6.9:  $C_2$  from Au+Au in different as a function of  $N_{part}$  compare with two p+p references in different partner  $p_T$ .

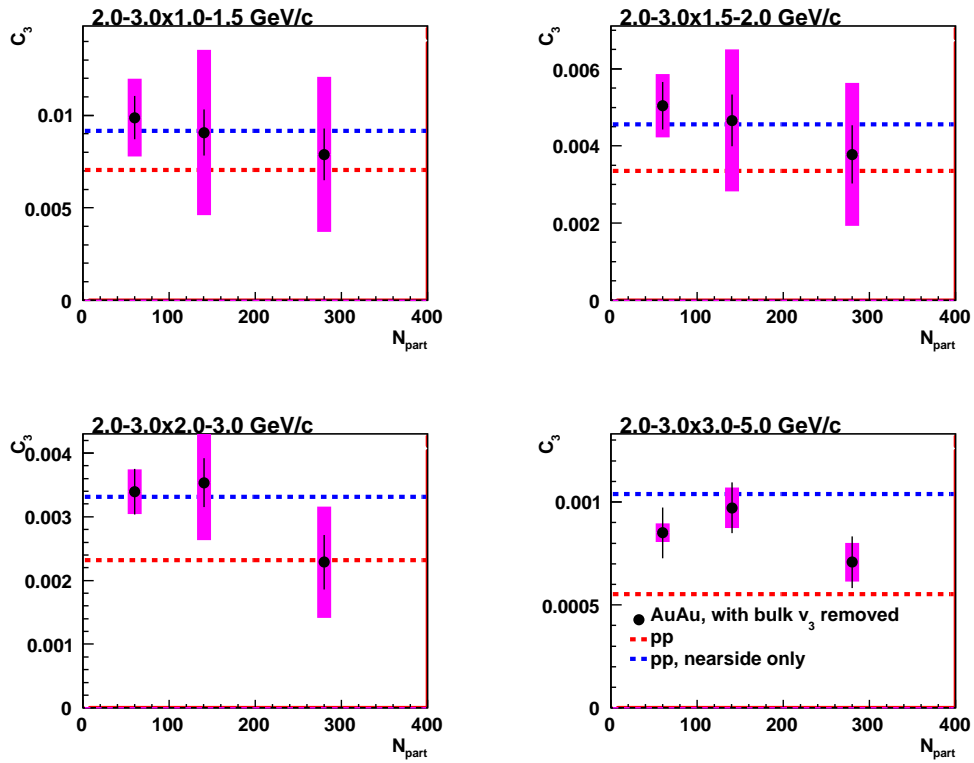


Figure 6.10:  $C_3$  from Au+Au in different  $p_T$  as a function of  $N_{part}$  compare with two p+p references in different partner  $p_T$ .



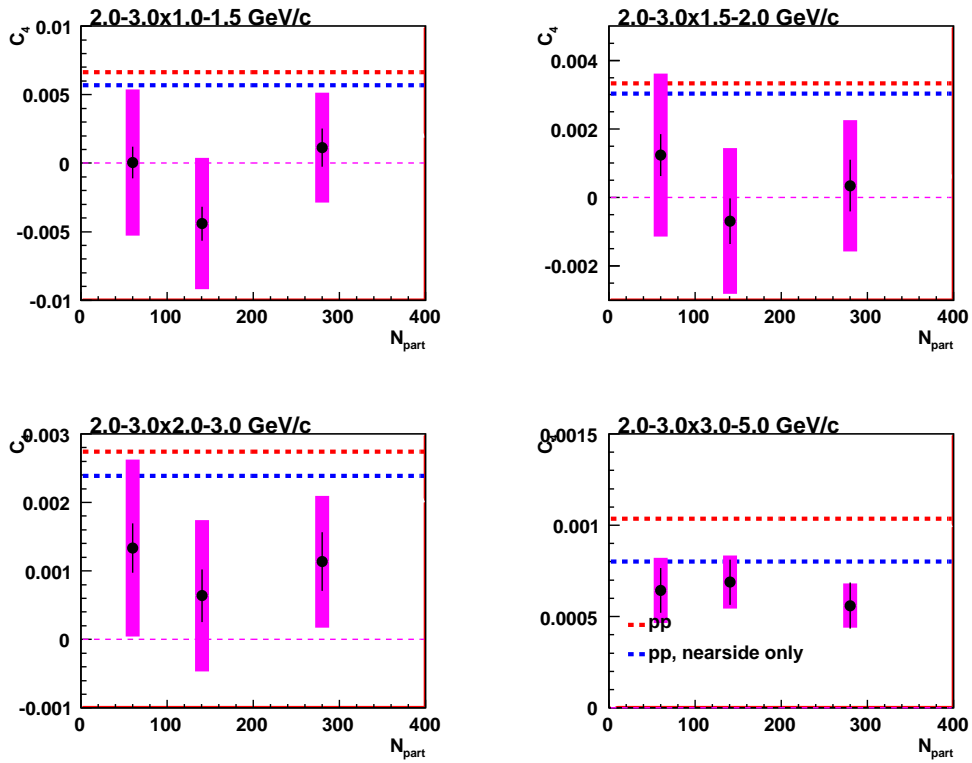


Figure 6.11:  $C_4$  from Au+Au in different centrality bins as a function of  $N_{part}$  compare with two p+p references in different partner  $p_T$ .

**Part IV**  
**Discussion**

## Chapter 7

### Discussion

#### 7.1 QGP: the Most Perfect Fluid

When the two nuclei undergo non-central collisions, or have a nonzero impact parameter,  $b$ , the colliding area forms an almond shape. This hot dense region equilibrates, expands and cools, and numerous particles are produced. The pattern of the particle emission depends on the mean free path of the particles,  $l$ , and the size of the system,  $R$ . When  $l$  is not much smaller than  $R$ , the emission pattern can be assumed to be the superposition of many nucleon-nucleon collisions, which are azimuthally isotropic. When  $l \ll R$ , then the behavior of a system in equilibrium can be described by relativistic hydrodynamics, and the emission pattern is mainly influenced by the shape of the system.

When system is locally thermalized, as described in Chapter 1.3, the system can be described by hydrodynamics. When the system expands, the particles flow collectively. This flow is due to the pressure gradients in the system. In the almond shape colliding area, the pressure should to be the greatest at the short direction, which is along the impact parameter.

As a result, we can measure the angular distribution of particles with respect to the event plane as:

$$\frac{dN}{d\phi} \propto 1 + \sum (2v_n \cos n(\phi - \psi_n)) \quad (7.1)$$

The Fourier coefficients,  $v_n$ , can provide a lot of information on the properties of quark-gluon plasma, and can be compared with hydrodynamical calculations.

### 7.1.1 $v_2$ and Geometry

PHENIX measured  $v_2$  in Au+Au and Cu+Cu collisions [18]. The  $v_2$  of inclusive charged hadrons is measured as a function of  $p_T$ , as shown in Fig. 7.1. In Fig. 7.1 (a) and (b),  $v_2$  increases from central to mid-central collisions, in parallel with the increased geometrical anisotropy. The  $v_2$  increases with  $p_T$  up to 3 GeV/c and then appears to saturate.

Cu+Cu is a smaller system than Au+Au. When both systems have a similar number of participants during the collision, the two may have different geometric shapes. In order to remove the geometrical effect of the system, the  $v_2$  is normalized by the eccentricity,  $\varepsilon$ . Since  $p_T$  integrated  $v_2$  is assumed to be proportional to the eccentricity of the system, it can be used as a proxy of eccentricity [18].

After normalizing by eccentricity (or the  $p_T$  integrated  $v_2$ ), all  $v_2$  values fall along a universal curve, independent of the colliding system and centrality as shown in Fig. 7.1 (c). This implies that the expansion of the system is universal, and suggests a rapid thermalization of the system at the partonic level [77, 78].

### 7.1.2 $v_2$ and Quark Number Scaling

$v_2$  as a function of  $p_T$  for different particle species are shown in Fig. 7.2 (a) [18].  $v_2$  of identified particles fall into two groups: mesons and baryons. At  $p_T < 2$  GeV/c,  $v_2$  of the mesons is larger than for baryons. At  $p_T > 2$  GeV/c, the  $v_2$  of mesons begins to saturate while the  $v_2$  of baryons continues increasing and shows some signs of saturation at 3 GeV/c. Fig. 7.2 (b) is the same data, but plotted vs transverse kinetic energy,  $\text{KE}_T$ , where  $\text{KE}_T = m_T - m$ .  $\text{KE}_T$  takes into account relativistic effects and the particle mass, and is a better way to check scaling with the energy. We see that all mesons line up together, as do the baryons.

We can take a step further and plot the  $v_2$  per valence quark:

$$v_2^{\text{meson}}(p_T) = 2v_2^{\text{quark}}(p_T/2) \quad (7.2)$$

$$v_2^{\text{baryon}}(p_T) = 3v_2^{\text{quark}}(p_T/3) \quad (7.3)$$

Fig. 7.3 shows the  $v_2/n_q$  vs  $p_T/n_q$  or  $\text{KE}_T/n_q$  scaling. After scaling by number of quarks, where  $n_q = 2$  for mesons and 3 for baryons,  $v_2/n_q$  vs  $\text{KE}_T/n_q$  of all particles align together and show a universal trend, visible in Fig. 7.3 (b). On the other hand, Fig. 7.3a, which is plotted vs  $p_T$ , does not show similar scaling properties. The fact that the flow scales with the quark content rather

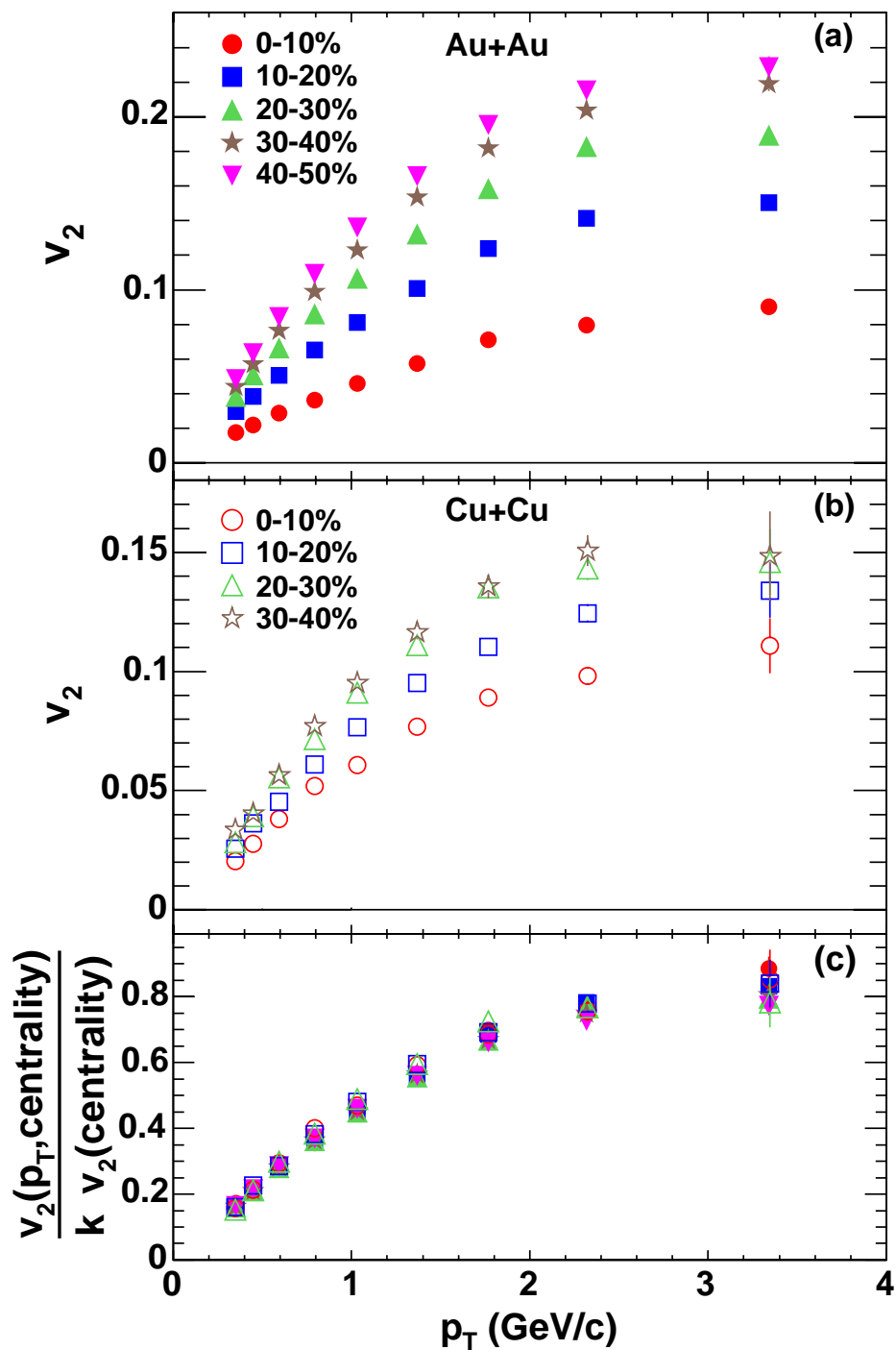


Figure 7.1:  $v_2$  measurement in (a) Au+Au; (b) Cu+Cu; (c)  $v_2$  scaled with  $p_T$  integrated  $v_2$  [18]

than the mass of the hadrons, suggests that quarks are the relevant degrees of freedom when the pressure gradients are built up. The magnitude of  $v_2$  implies that the collective flow is built up very quickly, before the expansion of the system restores geometrical symmetry.

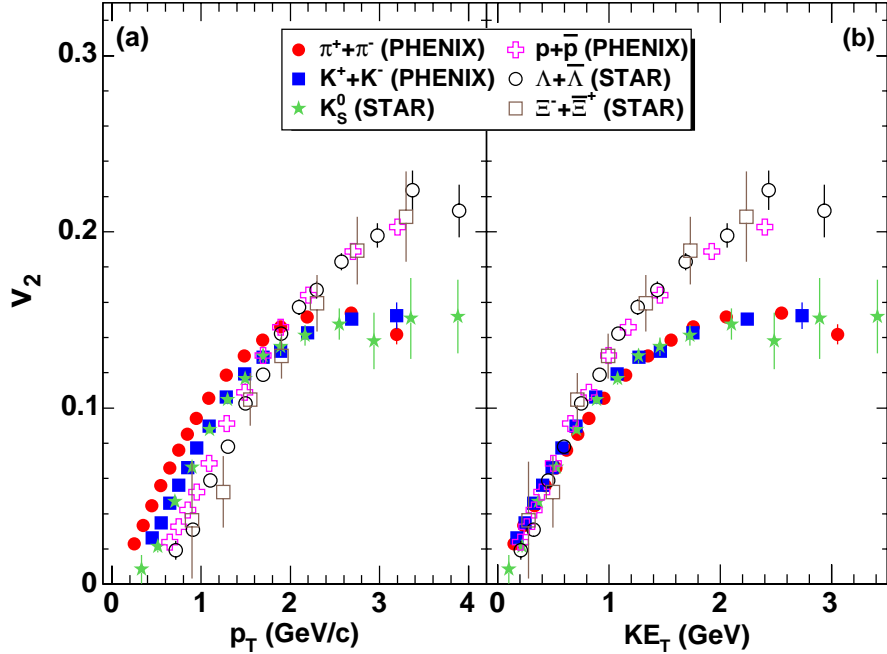


Figure 7.2: (a)  $v_2$  vs  $p_T$  and (b)  $v_2$  vs  $KE_T$  of identified charged hadrons in min-bias Au+Au collisions [18]. STAR data from [79, 80]

### 7.1.3 How Perfect is QGP? Extracting $\eta/s$

The significant flow,  $v_2$ , observed indicates the system expands collectively, and that it thermalized rapidly [77, 78]. This can be described by the relativistic hydrodynamics. But by assuming the system as perfect fluid, where there is no viscosity, the hydrodynamic models predict a stronger  $v_2$  than data [17]. Earlier calculations indicate that by introducing small but nonzero viscosity to the system, it can reduce the  $v_2$  [81]

When using relativistic hydrodynamics to calculate  $v_2$ , several parameters are necessary: the thermalization time,  $\tau_0$ , where the hydrodynamics starts;  $\tau_f$ , where the hydrodynamics stops; the initial state of the system when hydrodynamics starts. Here we focus on the initial state of the collision. There are two kinds of initial conditions. One is the Glauber model, which assumes

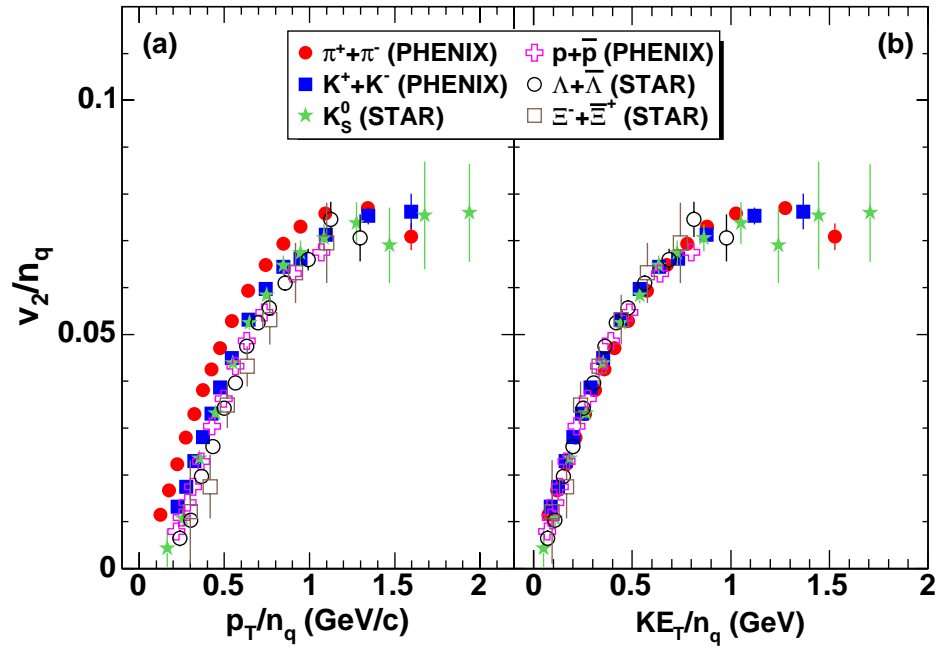


Figure 7.3: Quark number scaling of identified charged hadrons: (a)  $v_2/n_q$  vs  $p_T/n_q$  and (b)  $v_2/n_q$  vs  $KE_T/n_q$  [18]. STAR data from [79, 80]

that the nuclei consist of individual nucleons with nucleons distributed according to Woods–Saxen function. The other model is the Color Glass Condensate (CGC), which assumes that in the nuclei, the density of gluons is saturated. So the initial condition is determined by the gluon distribution inside the nuclei.

If the QGP behaves like a liquid, this raises the question of what the shear viscosity of this liquid might be. The shear viscosity,  $\eta$ , is the property of the liquid which describes the energy dissipation. The larger the viscosity, the easier energy gets lost. For perfect liquid, the shear viscosity is zero, which means energy can go through the medium without any dissipation.

But the QGP is not a normal "liquid". It has a high temperature, consists of quarks and gluons, and the interaction is described by QCD. With Anti–dilatator/Conformal Field Theory (AdS/CFT), people can transform the strong coupling problem into a 5–dimensional gravity dual, where the strong–coupled field theory is approximated as a gravitational field near a black hole. By this AdS/CFT correspondence, people calculate that there is a minimum value for the ratio of the shear viscosity over the entropy density, which is given by [82]

$$\frac{\eta}{s} = \frac{1}{4\pi} \tag{7.4}$$

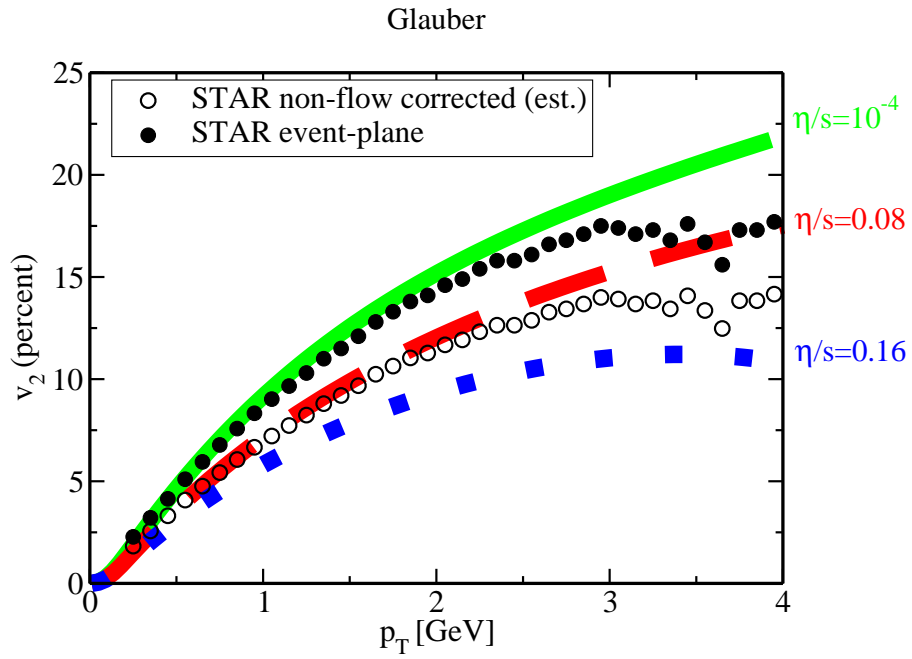
Eq. 7.4 tells us that there is a universal lower bound of the ratio  $\eta/s$ . Even though the ratio of  $\eta/s$  has a lower bound, the viscosity of the quark gluon plasma could still be large. So it is an important experimental goal to measure it.

Fig. 7.4(a) and Fig. 7.4(b) compare relativistic hydrodynamical calculations for  $v_2$  with two different initial conditions, Glauber and CGC [83]. The  $v_2$  data is from STAR [84]. The calculations show that if the viscosity to entropy ratio is zero, which is the case for a perfect fluid, both initial states over–estimate the measured  $v_2$  values.

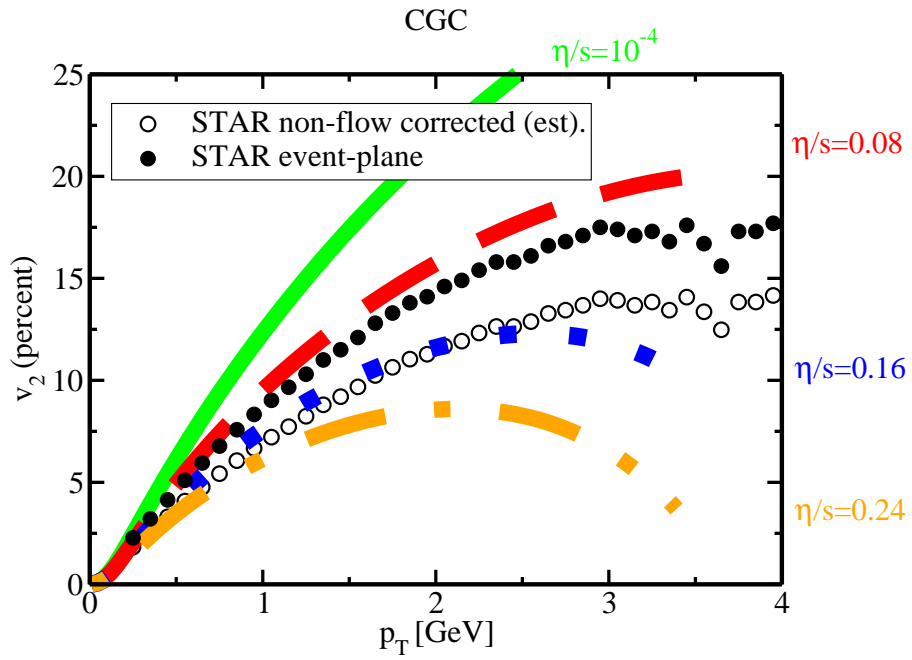
Further calculations assume different values of  $\eta/s$ , from 0.08 ( $1/4\pi$ ) to 0.24. The effect of the viscosity brings the calculated  $v_2$  down. The most interesting aspect of Fig. 7.4(a) and Fig. 7.4(b) is that with some finite viscosity, both Glauber and CGC describe the  $v_2$  trend equally well. For the Glauber initial state, the best value is  $\eta/s = 1/4\pi$ , while  $\eta/s = 2/4\pi$  for the CGC initial state.

From these calculations, we know that the QGP has a small but finite  $\eta/s$ , which is close to the value of the universal lower bound of a quantum system,  $\eta/s = 1/4\pi$ . Also, depending on the assumptions of different initial states, Glauber or CGC, the value of  $\eta/s$  is different. A key issue over the past several years has been how to remove this degeneracy with additional experimental information.





(a) Glauber initial state



(b) CGC initial state

Figure 7.4: Flow calculations with different initial state conditions with various  $\eta/s$  [83]. The data is from STAR [84]

### 7.1.4 Further Constraints on $\eta/s$ : $v_n$

To further constrain  $\eta/s$ , we need more parameters. The two different initial states (Glauber and CGC) give different values for  $\eta/s$  when compared with  $v_2$ . Comparing hydrodynamic calculations to higher harmonics ( $n > 2$ ) will provide additional constraints to distinguish between models and initial conditions.

Fig. 7.5 compares the  $v_2\{\psi_2\}$  and  $v_3\{\psi_3\}$  as a function of  $N_{part}$  with several theoretical calculations [72, 74, 70]. Alver et al. [72] assumed an energy profile using two initial conditions, Glauber and MC-KLN. The Glauber initial state condition was described previously in section 5.8, the energy profile is described by a Woods-Saxon function. MC-KLN [85, 86] is a particular implementation of the Color Glass Condensate, where the energy density is determined by gluon density in the transverse plane. The gluon density peaks at the center of the nuclei and decreases at the edge of the nuclei. Fluctuations are introduced in both initial conditions. These two initial conditions are paired with different  $\eta/s$  values:  $\eta/s = 1/4\pi$  for Glauber and  $2/4\pi$  MC-KLN respectively, as the two combinations describe  $v_2$  equally well. Petersen et al. [74] starts with Glauber initial conditions. Then the interaction is simulated by the Lund model [87] followed by fragmentation of color tubes, which is also known as the UrQMD transport model [9, 10]. The results are evolved with ideal hydrodynamics ( $\eta/s = 0$ ) event-by-event. At late hadron cascade stage when the system is dilute, the system is gradually transit from hydrodynamics to transport model. B. Schenke *et al.* [70] use event-by-event Glauber initial conditions to fully account for fluctuations in the initial positions of nucleons in the Au nuclei, and then evolves the medium with 3+1 dimensional viscous hydrodynamics, where several values of  $\eta/s$  have been used.

All models are compared with  $v_2\{\psi_2\}$  and  $v_3\{\psi_3\}$ . All calculations describe  $v_2\{\psi_2\}$  very well at  $p_T = 0.75$  GeV/c as shown in Fig. 7.5(a). At  $p_T = 1.75$  GeV/c, the MC-KLN calculation (red points) does not describe the data well at low  $N_{part}$ .

For  $v_3\{\psi_3\}$  at  $p_T = 0.75$  GeV/c, shown in Fig. 7.5(c) and (d), all calculations with Glauber initial conditions show good agreement with data. However, the MC-KLN calculation (red points) are significantly below the data. The deviation is even larger at higher  $p_T$ . By contrast, models with Glauber initial conditions with  $\eta/s = 1/4\pi$  still describe the data relatively well. This shows the constraining power of  $v_3$  to differentiate among the models.

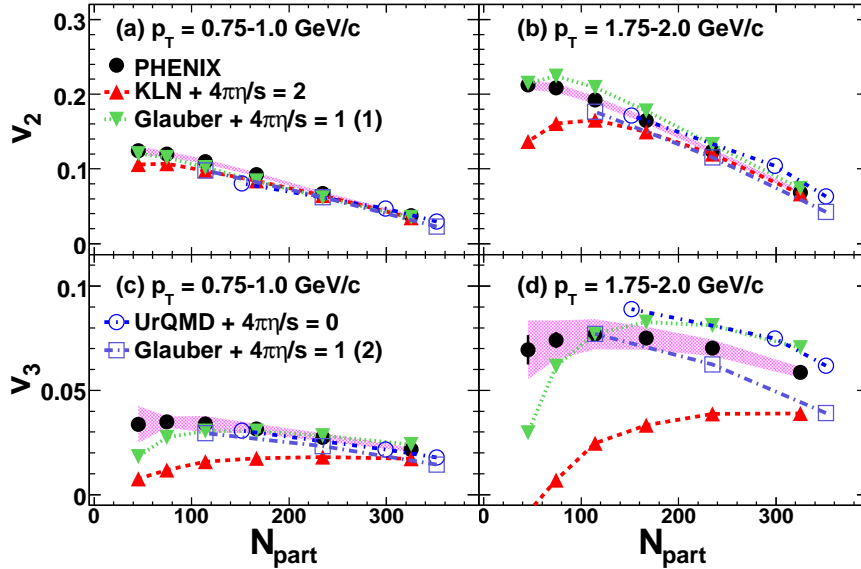


Figure 7.5:  $v_2$  and  $v_3$  compared with various theory calculations in Au+Au [68]

## 7.2 $v_n$ in Two Particle Correlation: the Ridge and Shoulder

### 7.2.1 The Ridge and Shoulder with $v_2$ -modulated Background Subtraction

With  $v_2$ -modulated underlying event background subtraction in the two particle correlation analysis, the novel structures of the ridge and shoulder are studied extensively in Chapter 4. Both the ridge and shoulder have some properties in common. Both yields strongly depend on the size of the medium and the yield increases with the size of the system. The spectra and truncated mean  $p_T$  show that both the ridge and shoulder are much softer than jets in p+p collisions. This tells us that neither the ridge nor the shoulder arise directly from hard scattering. The truncated mean  $p_T$  of the ridge and shoulder are closer to the bulk, which indicates that the origin of both should be related to the medium. The truncated mean  $p_T$  of the ridge and shoulder are also consistent with one another across various centralities, hinting that the mechanism for producing the ridge and shoulder is independent from the size of the medium.

Both the ridge and shoulder have inspired several theoretical explanations. Most of these theories treat the two phenomena separately. There are several physical pictures proposed to explain the production of the ridge: Jet–medium interactions may result in a momentum kick to particles in the bulk medium, boosting their momentum and producing a correlation with a traversing fast parton [38]. A correlated emission model describes radiation of soft gluons by a parton penetrating the medium; these gluons and their resulting hadronic fragments are boosted by longitudinal flow of the medium [39]. The Glasma model treats the ridge as arising from the flux tube formed early in the collision; longitudinal expansion elongates the ridge in  $\eta$  [40].

The shoulder structure has been suggested to arise from passage of a sound wave as the medium responds to shocks deposited by jet energy loss [41, 42, 43]. However, there is considerable debate as to whether it is possible to observe the resulting Mach cone–like structure [44, 45].

### 7.2.2 The Ridge, Shoulder and Higher Order $v_n$ Background Modulation

The idea of non–zero odd harmonics, especially  $v_3$ , changes the picture for the ridge and shoulder [67]. After higher harmonics are measured using a reaction plane defined at large  $\eta$  [68], we have a better way to describe the shape of the underlying event background.

After subtracting the underlying event, including the modulation of higher harmonics, from two particle correlations, both the ridge and shoulder disappear, as shown in Fig. 6.6. Instead of the ridge and shoulder, the jet function looks like a di–jet with a suppressed and possibly broadened awayside on top of a flat pedestal.

Fourier coefficients,  $C_n$  with  $n > 0$ , as defined in Eq. 6.1, are used to describe the shape of the correlation function. After subtracting backgrounds with higher harmonic modulations, the Fourier coefficient of the corresponding harmonics in Au+Au is consistent with the sum of a jet–like structure and the medium, as shown in Fig. 6.9, Fig. 6.10 and Fig. 6.11.

This tells us that the correlation function can be mostly described by the medium and jets. In other words, the ridge and shoulder arose because we did not consider the background shape correctly. However,  $v_n$  is a shape parameter. When integrated over  $2\pi$ , the  $v_n \cos n\Delta\phi$  term is zero, which means  $v_n$  changes the shape of the background, but not the absolute background level. In Fig. 6.6, the background level is fixed using the absolute normalizations [76]. This is a crucial step, because we calculate explicitly the background level of

the "totally uncorrelated" underlying background pairs. No matter how many  $v_n$  we include in the subtraction, the background level never changes.

This makes Fig. 6.8 an important result. Fig. 6.8 describes the total yield of the correlation function in Au+Au. At low partner  $p_T$ , the total yield in Au+Au is larger than in p+p collisions. This tells us that this extra yield comes neither from the uncorrelated background pairs nor from the jets.

Even though Fig. 6.8 shows that there is significant yield which is not from jets or the underlying event, we cannot separate this extra yield from the jets. The reason is that the awayside jet is suppressed, and we cannot tell the exact level of suppression. However, we can use studies of the ridge and shoulder shown in Fig. 4.19 to represent the extra yield or the pedestal. The general trend of the ridge and shoulder yields is an increase with  $N_{part}$ . In Fig. 4.28, the truncated mean  $p_T$  of the ridge and shoulder are roughly consistent with each other. So we know the truncated mean  $p_T$  of the pedestal, which should be the sum of the ridge and shoulder, and should be the same as the ridge and shoulder. This tells us the pedestal is slightly harder than the bulk, but softer than the hard scattering components, indicating that the source of this extra yield may come from some jet-medium interaction, which gives the medium extra energy and makes the truncated mean  $p_T$  slightly larger than the bulk medium.

### 7.2.3 Ridge, Shoulder and the Energy Loss

If the yields in the ridge and shoulder are coming from extra energy deposited in the medium, a natural question is where this energy comes from? One possible source is from the energy loss of the awayside jet.

In Fig. 4.13, we extract the yield of the awayside jet via the fitting method. It is clearly shown that the head region, or the awayside jet yield, is suppressed compared to p+p. This jet suppression is seen in all partner  $p_T$  bins. At the same time, the yield in the shoulder region increases while the head region is suppressed. Qualitatively, this is consistent with the idea of energy or momentum conservation, where the energy lost in the head region is recovered in the shoulder region.

However further studies do not agree with this simple assumption. We use  $p_T$  weighted yields to describe the momentum in all the components, which is shown in Fig. 4.25 and Fig. 4.26. In Fig. 4.26, the  $p_T$  of the associated particles is 1–5 GeV/c. Conservation of momentum tells us that the momentum lost by the high  $p_T$  associated particles must be recovered as low  $p_T$  particles. What we see in Fig. 4.26 is that the momentum carried by the near and awayside are both larger than the p+p case. But the increase of the nearside is much

larger than the increase of the awayside, indicating a momentum imbalance. Thus, conservation of momentum does not hold, and the observed increase in yield must come from a mechanism as yet unknown.

**Part V**  
**Conclusion**

## Chapter 8

### Conclusion

Inclusive photon-inclusive charged hadron  $\Delta\eta$ - $\Delta\phi$  correlations have been measured. The underlying event background has been removed in order to study the properties of the jet pairs. When subtracting the background pairs with  $v_2$  only modulations, exotic structures have been found in both the near side, the “ridge”, and the away side, the “shoulder”. The properties of the “ridge” and “shoulder” are very similar to one another in yield, spectra and truncated mean  $p_T$ . The truncated mean  $p_T$  of the ridge and shoulder are both softer than jet fragments in p+p collisions, and are slightly harder than inclusive charged hadrons. This indicates these two structures may come from some jet-medium interactions.

In order to study the effect of higher harmonics of the underlying event collective flow, higher harmonics have been measured using two methods: the reaction plane method and the two particle correlation method. The new measurement of higher harmonics provides two key pieces of physics. The first is an additional constraint in quantifying the viscosity, or  $\eta/s$ , of the quark-gluon plasma. When using  $v_2$  to quantify  $\eta/s$ , both Glauber and CGC initial state conditions describe the data well, but each correspond to a different  $\eta/s$ :  $\eta/s = 1/4\pi$  for Glauber and  $2/4\pi$  for CGC. With  $v_3$ , the data favors Glauber initial state with  $\eta/s = 1/4\pi$ .

The second impact of quantifying the higher harmonics is the impact of including them in the underlying event shape. Including higher harmonics in the subtraction of background under the jet function cause the “ridge” and “shoulder” disappear. The resulting jet function does show away side jet suppression and broadening.

There is extra yield observed as a pedestal in the jet functions when including the higher harmonic contributions. Since including higher harmonics do not change the yield, the source of the pedestal is mostly coming from particles originally assigned to the ridge and shoulder when consider only  $v_2$



modulations in the shape of the background.

In conclusion, when jets pass through the medium, the away side jet is suppressed and the shape is broadened. This also brings out extra particles with spectra slightly harder than the medium, but softer than jet fragments. These are probably from the jet-medium interaction.

## Bibliography

- [1] K. Nakamura and P. D. Group, Journal of Physics G: Nuclear and Particle Physics **37**, 075021 (2010)
- [2] S. Bethke, The European Physical Journal C - Particles and Fields **64**, 689 (2009)
- [3] D. J. Gross and F. Wilczek, Phys. Rev. Lett. **30**, 1343 (1973)
- [4] H. D. Politzer, Phys. Rev. Lett. **30**, 1346 (1973)
- [5] F. Karsch, Lecture Notes on Physics **583**, 209 (2002)
- [6] E. V. Shuryak, Sov. Phys. JETP **47**, 212 (1978)
- [7] E. V. Shuryak, Physics Letters B **78**, 150 (1978)
- [8] P. F. Kolb and R. Rapp, Phys. Rev. C **67**, 044903 (2003)
- [9] S. A. Bass *et al.*, Prog. Part. Nucl. Phys. **41**, 255 (1998)
- [10] M. Bleicher *et al.*, J. Phys. G **25**, 1859 (1999)
- [11] R. J. Glauber, Phys. Rev. **100**, 242 (1955)
- [12] P. Stankus, Annual Review of Nuclear and Particle Science **55**, 517 (2005)
- [13] S. Turbide, R. Rapp, and C. Gale, Phys. Rev. C **69**, 014903 (2004)
- [14] A. Adare *et al.* (PHENIX Collaboration), Phys. Rev. Lett. **104**, 132301 (2010)
- [15] D. d'Enterria and D. Peressounko, The European Physical Journal C - Particles and Fields **46**, 451 (2006)
- [16] A. Adare *et al.* (PHENIX Collaboration), Phys. Rev. C **81**, 034911 (2010)

- [17] K. Adcox *et al.*, Nuclear Physics A **757**, 184 (2005)
- [18] A. Adare *et al.* (PHENIX Collaboration), Phys. Rev. Lett. **98**, 162301 (2007)
- [19] A. Adare *et al.* (PHENIX Collaboration), Phys. Rev. Lett. **105**, 062301 (2010)
- [20] A. Adare *et al.* (PHENIX Collaboration), Phys. Rev. Lett. **101**, 232301 (2008)
- [21] S. S. Adler *et al.* (PHENIX Collaboration), Phys. Rev. Lett. **97**, 052301 (2006)
- [22] A. Adare *et al.* (PHENIX Collaboration), Phys. Rev. Lett. **98**, 232302 (2007)
- [23] A. Adare *et al.* (PHENIX Collaboration), Phys. Rev. C **78**, 014901 (2008)
- [24] A. Adare and other (PHENIX Collaboration), Phys. Rev. Lett. **104**, 252301 (2010)
- [25] B. I. Abelev *et al.* (STAR Collaboration), Phys. Rev. C **80**, 064912 (2009)
- [26] M. Harrison, T. Ludlam, and S. Ozaki, Nuclear Instruments and Methods in Physics Research Section A: Accelerators, Spectrometers, Detectors and Associated Equipment **499**, 235 (2003)
- [27] M. Adamczyk *et al.*, Nuclear Instruments and Methods in Physics Research Section A: Accelerators, Spectrometers, Detectors and Associated Equipment **499**, 437 (2003)
- [28] B. B. Back *et al.*, Nuclear Instruments and Methods in Physics Research Section A: Accelerators, Spectrometers, Detectors and Associated Equipment **499**, 603 (2003)
- [29] K. H. Ackermann *et al.*, Nuclear Instruments and Methods in Physics Research Section A: Accelerators, Spectrometers, Detectors and Associated Equipment **499**, 624 (2003)
- [30] K. Adcox *et al.*, Nuclear Instruments and Methods in Physics Research Section A: Accelerators, Spectrometers, Detectors and Associated Equipment **499**, 469 (2003)

- [31] M. Allen *et al.*, Nuclear Instruments and Methods in Physics Research Section A: Accelerators, Spectrometers, Detectors and Associated Equipment **499**, 549 (2003)
- [32] C. Adler, A. Denisov, E. Garcia, M. Murray, H. Strobele, and S. White, Nuclear Instruments and Methods in Physics Research Section A: Accelerators, Spectrometers, Detectors and Associated Equipment **499**, 433 (2003), the Relativistic Heavy Ion Collider Project: RHIC and its Detectors
- [33] K. Adcox *et al.*, Nuclear Instruments and Methods in Physics Research Section A: Accelerators, Spectrometers, Detectors and Associated Equipment **499**, 489 (2003)
- [34] L. Aphecetche *et al.*, Nuclear Instruments and Methods in Physics Research Section A: Accelerators, Spectrometers, Detectors and Associated Equipment **499**, 521 (2003)
- [35] J. T. Mitchell *et al.*, Nuclear Instruments and Methods in Physics Research Section A: Accelerators, Spectrometers, Detectors and Associated Equipment **482**, 491 (2002)
- [36] C. Adler *et al.* (STAR Collaboration), Phys. Rev. Lett. **90**, 082302 (2003)
- [37] B. Alver *et al.*, Phys. Rev. Lett. **104**, 062301 (2010)
- [38] C.-Y. Wong, Phys. Rev. C **78**, 064905 (2008)
- [39] C. B. Chiu and R. C. Hwa, Phys. Rev. C **79**, 034901 (2009)
- [40] A. Dumitru, F. Gelis, L. McLerran, and R. Venugopalan, Nuclear Physics A **810**, 91 (2008)
- [41] H. Stoecker, Nucl. Phys. **A750**, 121 (2005)
- [42] J. Casalderrey-Solana, E. V. Shuryak, and D. Teaney, J. Phys. Conf. Ser. **27**, 22 (2006)
- [43] R. B. Neufeld, Phys. Rev. C **79**, 054909 (2009)
- [44] R. B. Neufeld, Eur. Phys. J. **C62**, 271 (2009)
- [45] B. Betz *et al.*, J. Phys. G **35**, 104106 (2008)
- [46] A. Adare *et al.* (PHENIX), Phys. Lett. **B649**, 359 (2007)

- [47] B. B. Back *et al.* (PHOBOS), *Phys. Rev. Lett.* **94**, 122303 (2005)
- [48] S. Afanasiev *et al.* (PHENIX Collaboration), *Phys. Rev. C* **80**, 024909 (2009)
- [49] B. B. Back *et al.*, *Phys. Rev. Lett.* **91**, 052303 (2003)
- [50] A. M. Poskanzer and S. A. Voloshin, *Phys. Rev. C* **58**, 1671 (1998)
- [51] K. Miki, S. Esumi, T. Isobe, and Y. Miake, “ $\pi^0$  and direct photon  $v_2$  in run4  $\sqrt{s_{NN}} = 200$  gev au+au collisions at rhic-phenix,” AN518
- [52] M.SHIMOMURA, H.Masui, S.Esumi, and Y.Miake, “High  $p_t$  charged hadron  $v_2$  in au + au collisions at  $\sqrt{s_{NN}} = 200$  gev,” AN473
- [53] A. Adare *et al.* (PHENIX Collaboration), *Phys. Rev. C* **80**, 024908 (2009)
- [54] A. Adare *et al.* (PHENIX Collaboration), *Phys. Rev. D* **76**, 051106 (2008)
- [55] S. S. Adler *et al.* (PHENIX Collaboration), *Phys. Rev. D* **74**, 072002 (2006)
- [56] S. S. Adler *et al.* (PHENIX Collaboration), *Phys. Rev. C* **69**, 034910 (2004)
- [57] S. S. Adler *et al.* (PHENIX Collaboration), *Phys. Rev. Lett.* **95**, 202001 (2005)
- [58] J. Adams *et al.* (STAR Collaboration), *Phys. Rev. Lett.* **97**, 162301 (2006)
- [59] T. Renk, *Phys. Rev. C* **80**, 044904 (2009)
- [60] A. Majumder, *Phys. Rev. C* **75**, 021901 (2007)
- [61] V. S. Pantuev(2007), arXiv:0710.1882 [hep-ph]
- [62] S. S. Adler *et al.* (PHENIX), *Phys. Rev. C* **71**, 051902 (2005)
- [63] T. Renk, *Phys. Rev. C* **78**, 014903 (2008)
- [64] S. S. Gubser, S. S. Pufu, and A. Yarom, *Phys. Rev. Lett.* **100**, 012301 (2008)
- [65] V. Roy and A. K. Chaudhuri, *J. Phys. G* **37**, 035105 (2010)
- [66] A. D. Polosa and C. A. Salgado, *Phys. Rev. C* **75**, 041901 (2007)

- [67] B. Alver and G. Roland, Phys. Rev. C **81**, 054905 (2010)
- [68] A. Adare *et al.* (PHENIX Collaboration)(2011), 1105.3928
- [69] K. Adcox *et al.* (PHENIX Collaboration), Phys. Rev. Lett. **89**, 212301 (2002)
- [70] B. Schenke, S. Jeon, and C. Gale, Phys. Rev. Lett. **106**, 042301 (2011)
- [71] M. Csand, T. Csrg, A. Ster, B. Lrstad, N. Ajitanand, J. Alexander, P. Chung, W. Holzmann, M. Issah, and R. Lacey, The European Physical Journal A - Hadrons and Nuclei **38**, 363 (2008)
- [72] B. H. Alver, C. Gombeaud, M. Luzum, and J.-Y. Ollitrault, Phys. Rev. C **82**, 034913 (2010)
- [73] B. Alver, M. Baker, C. Loizides, and P. Steinberg(2008), 0805.4411
- [74] H. Petersen, G.-Y. Qin, S. A. Bass, and B. Müller, Phys. Rev. C **82**, 041901 (2010)
- [75] R. A. Lacey *et al.*, Phys. Rev. C **82**, 034910 (2010)
- [76] A. Sickles, M. P. McCumber, and A. Adare, Phys. Rev. C **81**, 014908 (2010)
- [77] E. Shuryak, Nuclear Physics A **750**, 64 (2005)
- [78] U. Heinz and P. Kolb, Nuclear Physics A **702**, 269 (2002)
- [79] J. Adams *et al.* (STAR Collaboration), Phys. Rev. Lett. **92**, 052302 (2004)
- [80] J. Adams *et al.* (STAR Collaboration), Phys. Rev. Lett. **95**, 122301 (2005)
- [81] D. A. Teaney, Journal of Physics G: Nuclear and Particle Physics **30**, S1247 (2004)
- [82] G. Policastro, D. T. Son, and A. O. Starinets, Phys. Rev. Lett. **87**, 081601 (2001)
- [83] M. Luzum and P. Romatschke, Phys. Rev. C **78**, 034915 (2008)
- [84] B. I. Abelev *et al.* (STAR Collaboration), Phys. Rev. C **77**, 054901 (2008)
- [85] T. Lappi and R. Venugopalan, Phys. Rev. C **74**, 054905 (2006)

- [86] H.-J. Drescher and Y. Nara, Phys. Rev. C **76**, 041903 (2007)
- [87] B. Andersson, G. Gustafson, G. Ingelman, and T. Sjostrand, Physics Reports **97**, 31 (1983)

## Appendix A

### Flow background shape

#### A.1 Introduction

In two particle correlations, in order to extract the underlying flow background, it is important to understand the shape of the flow background. We know the single particle azimuthal distribution can be written as Eq. A.1

$$\frac{dN}{d\phi} = \frac{N}{2\pi} (1 + 2\Sigma v_n \cos n(\phi - \psi_n)) \quad (\text{A.1})$$

, where  $v_n$  is the n-th order of anisotropy measured respect to  $\psi_n$ , the n-th order of event plane.

Originally, we only consider the simpler form where only the  $v_2$  term exists as

$$\frac{dN}{d\phi} = \frac{N}{2\pi} (1 + 2v_2 \cos 2(\phi - \psi_2)) \quad (\text{A.2})$$

and the particle pair distribution will be like Eq. A.3

$$\frac{dN^{AB}}{d\Delta\phi} = \frac{N^A N^B}{2\pi} (1 + 2v_2^A v_2^B \cos(2\Delta\phi)) \quad (\text{A.3})$$

In reference [68], we know  $v_2$ ,  $v_3$  and  $v_4$  all have significant contributions. It is important to consider their contribution in the pair distribution. What we try to do here is start with a more general Eq. A.1, and then derive the generalized Eq. A.3.



## A.2 Derivation

For single particle distribution, we have the following expression Eq. A.4 and Eq. A.5 (only show  $v_2$  and  $v_3$ , but without losing the generality):

$$\frac{dN^A}{d\phi} = \frac{N^A}{2\pi} (1 + 2v_2^A \cos 2(\phi - \psi_2) + 2v_3^A \cos 3(\phi - \psi_3)) \quad (\text{A.4})$$

$$\frac{dN^B}{d\phi} = \frac{N^B}{2\pi} (1 + 2v_2^B \cos 2(\phi - \psi_2) + 2v_3^B \cos 3(\phi - \psi_3)) \quad (\text{A.5})$$

so when integrated Eq. A.4 over  $2\pi$ , we have

$$\begin{aligned} & \int_0^{2\pi} \frac{dN^A}{d\phi} d\phi \\ &= \frac{N^A}{2\pi} \int_0^{2\pi} (1 + 2v_2^A \cos 2(\phi - \psi_2) + 2v_3^A \cos 3(\phi - \psi_3)) d\phi \\ &= \frac{N^A}{2\pi} 2\pi \quad (\text{A.6}) \\ &= N^A \quad (\text{A.7}) \end{aligned}$$

which gives us the total multiplicity  $N^A$ .

For particles A and B distributed as Eq. A.4 and Eq. A.5, the pair distribution,  $\frac{dN^{AB}}{d\Delta\phi}$ , where  $\Delta\phi = \phi^B - \phi^A$  or  $\phi^B = \phi^A + \Delta\phi$ , can be written as Eq. A.8

$$\frac{dN^{AB}}{d\Delta\phi} = \int_0^{2\pi} d\phi^A \frac{dN^A}{d\phi^A} \frac{dN^B}{d\phi^B} \quad (\text{A.8})$$

So here we explicitly calculate Eq. A.8:

$$\begin{aligned}
& \frac{dN^{AB}}{d\Delta\phi} \\
= & \int_0^{2\pi} d\phi^A \frac{dN^A}{d\phi^A} \frac{dN^B}{d\phi^B} \\
= & \int_0^{2\pi} d\phi^A \left( \frac{N^A}{2\pi} (1 + 2v_2^A \cos 2(\phi^A - \psi_2) + 2v_3^A \cos 3(\phi^A - \psi_3)) \right) \\
& \left( \frac{N^B}{2\pi} (1 + 2v_2^B \cos 2(\phi^B - \psi_2) + 2v_3^B \cos 3(\phi^B - \psi_3)) \right) \\
= & \frac{N^A}{2\pi} \frac{N^B}{2\pi} \int_0^{2\pi} d\phi^A (1 + 2v_2^A \cos 2(\phi^A - \psi_2) + 2v_3^A \cos 3(\phi^A - \psi_3)) \\
& (1 + 2v_2^B \cos 2(\phi^A + \Delta\phi - \psi_2) + 2v_3^B \cos 3(\phi^A + \Delta\phi - \psi_3)) \\
= & \frac{N^A}{2\pi} \frac{N^B}{2\pi} \int_0^{2\pi} d\phi^A (1 + 2v_2^A \cos 2(\phi^A - \psi_2) \\
& + 2v_3^A \cos 3(\phi^A - \psi_3) \\
& + 2v_2^B \cos 2(\phi^A + \Delta\phi - \psi_2) \\
& + 2v_3^B \cos 3(\phi^A + \Delta\phi - \psi_3) \\
& + 4v_2^A v_2^B \cos 2(\phi^A - \psi_2) \cos 2(\phi^A + \Delta\phi - \psi_2) \\
& + 4v_2^A v_3^B \cos 2(\phi^A - \psi_2) \cos 3(\phi^A + \Delta\phi - \psi_3) \\
& + 4v_3^A v_2^B \cos 3(\phi^A - \psi_3) \cos 2(\phi^A + \Delta\phi - \psi_2) \\
& + 4v_3^A v_3^B \cos 3(\phi^A - \psi_3) \cos 3(\phi^A + \Delta\phi - \psi_3))
\end{aligned} \tag{A.9}$$

We now integrate Eq. A.9 term by term:

$$\int_0^{2\pi} 1 d\phi^A = 2\pi$$

$$\int_0^{2\pi} 2v_2^A \cos 2(\phi^A - \psi_2) d\phi^A = 2v_2^A \times 0 = 0$$

$$\int_0^{2\pi} 2v_3^A \cos 3(\phi^A - \psi_3) d\phi^A = 2v_3^A \times 0 = 0$$

$$\int_0^{2\pi} 2v_2^B \cos 2(\phi^A + \Delta\phi - \psi_2) d\phi^A = 2v_2^B \times 0 = 0$$

$$\int_0^{2\pi} 2v_3^B \cos 3(\phi^A + \Delta\phi - \psi_3) d\phi^A = 2v_3^B \times 0 = 0$$

$$\begin{aligned} & \int_0^{2\pi} 4v_2^A v_2^B \cos 2(\phi^A - \psi_2) \cos 2(\phi^A + \Delta\phi - \psi_2) d\phi^A \\ = & 4v_2^A v_2^B \int_0^{2\pi} d\phi^A \frac{1}{2} [\cos(4\phi^A - 4\psi_2 + 2\Delta\phi) + \cos(2\Delta\phi)] \\ = & 4v_2^A v_2^B \left(\frac{1}{2}\right) (0 + 2\pi \cos(2\Delta\phi)) \\ = & 4\pi v_2^A v_2^B \cos(2\Delta\phi) \end{aligned} \tag{A.10}$$

$$\begin{aligned} & \int_0^{2\pi} 4v_3^A v_3^B \cos 3(\phi^A - \psi_3) \cos 3(\phi^A + \Delta\phi - \psi_3) d\phi^A \\ = & 4\pi v_3^A v_3^B \cos(3\Delta\phi) \end{aligned} \tag{A.11}$$

$$\begin{aligned} & \int_0^{2\pi} 4v_2^A v_3^B \cos 2(\phi^A - \psi_2) \cos 3(\phi^A + \Delta\phi - \psi_3) d\phi^A \\ = & 4v_2^A v_3^B \int_0^{2\pi} d\phi^A \frac{1}{2} [(\cos(5\phi^A - 2\psi_2 + 3\Delta\phi - 3\psi_3) \\ & + \cos(-\phi^A - 2\psi_2 - 3\Delta\phi + 3\psi_3))] \\ = & 4v_2^A v_3^B \left(\frac{1}{2}\right) (0 + 0) \\ = & 0 \end{aligned} \tag{A.12}$$

$$\int_0^{2\pi} 4v_3^A v_2^B \cos 3(\phi^A - \psi_3) \cos 2(\phi^A + \Delta\phi - \psi_2) d\phi^A = 0 \tag{A.13}$$

so the final result of Eq. A.9 is

$$\begin{aligned}
& \frac{dN^{AB}}{d\Delta\phi} \\
= & \int_0^{2\pi} d\phi^A \frac{dN^A}{d\phi^A} \frac{dN^B}{d\phi^B} \\
= & \frac{N^A}{2\pi} \frac{N^B}{2\pi} (2\pi + 0 + 0 + 0 + 0 + 4\pi v_2^A v_2^B \cos(2\Delta\phi) + 0 + 0 + 4\pi v_3^A v_3^B \cos(3\Delta\phi)) \\
= & \frac{N^A N^B}{2\pi} (1 + 2v_2^A v_2^B \cos(2\Delta\phi) + 2v_3^A v_3^B \cos(3\Delta\phi)) \tag{A.14}
\end{aligned}$$

To check the final pair distribution, we integrate Eq. A.14 over  $2\pi$ , then we have

$$\begin{aligned}
& \int_0^{2\pi} \frac{dN^{AB}}{d\Delta\phi} d(\Delta\phi) \\
= & \int_0^{2\pi} \frac{N^A N^B}{2\pi} (1 + 2v_2^A v_2^B \cos(2\Delta\phi) + 2v_3^A v_3^B \cos(3\Delta\phi)) d(\Delta\phi) \\
= & \frac{N^A N^B}{2\pi} (2\pi) \\
= & N^A N^B \tag{A.15}
\end{aligned}$$

which is exactly what we expect when we have two complete un-correlate particles A and B.

For a generalized form of Eq. A.14, we have

$$\begin{aligned}
& \frac{dN^{AB}}{d\Delta\phi} \\
= & \frac{N^A N^B}{2\pi} (1 + \sum 2v_n^A v_n^B \cos(n\Delta\phi)) \tag{A.16}
\end{aligned}$$

especially in the case we have  $v_2, v_3, v_4$ , Eq. A.16 become

$$\begin{aligned}
& \frac{dN^{AB}}{d\Delta\phi} \\
= & \frac{N^A N^B}{2\pi} (1 + 2v_2^A v_2^B \cos(2\Delta\phi) + 2v_3^A v_3^B \cos(3\Delta\phi) + 2v_4^A v_4^B \cos(4\Delta\phi)) \tag{A.17}
\end{aligned}$$